



HAL
open science

Fluid Structure Interactions of Microgels in Simple Microfluidic Systems

Charles Moore

► **To cite this version:**

Charles Moore. Fluid Structure Interactions of Microgels in Simple Microfluidic Systems. Fluid mechanics [physics.class-ph]. Institut Polytechnique de Paris, 2022. English. NNT : 2022IPPAX135 . tel-04106728

HAL Id: tel-04106728

<https://theses.hal.science/tel-04106728>

Submitted on 25 May 2023

HAL is a multi-disciplinary open access archive for the deposit and dissemination of scientific research documents, whether they are published or not. The documents may come from teaching and research institutions in France or abroad, or from public or private research centers.

L'archive ouverte pluridisciplinaire **HAL**, est destinée au dépôt et à la diffusion de documents scientifiques de niveau recherche, publiés ou non, émanant des établissements d'enseignement et de recherche français ou étrangers, des laboratoires publics ou privés.



INSTITUT
POLYTECHNIQUE
DE PARIS

NNT : 2022IPPAX135

Thèse de doctorat



Fluid structure interaction of microgels in simple microfluidic constrictions

Thèse de doctorat de l'Institut Polytechnique de Paris
préparée à École polytechnique

École doctorale n°626 École doctorale de l'Institut Polytechnique de Paris (EDIPP)
Spécialité de doctorat: Mécanique des fluides et des solides, acoustique

Thèse présentée et soutenue à Paris, le 16 Décembre, 2022, par

CHARLES PAUL MOORE

Composition du Jury :

Anne-Virginie Salsac Directrice de Recherche, Université de Technologie de Compiègne et Sorbonne Université (BMBI)	Président
François Gallaire Professeur Associé, École Polytechnique Fédérale de Lausanne (LFMI)	Rapporteur
José Bico Professeur Associé, École Supérieure de Physique et de Chimie Industrielles de la Ville de Paris (PMMH-ESPCI)	Rapporteur
Anne-Virginie Salsac Directrice de Recherche, Université de Technologie de Compiègne et Sorbonne Université (BMBI)	Examineur
Suzie Protière Chargé de Recherche, Université Pierre et Marie Curie (FCIH)	Examineur
Charles N. Baroud Professeur, École Polytechnique (LadHyX) et Institut Pasteur (Microfluidique Physique et Bio-ingénierie)	Directeur de thèse
Gabriel Amselem Professeur Assistant, École Polytechnique (LadHyX)	Co-directeur de thèse



**INSTITUT
PASTEUR**

I want to dedicate this thesis to my sister. You've come a long way from back home. I'm glad that long way ended up together here.

Résumé Substantiel

Quel est le rapport entre l'aspiration de perles de tapioca à travers une paille et les tests génétiques microfluidiques ? Tous deux impliquent de faire passer des billes déformables à travers une constriction. Comprendre le transport de ces particules molles est utile pour une large gamme de technologies microfluidiques, en particulier lorsque les particules subissent de grandes déformations. Dans cette thèse, j'étudie l'interaction fluide-structure de billes de gel déformables lorsqu'elles se pressent dans et à travers des constriction microfluidiques.

La première étude réalisée dans cette thèse examine comment une particule entre dans une constriction. Pour ce faire, l'écoulement est utilisé pour piéger une bille de gel sphérique dans une section étroite d'un microcanal. En augmentant la pression, la bille entre de plus dans le resserrement. La déformation de la bille peut être décrite par un modèle de Hertz, reliant la pression autour de la bille, son élasticité, et la géométrie des billes et du canal. En pratique, nos résultats forment la base d'une nouvelle méthode pour mesurer l'élasticité de particules dans un microcanal.

L'entrée d'une particule dans une constriction agit également comme une valve qui bloque l'écoulement de fluide. En effet, l'écoulement au niveau d'une bille piégée dans une constriction est une fonction non-linéaire de la pression : le débit commence par s'accroître avec la pression jusqu'à atteindre un maximum, puis diminue et finit par s'arrêter complètement aux hautes pressions. Cette diminution du débit est liée à l'augmentation, sur plusieurs ordres de grandeur, de la résistance hydrodynamique de la bille lorsqu'elle pénètre dans la constriction. Les simulations montrent que le gradient de pression hydrodynamique s'établit alors principalement dans une zone interstitielle, entre la bille et les parois du microcanal. La résistance hydrodynamique est directement reliée à la surface de cette zone, comme dans un écoulement de Poiseuille. En combinant un modèle hydrodynamique reliant la résistance hydrodynamique à la forme déformée du gel, ainsi qu'un modèle de mécanique reliant la déformation du gel à la pression, un nouveau modèle couplé est proposé, permettant de déterminer l'écoulement dans le canal en fonction de la pression imposée. Ce modèle de valve est capable de prédire pour quelle pression le débit est maximal au niveau de la bille, et montre que la valeur de ce flux maximum augmente linéairement avec l'élasticité du gel. Le modèle permet également de prédire la pression à laquelle une bille entre complètement dans une constriction.

La deuxième étude reprend après l'entrée d'un gel dans une constriction. Les billes de gel sont acheminées à travers un comparateur microfluidique afin de mesurer leur vitesse ainsi que la résistance hydrodynamique qu'elles

ajoutent au canal. La vitesse des billes suit de près celle du fluide environnant. La résistance ajoutée des billes dépend faiblement de leur taille et donc de la constriction du gel, ainsi que de leur élasticité. Des simulations de contact sont utilisées pour comprendre plus précisément comment les billes se déforment. Pour compléter le modèle, j'utilise la théorie de lubrification élastohydrodynamique pour montrer la dépendance de la résistance ajoutée aux propriétés du gel. Je trouve un très bon accord entre la friction lubrifiante prédite et la friction mesurée entre la bille et le microcanal. L'épaisseur de la couche de lubrification augmente à la fois avec la vitesse de l'écoulement et la contrainte exercée par le canal sur la bille.

En fournissant un aperçu de l'interaction fluide-structure du gel dans des systèmes simples, cette thèse ouvre également la voie à la compréhension et au contrôle de systèmes microfluidiques beaucoup plus complexes, et au-delà de l'aspiration de billes dans une paille.

Substantial Abstract

What does sucking a tapioca ball through a straw have to do with microfluidic digital genetic testing? Both involve flowing soft spheres through a constriction. Understanding the transport of these soft particles is useful for a wide range of microfluidic technologies, especially when the particles undergo large deformations. In this thesis I investigate the fluid structure interaction of soft gel particles as they squeeze into and through constrictions which would typically be found in a microfluidic device.

The first study done in this thesis looks at how a particle enters into a constriction. To do this, flow is used to trap a spherical gel bead at narrow section of the microchannel. By increasing the pressure behind the bead, the bead enters further and further into the constriction. Numerical simulations data is combined with the experimental data to show how the pressure drop is distributed across the bead. The deformation of the bead can be modeled by Hertzian mechanics, relating the applied pressure, bead and channel geometry, as well as the bead elasticity. In practice, this is a novel method for measuring the elasticity of particles in a single thickness microchannel.

The entry of a particle into a constriction also acts as a valve that blocks the fluid flow. In effect the flow past the bead increases with pressure until it reaches a maximum before then reducing and plugging entirely. The hydrodynamic resistance of the trapped bead increases several orders of magnitude over the course of the bead penetration. Fluid simulations show that pressure drops considerably at the point of minimal cross sectional area to flow, in the corners between the beads and the microchannel. This inverse squared of this area scales with resistance as would be the case for a Poiseuille flow. Combining the model for resistance as a function of deformation, with the model of deformation as a function of pressure, a new model is proposed relating pressure and flow past the trapped gel. This valve model is capable of predicting maximum flow rate and shows that this maximum flow rate scales linearly with the effective gel elasticity. It is also capable of predicting under what pressure a gel will squeeze completely into a constricting microchannel.

The second study picks up after a gel has entered into a constricting channel. Gel beads are flowed through a microfluidic comparator in order to measure the added resistance of the gel, as well as their velocity. The speed of the beads follows closely that of the surrounding fluid. Meanwhile, the added resistance of the beads is found to be weakly dependent upon the size and thus constriction of the gel, as well as their elasticity. To aid in this analysis, contact simulations were used to see more precisely how the beads deform. Fluid simulation around deformed

beads are used to relate the velocity to the pressure drop around the particle. To complete the model, I use elastohydrodynamic lubrication theory to show the dependence of added resistance upon the material properties of the gel and find strong agreement between predicted lubricating friction and measured friction between the bead and the microchannel. Lubrication thickness grows both with velocity and the constraining force of the channel upon the bead. I hypothesize this is due to the constrained gel forces flow through the lubrication layer more so than in unconstrained lubrication.

By providing insight into the fluid-structure interaction of gel in simple systems, this thesis also paves the way for understanding and controlling much more complicated microfluidic systems, and beyond sucking balls through a straw.

Acknowledgements

First and foremost, I would like to thank my two supervisors, Charles Baroud and Gabriel Amselem. Three and a half years ago I sent an email to Charles, not knowing if he would even see it. I know I wouldn't be here today if he hadn't. Charles has managed to keep me on track and focused these last three years, and I would like to think I have grown a lot as a scientist because of it. When I arrived at LadHyX I had no idea what PDMS was. Gabriel taught me so much since I arrived here, from how to make microchannels to how to present my work. I know I have made both of them late for lunch a few dozens of times. They are both excellent supervisors and I really was lucky to work with both of them. I don't think I can properly express my gratitude to both of them.

The first set of original research in this thesis had quite a bit of help. I owe Julien Husson a thank you for taking the time to teach me microindentation. A big thanks also to Arezki Boudaoud. I had very little solid mechanics experience when I started here, and Arezki was patient enough to go over the models I had made and working out the math really helped move the project forward.

I have had the privilege of working with quite a few talented interns at LadHyx. Hiba Belkadi, who was a great first intern. Not only during the internship, but even afterwards, Hiba continued to help with the microgel resistance project. I also must thank Brouna Safi, who was a delight to work with. I'm really proud of the work we did together on microgel resistance project. I would also like to thank Elio Gereige, Nalla Sai Kiran Kumar, and Antonion Mosciatti, for working with me to set the ground work for the work Brouna would take on.

While I owe a lot of thanks to many of my lab mates, I owe an extra big thank you to Mahdi Daei Daei. Learning how to put a working simulation together is challenging, and I'm not sure I would have been able to get half of this simulation work done if he hadn't sat down with me and explained how ABAQUS works.

My lab mates were also all a huge help. My desk mates Hassan Madkour, Claire Dessales, Mahdi Daei Daie (again), and Aude Sagnimorte at LadHyX were all a huge help whether it was to ask a piece of advice or a short chat. For the same reason, I would also like to thank my desk mates at the Pasteur Institute: Nadia Vertti, Salomé Gutierrez Ramos, Lena Le Quellec and Sebastien Sart. For making my time in both labs so enjoyable, and for always offering a piece of advice whenever asked, I would like to also thank Sara Barrasa Ramos, Claire Leclech, Clara Ramon Lozano, Taha Laroussi, Valentin Laplaud, Valentin Bonnet, Shreyansh Jain, Erik Maikranz, Thévy Lok, Gustave Ronteix, Andrei Aristov, Madison Lenormand, Silvia Corsini and Alessia Castagnino.

I would like to thank my tutors, Samy Gobaa and Romain Levayer. Their advice helped keep me on track with my thesis and realize that I wasn't quite as far behind as I was afraid of. I should also thank Samy for helping me make molds for some of my experimental microchannels, without which my experiments would have been a bust.

When I was accepted for my doctorat at Pasteur, I had less than three months to prepare to immigrate to France. Marie De Tarragon had everything organized for me so that despite my own disorganisation, I was able to come here and integrate into the lab Seamlessly. For that and more I owe her a debt of gratitude.

For helping teach me so much of the technical side of microfluidics, as well as always knowing how everything works, I should also thank Caroline Frot.

I would also like thank my defence jury. François Gallaire, José Bico, for acting as my defence committee referees. They were both gracious enough to referee my mid-thesis report and I'm grateful that they've both decided to return to see the finished product. I would also like to thank my examiners, Anne-Virginie Salsac, and Suzie Protière. I know going through a thesis like this is a commitment.

Of course I would be amiss if I did not thank the Institut Pasteur for funding my research these last three years, and especially for awarding me a bourse de soudure so that I could finish this thesis to the standard I thought it needed. This research would not be possible without their help.

Finally, I have quite a few people who helped and supported outside of my thesis work. My parents, Eileen and Andre, for always encouraging me to make my PhD an adventure, and getting me to where I am today. To my sister, Nicole who's been here these last two years when it was especially lonely. To my partner, Rini Bankhwal, who helped take care of me when I only had time to write. To my aunt and uncle, Cecile and Hervé Mazard, who without a hesitation helped set me up in Paris when I arrived, and who have done so much to make me feel welcome here. To my friend Kineshta Pillay, for giving me writing advice and support from even before I started this work. To the rest of my extended family here in France for including me on all our adventures. And of course to my friends back home in Canada, who've stayed with me despite the distance.

Everyone who has helped me during my thesis and who helped me before hand has contributed to this work. In that way, I owe you all a profound debt. I hope one day I can pay that debt forward.

Contents

1	Introduction	18
1.1	Microfluidic Constrictions in Nature and in the Laboratory	18
1.2	The Mechanics of Microfluidic Constrictions	19
1.3	Thesis Outline	23
2	Making Photopolymerized Microgels	27
2.1	Introduction	27
2.1.1	Microfluidic Hydrogels	27
2.1.2	PEG Hydrogels	28
2.1.3	Microgels	30
2.1.4	Chapter Outline	31
2.2	Microfluidic Design and Gel Production	33
2.2.1	Microfluidic Emulsion Devices	33
2.2.2	Droplet Stability	36
2.2.3	Hydrogel Making Microchannel Design	38
2.2.4	Hydrogel Preparation	40
2.2.5	Protocol	40
2.3	Microgel Characterization	41
2.3.1	Droplet to Microgel Size	41
2.3.2	Microgel Stiffness	42
2.4	Conclusion	44
3	Deformation of Trapped Microgels in a 1D Constriction	47
3.1	Introduction	47
3.2	Methods	50
3.2.1	Single Thickness Microfluidic Trap Design	50

3.2.2	Measuring Flow Rate From Streamlines	53
3.2.3	Carrier Fluid Viscosity	55
3.2.4	Microgel Characterization	56
3.2.5	Experimental Protocol	56
3.2.6	Solid and Fluid Simulation Setup	58
3.3	Results	60
3.3.1	Pressure From Bypass Flow	60
3.3.2	Microgel Displacement and Deformation in a Microfluidic Trap	61
3.3.3	Small and Soft Trapped Microgels	64
3.3.4	Simulated Trapped Microgel Deformation	66
3.4	Contact Theory and Microgel Deformation	68
3.5	Hertzian Contact Between a Microgel and Trap Corners	72
3.5.1	Modeling Microgel Displacement into Trap	72
3.5.2	Microgel Deformation from Microgel Displacement	76
3.6	Discussion	77
3.6.1	Extending Trapped Microgels to Penetrating Microgels	77
3.6.2	Elastic Modulus of Trapped Microgels	78
3.6.3	Limitations of the Microgel Trap	79
3.7	Conclusion	80
4	Non-Linear Leaky Flow Around A Deforming Trapped Particle	83
4.1	Introduction	83
4.2	Methods	84
4.2.1	Experimental Overview	84
4.2.2	Simulation Overview	86
4.3	Results	88
4.3.1	Proportion of Flow Trough a Microgel Trap	88
4.3.2	Added Resistance of a Trapped Microgel	88
4.3.3	Simulating Poiseuille Flow Around a Deformed Microgel	90
4.4	Poiseuille Flow Around Deformed Microgels	91
4.5	Valve Behaviour of Deformed Microgels	94
4.5.1	Simplifying the Valve Behaviour	95
4.5.2	Maximum Flow Rate Through a Microgel Valve	96
4.6	Discussion	98

4.6.1	Practical Application Trapped Microgels	98
4.6.2	Valve Model Limitations	98
4.7	Conclusion	99
5	Lubrication and Fluid Flow Around a Microgel Traveling Through a Square Channel	101
5.1	Introduction	101
5.2	Methods	102
5.2.1	Microfluidic Comparator: Measuring Resistance of Moving Microgels	103
5.2.2	Measuring Flow in a Comparator	105
5.2.3	Experimental Materials and Protocol	106
5.2.4	Solid and Fluid Simulation Design	109
5.3	Experimental Results	111
5.3.1	Microgel Velocity, Fluid Velocity and Microgel Confinement	111
5.3.2	Resistance of a Microgel in a Square Channel	113
5.3.3	Linking Microgel Velocity and Pressure	115
5.4	Simulated Dry Confinement of a Microgel in a Square Channel	115
5.4.1	Microgel Deformation	116
5.4.2	Contact Force on a Confined Microgel	118
5.5	Forces Balance of a Confined Microgel	119
5.5.1	Pressure Force	119
5.5.2	Normal Force	120
5.5.3	Friction Force	121
5.5.4	Analysis of Gutter and Lubrication Domains	121
5.6	Flow Through Microgel Gutters	122
5.6.1	Pressure Driven Flow	124
5.6.2	Boundary Velocity Driven Flow	124
5.6.3	Superposition of Flow	125
5.7	Flow in the Lubricating Layer	126
5.7.1	Friction and Lubrication	127
5.7.2	Conventional Soft Lubrication Modeling	129
5.7.3	Lubrication, Velocity and Contact Force	132
5.7.4	Empirical Models of Friction and Lubrication	134
5.8	Lubrication Film and Pressure	135
5.8.1	Film Thickness and Pressure	135

5.8.2	Mass Balance in the Lubricating Layer	136
5.9	Future Work	139
5.9.1	Solving the Lubrication Equations and Generalizing Confined EHL	139
5.9.2	Multiphasic Resistance	140
5.10	Conclusion	141
6	Conclusion and Prospects	143
6.1	Making and Testing Microgels	143
6.2	Microgel Deformation in a Constriction Trap	144
6.3	Valve Behavior of Trapped Microgels	145
6.4	Lubrication of a Microgel in a Square Channel	145
6.5	Concluding Remarks	146
A	Theoretical Flow Around a Microgel	149

List of Figures

1.1	Microfluidic constrictions occur both in nature, and in laboratory/industrial settings. (a) Blood flow through the circulatory system often involves red blood cells (RBC) passing through capillaries which are smaller in diameter than the RBC itself, forcing the RBC to bend in order to pass through. In this micrograph, healthy RBC are shown in white within the darker capillary. Figure reproduced from Guest <i>et al.</i> [69]. (b) Sorting RBCs at various stages of malaria infection, depending upon their ability to deform and pass through rectangular microfluidic capillaries. Different stages of infection will affect whether the cells can pass through constrictions of decreasing width. Flow, Q , is passing from right to left, as indicated by the arrows. Figure reproduced from Shelby <i>et al.</i> [150]. (c) Rapid genetic sequencing using transcriptome barcoded hydrogel beads. As water containing beads pass through a brief constriction, causing upstream pressure to mount, and the water to pinch off into droplets containing the beads and cells. Reproduced from Zilionis <i>et al.</i> [187].	20
1.2	Particles which pass through simple microfluidic constrictions go through three distinct phases of motion. Each phase requires different considerations with respect to particle deformation. The microparticle must (a) enter into a constriction, (b) pass through the constriction and finally (c) exit the constriction. The flow rate Q represents the direction of flow and particle velocity.	21
1.3	There exist a variety of possible geometries through which particles can become confined in microfluidic systems. This figure summarizes the most commonly studied geometries. In order, these are a cylindrical capillary (a), a one-dimensional constriction (b), a rectangular constriction (c), a tapered capillary (d), and a tapered microchannel (e). In these figures, the particle is represented as a blue sphere, with the microchannel shown in grey. Cartesian directions are shown on each of the figure pairs, (i) and (ii).	24

2.1 (a) A diagram showing the polymerization of a sphere of PEG gel. The diagram shows the activation via ultraviolet exposure, and the binding of PEG chains at their fictionalized acrylate group via initiator activity. The figure also shows schematically the inhibition of PEG polymerization via oxygen competition. Reproduced from Debroy *et al.* [45]. (b) A comparison of PEG gel polymerization throughout its exposure to UV. As the exposure time increases, the degree of polymerization, seen as the interface between the liquid and gel PEG, becomes more apparent, however the size of these regions remains constant. Reproduced from Debroy *et al.* [45]. (c-e) A series of PEG gels of identical chemical composition and light exposure for a range of diameters. While the inner polymerized region, shaded green, grows with the microgel, the un-polymerized region, shaded blue, remains approximately the same size regardless of total gel size. Reproduced from Krutkramelis *et al.* [101]. 29

2.2 (a) A diagram explaining stop-flow lithography for making PEG microgels with custom shapes. A valve is used to periodically stop the flow of a photoreactive PEG solution. A shutter then flashes UV through a transparent mask in the desired shape of the eventual PEG microgels. The PEG then polymerizes and is flowed out of the exposure region. Reproduced from Dendukuri *et al.* [52]. (b) A sample hollow square microgels made using stop-flow lithography as described in (a). Reproduced from Dendukuri *et al.* [52]. (c) An bicoloured acrylamide janus particle. Half of the particle is dyed with a fluorescent rhodamine isothiocyanate dye, while the other is dyed with fluorescent fluorescein isothiocyanate. Reproduced from Shepherd *et al.* [151]. (d) A core-shell tripropyleneglycol diacrylate microgel where the core has ruptured the shell of the microgel, making cup-shaped microgels. Reproduced from Nie *et al.* [129]. (e) A microfluidic device used in the inDrop genetic sequencing. Microgels containing barcoded reverse transcriptomes are flowed into droplets with single cells. These can then be used to rapidly genetically analyze individual cells. Reproduced from Klein *et al.* [99]. 32

2.3 A comparison of different droplet production methods. In order, a diagram of the flow focuser in the dripping (a) and jetting (b) regimes, a micrograph (c) flow focuser, and and a diagram (d) and micrograph (e) of step droplet producer. The diagram of a step producer in (d) is modified from Dangla *et al.*[41] 34

2.4 Micrographs of PEG droplets made using a carrier phase containing 0.5 % RAN (a), 3 % RAN (b) and 3 % RAN with 0.2 % SDS in the droplet phase (c). (d) A comparison of the diameters created during this process. Monodispersity is improved when increasing the RAN content as well as when adding 0.2 % SDS 37

2.5 (a) A reproduction of the microfluidic mask of the flow focuser used in this experiment. This flow focuser was designed as a single height microfluidic chip. A micrograph of droplet production at the flow focuser junction is included. Micro-channel dimensions are shown, with the neck width varying from $25\mu m$ (shown) to $66\mu m$. Microchannel height varied from $h = 80\mu m$ to $h = 200\mu m$ depending on desired droplet size. (b) A diagram of the experimental setup. Three syringes were connected to syringe pumps, and attached to the flow focuser, under a microscope. The droplets were measured during production to ensure proper sizing. UV light was provided to the flowing droplets. Microgels were collected in a collection tube. (c) The wash cycle protocol is illustrated. Microgels were washed by a cycle of adding solvent, mixing, centrifuging to separate the microgels from aspirant, and removing the aspirant. This cycle was repeated several times, adding FC-40, ethanol, water and finally 10 % aqueous SDS. 39

2.6 A comparison of 9 batches of microgel diameters before and after photo-crosslinking. The microgels in question contain a total of 65 % (v/v) PEG mw200 and PEGDA mw700 with varying proportion, as well as 5 % (v/v) PI and 1 % (w/v) SDS (aq). An inset shows a typical micrograph of gel particles which have been placed on a microscope slide in order to have their diameters measured. 43

2.7 (a) A diagram of microindentation, as described in Guillou *et al.* [70]. The cantilever is shown compared to its original position (faded) to illustrate the deflection at the base and at the indentation. (b) A micrograph of microindentation using an immobilized microgel. (c) A comparison of microgel elasticities measured by microindentation. All microgels contained 5 % (v/v) PI, 1% (w/v) SDS, and a total of 60 % (v/v) PEG mw 200 and PEGDA. Each point represents one sample, with $n \geq 6$ 45

3.1 Examples of different geometric types of constriction entrances. (a) A cell entering into a sudden axisymmetric constriction. In this case the cell is undergoing micropipette aspiration to assess the viscous modulus. Reproduced from González-Bermúdez *et al.* [64]. (b) A tapered capillary containing an acrylamide based microgel. As pressure increases the microgel is pushed further into the capillary, thereby measuring its Young's modulus. Images are provided in descending order of increased pressure. Reproduced from Wyss *et al.* [173]. (c) The passage of a red blood cell (RBC) through a tapered microfluidic constriction. The in plane height of the microchannel is kept constant. The constriction was placed in series with identical constrictions to measure the impact of repeated confinement and release. Reproduced from Guo *et al.* [73] (d) An elastic cell as it enters into a microchannel which suddenly decreases in height and width. A diagram of the microchannel is provided as well. Reproduced from Luo *et al.* [117]. 48

3.2 (a) A diagram of the region of interest for the microfluidic trapping channel. The bypass and thrupass are shown in full. Zooming in, the a diagram of the bypass/thrupass junction shows microgels passing and getting stuck in the trap. Further zooming in, a micrograph of a trapped and deformed microgel is shown. (b) A diagram of the microfluidic trap with relevant dimensions labeled. The thrupass is separated into the trap, where the gel rests and slit region, which constricts the gel and prevents passage. (c) A negative of the full microfluidic channel mask, presented at 2x scale. The microfluidic mask used in this work, is presented alongside the original design, which included ten parallel traps for each size of trap slit. 50

3.3 (a) A resistance diagram relating the flow through the thrupass and bypass of the microchannel, as well as the corresponding sections on the microchannel itself. (b) A reconstructed separatrix of flow at the junction of the thrupass and bypass lines. The streamlines are reconstructed using 53

3.4 (a) A diagram of a microfluidic comparator, with one inlet containing the reference solution of water and ink, Q_{H_2O} , and a second solution containing the SDS solution, Q_{SDS} . As downstream resistances are unequal due to changes in viscosity of the ink and SDS, there is a deflection of the streamline. (b) A micrograph of the microfluidic comparator used to characterize the SDS. (c) A resistance diagram of the comparator. When the flow from the ink passes entirely through the top channel, and the SDS solution passes entirely through the bottom, then the difference in resistance will be proportional to the difference in flow rates. 55

3.5 A diagram of the experimental setup. The microchannel is placed on a microscope and connected to two syringes on syringe pumps. A waste line is attached for fluid exiting the microchannel. Videos of the microchannel are recorded for analysis. 57

3.6 (a) A diagram showing the geometric setup of the contact simulation. The simulation was performed along the axes of symmetry of the geometry. Annotated for diameter, d , channel height, h , corner radius, r_c , and constriction width, w . A weight force, F_p (late replaced with a pressure distribution) is also included. The contact declarations of master and slave surface are annotated as well. (b) A diagram showing the fluid simulation, corresponding to an undeformed (spherical) gel. The simulation was performed along the axes of symmetry for the geometry. Boundary conditions are listed. Dimensions are identical to those of the contact simulation. (c) A diagram of the pressure distribution used on the second set of simulations. The coordinate Z was made internally to define how pressure tapers off from the maximum region. This is an approximation of the distribution found by fluid simulation. (d) Simulated pressure distribution on the underside of the microgel. In order, these simulations correspond to deformation at pressures of $P_{gel} = 0$, $P_{gel} = 2.4$ kPa and $P_{gel} = 4$ kPa. The scale bar describes the fraction of the inlet pressure experienced where $\Delta P = 1$ kPa. 59

3.7 A comparison of the pressure drop across the microgel, P_{gel} as the flow rate provided by the syringe pump increases. The legend provided separates data by slit width and by elasticity of the microgels. Note that the hard microgel, $E^* = 15 \text{ kPa}$ is in a channel of height $h = 85 \mu\text{m}$, while the other two gels, $E^* = 1.5 \text{ kPa}$ and $E^* = 0.11 \text{ kPa}$ are larger and are contained in a channel of height $h = 140 \mu\text{m}$. This was done to maintain $d \approx h$ 61

3.8 Micrographs comparing a trapped microgel undergoing increasing pressure. From left to right the pressure is (a) $P_{\text{gel}} = 10 \text{ Pa}$, (b) $P_{\text{gel}} = 500 \text{ Pa}$ and (c) $P_{\text{gel}} = 2288 \text{ Pa}$. The microgel in question corresponds to a microgel of batch "Gel B", with $E^* = 1.5 \pm 0.4 \text{ kPa}$ and $d = 139 \pm 2.1 \mu\text{m}$ 62

3.9 (a) A diagram of a trapped microgel being viewed through the microscope. The diagram is annotated with geometric parameters measured in this study. The microgel diameter, d is measured at the lowest flow rate tested, as is the slit width, w . The microgel displacement, l is measured from its back, while the penetration, l_f is measured relative to the front of the microgel at the lowest flow rate tested. The channel contact, b_c is measured as a surrogate for the actual radius of contact between the microgel and the trap. The dashed circle represents a microgel sitting in the trap undergoing no deformation. (b) A comparison of the displacement of the microgel with the pressure drop applied to the gel, P_{gel} . An inset provides the same data on a logarithmic scale in order to better view the data for the softer microgels. (c) A comparison of the penetration of the microgel with the displacement of the microgel in general. A unit line is provided for reference. (d) A comparison of the linear contact between the microgel and the channel, and the displacement of the microgel. 63

3.10 (a) A comparison of pressure and supplied flow rate for data corresponding to microgels from batch Gel C, corresponding to a diameter of $d = 84.2 \pm 1.1 \mu\text{m}$, and an effective elasticity of $E^* = 48.6 \pm 24.9 \text{ Pa}$. (b) A comparison of the penetration, l_f of microgels from batch Gel C with the pressure applied to the gel, P_{gel} . (c) A micrograph of a small, soft gel from batch Gel C which was stuck in the trap slit due to friction. The outline of the microgel has been highlighted in red for ease of viewing. . . 65

- 3.11 Data for the simulated microgel quarter section as it is pulled into the microfluidic constriction. This simulated microgel has a diameter of $d = 80 \mu\text{m}$, and elasticity of $E^* = 11.4 \text{ kPa}$, while the trap measures $w = 15 \mu\text{m}$ and $r_c = 15 \mu\text{m}$, with a height of either $h = 81 \mu\text{m}$ or $h = 85 \mu\text{m}$. See Fig. 3.6 for details. (a) The displacement l of the microgel compared with the maximum negative applied pressure P_{gel} . (b) The penetration of the microgel into the constriction, l_f , compared with the displacement of the microgel, l . A reference line is provided. (c) The contact between the simulated microgel and microchannel, b_c , compared with the displacement of the microgel, l . (d) A comparison of the overall deformation of the microgel, corresponding to $h = 85 \mu\text{m}$, and from left to right $P_{\text{gel}} = 800 \text{ Pa}$, $P_{\text{gel}} = 2400 \text{ Pa}$ and $P_{\text{gel}} = 4000 \text{ Pa}$. The scale bar indicates total nodal displacement relative to $P_{\text{gel}} = 0$. (e) An opposite view of the microgel highlighting contact between the microgel and the microchannel in white. Deformation states correspond from left to right to $P_{\text{gel}} = 800 \text{ Pa}$, $P_{\text{gel}} = 2400 \text{ Pa}$ and $P_{\text{gel}} = 4000 \text{ Pa}$ 67
- 3.12 (a) A comparison of the trap geometry (left) with the “sphere balanced between two cylinders” approximation made in this analysis (right). (b) A two dimensional projection of the microgel sitting on the trap corners, in both an undeformed (left) and deformed (right) state. The trap corners here are represented as two cylinders. The deformed microgel shows a comparison of the penetration length, l_c with microgel displacement, l , as well as the pressure and contact forces, F_p and F_c respectively. Note that the label for the leftmost F_c was omitted to facilitate reading. (c) Isometric view of the contact between the microgel and the trap corners, highlighting the major and minor radii of contact, a and b respectively. The gray material represents the fluid phase between the microgel and trap, shown as a quarter section for ease of viewing. 69
- 3.13 Three projections of pressure isobars onto the bottom of the microgel. Perspective is given from the bottom of the slit looking towards the microgel. Microgels shown from left to right correspond to 0 deformation, deformation under $P_{\text{gel}}/E = 0.12$ and $P_{\text{gel}}/E = 0.2$, respectively. The approximated region over which the pressure is applied is highlighted in green in the rightmost panel. The color bar shows the fraction of the inlet pressure, P , corresponding to each isobar. 71
- 3.14 A comparison of the displacement of the microgel predicted by Eq. 3.22 with that measured experimentally (color) and by simulation (white). The inset is simply included to remind readers the physical significance of l and d and where $l_{\text{theory}} = \mathcal{F}(w, r_c, d, P_{\text{gel}}, E^*)$. A reference line of $y = x$ is provided to compare goodness of fit of the model. Data shown is limited to $l/d < 0.3$ to better focus on the range of interest to this model. 73
- 3.15 A comparison of stress distribution within a simulated microgel. Microgels shown are undergoing (a) $P_{\text{gel}} = 800\text{Pa}$ and $l/d = 0.045$ and (b) $P_{\text{gel}} = 6400\text{Pa}$ and $l/d = 0.16$. Symmetry is imposed on the right side of the semicircle shown. Elemental Mises stresses are shown, with color bar provided. . . . 74

3.16	A comparison of the deformation of the microgel with that predicted by Hertzian contact theory. The left axis corresponds to experimental data, while the right corresponds to simulation data. The value of $b_C _{l=0}$ corresponds to the value of b_c for a single set of experiments with the same microgel for which displacement is 0, as indicated by the inset. The simulated a is measured directly. A referene line $y = x$ is provided for reference.	75
4.1	Soft valves effectively control flow through them by deforming depending upon the pressure applied, and are found in nature. (a) A cross sectional view of a xylem bordered pit membrane from <i>Pinus Sylvestris</i> . As pressure increases the membrane is forced to close, regulating water flow within the tree. Reproduced from Bauch <i>et al.</i> [19]. (b) A diaphragm septum in a cell wall which regulates flow through it. reproduced from Louf <i>et al.</i> , originally from Boekhout <i>et al.</i> [115, 22] (c) A model of the septum diagram shown in part (b), demonstrating two modes of regulating flow in response to changes in pressure difference. Reproduced from Louf <i>et al.</i> [115].	84
4.2	A review of the experiment explained in detail in the previous chapter. (a) A diagram of the microfluidic channel used in this experiment. Zooming in there is the thrupass line where the microgel is trapped, and zooming further there is a micrograph of a trapped microgel. (b) A resistance diagram corresponding to the microchannel, including highlighting the resistances due to the bypass, R_{byp} , thrupass, R_{thru} and microgel, R_{gel}	85
4.3	(a) A diagram of the simulated microchannel with an undeformed, spherical microgel cutout. The microchannel is cut into quarter sections, and dimensions for the channel width, w_{ch} , height, h , constriction/slit width w and channel corner, r_c are included, as well as the microgel diameter, d . To capture flow downstream from the microgel, a $z = 60 \mu\text{m}$ length of the constriction is also included. (b) The same diagram of the simulated microchannel as in (a), annotated with the boundary conditions on each surface. Inlet and outlet pressures are provided as uniform P_{in} and P_{out} respectively.	86
4.4	(a) A comparison of the flow through the thrupass, Q_{thru} with the total inlet flow rate Q for microgels where $E^* = 15 \pm 9 \text{ kPa}$ and diameter $d = 83.4 \pm 2.9 \mu\text{m}$. This is compared with the flow relationship for an empty microchannel, $h = 85 \mu\text{m}$ and $w = 31 \mu\text{m}$. The inset shows a micrograph of a trapped microgel with flow rate directions labeled. Streamlines reconstructed from videos of the tracer beads in flow are overlaid to the micrograph in order to show how Q_{thru} and Q_{byp} are determined. (b) A comparison of flow through the thrupass with inlet flow rate for all different microgels tested. This is placed on a log-log plot in order compare the different scales for each of the microgels.	87

4.5 (a) The added hydrodynamic resistance of a trapped microgel compared with the flow rate at the channel inlet. An inset is provided showing the same data on a log-linear scale to aid the reader. (b) The added hydrodynamic resistance of a trapped microgel compared with the displacement of the microgel into the microchannel. The inset shows a diagram of a deformed microgel with displacement labeled. 89

4.6 (a) The simulated hydrodynamic resistance of deformed and trapped microgels, compared with their displacement. (b) Simulation of the flow around an undeformed microgel (left), and a one deformed under a simulated pressure of $P_{\text{gel}} = 4$ kPa (right). Color indicates the pressure normalized by the inlet pressure P . Isobars are shown in white. Note how the deformed microgel focuses the pressure drop into a narrow area. x and y directions represent the imaging plane. 90

4.7 Streamlines of flow around trapped microgels. Microgels from left to right, are deformed under pressures of (i) $P_{\text{sim}}/E = 0$, (ii) $P_{\text{sim}}/E = 0.12$ and (iii) $P_{\text{sim}}/E = 0.2$. Streamline colors represent the value of the pressure along the streamline. (b) A magnified diagram showing the dimensional makeup of Λ . (c) A comparison of the base and height of the triangle which makes up Λ , each normalized by the microgel diameter. 92

4.8 The measured gel hydrodynamic resistance R_{gel} as a function of the area Λ of the triangle through which the flow must pass (see inset). R_{gel} and Λ are respectively normalized by the resistance to flow R_0 and the area Λ_0 in the absence of gel deformation. A unity line is provided for reference. 94

4.9 Comparison of flow rate through the obstructed thrupass channel, shown in points, with the predicted flow rate, shown as dashed lines. Normalized flow rates, \mathcal{Q} , are given as a function of the normalized pressure \mathcal{P} for the full range of pressures tested experimentally. The data here is limited to $l/d > 0.3$ for ease of reading. 96

4.10 (a) Maximum experimental flow rate Q_{max} past the microgel as a function of the Young's modulus E^* of the trapped bead. Points: Experimental data. Error bars represent 1 standard deviation. Line shown represents the linear best fit. (b) A comparison of flow rate through the obstructed thrupass channel, normalized to the predicted maximum flowrate, Q_{max} and the pressure normalized to the pressure predicted to achieve the maximum flow rate, P_{max} 97

4.11 The theoretical flow rate predicted by Eq. 4.15 for a microgel with a diameter of $d = 80$, undeformed resistance of $R_0 = 1$ and elasticity of $E^* = 1$. (a) Predicted flow rates for a microfluidic trap with a corner radius of $r_c = 15$ for a range of different w . (b) Predicted flow rates for a microfluidic trap with a width of $w = 15$ for a range of different r_c 98

5.1	(a) Diagrams of various comparators as viewed from above. These comparators are controlled either by inlet pressure (i and ii) or by inlet flow rates (iii). Pressure controlled comparators measure the added resistance starting from the inlet, while flow driven comparators measure the resistance starting from after the comparator. The interface between the two flow streams can be read either as the streams merge towards the outlet (i) or relative to a split in the streams (ii and iii). The perturbing object (e.g. droplet or particle) is shown in blue in the test channel. The region of interest corresponds with the test channel and the comparator itself. (b) Resistance diagrams for various types of microfluidic comparators, corresponding to those in (a). (c) A micrograph of a flow driven comparator as a microgel enters into the comparator region (left), and as it passes through the comparator channel (right).	104
5.2	(a) The microfluidic mask used in this design, containing two different comparator channels. The principle difference between the two channels is the inclusion of a third inlet used to balance suspended gels and carrier fluid. The two inlet channel was used for measuring viscosity. The mask is shown at 2x scale. (b) An annotated diagram of the microfluidic comparator. Interface deflection measurements are indicated by X_{cr} at the comparator and X further down the channel. (c) A diagram showing the experimental setup. This includes syringe pumps, the microfluidic channel, microscope, camera, data acquisition and waste.	107
5.3	(a) A diagram showing the contact simulation between the microgel (blue) and microchannel (grey). Channel and microgel dimensions are listed, as well as the cut planes of symmetry. The master and slave designations refer to the contact declarations done for the static explicit simulation. Contact was undertaken by advancing the microchannel a distance of Δw towards the microgel. An inset highlighting the cut plane on an experimental micrograph of a moving microgel is provided for reference. (b) A deformed microgel in contact with the advancing microchannel wall. Colouring represents total displacement in order to better illustrate the deformation. The displacement of the microchannel walls corresponds with $\Delta w = 7.5 \mu\text{m}$.	109
5.4	(a) A diagram outlining the model parameters for the simulated flow around the confined microgel. The domain was cut along the lines of symmetry. This microgel in particular is undeformed, i.e. $d = 100 \mu\text{m}$. The microgel surface was set to move at a constant velocity, u_{gel} , the outlet was set to a constant pressure $P = 0$ and inlet pressure was declared to correspond with pressure drop across the microgel, $P = P_{\text{gel}}$. (b) A simulated fluid domain corresponding with $d = 104 \mu\text{m}$. (c) A simulated fluid domain corresponding with $d = 115 \mu\text{m}$.	110

5.5 (a) Sample micrographs showing the progression of a microgel entering into the comparator region and progressing into the test channel. The microgel in question corresponds with a diameter of $d = 102 \mu\text{m}$ and an elasticity of $E^* = 5.2 \pm 1.2\text{kPa}$. (b) The position of the microgel shown in (a) over time, relative to when the microgel enters the test channel. (c) A comparison of the velocities of microgels with the mean fluid velocity, $u_{\text{fluid}} = (Q - \Delta Q)/wh$, and microgel diameter. 112

5.6 (a) A comparison of the added resistance to flow in the test channel R_{gel} with the diameter of the microgels d and the flow passing through the test channel, $Q - \Delta Q$. (b) A comparison of the pressure drop which occurs across the moving microgel, P_{gel} with its diameter, d and the microgel velocity u_{gel} . Symbols classify experiments by microgel elasticity, E^* and the fluid viscosity μ 114

5.7 A comparison of normalized pressure drop across the microgel P_{gel}/E^* with degree of confinement, d/w . Data has been separated into that using a water solution and that using a glycerol solution. . . . 115

5.8 A comparison of the change in relative velocity, u_{gel}/u with changes in microgel confinement d/w , as well as the relative pressure P_{gel}/E^* 116

5.9 (a) The simulated contact pressure distribution across a quarter section of a microgel as the microchannel walls are moved towards the microgel by a distance of Δw . Color bars represent contact pressure, in Pa . (b) Simulated contact area as a function of the rescaled microgel diameter. The microgel diameter was rescaled such that $w = 100 \mu\text{m}$, and contact area was rescaled accordingly. A range of Poisson ratio, ν was also tested to validate the use of $\nu = 0.35$ for the model microgel. The best fit for $\nu = 0.35$ is plotted alongside the data. (c) Simulated cross sectional area as a function of rescaled microgel diameter. The microgel diameter was rescaled such that $w = 100 \mu\text{m}$, and cross sectional area was rescaled accordingly. The solid line represents the best fit described in the text. The inset shows visually the cross sectional view of the microgel. (d) Contact pressure as a function of rescaled microgel diameter. The solid line represents the best fit described in the text. The inset shows the growing area and contact pressure as confinement increases. The microgel diameter was rescaled such that $w = 100 \mu\text{m}$. Force was rescaled assuming $E^* = 1 \text{ kPa}$ 117

5.10 The forces on a microgel during steady state transit through a test channel. At steady state, the frictional F_f and pressure driven F_p forces are balanced. The compressive forces due to confinement and fluid pressure, F_n are balanced with themselves. The direction of fluid flow and microgel motion are indicated. The lubrication layer is approximated by the height t . Due to the approximately square geometry of the microchannel, the force balance is the same from the top and side of the microgel. . . 119

5.11 (a) A sample superposition of Poiseuille flow and Piston-Couette flow around a deformed microgel. The microgel in question corresponds with $d/w = 1.08$, $\nu = 0.35$. (b) The relative mean fluid velocity as a function of microgel confinement for Poiseuille and piston-Couette flow. The reference velocity, u_0 is the microgel velocity for piston/Couette flow and the mean velocity in an empty microchannel for Poiseuille flow. (c) The simulated relative resistance, $R_{\text{gel},0}/R_0$, compared with the minimal relative fluid cross sectional area, $1 - \Lambda_{cs}/w^2$. The reference resistance is that of an empty microchannel, $R_0 = 28 \frac{\mu z c h}{w^4}$. The dashed line represents the scaling law predicted by integrating the resistance over an approximation of the microgel body. The solid line represents the best fit described in the text. (d) The mean fluid velocity relative to the microgel velocity, $u_{\text{fluid}}/u_{\text{gel}}$ with the occlusion of the the microchannel by the microgel, Λ_{CS}/w^2 . The solid line represents the best fit described in the text. 123

5.12 A comparison of the fluid flow predicted by superposition of the Poiseuille flow past a static microgel and the piston/Couette flow from a moving microgel, with the experimental fluid flow rate. A unity line is provided for reference. 126

5.13 (a) A comparison of the steady state frictional force, $F_f = F_p$ acting on the microgel with the compressive force, F_n and the viscous velocity, μu_{gel} . A free body diagram of the microgel is provided as an inset. (b) The mean lubricating thickness, \bar{t} as a function of microgel diameter, d and velocity u_{gel} . 128

5.14 (a) A typical solution for pressure and film thickness for an elastohydrodynamic lubricating contact. Adapted from Zargari *et al.* [181] (b) A diagram of elastohydrodynamic lubrication regimes depending on the parameters $\mathcal{G}_e = \mathcal{W}^{8/3}/U^2$ and $\mathcal{G}_v = \mathcal{G}\mathcal{W}^3/U^2$. The regions are divided into the piezo viscous rigid (PR), piezo viscous Elastic (PE), isoviscous rigid (IR) and isoviscous elastic (IE) regions. Adapted from Esfahanian *et al.* [58] (c) A diagram of the microgel (blue) separation from the wall (grey, hatched) due to the lubricating layer of height t . The local deformation t_0 is illustrated as well, relative to the undeformed microgel outline in red. The profile of t is a rough estimation of a typical EHL. (d) A diagram of a half section of the microgel with the lubrication region, Λ_{ct} highlighted. This region corresponds with the area of the microgel in contact with the microchannel in the absence of any lubricating fluid. 129

5.15 (a) Friction coefficient presented as a function of the nondimensionalized velocity and compression. (b) Lubricating thickness coefficient presented as a function of the nondimensionalized velocity and compression. 133

5.16 (a) A best fit of the friction coefficient with the normalized velocity and constriction. This is also compared with the microgel confinement. Data has a coefficient of determination. A reference line is provided to aid comparing the fit of the data. (b) A best fit of the lubrication layer thickness with the normalized velocity and constriction. This is also compared with the normalized mean pressure. Data has a coefficient of determination. A reference line is provided to aid comparing the fit of the data. . . . 134

5.17 The lubrication layer thickness compared with the predicted thickness, including a contact force term, a velocity term and a mean pressure term. 136

5.18 (a) A diagram of a confined microgel, highlighting the lubrication domain (yellow) and the gutters (violet) around the microgel. The in question microgel is cut perpendicular to the channel at its midpoint. (b) A comparison of the flow through the lubricating film, represented by $(u_{\text{fluid}} - u_{\text{Piston}} - u_{\text{Poiseuille}})/u_{\text{gel}}$, compared with the nondimensional contact force, \mathcal{W} and pressure, \mathcal{P} 137

A.1 (a) A diagram of the gutter around a microgel passing through a square confinement. The serial sections through which flow passes are labeled for the gutter and dome parts of the deformed microgel. (b) A comparison of the relative predicted microgel resistance $(2R_{\text{dome}} + R_{\text{cso}})/R_0$ with the relative contact radius, a/d 150

List of Tables

1.1	A brief overview of some studies of single particle, capsule or cell passage through microfluidic constrictions, classified by the geometry of constriction and whether the particle is entering or passing through the constriction.	25
3.1	The resistances calculated for the bypass and thrupass lines for various channel heights, h , and trap slit widths, w . Resistances are calculated for 10 % (aq) SDS. Note that the actual resistance for the bypass channel is calculated based on the channel width measured under the microscope for each individual microchannel.	52
3.2	Microgel bead sizes and formulations used in this study, and their elasticity as measured using microindentation [70]. The elasticity was controlled by varying the amount of PEG-Diacrylate (PEGDA), as well as changing the molecular weight of the PEGDA. The microgels had a total of 65 % (v/v) PEG and PEGDA, with 5 % (v/v) photoinitiator 2-hydroxy-2-methyl-1-phenyl-propan-1-one and 1 % (aq) (w/v) SDS.	56
3.3	A comparison of microgel elasticities as measured by microindentation and by the microfluidic slit-trap. Note that elasticities measured by the trap had data limited to within the range $l/d < 0.2$	79
5.1	Summary of PEGDA microgels tested. All microgels were made of an aqueous solution containing 5 % (v/v) photoinitiator (2-hydroxy-2-methyl-1-phenyl-propan-1-one, Sigma Aldrich, Darmstadt Germany), contained a total of 65 % (v/v) PEG (mw 200) and PEGDA (mw 700), and 1 % SDS. Gels were photopolymerized in a flow focusing channel as described in Ch. 2. Elasticity measurements were made using the elasticity trap described in Ch. 3 ($n \geq 3$).	108
5.2	A summary of some models of soft EHL between a spherical particle and flat surface. Models predict both friction and lubrication layer thickness.	132

Chapter 1

Introduction

1.1 Microfluidic Constrictions in Nature and in the Laboratory

Oftentimes when transporting objects such as cells, particles or even drops through microfluidic systems, the objects must pass through a channel which is narrower than the object passing through it. In order to pass through this constriction, the object must deform and change its shape. Otherwise the object will become stuck at the entry of the constriction, diverting flow around itself. The human circulatory system, for example, is made of networks of capillaries which are smaller than the red blood cells that pass through them [69], see Fig. 1.1a. Whether or not the blood cells can deform and pass, is also a matter of life or death, especially since diseases like malaria and sickle cell anemia drastically altering this crucial physiological process [150, 149, 9]. Blood flow is but one example among many which highlight the importance of the mechanics of soft objects passing through narrow constrictions. Other such examples include cancer metastasis [13, 90], propagation of parasitic worms [83, 160, 169], and industrial sieving [92].

Sickle cell disease, malaria, and even sepsis all affect the bio-mechanical properties of blood cells [150, 149, 9, 175, 136]. Separating healthy blood from diseased has in recent years shown considerable promise in the realm of lab on a chip technology. One of the earliest examples of this application was performed by Shelby *et al.* [150]. In this case, cells infected with progressive stages of malaria were flowed into a narrow microfluidic channel, at which point healthy cells would pass, while the progressively diseased cells would become stuck, as shown in Fig. 1.1b. More recent examples of constriction based cell sorting include separating white and red blood cells by size and spike cancer cells from whole blood due to differences in deformability [65, 185].

Expanding from sorting cells and particles by their passage through microfluidic constrictions, mechanical properties can also be directly measured using flow through microfluidic constrictions. Micropipette aspiration is a technique used to measure the elastic properties of a cell or particle by aspirating it into a micropipette, and relating the deformation back to the elastic properties of the cell or particle [157]. This principle has been extended to a

range of microfluidic platforms, from putting these micropipettes in parallel [104, 105, 73, 57], to allowing measuring instantaneous elasticity of cells as they deform [117] to estimating the pressure necessary to push a particle entirely through a constriction [117, 139]. More recently, several studies of cellular behaviour have used microfluidic constrictions to measure the cell response to physical stress [177, 119, 85]. In effect, by repeatedly flowing these particles or cells into constrictions and forcing them to deform, it is possible to measure stiffening by measuring the readiness to deform at the proceeding constriction cycle.

Forcing particles to pass through a microfluidic constriction also has a direct effect on the flow around the particle. As the particle enters into a microfluidic constriction, the space through which flow can pass is suddenly drastically reduced, if not cut off entirely. As a consequence, flow through the channel decreases and pressure upstream increases until either the pressure rises sufficiently to force the particle through the constriction or the limits of the system are reached. Clogging and fouling are frequent issues in microfluidic systems as well as industrial processes [54], as either individual particles too big for part of a microchannel [179, 54], or a collection of particles and debris collect at the constriction [54, 10], thereby reducing flow through the opening. This has led to a number of design strategies to avoid such clogging, such as filtering fluids as they enter the microfluidic system [179, 102].

The effect particles have on flow through constrictions is not always something to be avoided. A long standing challenge in droplet microfluidics has been the Poisson distribution of particles or cells contained in each test droplet. One strategy to remedy this is triggered droplet encapsulation [3, 4]. As fluid containing soft microparticles flows into a microfluidic emulsion channel, the particles pass through a narrow constriction. As pressure upstream increases, the fluid containing the microparticle is forced to pinch off into a distinct droplet. This effectively guarantees a single particle occupies each droplet, greatly increasing experimental efficiency. This technique is also the basis of several droplet based genetic sequencing techniques such as inDrops [187, 99, 98], see Fig. 1.1c. There, due to the near 1:1 occupancy rate of droplets to genetically barcoded hydrogel particles, it is possible to efficiently analyze tens of thousands of cell samples in a single experiment [187, 99, 98].

1.2 The Mechanics of Microfluidic Constrictions

The diverse range of both natural and practical applications of microfluidic constrictions is reflective of the wide variety of physics at play. The physics of microfluidic constrictions consists of a fluid-structure interaction, where the bulk flow pulls an object into a constriction, thereby deforming it, and simultaneously changing the flow streamlines to accommodate the obstruction created by the object. In order to pass through a constriction, a body must first enter, then travel through the constriction, and then finally exit the constriction. The physics of each part of this process is strongly affected by the geometry of the constriction itself. Finally, in addition to the geometry of the constriction, what is being pulled through the constriction, be it a cell, solid particle or droplet, has a major effect on the physics at play. With the different combinations of geometry and mechanics of what is being pulled through

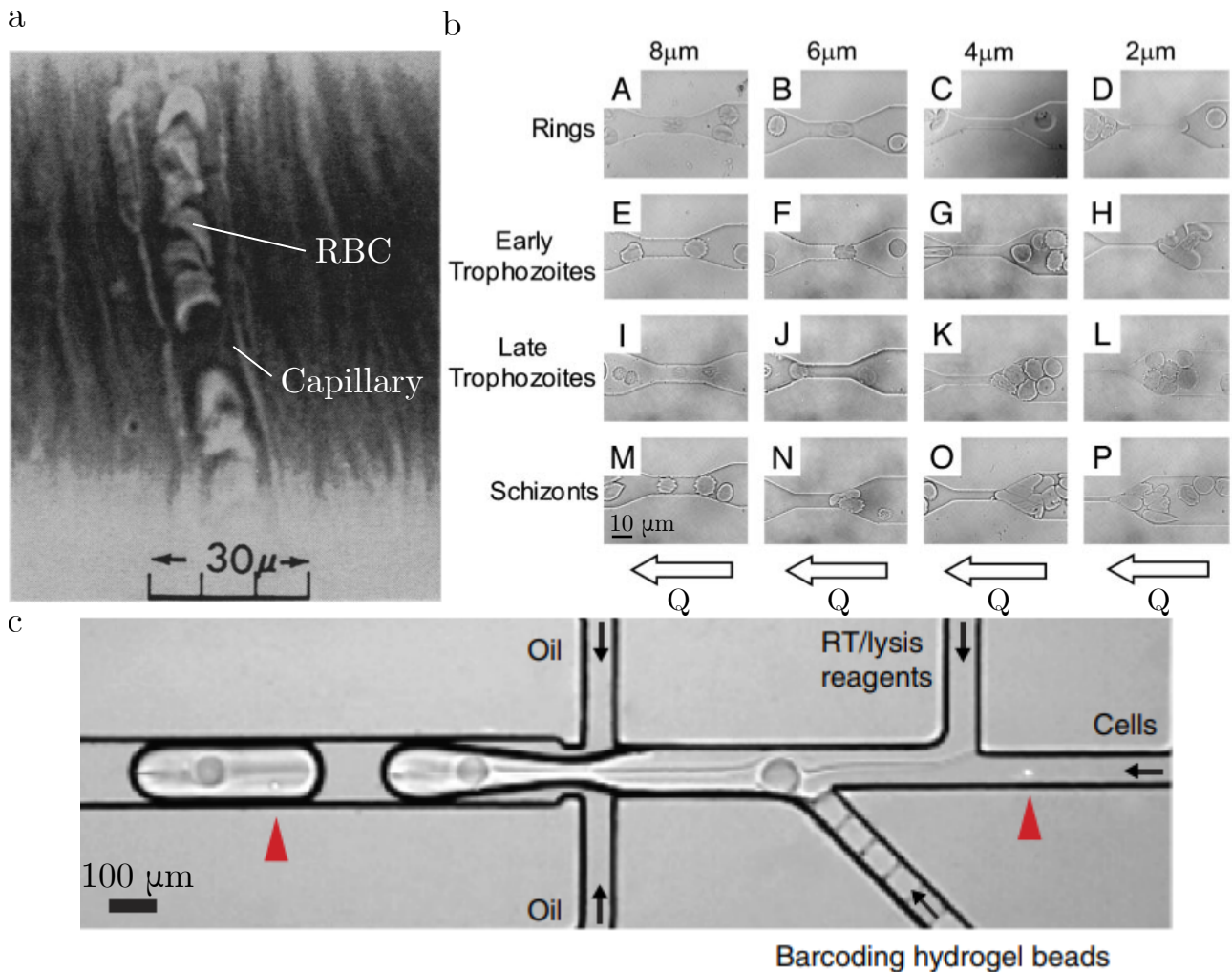


Figure 1.1: Microfluidic constrictions occur both in nature, and in laboratory/industrial settings. (a) Blood flow through the circulatory system often involves red blood cells (RBC) passing through capillaries which are smaller in diameter than the RBC itself, forcing the RBC to bend in order to pass through. In this micrograph, healthy RBC are shown in white within the darker capillary. Figure reproduced from Guest *et al.* [69]. (b) Sorting RBCs at various stages of malaria infection, depending upon their ability to deform and pass through rectangular microfluidic capillaries. Different stages of infection will affect whether the cells can pass through constrictions of decreasing width. Flow, Q , is passing from right to left, as indicated by the arrows. Figure reproduced from Shelby *et al.* [150]. (c) Rapid genetic sequencing using transcriptome barcoded hydrogel beads. As water containing beads pass through a brief constriction, causing upstream pressure to mount, and the water to pinch off into droplets containing the beads and cells. Reproduced from Zilionis *et al.* [187].

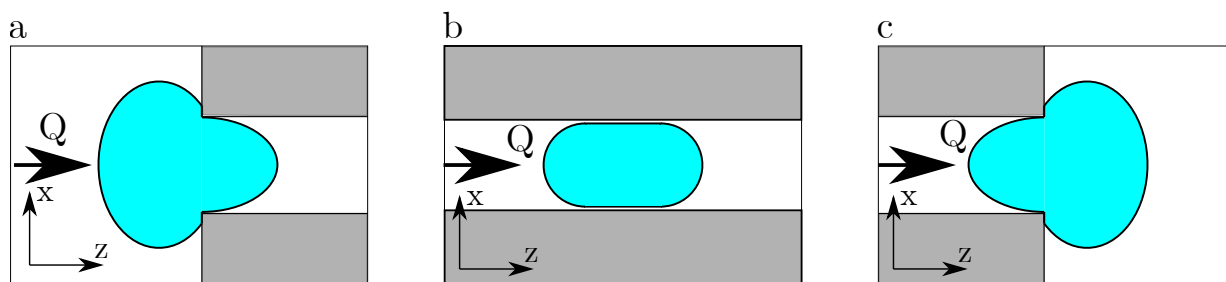


Figure 1.2: Particles which pass through simple microfluidic constrictions go through three distinct phases of motion. Each phase requires different considerations with respect to particle deformation. The microparticle must (a) enter into a constriction, (b) pass through the constriction and finally (c) exit the constriction. The flow rate Q represents the direction of flow and particle velocity.

each phase of the constriction, a distinct set of physical considerations is necessary to predict how flow and object deformation interact.

Passage through a single microfluidic constriction can be categorized in three stages: entry, passage and exit, as illustrated in Fig. 1.2. During a particle (or cell, droplet *etc.*) entry into a microfluidic constriction, the particle undergoes rapid deformation, from a relaxed (often approximately spherical) shape to a transitional shape (shown in Fig. 1.2a), to a shape fitting into the constriction (shown in Fig. 1.2b). In addition to friction, which is always a consideration in flow through constrictions, the entry of a particle into a constriction involves normal contact forces opposite the particle motion. This balance of forces results in reversible equilibrium states, where the pressure on the particle is balanced by contact forces. This is essentially the physical basis of micropipette aspiration, where pressure and contact mechanics are balanced as the particle is pulled into the pipette [157, 104, 72, 73].

Before the particle can exit a constriction, it may pass through a section of constant cross sectional dimensions, see Fig. 1.2b. This section does not further deform the particle, which has already squeezed into the channel. Passage through this section is a balance of pressure pushing the particle forward and friction resisting this motion. In addition to the deformation forced by the confinement of the microchannel itself, the flow can further affect the shape of the particle, such as in the creation of a lubricating cushion of fluid between the particle and channel walls [84, 28, 96].

Finally, upon exiting the microfluidic constriction, the particle again undergoes a dramatic change in shape, returning to its original shape, see Fig. 1.2c. While this may geometrically resemble entry into a constriction, the physics are quite different. Upon exiting a microfluidic constriction, there is no contact force between the particle and the channel to resist the particle motion. If present at all, it accelerates the particle's exit from the constriction. This allows the particle to relax from its deformed shape, however the relaxation may not result in a return to the pre-constricted form. Cells in particular respond to repeated constrictions, often becoming slower to relax back to their original shape as they undergo further cycles of constriction and thus stress [177].

Each phase of constriction is further complicated by the geometry of the constriction cross section. For simplicity these can be summarized as either circular capillary constrictions, (Fig. 1.3a and d), one dimensional constriction,

(Fig. 1.3b and e), or rectangular, (Fig. 1.3c). These constrictions can also be sudden, (Fig. 1.3a-c), or tapered (Fig. 1.3d-e). It should be stressed that this summary is not exhaustive, as for example there is no reason why a triangular constriction cannot exist. Instead, these constriction shapes are the most commonly found in literature, see Tab. 1.1. While in the case of sudden constrictions, the particle diameter (or cell, or droplet *etc.*) is larger than the width or diameter of the constriction, $d > w$, this cannot be said about tapered constrictions, whose level of confinement is dependant upon the taper angle, θ , and the particles position within the confinement. This concept of tapered channels can also be extended to non-constant tapers, *e.g.* curved rather than strait tapers, or even sinusoidal tapers used to test repeated stress response [85].

The modeling of circular capillaries, both strait and tapered, benefits from the trait of axisymmetry. Because in many cases the particles passing through confinement are nearly spherical, the problem can be reduced to be two dimensional. This also means that the particle will plug the capillary, forcing the fluid to move the particle, or push the particle away from the microchannel wall and pass through this lubricating layer. Li *et al.* was able to use this fact in order to analytically model the passage of microgel particles through a microfluidic constriction [111]. In this model, the pressure necessary to force a particle through a microfluidic capillary was shown to scale as $P/E \sim (d/w)^{14/3}$, where E represents the microgel elastic modulus. More recent studies have also extended this analysis to describe the pressure buildup in neo-Hookian materials as well [109].

Unlike circular capillaries, rectangular and one-dimensional constrictions are not axisymmetric. While for small square constrictions the particle may plug flow, and may be approximated by a circular capillary [104, 105], for less dramatic confinement, gutters exist between the particle and the corners of the constriction, allowing flow to pass through [28, 139, 171, 18]. In the case of one dimensional confinements, this effect is exaggerated, with space on two sides of the particle. A consequence of this flow around the particle is that even when stuck in place, flow can pass through the channel, while having only the hydrodynamic resistance affected. Practically speaking, the presence of flow around the confined particle substantially complicates its modeling, with most studies resorting to numerical methods to account for passage through rectangular constrictions with gutters [117, 139].

The way that an object responds to different confinement geometries will depend heavily on what the object in question is. Droplets and bubbles passing through microfluidic confinement have been extensively studied [18, 171, 25, 166, 96, 148]. Droplets and bubbles are entirely fluid, meaning that they have an internal flow which relates to the external flow through their surfaces. The surface tension of the droplet or bubble enforces a constant radius of curvature on its surface at equilibrium, thereby dictating the shape of the droplet or bubble, often pulling them away from the walls of the constriction. The impact of geometry on the physics is highlighted by their interplay with respect to the velocity of the droplet or bubble, U_{drop} , relative to the carrier fluid U_{flow} . In both the case of a circular and rectangular constriction, the velocity can be described in terms of the droplet capillary number, $Ca = \frac{U_{\text{drop}}\mu}{\gamma}$, where μ is the droplet viscosity and γ the surface tension. In the case of a circular confinement, the velocity of the droplet relative to the carrier fluid scales such that $\frac{U_{\text{drop}} - U_{\text{flow}}}{U_{\text{drop}}} \sim Ca^{2/3}$ [18, 148]. In the case of rectangular confinement

however, flow through the gutters changes both the flow inside and outside of the drop or bubble, resulting in a relative velocity of $\frac{U_{\text{drop}} - U_{\text{flow}}}{U_{\text{drop}}} \sim Ca^{-1/3}$ [18, 171].

Unlike droplets, particles such as microgels have an elasticity, and lack internal flow (excluding porous flow). The forces exerted by particles behave as one would expect for an elastic solid [112, 111, 109, 72, 73, 173]. Rather than be described by the capillary number, the behaviour of these particles is better described by the ratio of pressure, P to elastic modulus, E , or in some cases the Cauchy number, $Cy = \rho U_{\text{flow}}^2 / E$, where ρ is the fluid density.

Between droplets and particles exist capsules. These elastic membranes encapsulate fluid within them, but the membrane itself is not subject to flow. Flow of capsules through microfluidic constrictions deforms the capsule to a bullet like shape, rounded in the front and cut off at the rear. Hu *et al.* demonstrated using numerical methods the importance of channel geometry on the deformation of confined capsules [84]. While passage through circular capillaries resulted in an axisymmetric capsule, passage through square channels resulted in a fully 3-dimensional deformation.

While they are the focus of many experiments using microfluidic constrictions, cells themselves do not constitute a coherent class of material. Instead, cells behave as a combination between droplets, particles and capsules [172]. Cells have been modeled primarily as elastic [178, 117, 139, 102, 112], as capsules [178, 57, 73] and even as droplets [178, 96, 73]. The choice of model depends heavily on the application, as biological material spans a wide array of properties. Considerable work has been done modeling the passage of droplets and capsules through confinements [84, 18, 148, 171, 25], which has then been applied to the modeling of cell motion. There is however only limited modeling in literature of particles passing through non-axisymmetric geometries, often relying on empirical simulation [117, 139].

1.3 Thesis Outline

The objective of this thesis is to understand the mechanics of particles passing through microfluidic constrictions. Specifically this thesis focuses on the passage of spherical particles through rectangular and one-dimensional constrictions. Because of the mismatch in particle and container shape, there exist gaps between the particle and container, allowing flow to pass around the particle, while also applying pressure on it. This introduces a number of unique fluid-structure interactions, both during entry into, and passage through the microfluidic constriction.

First, in **Chapter 2**, I overview the process of particle production and characterization, which will be used throughout the thesis. I chose polyethylene-glycol based hydrogel particles as the test material to use in these experiments, because their of range of elasticity, as well as the versatility offered by photo-polymerization. After photo-polymerizing hydrogel droplets within a microfluidic chip, I describe how I measured the elastic modulus of these microgels along with their size.

The first experiments undertaken in this thesis involve the entry of microgel particles into a one dimensional

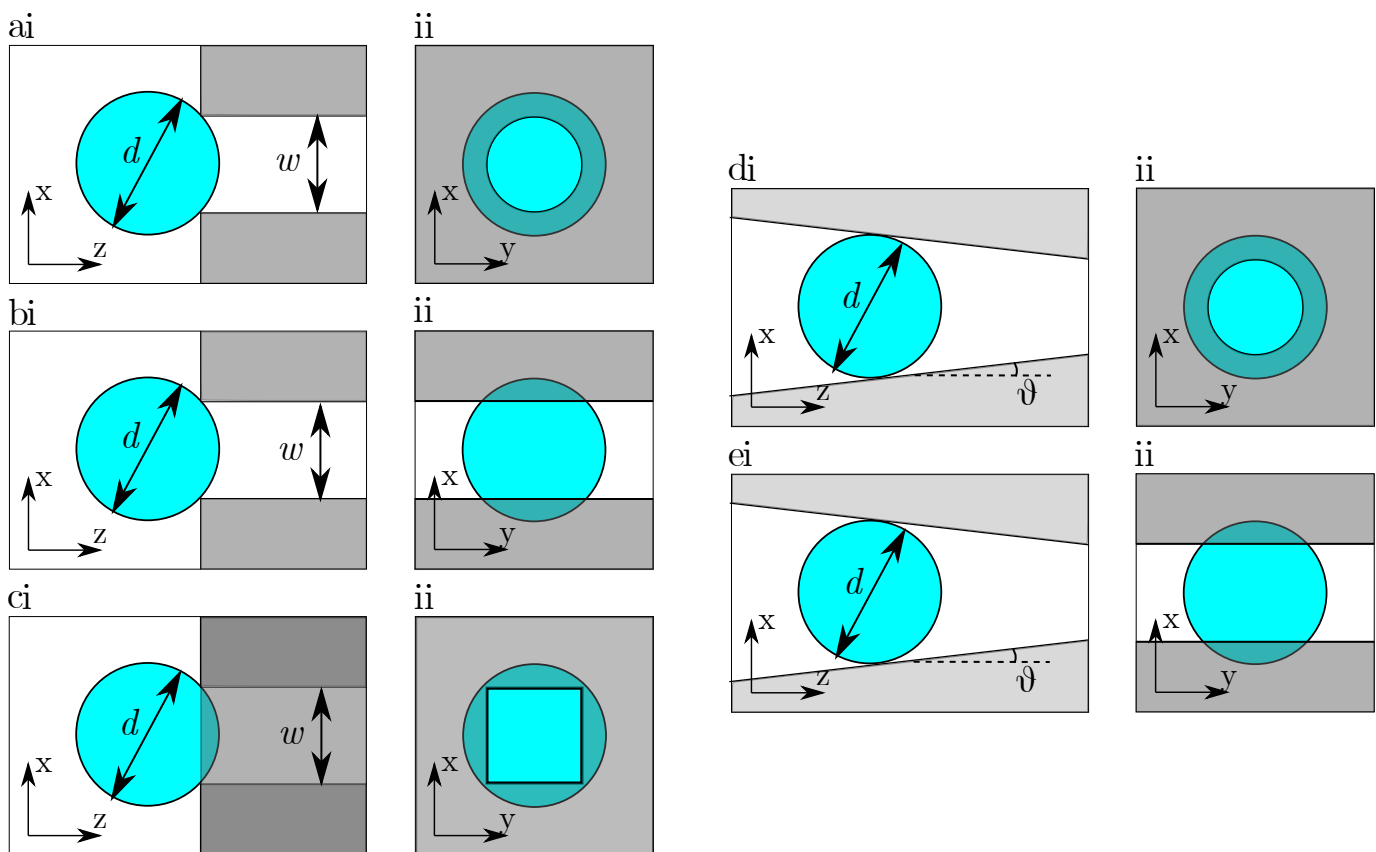


Figure 1.3: There exist a variety of possible geometries through which particles can become confined in microfluidic systems. This figure summarizes the most commonly studied geometries. In order, these are a cylindrical capillary (a), a one-dimensional constriction (b), a rectangular constriction (c), a tapered capillary (d), and a tapered microchannel (e). In these figures, the particle is represented as a blue sphere, with the microchannel shown in grey. Cartesian directions are shown on each of the figure pairs, (i) and (ii).

Author	Constriction Type	Transport Phase	Material	Summary
Li <i>et al.</i> [110]	Tapered and cylindrical capillary	Entry and passage	Agarose microgel in mineral oil	Measured the equilibrium pressure entering a tapered channel, varying particle diameter. Cyclic passages through constriction tested particle memory
Li <i>et al.</i> [111]	Tapered and cylindrical capillary	Entry and Passage	Agarose microgels in water	Modeled entry pressure for particle entering tapered constriction for particles of varying particle diameters and channel tapers. Modeled passage through constriction, along with volumetric changes to particle.
Li <i>et al.</i> [109]	Cylindrical capillary	Entry and passage	Polyacrylamide microgels in water	Modeled analytically pressure moving microgel through capillary, experimentally varying particle size.
Cartas-Ayala <i>et al.</i> [28]	Square channel	Passage	HL-60 cells in a high viscosity cell media	Empirically modeled friction and deformation of cells passing through a square microchannel for a range of confinements.
Fitz-Gerald <i>et al.</i> [60]	Cylindrical capillary	Passage	Red blood cells in blood	Modeled the passage of blood cells through a strait capillary, modeling hydrodynamic resistance and blood cell velocity. Model considered capillary porosity as well as non-axisymmetric positioning.
Khan <i>et al.</i> [96]	Square constriction	Passage	PDMS particles, various cells	Transit time of cells and particles were compared with visco-elasticity and particle size. Transit time was capable of identifying.
Wyss <i>et al.</i> [173]	Tapered capillary	Entry	polyacrylamide microgels	Measured the elastic modulus of trapped particles by comparing pressure with equilibrium position of particle in tapered capillary.
Luo <i>et al.</i> [117]	Rectangular channel	Entry and passage	Lung tumor cell	Numerical simulation was used to describe the deformation of a visco-hyperelastic particle into a constriction, first in width, then in height. Cellular deformation linked to instantaneous elastic properties.
Preira <i>et al.</i> [139]	Rectangular channel	Entry and passage	Human THP-1 cells	Modeling, simulation and experimental results of a cells entering and passing through a square constriction. Pressure drop in both entry and passage modeled.
Guo <i>et al.</i> [72]	Tapered rectangular channel	Entry and exit	Neutrophil, RT4 and lymphoma cells	Measured cell deformability and mechanical characteristics by forcing cells through repeated tapered rectangular channels. Modeled pressure required for cell entry.
Shelby <i>et al.</i> [150]	Rectangular channel	Passage	Erythrocytes	Used a constriction channel to test for Plasmodium falciparum, as infection stiffens cells and prevents passage.
Hu <i>et al.</i> [84]	Rectangular channels and circular capillaries	Passage	Ovalbumin capsules	Numerically modeled the change in shape of a neo-Hookean elastic capsule flowing through strait circular and rectangular channels.
Xue <i>et al.</i> [178]	Rectangular channels and tapered channels	Review	Various cells	This review presents a number of studies which describe various methods of mechanically characterizing cells using microfluidic constrictions.

Table 1.1: A brief overview of some studies of single particle, capsule or cell passage through microfluidic constrictions, classified by the geometry of constriction and whether the particle is entering or passing through the constriction.

constriction, that is to say, where the microchannel constrains the the particle along the channel width, but not the channel height. To test this, I trap microgels at a sudden constriction in microchannel width, and measure the relationship between pressure, flow and deformation of the microgel at equilibrium.

Because of the nature of this experiment, it is possible to look at the fluid structure interaction as a weakly coupled problem in two parts. The first part, **which occupies Chapter 3 of this thesis**, looks at the deformation of the microgel as pressure on it increases. Supporting my experimental results with simulations, I apply Hertzian contact mechanics in order to model the deformation of a trapped microgel as pressure mounts, pushing it further into the constriction.

The second part of this analysis, **discussed in Chapter 4 of this thesis**, looks at the flow around a microgel trapped in a one dimensional constriction. First, I model the flow around the microgel with respect to how the microgel deforms. Then, having looked at the fluid and structural elements of this problem separately, I answer the question: how does the pressure which deforms a trapped particle affect flow around a deformed particle?

The final set of experiments, **discussed in Chapter 5**, investigates the propagation of particles through a square constriction. I investigate how the microgel elasticity, fluid viscosity and flow rate affect the passage of microgels when they are confined up to diameters 1.4 times the width of the channel. In order to measure the pressure drop across the microgel, I employ a microfluidic comparator which allows for visual interpretation of hydrodynamic resistance, and thus pressure. I also measure the microgel velocity and compare it with the velocity of the surrounding fluid.

Yet again, I approach the fluid-structure problem as two separate but coupled problems. Using a simulation of the deformation of a microgel without any flow, I separate the fluid domain into two regions: one where fluid passes around the microgel without deforming the microgel, and a second where a lubricating fluid film deforms the microgel to an equilibrium position. Combining these two models together, I attempt to empirically describe the coupled pressure, velocity and deformation of microgels passing through a square constriction. I also explore the implications this has on the lubricating thickness as the microgel becomes increasingly confined.

The work presented in this thesis builds towards a more complete model of the motion of particles through non-axisymmetric (*i.e.* non circular) constrictions. This thesis however is only the groundwork of such a problem. The experiments are limited to steady state flows, neglecting how the particles react to dynamic flow conditions or dynamic particle deformation. Nevertheless, this thesis lays a simple groundwork for further investigation into the fluid structure interaction of soft particles interacting with simple microfluidic constrictions.

Chapter 2

Making Photopolymerized Microgels

2.1 Introduction

2.1.1 Microfluidic Hydrogels

In the field of biomedical microfluidics, hydrogels have emerged as a crucial component for a wide array of systems, ranging from micro-sensors [147, 162, 108, 128], to cellular environments [35, 141, 146, 143, 36] to artificial tissue [180, 21, 31, 40, 35, 167, 126]. Hydrogels are materials which are porous, hydrophilic polymers, with a diverse set of physical characteristics [153, 35, 66, 2]. Like a sponge, these materials readily absorb water, and can swell to several times their original volume [163, 74, 2]. Due to their chemistry and physical structure, hydrogels have a wide range their elastic properties, exhibit poroelasticity, and can be extremely soft (Youngs moduli $E < 10$ MPa) [40, 33, 134, 121]. Finally, hydrogels are malleable from their pre-gel state, transitioning from liquid to gel after a chemical reaction [40, 34, 35, 180, 31].

A wide variety of hydrogels have been used in microfluidics depending on the application, and required gel chemistry [40, 32, 35, 66, 33]. Bio-compatibility varies considerably between microgels due to differences in chemistry and polymerization, allowing hydrogels to range from extremely cytotoxic to engineered microenvironments [180, 21, 31, 40, 35, 141, 146, 143, 153]. Other chemical compatibility must be considered as well, as some solutes will strongly affect the state of the hydrogel [74]. The physical properties of hydrogels is also a very important consideration. Poorly optimized elasticity or porosity may make the hydrogel insufficiently porous for cellular growth, or unable to adequately deliver solutes [153, 35, 40, 106].

While the end state of the hydrogel is important, how the hydrogel is made is can be equally important in microfluidic systems, where conventional machining and molding is not generally possible. The method of polymerization is therefore a particularly practical classification of hydrogels when deciding which hydrogel is appropriate for a given microfluidic application. Hydrogels can polymerize via heating or cooling such as agarose or collagen gels,

photo-polymerization, such as with Polyethylene-Glycol (PEG) gels, or by mixture of chemicals such as alginate with a cationic solution [35, 40, 33, 2]. Chung *et al.* for example categorizes a variety of microfluidic hydrogels used in tissue engineering by task, monomer chemistry and mode of polymerization [35]. Consideration of polymerization can be crucial in biomedical applications, as a hydrogel may be unsuitable if it only remains solid at a certain temperature range, or requires exposing cells to harmful light [75, 2]. This distinction is especially important in microfluidic environments, where the ability to selectively expose the material to heating, mixing or light can be done at a micro-scale [51, 50, 124]. The selectivity of microfluidic systems can be a double edged sword, as while microfluidic systems may allow for micro-scale control of hydrogel properties, they may also create wide variation between samples, with uncertainties of elasticity and porosity being above 20 % [40, 66].

In studying fluid-structure interaction of microfluidic systems, hydrogels present themselves as excellent materials for study. Their biocompatibility allows for the investigation of these microfluidic physics to be applied directly in more applied studies. They are soft enough to readily deform with the fluid forces. When selecting a hydrogel material for use, the elasticity must be capable of being tuned to the desired range of values, and that range should be wide enough to adequately capture even more subtle effects of elasticity on such interactions. This allows for a variety of experiments to be performed with minimal retooling.

2.1.2 PEG Hydrogels

PolyEthylene-Glycol (PEG) is a hydrogel of particular interest to this thesis. One of the main reasons for this interest is PEG can be photo-polymerized to transition from liquid to gel, allowing for flexibility in production, [35, 66, 126]. These photo-polymerized gels are formed when a functionalized PEG monomer, typically PEG-Diacrylate (PEGDA), is crosslinked by the action of a photoinitiator (PI) under the exposure to ultraviolet light (UV), as illustrated in Fig. 2.1a [35, 45, 46]. PEG based gels are relatively insensitive to operating temperature, requiring no cooling to remain solid. Finally, the chemical precursors of PEG microgels can be used to tune a wide range of material properties, and remain stable for long periods of time.

The primary component of PEG microgels is the functionalized PEGDA, which forms polymer chains upon crosslinking. It follows that control of this component of the hydrogel will strongly affect its material properties. As the concentration of aqueous PEGDA is increased, there is a greater density of material to bind between [11]. This leads to an increase in the overall stiffness of the material after polymerization [47, 61]. The relationship between the quantity of PEGDA and elasticity is nonlinear, with elastic moduli spanning the $E \sim 100 \text{ Pa}$ to $E \sim 10 \text{ MPa}$ [47, 121]. Furthermore, the molecular weight of PEGDA chains has a strong influence on eventual elasticity, with lower weight chains resulting in lower elastic modulus [47, 182]. Additionally, as the PEG microgel elastic modulus increases, it also becomes more brittle, shearing at considerably lower strains [121].

The addition of non-functionalized PEG with the PEGDA allows for even finer tuning of the properties of the PEG

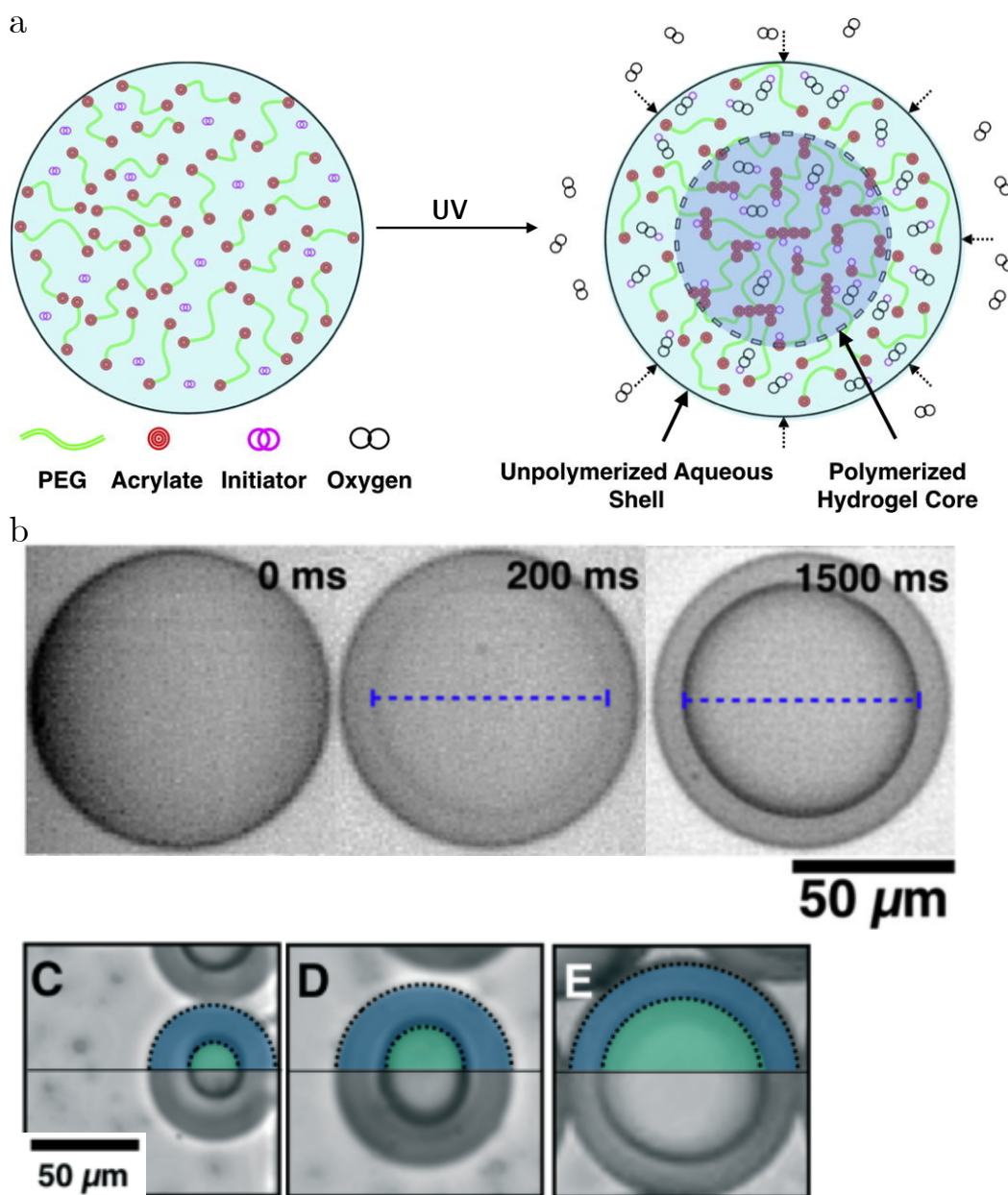


Figure 2.1: (a) A diagram showing the polymerization of a sphere of PEG gel. The diagram shows the activation via ultraviolet exposure, and the binding of PEG chains at their fictionalized acrylate group via initiator activity. The figure also shows schematically the inhibition of PEG polymerization via oxygen competition. Reproduced from Debroy *et al.* [45]. (b) A comparison of PEG gel polymerization throughout its exposure to UV. As the exposure time increases, the degree of polymerization, seen as the interface between the liquid and gel PEG, becomes more apparent, however the size of these regions remains constant. Reproduced from Debroy *et al.* [45]. (c-e) A series of PEG gels of identical chemical composition and light exposure for a range of diameters. While the inner polymerized region, shaded green, grows with the microgel, the un-polymerized region, shaded blue, remains approximately the same size regardless of total gel size. Reproduced from Krutkramelis *et al.* [101].

gels beyond what is achieved with PEGDA alone. Unlike water, PEG does interact with the PEGDA during polymerization, however, lacking acrylate groups, the PEG does not propagate the gel chains, resulting in a decrease in elastic modulus, and decreasing the degree of polymerization [27, 45, 126]. This allows for precursor gels which are similarly viscous to higher PEGDA concentration gels, with lower effective elastic modulus and greater swelling.

While the specific mix of chemicals has a major impact on gel properties, these are not the only factors in polymerizing PEG gels. Both the intensity and duration of light exposure, as well as the concentration of oxygen in the surrounding fluid will have an effect on the polymerization process. The mechanism of crosslinking PEGDA chains together utilizes a photoinitiator (PI) present to bind the acrylate groups together, as shown in Fig. 2.1a [45, 46]. Oxygen is consumed by the PI preferentially over reacting with the PEGDA, thereby not crosslinking where oxygen is present. As the gel is exposed to light of a given intensity, a shell of gel will achieve homeostasis between the diffusion and consumption of oxygen, thereby remaining liquid. In effect this means that regardless of UV exposure time and the overall size of the gel, a standard thickness of gel will remain un-polymerized due to oxygen inhibition, as shown in Fig. 2.1b-e [45, 101]. Multiple strategies exist for mitigating these effects in practice, ranging from increasing the proportion of PI, to increasing light intensity, to adding oxygen scavengers to surrounding the microchannel with inert gas instead of air [45, 101, 53, 20]. Generally, a greater degree of crosslinking and rigidity, as well as reduced swelling occurs where light exposure is more intense and longer, although this increase in crosslinking is limited to where oxygen is not present [56, 11, 75].

To summarize, the density of the gel polymer network is shown to increase with increases in PEGDA monomer concentration and acrylate density. The polymerization process is also important, as greater photo-activation, be it from decreased oxygen, increased light intensity, or increased PI concentration will increase the gel network density and stiffness. Meanwhile, by replacing the water with non-functionalized PEG, it is possible to polymerize increasingly soft gels, by competing with the acrylate in the un-polymerized PEG gel. While these trends may act as guidelines to how changes in gel formation will change the final product, they also reveal a complicated interplay between the various PEG precursors and the polymerization process. In other words, PEG gels are not easily characterized simply by observing the aforementioned trends, and still require direct investigation.

2.1.3 Microgels

As hydrogels can be set in liquid form and then turned solid, particularly via photo-polymerization, they offer the ability to form into any variety of shapes. Several lithography techniques exist which utilize the selective exposure to ultraviolet light (UV) to polymerize hydrogels into arbitrary two dimensional columnar shapes [51, 52, 49, 152, 49, 66]. For example stop flow lithography, shown in Fig. 2.2a-b, will stop the flow of liquid photoreactive PEG, rapidly expose the static fluid to UV through a mask, and then flow again to remove the custom particles [152, 183, 86, 52, 49]. Furthermore, hydrogel fibers have been created by selectively polymerizing flowing hydrogels, as well as using

lithographic masking [56, 35].

Still, perhaps the simplest and one of the most versatile formulations of microfluidic hydrogels are spherical hydrogel particles, or microgels. The simplest method to make these microgels is to polymerize the gel as spherical droplets [49, 40, 45, 174]. Unlike with the lithographic polymerization, droplet based microgels can be polymerized by any method, be it purely chemical, photolithographic, or thermal [66, 182, 40]. This is because by isolating the hydrogel in an emulsion, the particles can solidify independently and be controlled in their formation that way.

Emulsification also offers the possibility of creating layered microgels. This is especially potent when combining droplet microfluidics with lithography. In doing so, it is possible to freeze solid two different hydrogel chemical components in a Janus particle, such as that shown in Fig. 2.2c, where each half of the particle has a different composition [49, 40, 130, 151, 132]. Lithography presents several options for creating composite particles, such as core-shell microgels, shown in Fig. 2.2d, or the aforementioned Janus particles [49, 40, 129, 168].

The transport of microgels is often a crucial aspect of their deployment in their applications. An advantage of the porosity of microgels is their ability to carry other chemicals within them, and diffuse them once they have reached their end destination [40, 183]. Microgels can also be transported into droplets in order to isolate them from one another and move them within a microfluidic system [48, 3, 4, 40]. Furthermore, microgels can be barcoded to allow for identifying different solutes contained within the gel. This is the basis for digital droplet genetic testing, such as DropSeq or InDrops [99, 98, 118, 187, 37]. By encapsulating barcoded microgels containing different reverse transcriptase bases with single cells, a large volume of genetic sequencing can be independently undertaken, shown in Fig. 2.2e.

While many applications of transported microgels depend on traits such as their ability to diffuse solutes, or their non-toxicity, the transport itself is dictated by the interaction of the transporting flow, and the hydrogel body. In cases where the microgels are confined, their stiffness, as well as size and surface roughness will play a part in their transport, affecting friction and flow around the microgel [96, 63].

2.1.4 Chapter Outline

This thesis focuses on the fluid structure interactions of microgels in microfluidic systems. It follows that an understanding and characterization of these microgels is a necessary component to understanding these interactions. This chapter outlines the process for making microgels, which is used throughout the project. This outline includes the protocol used for making microgels, as well as the reasoning behind both the method of droplet formation and PEG gel chemistry. Furthermore, this chapter outlines the methods used to characterize these particles for their size, and elastic properties. Finally, in reviewing some simple experimental measurement of microgel size and elasticities, we highlight the governing trends of these properties, and emphasize the need to individually characterize different batches of microgels.

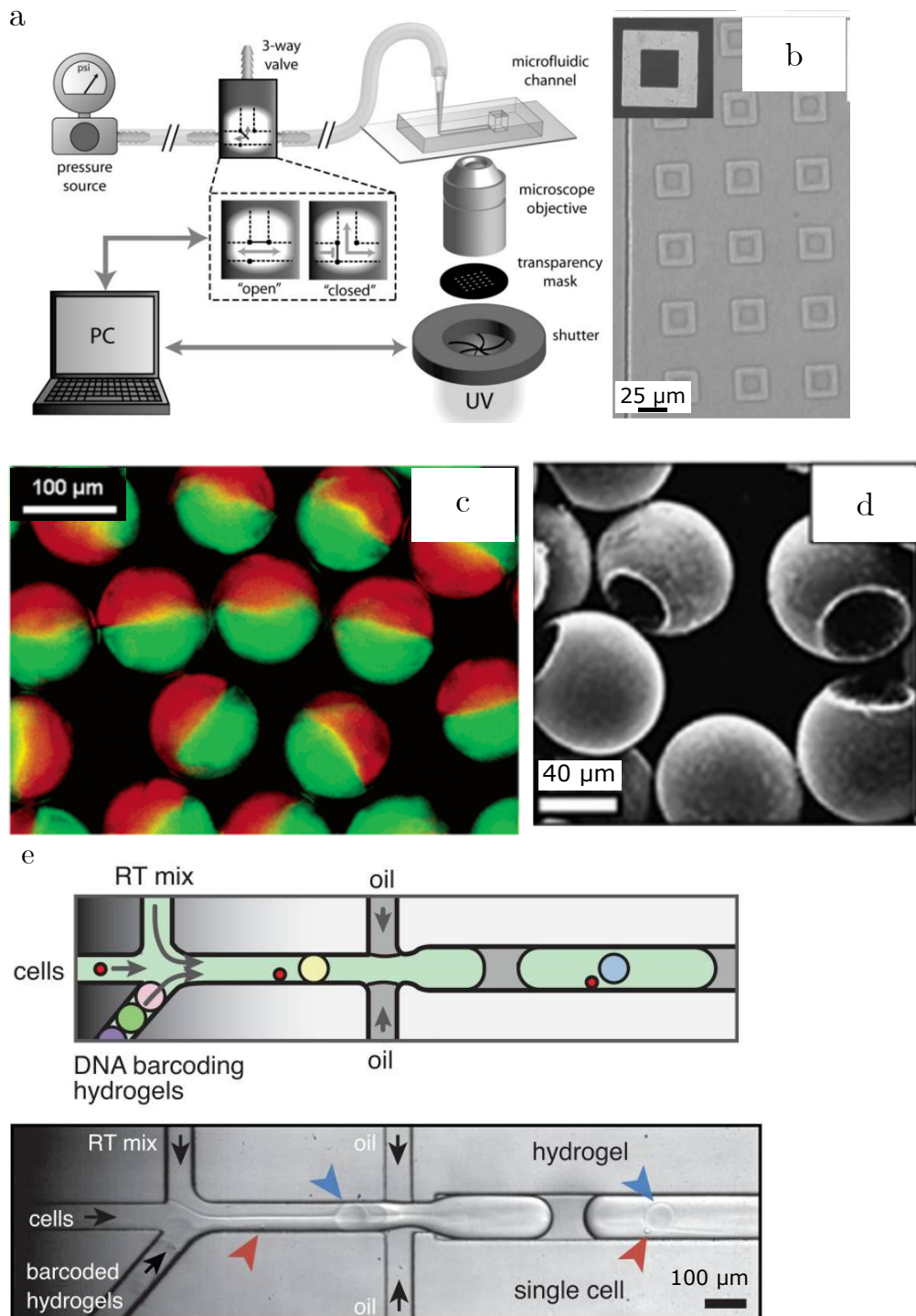


Figure 2.2: (a) A diagram explaining stop-flow lithography for making PEG microgels with custom shapes. A valve is used to periodically stop the flow of a photoreactive PEG solution. A shutter then flashes UV through a transparent mask in the desired shape of the eventual PEG microgels. The PEG then polymerizes and is flowed out of the exposure region. Reproduced from Dendukuri *et al.* [52]. (b) A sample hollow square microgels made using stop-flow lithography as described in (a). Reproduced from Dendukuri *et al.* [52]. (c) An bicoloured acrylamide janus particle. Half of the particle is dyed with a fluorescent rhodamine isothiocyanate dye, while the other is dyed with fluorescent fluorescein isothiocyanate. Reproduced from Shepherd *et al.* [151]. (d) A core-shell tripropyleneglycol diacrylate microgel where the core has ruptured the shell of the microgel, making cup-shaped microgels. Reproduced from Nie *et al.* [129]. (e) A microfluidic device used in the inDrop genetic sequencing. Microgels containing barcoded reverse transcriptomes are flowed into droplets with single cells. These can then be used to rapidly genetically analyze individual cells. Reproduced from Klein *et al.* [99].

2.2 Microfluidic Design and Gel Production

2.2.1 Microfluidic Emulsion Devices

For these experiments, I chose to use photo-reactive poly(ethylene-Glycol) (PEG) based microgels. The un-polymerized gel came in the form of a viscous aqueous mixture of PEG, PEGDA and PI, which could be emulsified into droplets, surrounded by a carrier oil. These liquid drops would then be exposed to ultraviolet (UV) light until solidified. Microfluidic emulsification allows for controlling the size of droplets, to create mono-disperse droplets which could then be made into a batches of tens of thousands of identical microgel spheres. (Furthermore, as this thesis focuses on fluid structure interaction, it was fitting to have the microgels which would be injected into other microfluidic systems made via microfluidic emulsion.)

A number of on-chip methods exist for creating gel emulsions, where aqueous gel droplets are formed in an immiscible carrier oil. Both Anna and Baroud *et al.* highlights three such devices; the T-junction, co-flow and flow focuser droplet producers [18, 12]. These methods rely on the geometry and flow of oil and aqueous gel in order to reliably pinch off droplets. This droplet formation can happen by dripping or jetting, shown in Fig. 2.3a and b respectively, although depending on the geometry, other droplet formation regimes can also exist. In dripping, droplets form directly at the meeting of aqueous and oil flows. There, droplets are sheared off the aqueous stream. In the jetting mode, the inner aqueous phase is carried along with the oil to make a fluid column until Rayleigh Plateau instabilities cause droplet formation. The transition between the modes of droplet production are a function of the junction geometry, as well as surface tension, viscosity and flow velocities of both fluids.

Flow focusers produce droplets continuously, with the mode, size and frequency of production dictated by the fluids involved, their flow rates, and the microchannel geometry, and can be seen illustrated in Fig. 2.3 a-c. Several studies have identified general trends for describing droplet production with these parameters, showing a dependence on the Capillary number, $Ca = \mu U / \gamma$, where μ is the fluid dynamic viscosity, U the mean flow velocity and γ the surface tension between the two phases [18, 103, 62, 12, 38, 107]. Production also depends on the ratio of carrier to droplet flow rates, however to date there exists no universal law describing droplet production phase, e.g. dripping or jetting, nor droplet size. Recently efforts have been undertaken to utilize machine learning modeling to describe droplet production, but this model does little to provide insight into its mechanics [103].

In addition to droplet production by flowing carrier and droplet phase, it is possible to make droplets by only flowing the droplet phase. Step and slope droplet production use the geometry of the microchannel junction to force droplet production via surface tension [42, 41]. Briefly, as the droplet phase is pushed into the continuous phase, the droplet phase is allowed to expand. In order to maintain a constant radius of curvature of the droplet surface, the droplet phase will then pinch off creating distinct droplets. This mechanism is demonstrated in Fig. 2.3 d and e.

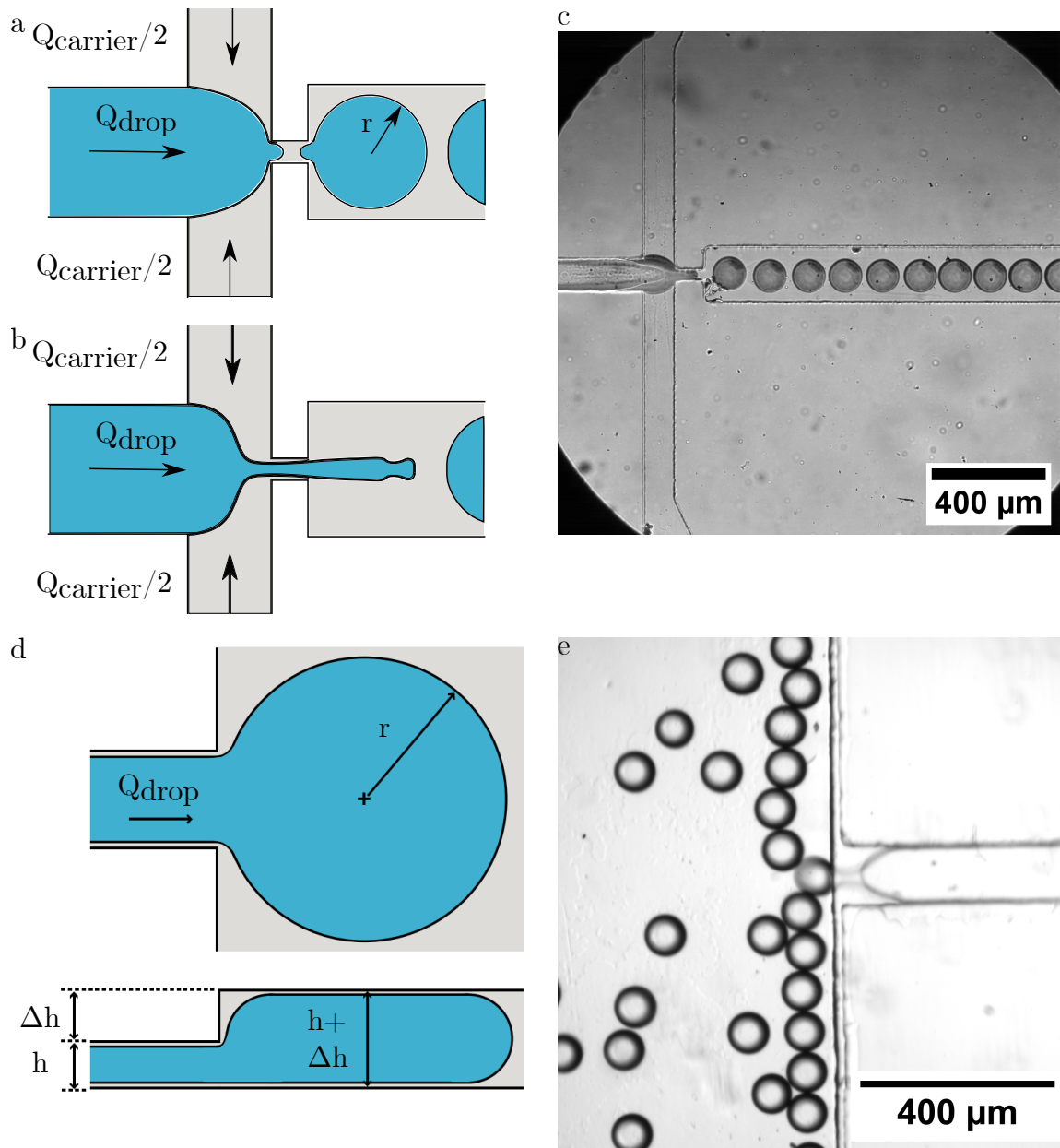


Figure 2.3: A comparison of different droplet production methods. In order, a diagram of the flow focuser in the dripping (a) and jetting (b) regimes, a micrograph (c) flow focuser, and a diagram (d) and micrograph (e) of step droplet producer. The diagram of a step producer in (d) is modified from Dangla *et al.*[41]

Dangla *et al.* showed that the droplet formation follows the form

$$\frac{1}{2}(r - r^*) \sim \sqrt{Q_{\text{drop}}} \quad (2.1)$$

where r and r^* are the final and critical droplet radii respectively, and Q is the droplet phase flow rate [41]. The critical radius in this case is that of the droplet bulb before the droplet must have a negative curvature in the plane of the channel to maintain overall curvature. Where the step height is larger than the inlet height, $\Delta h > h$ this critical radius is $r^* = h$. The other aspect that makes this emulsification method unique is its relative insensitivity to flow rate. In effect, the main contribution to droplet size is its surface tension and the step geometry (although sufficiently large Q will create noticeable variation in droplet size).

In designing a protocol for gel making, we considered both flow focusers and step producers. Both methods were capable to produce consistent droplets with a high degree of monodispersity when properly tuned, such as illustrated in Fig. 2.3c and e, however scaling up the production of droplets using the step producer proved challenging. Increasing flow rates would often result in overly large droplets, as predicted by 2.1. In order to increase production, parallel steps were necessary. This also proved challenging: despite having channels of nominally equal hydrodynamic resistance, the flow through each channel was not equal. This is because the droplet phase entering into the oil phase creates variations in each channels resistance, which were magnified rather than dampened by the interaction of the two phases. These variations were sufficient to create droplets more than twice the desired size, while other junctions produced the desired droplets, or no droplets at all.

Flow focusers, unlike step producers are extremely sensitive to the flow rates of both the carrier and droplet phases. In practice this is both a challenge and an advantage. Achieving reproducible droplet production between experiments requires care, as small variations in the viscosities or surface tension means tuning of the carrier and droplet flow rates must be performed each batch. Furthermore, this droplet production can hide higher order instabilities in the production of droplets, periodically changing the size of produced droplets if not tuned correctly. When these factors are carefully controlled however, flow focusers allow for consistent tuning of multiple droplet sizes and production rates without changing microchannel geometry. This allows for modifying droplet size on the fly, without requiring multiple chips to be made.

Some of our early tests for making microgels utilized a step droplet producer, as when simplified to only a few parallel channels, it was capable of making monodisperse droplets, albeit at a slow pace. Because of the versatility provided by the flow focuser, we opted to use flow focusers to create our microgels. This decision was largely so that a single microfluidic chip design would be capable of consistently creating droplets of a range of sizes, rather than be confined by the step height, as is the case for step emulsifiers.

2.2.2 Droplet Stability

A major consideration in producing droplets to be transformed into monodisperse microgels is the stability of these droplets. While tuning the droplet production at the flow focuser could be used to ensure that only identical droplets were initially created, surface tension between the droplet and carrier phases creates a tendency for droplets to fuse together when disturbed (furthermore, the surface tension between droplet and carrier is a major factor in droplet formation, as flow focuser droplet production has been shown to depend upon the droplet Capillary number [18, 16, 15]). Using microchannel geometry, it is possible to force two droplets into contact with one another, while simultaneously straining the droplet surfaces [18, 24, 133]. As the two surfaces are strained and in contact, a bridge of fluid can be formed between the two droplets, which will then be pulled together by the same surface tension forces. Understanding the kinetics involved in droplet fusion is crucial to ensuring monodisperse gels are made, especially as droplet fusion was observed in early experiments to be stochastic, and the resulting gels polydisperse.

Once the droplet interfaces are pushed into contact with one another, the mechanics of the droplet interface come into play with respect to fusion. The addition of surfactants is one way to mechanically create a barrier to droplet fusion [18, 15]. Surfactants are molecules or particles which sit within the droplet surface. Limiting focus to chemical surfactants such as those used in this thesis, the surfactant contains a hydrophilic and hydrophobic component, and adsorbs/desorbs between the fluid bulk and the droplet interface [120, 15]. These surfactants have the effect of reducing the droplet surface tension. The surfactants themselves raise the energy necessary to bring two droplets into contact at the microscopic level. Steric repulsion of the surfactant molecules at the surface of the droplets maintains a separation [15]. Additionally, the Marangoni effect, where surfactant gradients upon a surface create a flow in the bulk fluid, also resists the drainage of fluid separating the droplets [15]. Previous experiments have used this fact in order to control the fusion of two droplets, without moving the droplets themselves [16, 15]. This is especially important when considering the spontaneous fusion of unperturbed droplets in contact with one another. In the early experiments for droplet production, droplet fusion events were common, especially for liquid PEG droplets, which had a high surface tension compared to the carrier oil.

A simple comparison of droplets made and allowed to rest using 0.5 and 3 % RAN surfactant (008-fluorosurfactant, RAN biotechnologies, Beverly MA) in the carrier phase as well as 3 % RAN in the carrier phase and 0.2 % sodium dodecyl sulfate (aq) (SDS, Sigma Aldrich, Darmstadt Germany) surfactant in the droplet phase, shows the necessity for sufficient surfactant presence in droplet production. The droplets are made of an aqueous mixture of 30 % PEGDA, 30 % PEG and 5 % PI, with FC-40 (Fluorinert FC-40, Sigma Aldrich, Darmstadt Germany) containing RAN surfactant as the oil phase. These droplets were made using a step droplet producer to allow for identical flow rates without influencing production with surface tension. The results can be seen in Fig. 2.4. There is a clear improvement in stability when increasing from 0.5 to 3 % RAN, and again with the addition of SDS to the droplet phase. These tests showed the necessity of surfactants in both the carrier and droplet phases.

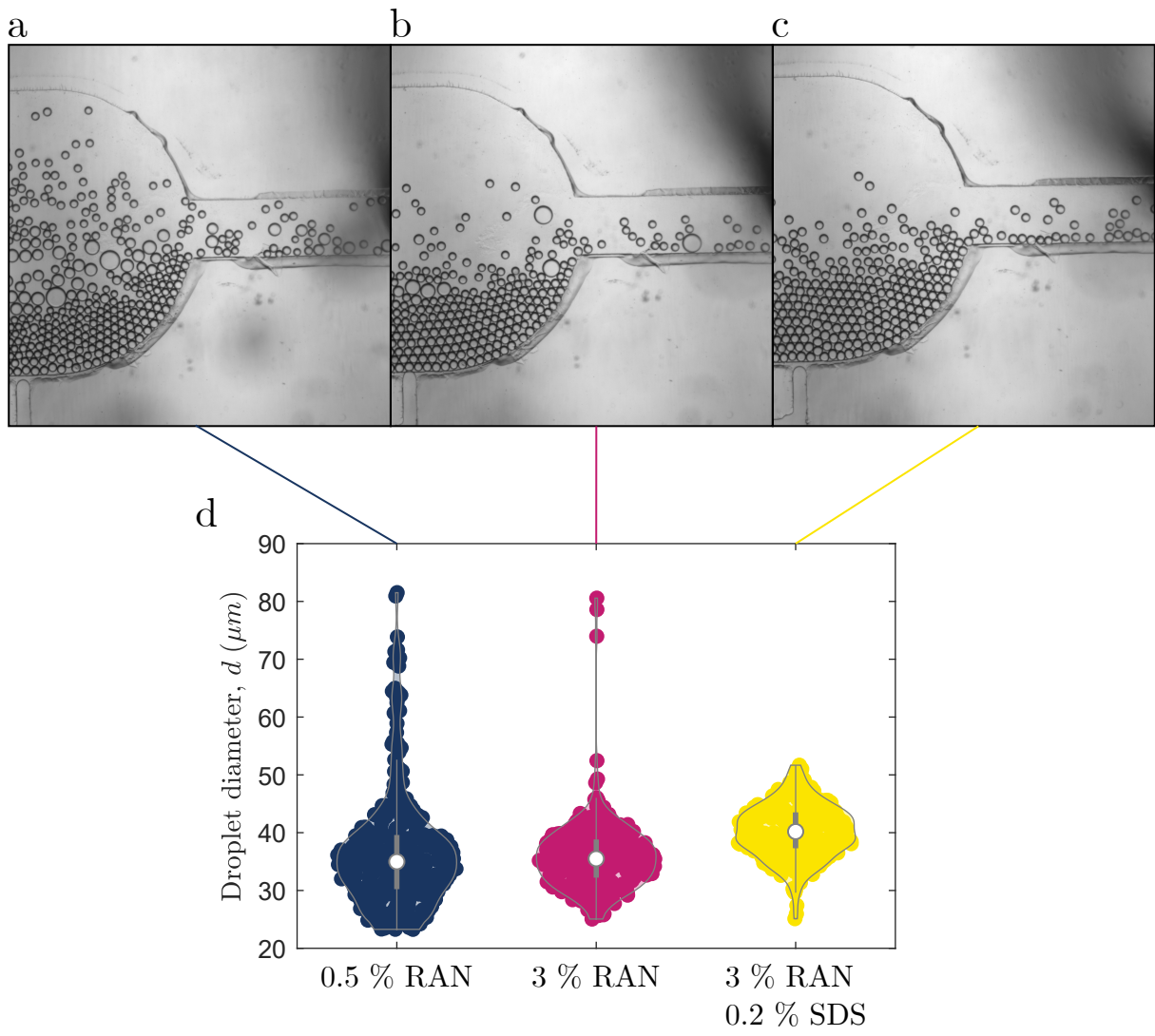


Figure 2.4: Micrographs of PEG droplets made using a carrier phase containing 0.5 % RAN (a), 3 % RAN (b) and 3 % RAN with 0.2 % SDS in the droplet phase (c). (d) A comparison of the diameters created during this process. Monodispersity is improved when increasing the RAN content as well as when adding 0.2 % SDS

2.2.3 Hydrogel Making Microchannel Design

Both on and off chip photo-polymerization were tested with the PEG drops. Off chip polymerization posed several practical problems, mainly with respect to monodispersity. Between droplet formation and collection off chip, the droplets underwent changes in confinement, which resulted in some drops fusing. Furthermore, some droplets would solidify at their core, fuse and then further solidify, creating oddly shaped particles. While the addition of extra surfactants within the carrier and droplet phases mitigated this, it was still not sufficient to make monodisperse microgels. On the other hand, on chip polymerization had the advantage of polymerizing droplets exactly as they were seen under the microscope, preventing fusion events during transport.

The flow focuser channels designed here had three inlets and a single collection outlet for collecting polymerized gel droplets, as seen in Fig. 2.5a. The oil and water inlets connected at the flow focuser itself were used to control the formation of the droplets themselves, tuning flow rates for desired droplet size and production frequency. The second oil inlet was used to control the speed of droplets as they passed below the UV lamp.

Several iterations of flow focuser design were tested. The first iterations were modifications of a simple flow cross, with no neck, (the neck being the narrow $25\mu\text{m}$ section of the microchannel in Fig. 2.5a). In general, this produced larger droplets, and so the height of the flow focuser was reduced to limit droplet volumes. These droplets would often contact the top and bottom of the channel, resulting in pancake shaped gels, rather than the desired spherical gels. A step was introduced to the channel where the second oil flow meets the droplet and first oil inlet, which allowed the drops to relax from their pancake shape to a sphere. This is similar to the steps described in Fig. 2.3d and e, where the channel height increases, after which the channel height would be greater than the droplet diameter. This step had the unfortunate drawback of often causing droplet fusion, as droplets would undergo rapid changes in shape when passing the step. Ultimately this design was updated to the design shown in Fig. 2.5a, where a neck was added to the flow focuser. This allowed for smaller, spherical droplets to be manufactured while using a single layer channel. Molds of heights $h = 80, 100, 150$ and $200\ \mu\text{m}$ were made to allow for a wide range of droplet sizes. This single layer design allowed for droplets to be fully relaxed without any changes in confinement after formation.

Micro-channels were made in Polydimethylsiloxane (PDMS, SYLGARD 184, Sigma Aldrich, Darmstadt Germany), using standard soft lithography [140, 125]. To summarize the process, to scale lithographic masks were used to create a mold of the channel in SU-8 (SU-8-2000 series, Kayaku Advanced Materials, Westborough MA), as described by the manufacturer. The SU-8 was spin coated on the silicon wafer and heat treated, before exposure to UV solidifies the SU-8. Afterwards, further heat treatment and a chemical bath removed the excess SU-8, leaving a 3 dimensional mold in the shape of the lithographic mask. The height of these molds were measured using a scanning profilometer (Kinexus Ultra+, Malvern Panalytical, Malvern UK) These molds were then covered in approximately 1 cm of PDMS (10:1 base to crosslinker), and degassed in a vacuum chamber. The PDMS was

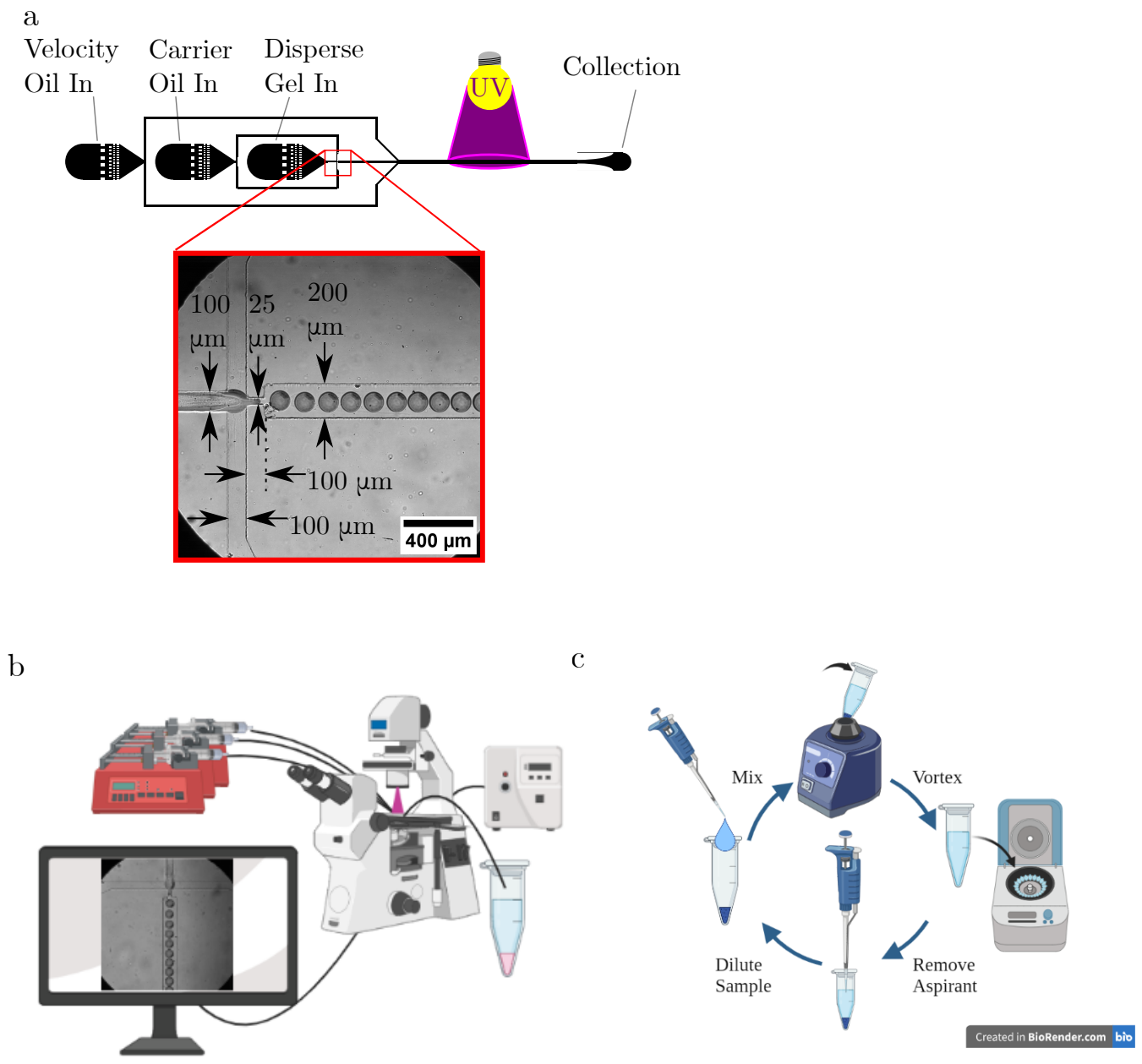


Figure 2.5: (a) A reproduction of the microfluidic mask of the flow focuser used in this experiment. This flow focuser was designed as a single height microfluidic chip. A micrograph of droplet production at the flow focuser junction is included. Micro-channel dimensions are shown, with the neck width varying from $25\mu m$ (shown) to $66\mu m$. Microchannel height varied from $h = 80\mu m$ to $h = 200\mu m$ depending on desired droplet size. (b) A diagram of the experimental setup. Three syringes were connected to syringe pumps, and attached to the flow focuser, under a microscope. The droplets were measured during production to ensure proper sizing. UV light was provided to the flowing droplets. Microgels were collected in a collection tube. (c) The wash cycle protocol is illustrated. Microgels were washed by a cycle of adding solvent, mixing, centrifuging to separate the microgels from aspirant, and removing the aspirant. This cycle was repeated several times, adding FC-40, ethanol, water and finally 10 % aqueous SDS.

then baked until solid at 70°C, for 2-24 hours. The PDMS was cut out of the mold, holes were punched using a 1 mm biopsy punch, and plasma bonded to a glass microscope slide. After plasma bonding, the PDMS and glass were made hydrophobic/fluorophilic by injecting an electronics coating (NOVEC 1700, 3M Company, St Paul MN) into the channel and baking at 110°C for 30 min. This coating was repeated twice over before the microchannel was ready to be used.

2.2.4 Hydrogel Preparation

The PEG gel chemical composition used in this work was selected based on the work of Duprat *et al.* [56], describing how PEG can be balanced with PEGDA during gel formation. In the case of this thesis, the hydrogels used were PEG based. A mixture of PEG, PEGDA, and photoinitiator (PI, 2-hydroxy-2-methyl-1-phenyl-propan-1-one, Sigma Aldrich, Darmstadt Germany) were mixed in an aqueous solution before being injected into the microchannel to be polymerized. The PEG used here had a molecular weight of 200, and PEGDA had either a molecular weight of 575 or 700, depending on the desired gel elasticity. This allowed for an additional flexibility in tuning the microgel stiffness. Additionally, in order to make tracking the motion of solidified particles easier, fluorescent 1 μm microbeads (Polybead Polystyrene 1 μm microspheres, Polysciences Inc., Warrington, PA, USA) were added, in low enough concentrations so as to not effect overall chemistry or material properties (0.1 % solid w/v). Finally, for some microgels, SDS was added to the gel mixture to reduce the surface tension between itself and the oil phase. This surfactant is non-reactive with the PEG, remaining in the surrounding water, although its overall effects on the eventual properties of the microgels were not tested here. Early mixtures tested varied the relative quantities of the above components wildly, but it was realized that a mixture including 5 % PI, and 65 % PEG and PEGDA combined, with approximately 10-15 % PEGDA, would achieve soft and stable and reproducible microgels.

Due to the light sensitivity of the PEG mixture, it was prepared by mixing in an ultraviolet light free environment. Furthermore, once this liquid was loaded into a syringe, the syringe and tubing were wrapped in aluminium foil to prevent light penetration. The gel precursors were vortexed to ensure full mixture of all components, both during preparation and immediately before loading into the syringes, as some components may separate if left for long periods.

2.2.5 Protocol

In order to make microgels, one syringe filled with the PEG mixture, and two with the FC-40 and surfactant mixture are connected to the microchannel inlets, as shown in Fig. 2.5a. The syringes are then connected to a syringe pump (Nemesis, Cetoni GmbH, Korbussen Germany) as shown in Fig. 2.5b. The microfluidic channel is placed on an inverted microscope (Eclipse Ti, Nikon Europe BV, Netherlands), with the 10x objective aimed at the desired UV exposure zone. This region of the microchannel is shown in Fig. 2.5a, approximately midway on the strait portion

of the channel leading up to the outlet. The outlet of the channel is connected via 1 mm outer diameter tubing to a collection tube. The oil (FC-40 containing 1.5 % w/v RAN fluorosurfactant) fills the channel in order to eliminate bubbles.

Once all bubbles are eliminated, the flow rates for the drop phase, carrier phase and transport oil are set to create the desired droplet sizes. The droplet size is measured digitally via a high speed digital camera (SA3 fastcam, Photron Europe Ltd., Wycombe UK). To aid with the process, a first estimate of relevant flow rates is made using a droplet size prediction tool [103]. Once the desired droplet sizes are achieved, the UV lamp (X-Cite@120 Fluorescent Lamp, EXFO Photonic Soln., Mississauga Canada), connected to the inverted microscope is turned on at full strength. This ensures the diameter of the microgel most closely matches the droplet diameter, accommodating any oxygen inhibition. The channel is exposed to UV as indicated in Fig. 2.5a, with care to ensure any area upstream of the flow focuser is not exposed so as to remain liquid.

Polymerized droplets continue to flow through the outlet tubing and into a collection tube (occasionally, the user should check to ensure the channel has not become clogged with microgels, which can on rare occasion occur). Once a sufficient volume of microgels have been recovered, at least 0.2ml of gel, water is added to the microgels. This ensures the microgels do not fuse together and then continue polymerizing, creating non-spherical gels. Then gels are washed to allow them to be injected into aqueous flows. The washing cycle is illustrated in Fig. 2.5c. The microgels are washed first with pure FC-40 to remove any surfactant, then with ethanol (70 % (aq)) to ensure all FC-40 is removed, and then twice with water to ensure all ethanol is removed. Finally the gels are suspended in 10 % SDS (aq) to prevent the microgels from sticking. These microgels are left to swell overnight before being characterized for size and material properties.

2.3 Microgel Characterization

2.3.1 Droplet to Microgel Size

The first and simplest characteristic of microgels are their sizes after creation. Fig. 2.6 shows a sample comparison of gel droplet sizes with their polymerized and swollen counterparts. There is a clear correlation of microgel size with their un-polymerized droplets. Interestingly, the ratio of liquid to gel diameters is not consistent across the different PEGDA concentrations, nor across the different gel sizes. This trend reflects the two competing factors impacting changes in droplet size: inhibited polymerization by oxygen and swelling. Previous studies have shown that a constant thickness of liquid gel will exist after polymerization due to oxygen diffusion [101, 45]. Swelling meanwhile is expected to increase with gel volume. This would lead to an expected correlation of increasing in relative diameter, $d_{\text{gel}}/d_{\text{drop}}$. Fig. 2.6 however shows no clear correlation between $dd_{\text{gel}}/dd_{\text{drop}}$ and d_{drop} . From these facts combined, it is clear that a factor beyond the chemistry of the microgels is affecting the balance of

swelling and oxygen inhibition.

The trends of droplet and gel diameters across PEGDA concentrations being insensitive or even opposite the expected swelling and oxygen inhibition is hypothesized to be primarily due to differences in UV exposure time during initial polymerization. In general, smaller droplets were made using lower droplet and higher carrier flow rates, as is typical during dripping droplet production [18, 12]. In order to maintain a high droplet production rate however, this results in an overall increase in flow rate through the microchannel, and therefore a decrease in time exposed to UV. There are further complicating factors, which also may affect the final droplet size, ranging from the time under UV exposure [45], to the concentration of PEGDA [163] to microchannel thickness affecting oxygen diffusion. Furthermore microgels were exposed to light after polymerization and were allowed to swell in a water bath. The interaction of these factors is complicated, and as they were not controlled for it is difficult to draw conclusions as to which is responsible for the trends between droplet and particle diameters. The challenge of controlling for all possible factors influencing the microgel size highlights the need to avoid over reliance on bulk measurements to predict microgel swelling/oxygen inhibition.

Additionally, the gels created through this method have high degree of monodispersity, with a standard deviation of 2-5 % in both the liquid and photo-activated stages. Some of the variation in droplet size was observed during droplet making, where periodically, the droplet size would vary slightly. This may be attributed to the choice to use a flow controlling syringe pump, rather than a microfluidic pressure controller, which avoids any periodic inflation of the microchannel due to any air which may still be in the system. Practically speaking however the use of syringe pumps was deemed more versatile and easy to use, with less need to calibrate the entire setup when making microgels. Furthermore, as we will see in future chapters, some degree of polydispersity is not detrimental to the experiments performed in this thesis.

2.3.2 Microgel Stiffness

Generally hydrogels exhibit a porous, viscoelastic behavior [164, 134]. For many applications however, the simpler linear elastic model is sufficient to describe most microgel behaviour [134]. In this thesis I use both microindentation and microfluidic traps to measure the elastic modulus. The method using microgel traps, not dissimilar to micropipette aspiration, will be described in a later chapter. Microindentation is described by Guillou *et al.* as a method to measure microgel moduli using an indenting cantilever, shown in Fig. 2.7 a and b [70]. In short, microgels are trapped by a lightly aspirating pipette. A custom cantilever hammer is then pressed against the microgel using a piezo controller. A microscope measures the displacement and force on the cantilever head, and determines the apparent stiffness, $E^* = \frac{E}{1-\nu^2}$ of the particle by Hertzian contact as

$$E^* = \frac{3F}{4r^{1/2}l^{3/2}} \quad (2.2)$$

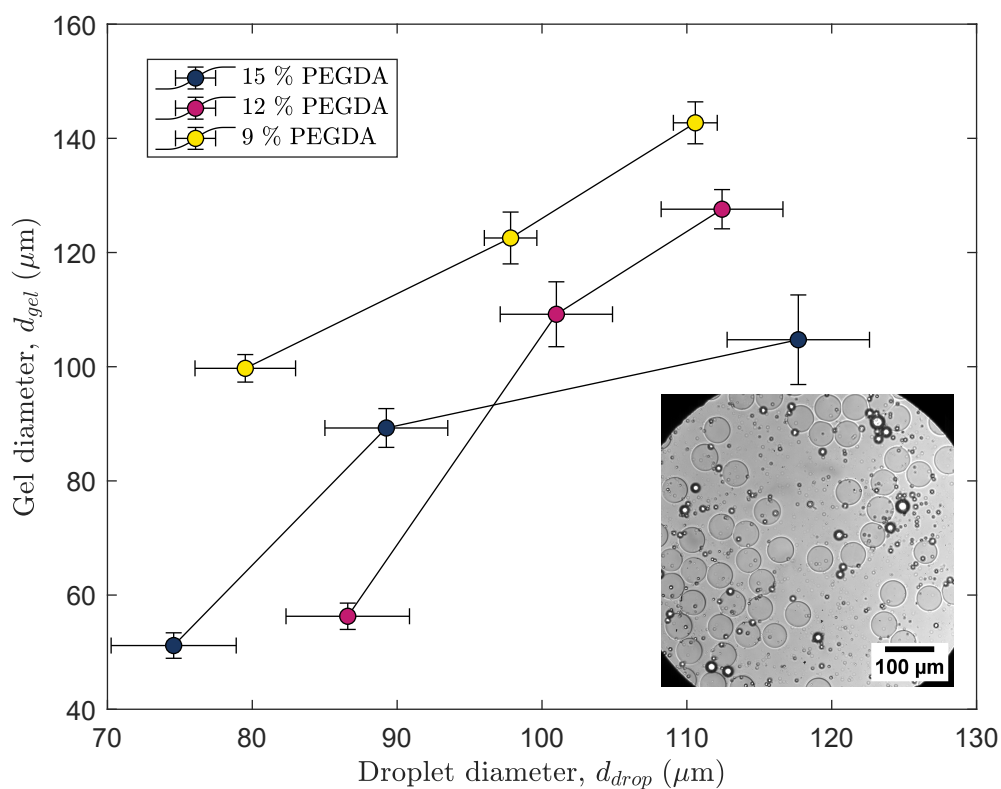


Figure 2.6: A comparison of 9 batches of microgel diameters before and after photo-crosslinking. The microgels in question contain a total of 65 % (v/v) PEG mw200 and PEGDA mw700 with varying proportion, as well as 5 % (v/v) PI and 1 % (w/v) SDS (aq). An inset shows a typical micrograph of gel particles which have been placed on a microscope slide in order to have their diameters measured.

Where F is the contact force between microgel and cantilever, r is the effective radius and l the deflection of the cantilever into the microgel. The apparent stiffness is defined in terms of the elastic modulus E and the Poisson ratio ν of the microgel. Because the cantilever has an elasticity several orders of magnitude greater than that of the gel, its contribution to E^* is neglected in this formulation. The effective radius, r is defined in terms of the microgel, r_{gel} and cantilever probe radii, r_{probe} as $r = \left(r_{\text{gel}}^{-1} + r_{\text{probe}}^{-1} \right)^{-1}$. The force F applied to the microgel is related to the deflection of the probe into the gel, l , by the probe spring constant, k , and the difference between deflection at the base, l_{base} and tip of the probe l , such that

$$F = k(l - l_{\text{base}}). \quad (2.3)$$

We compare the elastic modulus of four different microgels by microindentation, as shown in Fig. 2.7c. Importantly, this shows that by varying the concentration of PEGDA within the microgels from 10 to 15 % (v/v), a change in elasticities from $E^* \sim 100$ Pa to $E^* \sim 10$ kPa can be achieved. Furthermore, changing to a lower molecular weight polymer, 700 to 575 mw PEGDA, changed the stiffness by an order of magnitude. These microgels are on the softer side for PEGDA based microgels, with many in literature reaching the $E^* \sim 1$ MPa range [47, 121]. In general, the microgels made using a lower fraction of PEGDA tend to have a lower stiffness, while a decrease in molecular weight also increases the microgel stiffness. This is broadly in agreement with literature, as more densely packed PEGDA chains will result in a tighter gel matrix [47, 61, 121, 182]. There is also a slight increase in elastic modulus with microgel diameter when comparing the 10 % PEGDA mw700 microgels. This may relate to the oxygen inhibition present, as smaller gels will be inhibited closer to their core, polymerizing at a slower rate, or it may be the result of variations in the time under the UV lamp, as this was not rigorously controlled for.

A second aspect of these microgels is the wide distribution of microgel elasticities within each sample. In the realm of microgels, large uncertainties e.g. greater than 20 %, in material properties are not entirely uncommon [121, 61]. Variations between individual microgels in time under the UV light may contribute to the changes in elasticity, as microgels which passed at the centre of the UV exposure channel would travel at a faster velocity and thus receive less exposure. There is also the possibility of small variations in chemical composition between gels which may have a magnified effect gel to gel if for example the liquid gel has some species variation after mixing, or some settling occurs during the time it takes to inject the gel solution. This variation also highlights the physical properties of hydrogels which are not necessarily present in bulk hydrogel analysis [40].

2.4 Conclusion

This chapter has gone over the creation of microgels which will be used throughout this thesis. Using a flow focusing microfluidic channel, PEG droplets were made, and polymerized in the channel when exposed to UV light. These particles were then washed and allowed to swell before being characterized and used in future experiments. PEG

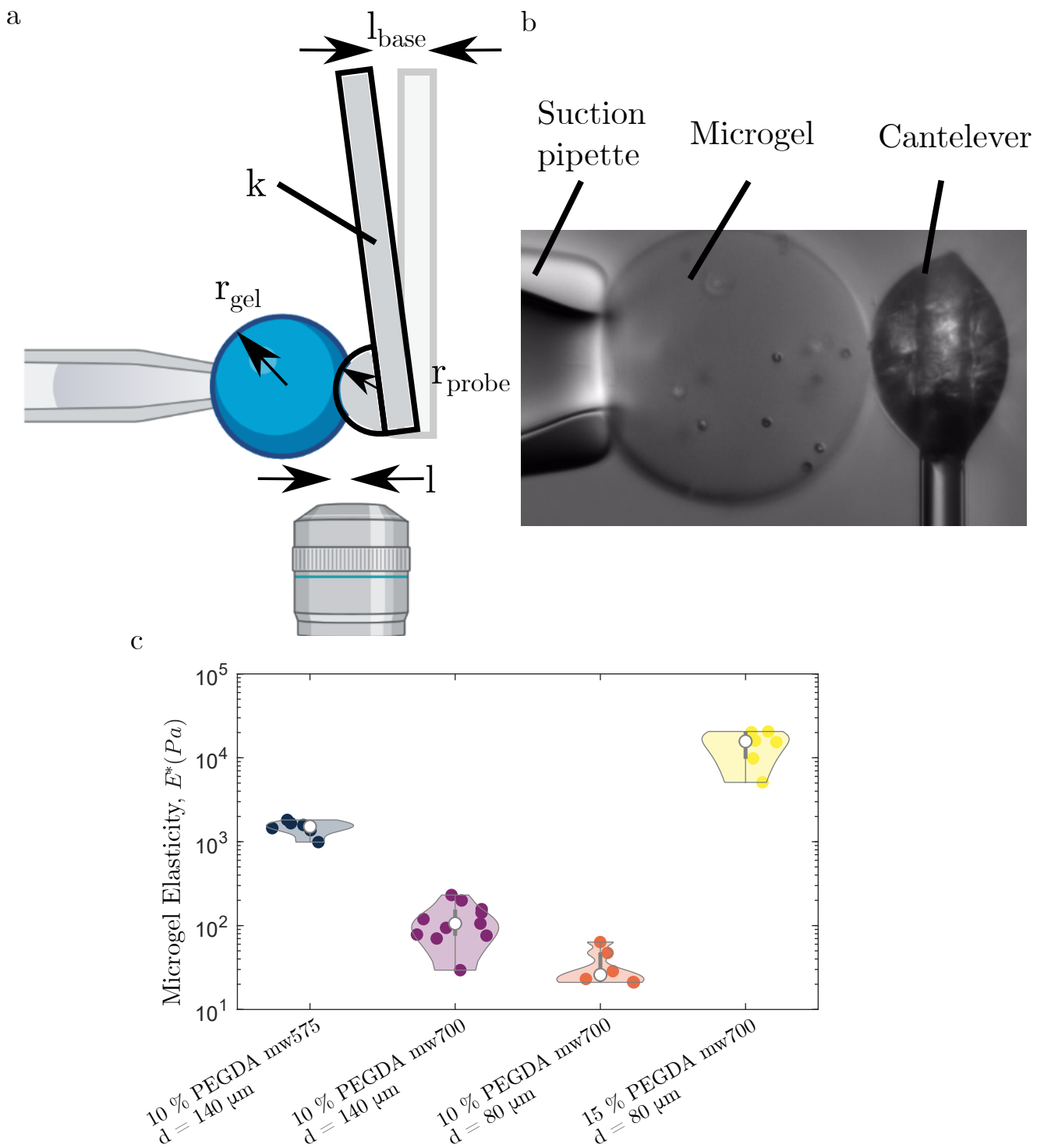


Figure 2.7: (a) A diagram of microindentation, as described in Guillou *et al.* [70]. The cantilever is shown compared to its original position (faded) to illustrate the deflection at the base and at the indentation. (b) A micrograph of microindentation using an immobilized microgel. (c) A comparison of microgel elasticities measured by microindentation. All microgels contained 5 % (v/v) PI, 1% (w/v) SDS, and a total of 60 % (v/v) PEG mw 200 and PEGDA. Each point represents one sample, with $n \geq 6$.

was selected as the gel to use in these experiments in part because of the versatility photo-polymerization allows for, in conjunction with the range of physical properties which can be tuned for by carefully controlling the chemical makeup of the particles, in particular the elastic behavior of the particles.

The PEG droplets made here had a high degree of monodispersity both before and after polymerization and swelling. The droplet sizes could easily be tuned to the desired size. While both oxygen inhibition and swelling were observed, the degree of each was not consistent between tests, resulting in final particle sizes which were difficult to predict. This is likely due to other factors in droplet/microgel production which were not controlled for. The gels made here have a large range of stiffness, ranging as low as $E^* \sim 100$ Pa. This was achieved by polymerizing gels with low concentrations of PEGDA relative to the PEG content, as well as allowing the gels to swell. Some tuning was required in order to achieve the desired elastic properties (similarly to tuning for microgel size). In both cases, no complete guide to these properties exist, as both involve many interacting variables; flow rates and geometry in the case of the flow focuser for droplet size and the gel chemistry and UV exposure for its mechanical properties. While certain trends have been highlighted in the literature, no complete guide exists. Furthermore, unlike with gel sizes, the elasticities of these microgels were relatively polydisperse (see Fig. 2.7). This is to be expected for particles of this size, where the range of elasticities is logarithmic. In all cases, these experiments highlight the necessity to test the properties of the gels made for every batch and set of tests, and not to rely too heavily on literature estimates.

Microgels are in many ways an ideal soft solid to measure fluid structure interactions in microfluidic environments. To date, extensive research has been done on the subject of fibers and films, however as spheres are compact, the cases where fluid forces are capable of deforming them are more rare. These scenarios only occur where the spherical body in question is extremely soft relative to its environment, such as the case for soft microgels, be they cellular environments, a proxy for biological/tissue materials, chemical carriers, or soft sensors. In the coming chapters, I will expand upon the deformation these microgels undergo in non-axisymmetric environments, such as those of a typical microfluidic chip, where the particles are subjected to a coupled balance between the forces of the fluid flow, and the microgels own deformation.

Chapter 3

Deformation of Trapped Microgels in a 1D Constriction

3.1 Introduction

Micro-particles moving through microfluidic constrictions must first enter into the constriction before they can pass through it. During their entry, these particles undergo considerable change in shape, from spherical to conforming to the microchannel. It follows that the process of deformation which these particles undergo is crucial to understanding more broadly the passage of soft microparticles through constricting channels. In the case of cells, the deformation from penetrating into a micro-constriction can have lasting effects to their cellular mechanics and physiology [39, 119, 73, 85].

The geometry of the particle and microchannel play a large role in the fluid-structure interaction of particles entering into a constriction. One of the simplest geometries is the axisymmetric particle and constriction. In this case, a spherical particle, such as a cell or microgel, flows into a cylinder or conical section with a smaller radius than the particle, see Fig. 3.1 a-b. One of the earlier examples of a microfluidic constriction being described mechanically was done by Theret *et al.*, where cells were aspirated into a micropipette to mechanically characterize them [157]. This model looked specifically at pipettes significantly smaller than the cells they would aspirate, but more generally this laid the groundwork for a range of variations on micropipette aspiration [71, 64, 80, 104, 105, 112, 64]. More recently, this same methodology has been adapted for microfluidic channels [104, 105, 57]. In these cases, the micropipette was approximated by a small square opening within a microfluidic channel allowing for rapid fabrication using conventional soft lithography. In the case of Elias *et al.* the micropipette approximation was further developed, accounting for the change in curvature of a vesicle induced by the square geometry, providing a more accurate description of micropipette aspiration in non-circular geometries [57].

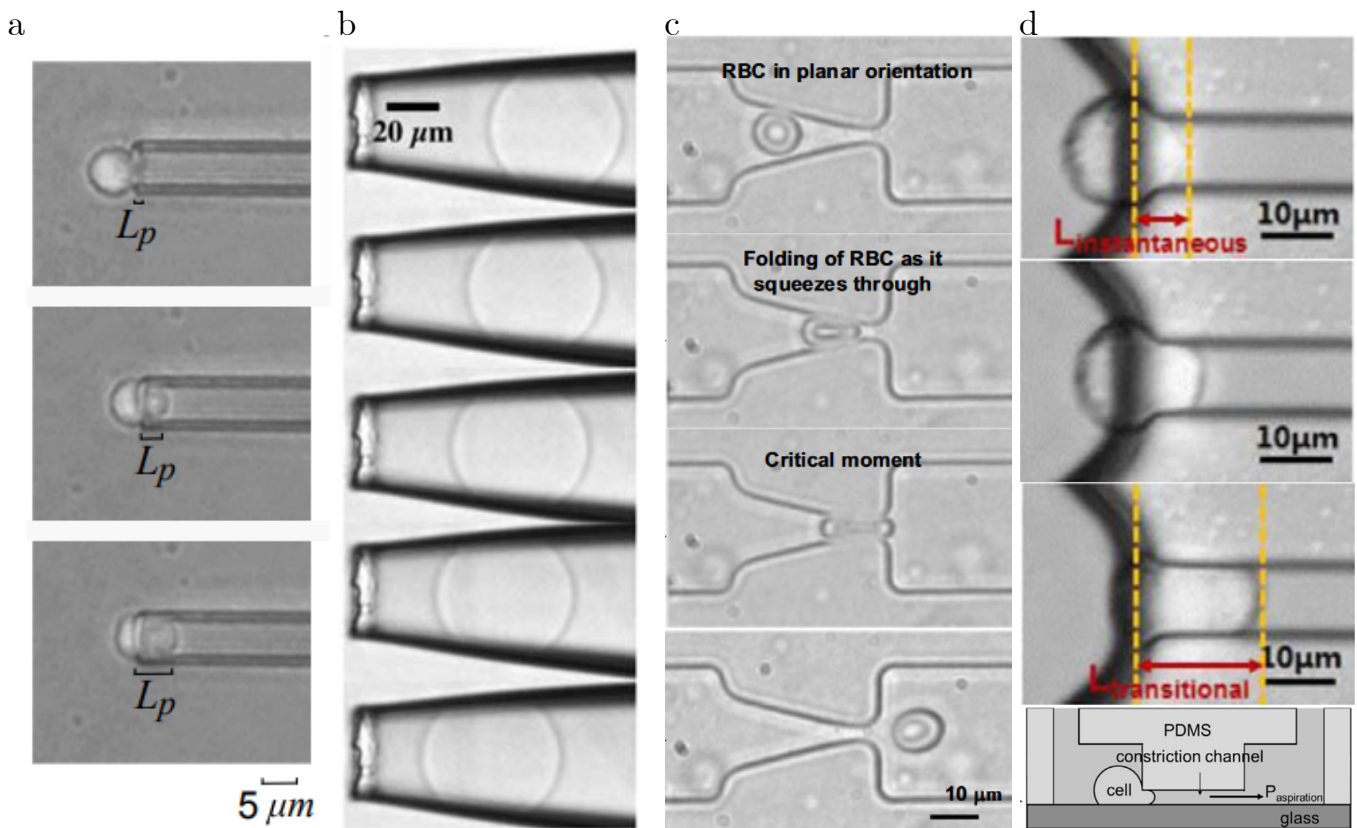


Figure 3.1: Examples of different geometric types of constriction entrances. (a) A cell entering into a sudden axisymmetric constriction. In this case the cell is undergoing micropipette aspiration to assess the viscous modulus. Reproduced from González-Bermúdez *et al.* [64]. (b) A tapered capillary containing an acrylamide based microgel. As pressure increases the microgel is pushed further into the capillary, thereby measuring its Young's modulus. Images are provided in descending order of increased pressure. Reproduced from Wyss *et al.* [173]. (c) The passage of a red blood cell (RBC) through a tapered microfluidic constriction. The in plane height of the microchannel is kept constant. The constriction was placed in series with identical constrictions to measure the impact of repeated confinement and release. Reproduced from Guo *et al.* [73] (d) An elastic cell as it enters into a microchannel which suddenly decreases in height and width. A diagram of the microchannel is provided as well. Reproduced from Luo *et al.* [117].

Tapered constrictions, such as that shown in Fig. 3.1b, have also been explained mechanically. By forcing particles into a conical constriction, dubbed capillary micromechanics, the elastic modulus of particles can be measured, compared with the contact pressure provided by the tapered capillary [173, 71, 7]. This methodology has been applied to both polymeric particles [173, 71, 100], as well as cellular materials [7]. Suction into these tapered capillaries have been described analytically in full, including not only as they enter the tapered region, but also as they exit it into a straight constriction [110, 111].

One aspect which considerably simplifies the analysis of axisymmetric constrictions is that the microparticle completely plugs the flow, leading to an even distribution of pressure on either side of the particle. Additionally, by treating the particle as axisymmetric, the analysis of the forces deforming the particle becomes considerably simpler, as the problem becomes two dimensional. While numerous studies have been performed observing the entry of particles or cells into rectilinear microfluidic constrictions [177], only a handful have specifically attempted to model the deformation of these particles. Guo *et al.* has created a model for the entry of red blood cells into a constriction [72, 73]. In this case, the constriction is gradual, maintaining a constant microchannel height, and angling the walls of the microchannel together, as shown in Fig. 3.1c. This modeling has also been serialized in order to describe the effects of repeated deformation [119]. More recently a model for microgels in a similar geometry was described by Xu *et al.*, but this time, the study focused on microgels, which behave more like a conventional soft solid than a fluid capsule. This also parallelized the process, allowing for simultaneous observations of multiple microgels.

More abrupt constrictions have also been considered. As well as the general geometric differences to other constrictions, these sudden constrictions also emphasize the fact that the particles entering do not fully plug their microchannels, leading to leaks around them. Preira *et al.* developed a model of cellular entry into a one dimensional constriction, modeling the cell entry as a viscous drop [139]. This notably accounted for flow around the cell, approximating it as a droplet described by the Bretherton model. Luo *et al.* and later Davidson *et al.* used a combination of numerical modeling and experimental data to model the entry of cells into a sudden reduction in microchannel height and width, see Fig. 3.1d [117, 43]. Using this geometry, it is possible to characterize the instantaneous elastic modulus of cells undergoing deformation [117, 43, 112]. The description of cellular passage into abrupt one dimensional constrictions to date however has been limited to either using more established models of droplets, or has relied heavily on empirical modeling to describe the behavior.

In this chapter, I aim to create a model of microgels entering into a one-dimensional constriction, using a combination of experimental and numerical data. The model used in this chapter is based on fundamental principles in contact mechanics, as well as laminar fluid mechanics, in order to describe the three dimensional deformation of a solid microgel particle in the early stages of penetrating a constriction. Similar to many other applications of microfluidic constrictions, this model can be used as a novel method of analyzing the elastic properties of the microgels in question. Finally, in describing the way in which fluid forces deform a microgel entering a constriction, I lay the groundwork for looking at the same problem in reverse and answering the question of how the entry of a

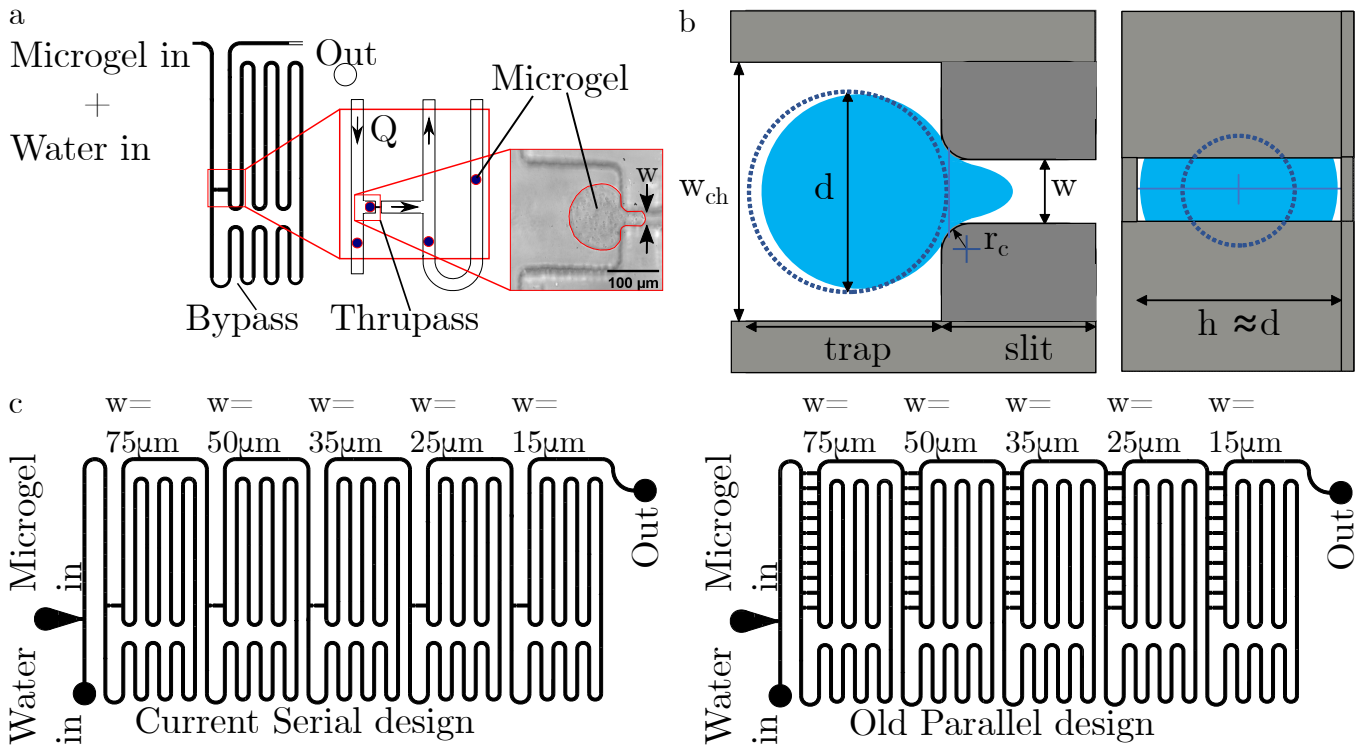


Figure 3.2: (a) A diagram of the region of interest for the microfluidic trapping channel. The bypass and thrupass are shown in full. Zooming in, the a diagram of the bypass/thrupass junction shows microgels passing and getting stuck in the trap. Further zooming in, a micrograph of a trapped and deformed microgel is shown. (b) A diagram of the microfluidic trap with relevant dimensions labeled. The thrupass is separated into the trap, where the gel rests and slit region, which constricts the gel and prevents passage. (c) A negative of the full microfluidic channel mask, presented at 2x scale. The microfluidic mask used in this work, is presented alongside the original design, which included ten parallel traps for each size of trap slit.

microgel into a constriction affects the flow around it.

3.2 Methods

3.2.1 Single Thickness Microfluidic Trap Design

The design of the microfluidic trap is composed of four sections: the inlet, a "thrupass" line containing a microfluidic trap, a channel bypassing the trap, and the outlet of the channel. A flow containing a dilute suspension of microgels passes through the channel, and a microgel will flow preferentially into a trap, at which point the trap will be occupied and other gels will then flow through the bypass line, as shown in Fig. 3.2a. Once the trap is occupied it begins to plug, and pressure is controlled by flow through the bypass line. As flow and thus pressure are increased, the microgel is pushed further into the trap.

In order to maximize adaptability, a single mask design was used to make microchannels of different heights. In order for the single microfluidic mask to be usable with microgels of different sizes, the main channel width was set be $w_{ch} = 200 \mu\text{m}$ except at the trap slit, which was larger than any microgel tested. A diagram of the trap is

shown in Fig. 3.2b, and the full mask is shown in Fig. 3.2c. The width of the trap slit was selected to cover a range of possible microgel sizes, measuring $w = 75, 50, 35, 25, 15 \mu\text{m}$ at each successive trap. This allowed for a single microchannel to test several microgels at once, and test the effect of varying w on the gel deformation. Ultimately, for the range of microgel sizes/elasticities tested here, only the widths $w \leq 35 \mu\text{m}$ were actually tested, with the larger sizes kept as an option for future tests. Additionally, while corners were right angles in the microfluidic mask, they were in practice rounded, with radii r_c measured each test.

Initial designs of the microchannel included multiple parallel thrupasses for a single bypass. This was done with the intention of rapidly measuring the deformation of multiple microgels at once. This aspect of the design had to be abandoned however, as upon early testing, it became apparent that microgels would plug their respective traps at different rates. This made measuring the pressure applied to the microgels challenging and significantly reduced the pressure experienced for gels downstream. This effect has been studied by Guernonprez *et al.* [68], who showed the differences in flow for identical channels in parallel. The uneven flow was exaggerated by the fact that the microgels themselves had an effect on the hydrodynamic resistance of each thrupass. Any microgel which did not plug its trap as much as the others would let flow pass through that trap, and limiting flow through the bypass, making the system unusable. Ultimately, this aspect of the design was cut out, leaving only the five microfluidic traps per chip, see Fig. 3.2c for comparison.

For the traps to be effective, they had to be designed to trap a single microgel each at a time. This meant that the channel height had to be nearly the same as that of the microgels being tested. Therefore the height of the microchannel, h , was set to be approximately that of the microgel which was undergoing testing, which in the case of this study was $h = 85 \mu\text{m}$ and $h = 140 \mu\text{m}$.

Hydrodynamic resistance is a principal concern when designing the specific geometry of the thrupass/bypass channels. Resistance is defined as the ratio of flow to pressure through a channel, such that

$$R = \frac{P}{Q}, \quad (3.1)$$

where P is the pressure difference from the entry to exit of a section of flow, and Q is the flow rate in the channel. Where two channels exist in parallel, flow will preferentially pass through that of the lower resistance. In effect this process is analogous to electronic resistance, where pressure is an analogue for voltage, and flow rate is analogous to current. Resistance in a rectangular channel is described in detail in Mortensen *et al.* [127] and is calculated as

$$R_{\text{ch}} = \frac{\alpha \left(\frac{w_{\text{ch}}}{h} \right) \mu z_{\text{ch}}}{w_{\text{ch}}^2 h^2}, \quad (3.2)$$

where z_{ch} is the length of the channel, μ is the fluid dynamic viscosity. $\alpha \left(\frac{w_{\text{ch}}}{h} \right)$ is the shape factor for the rectangular

	$h = 85 \mu\text{m}$	$h = 140 \mu\text{m}$
$R_{\text{byp}}(w_{\text{ch}} = 200 \mu\text{m})$	$2.7 * 10^{12} \text{ Pa s m}^{-3}$	$7.7 * 10^{11} \text{ Pa s m}^{-3}$
$R_{\text{thru}}(w = 15 \mu\text{m})$	$9.9 * 10^{11} \text{ Pa s m}^{-3}$	$5.6 * 10^{11} \text{ Pa s m}^{-3}$
$R_{\text{thru}}(w = 25 \mu\text{m})$	$2.8 * 10^{11} \text{ Pa s m}^{-3}$	$1.4 * 10^{11} \text{ Pa s m}^{-3}$
$R_{\text{thru}}(w = 35 \mu\text{m})$	$1.4 * 10^{11} \text{ Pa s m}^{-3}$	$6.3 * 10^{10} \text{ Pa s m}^{-3}$

Table 3.1: The resistances calculated for the bypass and thrupass lines for various channel heights, h , and trap slit widths, w . Resistances are calculated for 10 % (aq) SDS. Note that the actual resistance for the bypass channel is calculated based on the channel width measured under the microscope for each individual microchannel.

channel defined as

$$\alpha\left(\frac{w_{\text{ch}}}{h}\right) = \frac{\pi^3\left(\frac{w_{\text{ch}}}{h}\right)^2}{8} \left(\sum_{n=1,3,5,\dots} \frac{\left(\frac{w_{\text{ch}}}{h}\right)}{\pi n^4} - \frac{2}{\pi^2 n^5} \tanh \frac{n\pi\left(\frac{w_{\text{ch}}}{h}\right)}{2} \right)^{-1}. \quad (3.3)$$

The bypass length was selected to be $z_{\text{ch}} = 101 \text{ mm}$, such that the resistance of the bypass line would be greater than the thrupass, $R_{\text{thru}} < R_{\text{byp}}$. This means that flow, and therefore the microgels, would preferentially travel through the thrupass line, getting trapped. The trap and bypass resistances can be found in Tab. 3.1 for the two channel heights tested here. While these resistances are calculated for the viscosity of an aqueous solution of sodium dodecyl sulfate (SDS, Sigma Aldrich, Darmstadt Germany), the resistances would be proportionally the same, as $R_{\text{ch}} \propto \mu$. In order to maximize precision, the thrupass resistances were recalculated based on the actual value of w measured on each micrograph, as slight variations in width, *i.e.* $\sim 1 \mu\text{m}$, would modify the values of R_{thru} enough to affect the results presented.

The microfluidic channel itself was manufactured using the same methodology described in a previous chapter, using conventional spin-coating SU-8 soft lithography [140]. After the microfluidic channel was designed in a vector editing software, a high resolution photomask was printed to scale. Su-8-2000 (Kayaku Adv. Mat., Westborough MA, USA) was spin coated on a silicon wafer and exposed to ultraviolet light through the photomask, as per manufacturer instructions. The excess was washed off, and the mold soft baked. The mold height was measured using a scanning profilometer to verify it matches the desired size to within $5 \mu\text{m}$. Over the mold, a mix of 10:1 polydimethylsiloxane to crosslinking agent (PDMS, SYLGARD @186, Sigma Aldrich, Darmstadt, Germany) is poured over the mold and baked for 2-12h at 70°C . The channel was cut out, and $1 \mu\text{m}$ holes were punched at the appropriate locations before plasma bonding to a glass microscope slide. To limit any possible adhesion between the microgels and the PDMS, the microchannel was treated with a hydrophobic electronics coating (NOVEC 1700, 3M Company, St Paul MN), injecting the coating fluid and heating the microchannel to 110°C for 30 minutes. The coating was repeated twice.

Due to the limitations of soft lithography with such sharp changes in scales and large aspect ratios, there was some variation between the microfluidic mask and the width measured in the microfluidic channels. The slit width in particular was prone to varying from its prescribed width. While the microfluidic mask had slit widths of $w = 15 \mu\text{m}$, $w = 25 \mu\text{m}$ and $w = 35 \mu\text{m}$, in practice in our experiments these widths measured $w = 21.1 \pm 1.1 \mu\text{m}$, $w = 30.7 \pm 1.9 \mu\text{m}$ and $w = 44.2 \pm 5.2 \mu\text{m}$ respectively. Similarly, the microfluidic design calls for angular corners, however in practice, the microchannel had corners of radius $r_c = 10.8 \pm 4.1 \mu\text{m}$.

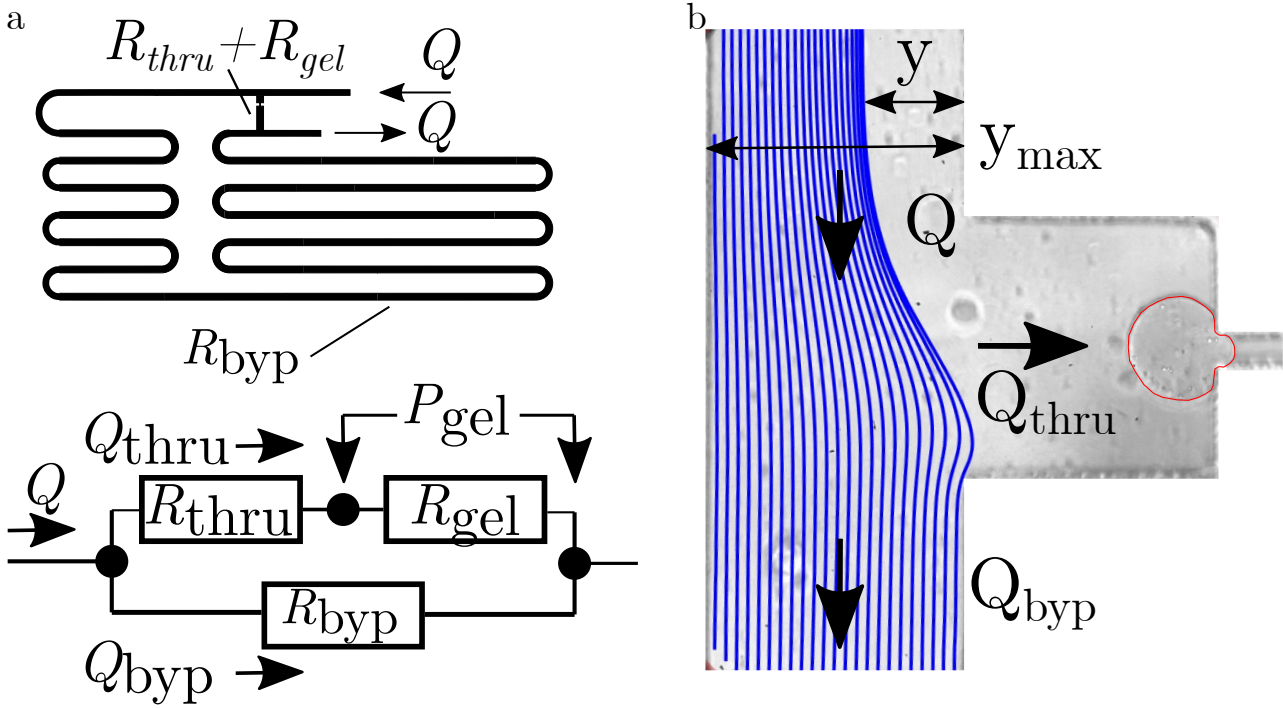


Figure 3.3: (a) A resistance diagram relating the flow through the thrupass and bypass of the microchannel, as well as the corresponding sections on the microchannel itself. (b) A reconstructed separatrix of flow at the junction of the thrupass and bypass lines. The streamlines are reconstructed using

3.2.2 Measuring Flow Rate From Streamlines

Knowing the flow rate past the bypass and thrupass lines is necessary to determine the pressure drop across the microgel. A resistance diagram of the bypass, thrupass and microgel can be seen in Fig. 3.3a. Because the pressure at start and end of the bypass and thrupass lines must be identical, the flow rate between the two components can be written as

$$P = R_{byp}Q_{byp} = (R_{thru} + R_{gel})Q_{thru}, \quad (3.4)$$

where the subscripts *byp* and *thru* refer to the bypass and empty thrupass respectively, while *gel* refers to the trapped microgel. Noting a simple mass balance, that the total flow from the inlet must be equal to that of the bypass and thrupass, this can be rewritten as

$$R_{gel} = \frac{(Q - Q_{thru})R_{byp}}{Q_{thru}} - R_{thru}. \quad (3.5)$$

The flow in this microchannel are laminar in all tests performed. The largest Reynolds number across all tests was measured as $Re = \frac{2Q\rho}{\mu(w+h)} = 2 \frac{(100\mu\text{l}/\text{min})(1\text{kg}/\text{l})}{(0.002\text{Pas})((200\mu\text{m})+(80\mu\text{m}))} = 6$, which is well within the laminar regime. Because of this, it is reasonable to assume that the added resistance from the microgel is entirely localized at the microgel, such that the pressure drop across the microgel can be measured as $P_{gel} = R_{gel}Q_{thru}$. With this in mind, Eq. 3.5

can be written in terms of the pressure drop across the microgel

$$P_{\text{gel}} = (Q - Q_{\text{thru}})R_{\text{byp}} - R_{\text{thru}}Q_{\text{thru}}. \quad (3.6)$$

The resistance of the bypass and thrupass channels are described by Eq. 3.2, and the inlet flow rate, Q is set by the syringe pump, however the amount of fluid passing by the microgel, Q_{thru} must be measured. To measure this, the flow streamlines where the bypass and thrupass meet must be reconstructed from videos of tracer particles passing through the microchannel. A dilute suspension of micron sized beads (Polybead Polystyrene 0.5 μm microspheres, Polysciences Inc., Warrington, PA, USA) were added to the carrier fluid, at a concentration of 0.025 % (w/v). To capture the motion of these tracer particles, videos were taken using a high speed camera (SA3, Phototron Europe Ltd., UK) at 4000 fps. The flow streamlines were reconstructed using a methodology called Particle Image Velocimetry (PIV) [158]. The specific PIV analysis code was adapted from PIVlab [158]. Because flow is set to be steady state, an ensemble analysis is used, which averages the flow field over the entire video.

Once the streamlines were reconstructed a separatrix was created, as shown in Fig. 3.3b. The separatrix divides the fluid going to the thrupass and the bypass channels, according to:

$$\frac{Q_{\text{thru}}}{Q} = \frac{\int_0^h \int_0^y U(x, y) dy dx}{\int_0^h \int_0^{y_{\text{max}}} U(x, y) dy dx}, \quad (3.7)$$

where $U(x, y)$ is the theoretical fully developed flow speed in a rectangular channel of a height h and width $y_{\text{max}} = w_{\text{ch}}$. The dividing point y is measured at least one channel width w_{ch} upstream to ensure it represents fully developed flow in a rectangular channel, see Fig. 3.3b.

The fully developed flow in a rectangular channel for Poiseuille flow was first solved by Boussinesq [23] as

$$U(x, y) = -\frac{dP}{dz} \frac{y(y_{\text{max}} - y)}{2\mu} + 4 \frac{dP}{dz} \frac{y_{\text{max}}^2}{\mu\pi^3} \sum_{n=1}^{\infty} \frac{\sinh \frac{(2n-1)\pi z}{y_{\text{max}}} + \sinh \frac{(2n-1)\pi(h-z)}{y_{\text{max}}}}{(2n-1)^3 \sinh \frac{(2n-1)\pi h}{y_{\text{max}}}}, \quad (3.8)$$

where $\frac{dP}{dz}$ is the rate of pressure drop across the channel. This pressure drop can be ignored, as it will cancel out when calculating Q_{thru} using 3.7. While precise, this series is still relatively complicated. To simplify the calculations, a substitution was made according to Vanapalli *et al.* [165], which was adapted specifically for use in measuring the flow as a result of displaced streamlines. The flow profile in this case is described by

$$U(x, y) = U_{\text{max}} \left(1 - \left(\frac{x}{h} - 1 \right)^2 \right) \left(1 - \left(\frac{y}{y_{\text{max}}} - 1 \right)^m \right), \quad (3.9)$$

where U_{max} is the velocity at the centre of the rectangular section. The geometric factor $m = \sqrt{2} \frac{y_{\text{max}}}{h} + 0.89 \frac{h}{y_{\text{max}}}$ accounts for the channel being wider than it is high.

The PIV code was combined with a longer MATLAB code. This code reconstructed streamlines from the videos

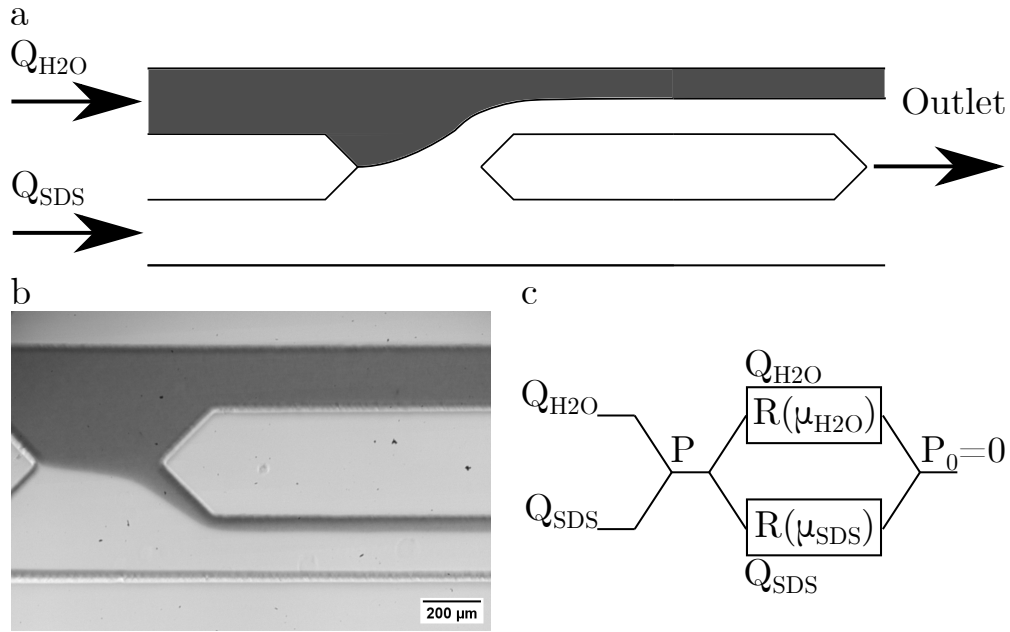


Figure 3.4: (a) A diagram of a microfluidic comparator, with one inlet containing the reference solution of water and ink, Q_{H_2O} , and a second solution containing the SDS solution, Q_{SDS} . As downstream resistances are unequal due to changes in viscosity of the ink and SDS, there is a deflection of the streamline. (b) A micrograph of the microfluidic comparator used to characterize the SDS. (c) A resistance diagram of the comparator. When the flow from the ink passes entirely through the top channel, and the SDS solution passes entirely through the bottom, then the difference in resistance will be proportional to the difference in flow rates.

of the deformed microgels, and measured the fraction of flow passing through the thrupass from the streamlines as described in 3.7 and 3.9.

3.2.3 Carrier Fluid Viscosity

For these experiments, microgels were suspended in a solution of 10 % (w/v) (aq) SDS. In early experiments, this gave the impression of reducing friction between the microgels and the PDMS microchannel. Because the microgels were in contact with the trap, it was possible that friction between the microgel and microchannel could have some impact on the deformation, and so reducing this friction was desirable.

The viscosity of the SDS solution was measured using a microfluidic comparator. In effect this was done by modulating the flow rates at the inlets of a comparator such as that shown in Fig. 3.4 a-c, and based on that used in Vanapalli *et al.* [166]. Once the dividing line between the water containing black china ink and SDS solution was horizontal, the viscosity could be calculated as the ratio of inlet flow rates $\frac{\mu_{SDS}}{\mu_{H_2O}} = \frac{R(\mu_{SDS})}{R(\mu_{H_2O})} = \frac{Q_{SDS}}{Q_{H_2O}}$. This corresponds to where the inlet flow from both the water and SDS solutions pass entirely through their respective channels. As the dimensions are the same, the only difference in resistance will be due to viscosity. In this case, the viscosity was measured as $\mu_{SDS} = 0.002$ Pas.

	Gel A/Stiff	Gel B/Medium	Gel C/Soft	Gel D/Soft
Diameter, d (μm)	83.4 ± 2.9	139 ± 2.1	84.2 ± 1.1	129 ± 1.8
Effective Elasticity, E^* (Pa)	$(1.5 \pm 0.9) * 10^4$	$(1.5 \pm 0.4) * 10^3$	48.6 ± 24.9	110 ± 87
PEGDA mw	700	500	700	700
PEGDA (% v/v)	15	10	10	10

Table 3.2: Microgel bead sizes and formulations used in this study, and their elasticity as measured using microindentation [70]. The elasticity was controlled by varying the amount of PEG-Diacrylate (PEGDA), as well as changing the molecular weight of the PEGDA. The microgels had a total of 65 % (v/v) PEG and PEGDA, with 5 % (v/v) photoinitiator 2-hydroxy-2-methyl-1-phenyl-propan-1-one and 1 % (aq) (w/v) SDS.

3.2.4 Microgel Characterization

Four different PolyEthylene-Glycol (PEG) microgel samples are tested in this chapter. The microgels were made by photo-polymerizing drops of PEG in a flow focuser emulsion device. Microgel diameters were controlled by the emulsion device, and once photo-polymerized, the microgels were allowed to swell in a bath of 10 % SDS (aq) overnight. The effective elastic moduli, $E^* = E/(1 - \nu^2)$, where E is the Young's modulus and ν is the Poisson ratio, of the microgels were tested using microindentation [70]. These microgels are summarized in Tab. 3.2. The full description of the production of the PEG gels and their testing is presented in Ch. 2.

3.2.5 Experimental Protocol

The experimental setup is illustrated in Fig. 3.5. A syringe containing a dilute suspension of microgels and a syringe containing carrier fluid and a dilute suspension of tracer beads are connected via 1 mm tubing to the microchannel, and a waste tube is also connected. The syringes are then placed on a syringe pump (Nemesis, Cetoni GmbH, Korbussen Germany). The microchip is placed upon an inverted microscope (Eclipse Ti, Nikon Europe BV, Netherlands) with its objective set to 20x, further magnified by 1.5x, imaging in bright-field.

Once all bubbles have been removed from the microchannel, the microgel suspension is flowed into the system until each microfluidic trap is occupied with a single microgel. To avoid having more than one microgel in a single trap, it may be necessary to alternately apply suction and pressure. Once the traps are occupied, flow from the microgel line is stopped, and flow containing tracer beads is provided. Starting at a low flow rate and gradually increasing, successive videos of trapped microgels are taken, each long enough to reconstruct the flow streamlines. Each video is taken when for a given flow rate, the microgel has reached a stable state, *i.e.* the microgel has stopped deforming. Early tests also decreased flow rate from the maximum to test whether the microgel experienced hysteresis. The range of flow rates tested depended on the microgel, and was decided empirically starting with a flow small enough to not noticeably deform the trapped microgel, and stopping slightly below the pressure necessary to push the microgel through the traps slit.

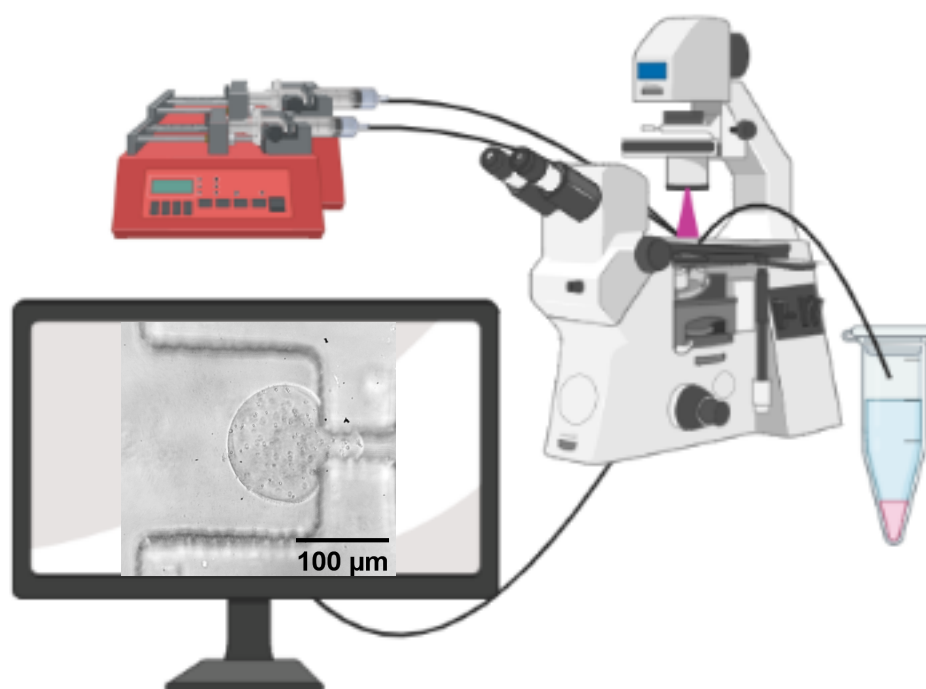


Figure 3.5: A diagram of the experimental setup. The microchannel is placed on a microscope and connected to two syringes on syringe pumps. A waste line is attached for fluid exiting the microchannel. Videos of the microchannel are recorded for analysis.

3.2.6 Solid and Fluid Simulation Setup

Because of the geometry of this experiment, the deformation of the microgel was three dimensional, however the bright field imaging was unable to capture changes in depth. To allow for a more precise and complete picture of the deformation of the microgel, a series of simulations were performed for a spherical microgel passing into the trap slit. Numerical contact simulations were performed in the ABAQUS CAE environment (Dassault Systems, Vélizy-Villacoublay, France). These simulations provided three dimensional models of deformed microgels at various positions while entering the trap slit. These computer aided design models were then exported into a fluid simulation in the COMSOL multiphysics environment, (COMSOL, Grenoble, France) to better understand the forces applied on the microgel. Finally, an approximation of the pressure distribution predicted by the fluid simulation was applied on a second set of contact simulations to ensure the results were physically accurate.

Both solid and fluid simulations were performed using a quarter section of a trapped gel, cutting along the axes of symmetry, see Fig. 3.6a-b. To measure the effect of confinement between the floor and ceiling of the channel and the microgel, microchannel heights of $h = 81 \mu\text{m}$ and $h = 85 \mu\text{m}$ were tested for a microgel of diameter $d = 80 \mu\text{m}$. The simulated microgel had an elasticity of $E = 10 \text{ kPa}$ and Poisson ratio of $\nu = 0.35$, selected to be representative of a typical PEG microgel [27]. Similar to the experimental microfluidic traps, the simulated trap had corners of $r_c = 15 \mu\text{m}$, and a slit width of $w = 15 \mu\text{m}$. The channel is set to be rigid, as its elasticity is significantly greater than the microgels in question, with a typical Young's modulus of $E \sim 1 - 10 \text{ MPa}$ [89, 95].

The contact simulations were done using a dynamic explicit solver. Contact was declared between the microgel quarter sphere and the surfaces of the channel, with the channel being declared the master surface, as it is static. Symmetry condition was applied to all the symmetrically cut surfaces. The first set of solid deformations were calculated by giving the microgel a weight. This weight increased up to a maximum of $F_p = 45 \text{ pN}$ gradually. The second set of solid deformations, based on the pressure distribution found by the fluid simulation, ranged up to maximum pressure of $P_{\text{gel}} = 6400 \text{ Pa}$, which was maximum at the bottom centre of the gel, as shown in Fig. 3.6c. The maximum pressure was chosen in order to be representative of the values seen in the experiments while maintaining a stable simulation. The distribution in the region where the pressure gradually decreases was calculated to be second order smooth, starting at the maximum pressure and decreasing to $P = 0$. The results of these simulations are used to validate the modeling done in this chapter.

The fluid simulations were performed assuming laminar flow, with water as the fluid. A negative of the solid simulation was made by exporting the deformed microgel model to the fluid simulation, and subtracting it from the volume of an unoccupied microchannel. In order to overcome the challenges of simulating precisely overlapping surfaces, the microgel was simulated as having been moved into the microchannel by $0-0.5 \mu\text{m}$ to create a significant overlap. This did not significantly alter the flow, but resulted in a more realistic pressure distribution, as in this case there was no thin film flow between the microgel and microchannel, which should not occur during contact.

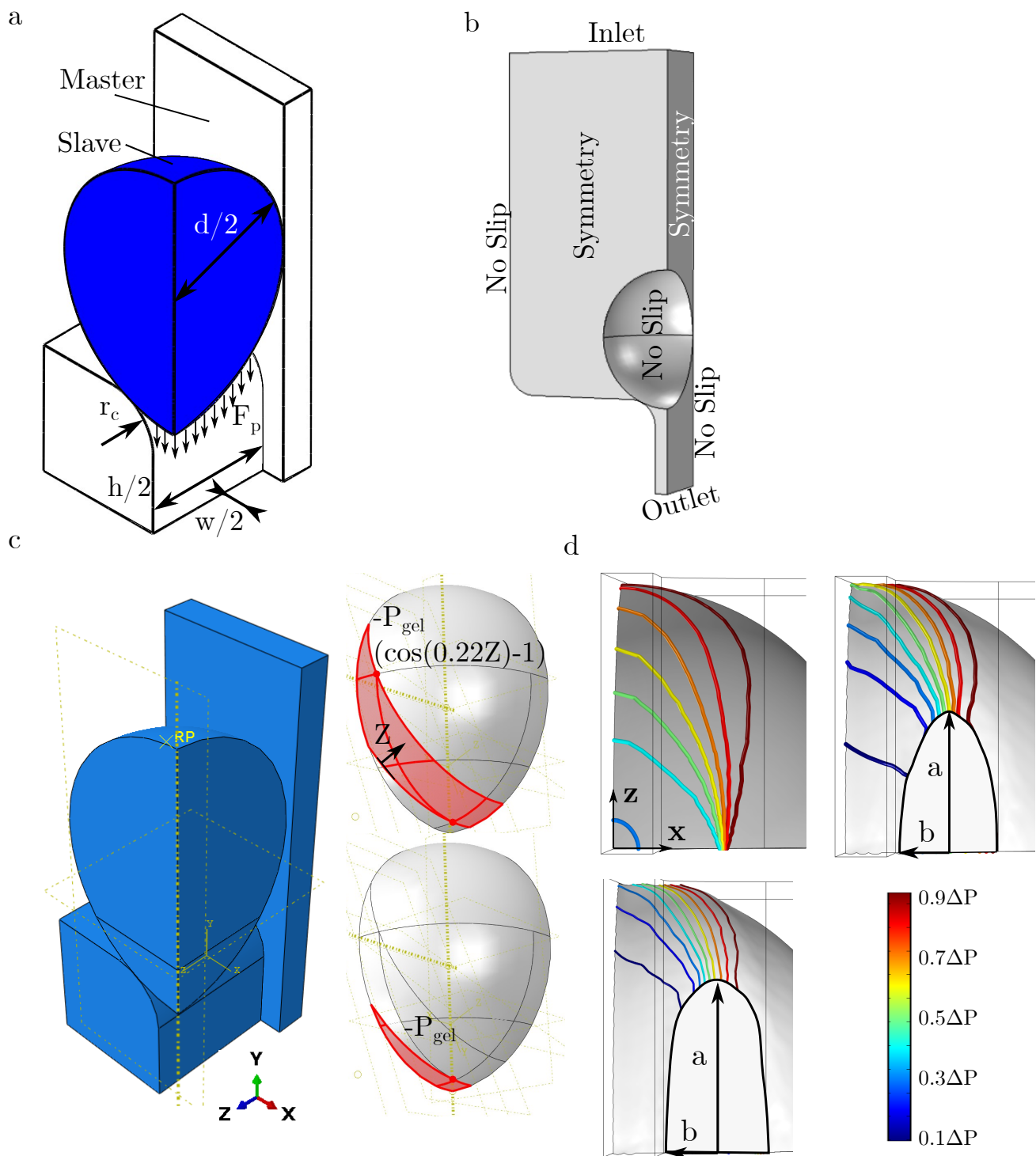


Figure 3.6: (a) A diagram showing the geometric setup of the contact simulation. The simulation was performed along the axes of symmetry of the geometry. Annotated for diameter, d , channel height, h , corner radius, r_c , and constriction width, w . A weight force, F_p (late replaced with a pressure distribution) is also included. The contact declarations of master and slave surface are annotated as well. (b) A diagram showing the fluid simulation, corresponding to an undeformed (spherical) gel. The simulation was performed along the axes of symmetry for the geometry. Boundary conditions are listed. Dimensions are identical to those of the contact simulation. (c) A diagram of the pressure distribution used on the second set of simulations. The coordinate Z was made internally to define how pressure tapers off from the maximum region. This is an approximation of the distribution found by fluid simulation. (d) Simulated pressure distribution on the underside of the microgel. In order, these simulations correspond to deformation at pressures of $P_{gel} = 0$, $P_{gel} = 2.4$ kPa and $P_{gel} = 4$ kPa. The scale bar describes the fraction of the inlet pressure experienced where $\Delta P = 1$ kPa.

To measure the distribution of pressure across the microgels, an inlet pressure of $P = 1$ kPa and outlet pressure of $P = 0$ were set for all simulations. This is because, as these simulations are uncoupled from the solid simulations, only the distribution of pressure along the microgel surfaces was important to understand. No slip boundary conditions were applied to all solid surfaces with symmetry applied appropriately on the cut planes, as shown in Fig. 3.6b. The pressure distribution on the microgel can be seen in Fig. 3.6d. A rough approximation of this region was made assuming that from where the microgel contacted the corner of the channel to where it touched the floor of the channel, a smooth pressure drop occurred, with the greatest negative pressure occurring approximately evenly distributed at the bottom of the microgel, as shown in Fig. 3.6d. To avoid having to implement a properly coupled fluid-structural simulation, which would have been computationally costly and laborious to implement, we stopped the simulation results at gel penetration of $l/d \approx 0.2$, as beyond this the pressure distribution becomes increasingly unrealistic. Furthermore at this point, the gel is so deformed as to invalidate the assumption of simple linear elasticity used in this model.

Meshing was performed mostly ad-hoc in this work, as results could be easily validated by comparison with experimental data. In the case of ABAQUS, the mesh was seeded several ways, with the final simulation using a general seed density of $2 \mu\text{m}$ along the edges, and $1.2 \mu\text{m}$ in the region of contact. Otherwise default ABAQUS tetrahedral meshing was used. In the fluid simulations, the built in COMSOL physics based mesh at normal and fine were both tested, finding no change in results. Additionally, the solid simulations had a mass scaling factor of 20 included to provide a stable but fast solution.

3.3 Results

3.3.1 Pressure From Bypass Flow

The pressure drop due to flow across the trapped microgel, P_{gel} , was measured from analysis of the recorded streamlines according to Eqs. 3.6-3.9, see Fig. 3.3. P_{gel} increases with increasing inlet flow rate, Q , see Fig. 3.7. This correlation is linear, with two different slopes. The greater slope corresponds with the stiff microgels, $E^* = 15 \pm 9$ kPa, while the soft, $E^* = 0.11 \pm 0.09$ kPa and medium, $E^* = 1.5 \pm 0.4$ kPa microgels fall roughly along a second, lower slope. The microgel and microchannel were selected to have matching height: $h = 85 \mu\text{m}$ for the stiff microgels, compared with $h = 140 \mu\text{m}$ for the other two. As flow passes through the bypass line, the resistance will be greater for the smaller channel resulting in a greater pressure at a given flow rate. The ratio of the resistance of the bypass line for the smaller channel to larger channel is $\frac{R_{\text{byp}}|_{h=85\mu\text{m}}}{R_{\text{byp}}|_{h=140\mu\text{m}}} = 3.5$, compared to the ratio of slopes in Fig. 3.7 $\left(\frac{dP_{\text{gel}}}{dQ}\right)|_{h=85\mu\text{m}} / \left(\frac{dP_{\text{gel}}}{dQ}\right)|_{h=140\mu\text{m}} = 3.3$. Both of these pressure-flow trends show a strong linearity, with $R^2 = 0.95$ in the case of the stiffest gel, and $R^2 > 0.99$ in the case of the soft and medium gels.

The stiff microgel achieves a linear profile after only after a certain flow rate is applied, approximately $Q =$

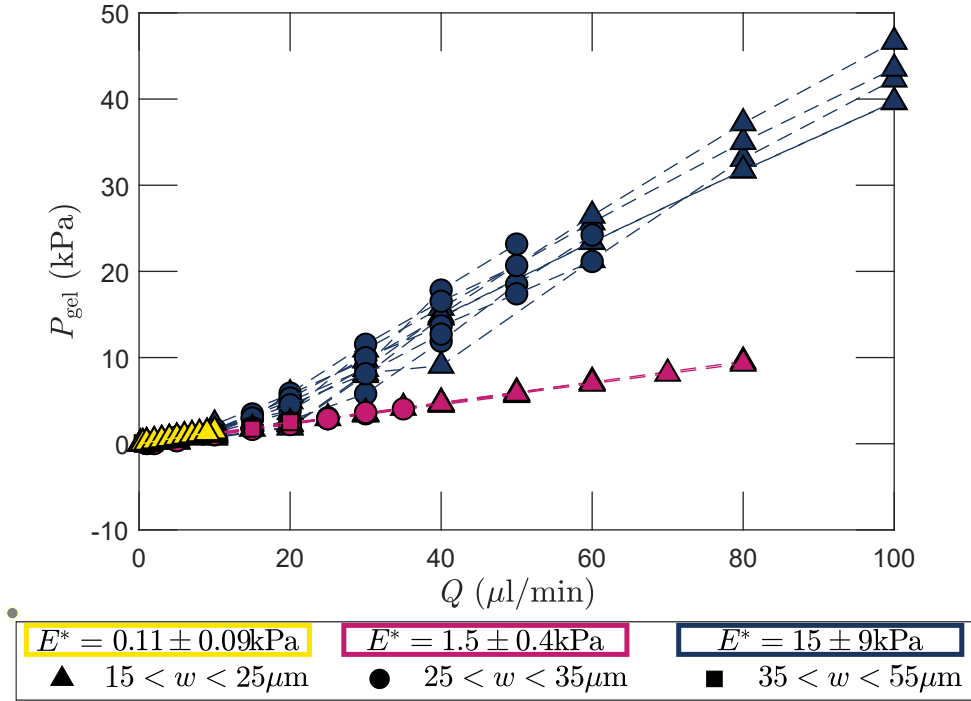


Figure 3.7: A comparison of the pressure drop across the microgel, P_{gel} as the flow rate provided by the syringe pump increases. The legend provided separates data by slit width and by elasticity of the microgels. Note that the hard microgel, $E^* = 15 \text{ kPa}$ is in a channel of height $h = 85 \mu\text{m}$, while the other two gels, $E^* = 1.5 \text{ kPa}$ and $E^* = 0.11 \text{ kPa}$ are larger and are contained in a channel of height $h = 140 \mu\text{m}$. This was done to maintain $d \approx h$.

$15 \mu\text{l}/\text{min}$. As the empty thrupass resistance is smaller than the bypass resistance, see Tab. 3.1. Pressure from entry to exit of the bypass and thrupass is described by

$$P_{\text{thru}} + P_{\text{gel}} = Q \left(\frac{1}{R_{\text{byp}}} + \frac{1}{R_{\text{thru}} + R_{\text{gel}}} \right)^{-1}, \quad (3.10)$$

where P_{thru} is the pressure drop from the inlet to the outlet of the thrupass, excluding that pressure due to the microgel. At lower flow rates the stiff microgels have not become the dominant source of resistance, leading to a lower drop in pressure compared to when flow only passes the bypass line. Meanwhile the soft and medium microgels plug their thrupass line much more readily, leading to a consistent linear relationship. The pressure drop across the microgel can therefore only be inferred by the bypass resistance and supplied flow rate when the microgel is already the dominant source of resistance, plugging the thrupass. Otherwise, it is necessary to account for changes in R_{gel}

3.3.2 Microgel Displacement and Deformation in a Microfluidic Trap

The increase of pressure has a noticeable effect on the shape of the trapped microgel, see Fig. 3.8. Qualitatively, as pressure increases the whole body of the microgel moves in towards the narrow "slit" region of the trap, displacing

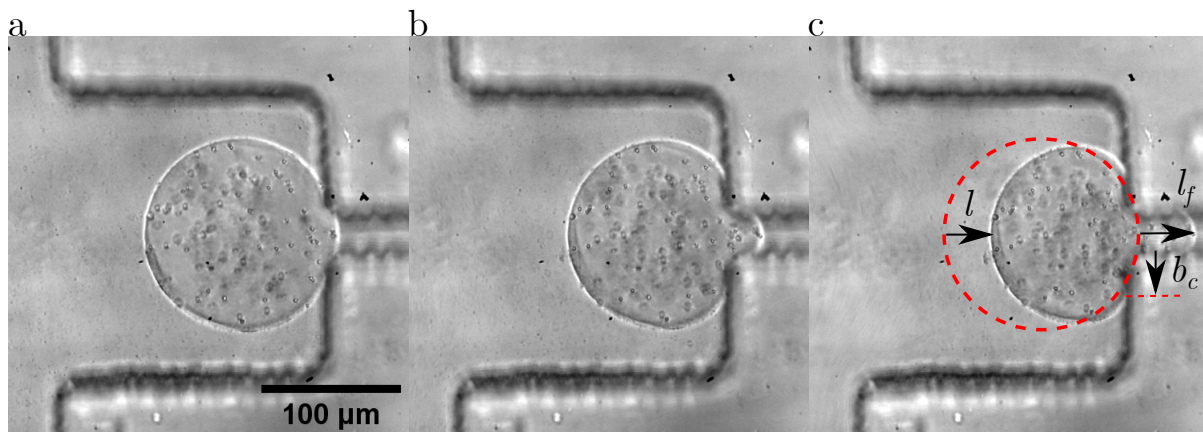


Figure 3.8: Micrographs comparing a trapped microgel undergoing increasing pressure. From left to right the pressure is (a) $P_{\text{gel}} = 10\text{Pa}$, (b) $P_{\text{gel}} = 500\text{Pa}$ and (c) $P_{\text{gel}} = 2288\text{Pa}$. The microgel in question corresponds to a microgel of batch "Gel B", with $E^* = 1.5 \pm 0.4\text{ kPa}$ and $d = 139 \pm 2.1\ \mu\text{m}$.

by a distance of l , measured from the rear of the microgel. More dramatically, as the microgel moves forward, it squeezes into the slit, changing its shape so that a finger of length l_f protrudes forward. This occurs as the gel presses up against the channel, slumping outwards. The apparent amount of microgel in contact with the channel, b_c , also increases as the gel moves into the channel. These deformations are summarized in Fig. 3.9a.

As the pressure increases, the microgels are pushed further towards the slit, as shown in Fig. 3.9b. The displacement of the microgels, l , is greater with respect to P_{gel} with decreasing elasticity, E^* . Controlling for this, the relationship between displacement and pressure appears at first glance to be linear. Closer examination, particularly of the stiff microgels, reveals that this increase is slightly less than linear. On a logarithmic scale however, see inset of Fig. 3.9b, the increase in l with respect to P_{gel} is revealed to increase as a power law such that $l \sim P_{\text{gel}}^n$. The relationship is closer to $n = 1/2$, with $n = 0.56$, $n = 0.38$ and $n = 0.53$ for the stiff, medium and soft microgels respectively ($R^2 > 0.75$ in all cases). Comparing the actual rates at which l increases with P_{gel} , the slope l versus P_{gel} of the medium stiffness microgels is 3.9 times that of the soft microgels, while the stiff microgels are 11.1 times that of the medium microgel.

Although less striking than the differences in microgel displacement from pressure due to differences in microgel elasticity, there is an effect of the width of the microfluidic trap slit, w . In general, as the trap increases in width, the motion of the microgel also increases. In the case of the soft microgels, any slit width larger than $w = 25\ \mu\text{m}$ resulted in microgels passing through the trap too easily to reliably measure their deformation. Therefore, this width is only considered in the case of the stiff and medium microgels. Furthermore, due to their smaller size, the stiff microgels were not tested for widths larger than $w = 25\ \mu\text{m}$.

While the microgel moves further into the trap, its penetration into the trap, l_f increases proportionately with l , see Fig. 3.9c. There is a strong linearity between the two, where $l_f/l = 1.23$ with a linearity of $R^2 = 0.96$. The proportionality remains approximately the same regardless of microgel elasticity E^* or trap width w , although there

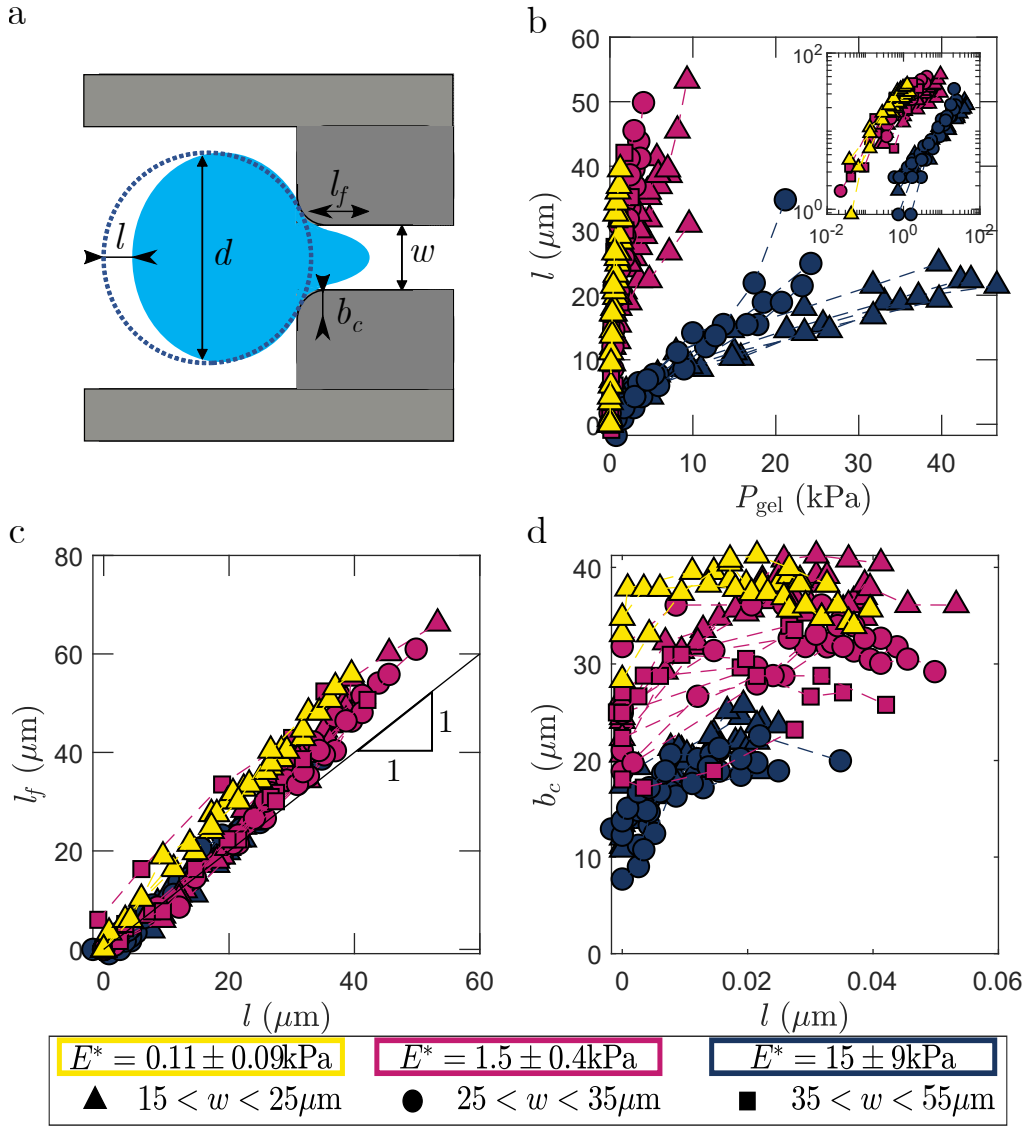


Figure 3.9: (a) A diagram of a trapped microgel being viewed through the microscope. The diagram is annotated with geometric parameters measured in this study. The microgel diameter, d is measured at the lowest flow rate tested, as is the slit width, w . The microgel displacement, l is measured from its back, while the penetration, l_f is measured relative to the front of the microgel at the lowest flow rate tested. The channel contact, b_c is measured as a surrogate for the actual radius of contact between the microgel and the trap. The dashed circle represents a microgel sitting in the trap undergoing no deformation. (b) A comparison of the displacement of the microgel with the pressure drop applied to the gel, P_{gel} . An inset provides the same data on a logarithmic scale in order to better view the data for the softer microgels. (c) A comparison of the penetration of the microgel with the displacement of the microgel in general. A unit line is provided for reference. (d) A comparison of the linear contact between the microgel and the channel, and the displacement of the microgel.

is a slight increase in dl_f/dl for the soft microgels. In general this seems to reflect the squeezing of the microgels into the slit, where to partially conserve volume, noting that $\nu < 0.5$ for typical PEG gels [27], the microgel must extend on one side. What is unexplained is that this does not seem to be affected by the width w , as a wider slit would compress the microgel less. Here however neither d nor w have an effect on dl_f/dl . It is reasonable to assume therefore that deformation in the plane of the microscope explains the unaccounted for volume.

The width of contact between the microgel and the microchannel, b_c increases with displacement of the microgel, before tapering off, as shown in Fig. 3.9d. Similar to the penetration of the microgel, the microgel is forced to deform outwards to maintain its volume, increasing the contact. This increase in contact however quickly tapers off as the microgel progressively enters into the slit, and in some cases slightly decreases. This again is to be expected from simple geometric argument that in order to fully enter into the constriction, the microgel contact with the entry to the constriction will necessarily have to decrease. This is best illustrated by considering the extreme case where the microgel has been pulled entirely into the constriction, in which case $b_c = 0$. The contact b_c increases as both the elasticity E^* and slit width w decrease. The effect of elasticity itself however seems to be less influential than that of the microgel size, as both $E^* = 0.11 \pm 0.09$ kPa and $E^* = 1.5 \pm 0.4$ kPa microgels have nearly the same contact when comparing only the gels trapped in channels with $w < 25$ μm . The projection of the slit onto the gel increases with w , resulting in less area of the microgel available to contact the entry to the trap constriction. The decrease in b_c with w is also partially explained by the partial conservation of volume, as larger w correlates with less constriction and therefore less bulging outwards. This may help explain why the change in constriction has a negligible effect on dl_f/dl , as the deformed volume is accounted for elsewhere.

3.3.3 Small and Soft Trapped Microgels

As mentioned above, the small, $d = 83.4 \pm 2.9$ μm and soft $E^* = 48.6 \pm 24.6$ Pa microgel batch, Gel C in Tab.3.2, was tested but is separated from the general analysis. The pressure-flow relationship, see Fig. 3.10a, for these microgels follows the same trends as seen with the other microgels, having the same R_{byp} as the stiff, $E^* = 15 \pm 9$ kPa microgel. The penetration of the soft and small microgel increases with pressure, see Fig. 3.10b, similar to the other microgels tested, however there is a much wider variation between samples. These microgels would penetrate quite far into the constriction at relatively low applied pressures, such as in the micrograph shown in Fig. 3.10c. These microgels would often become stuck in the constriction, and upon stopping applied flow, they would remain in place. This is in opposition to the other microgels tested which would return to their original position upon cessation of flow. This seems to be due to a combination of the elasticity of these microgels, and their size, as neither the other microgels with similar elasticity, $E^* \sim 100$ Pa, nor diameter, $d \approx 80$ μm had this occur. It may be that the relative size of the microgel, d/w combined with the low E^* , allowed these microgels to easily enter into the trap constriction at which point friction would dominate over the microgels elastic forces to push the microgel out. In this case a

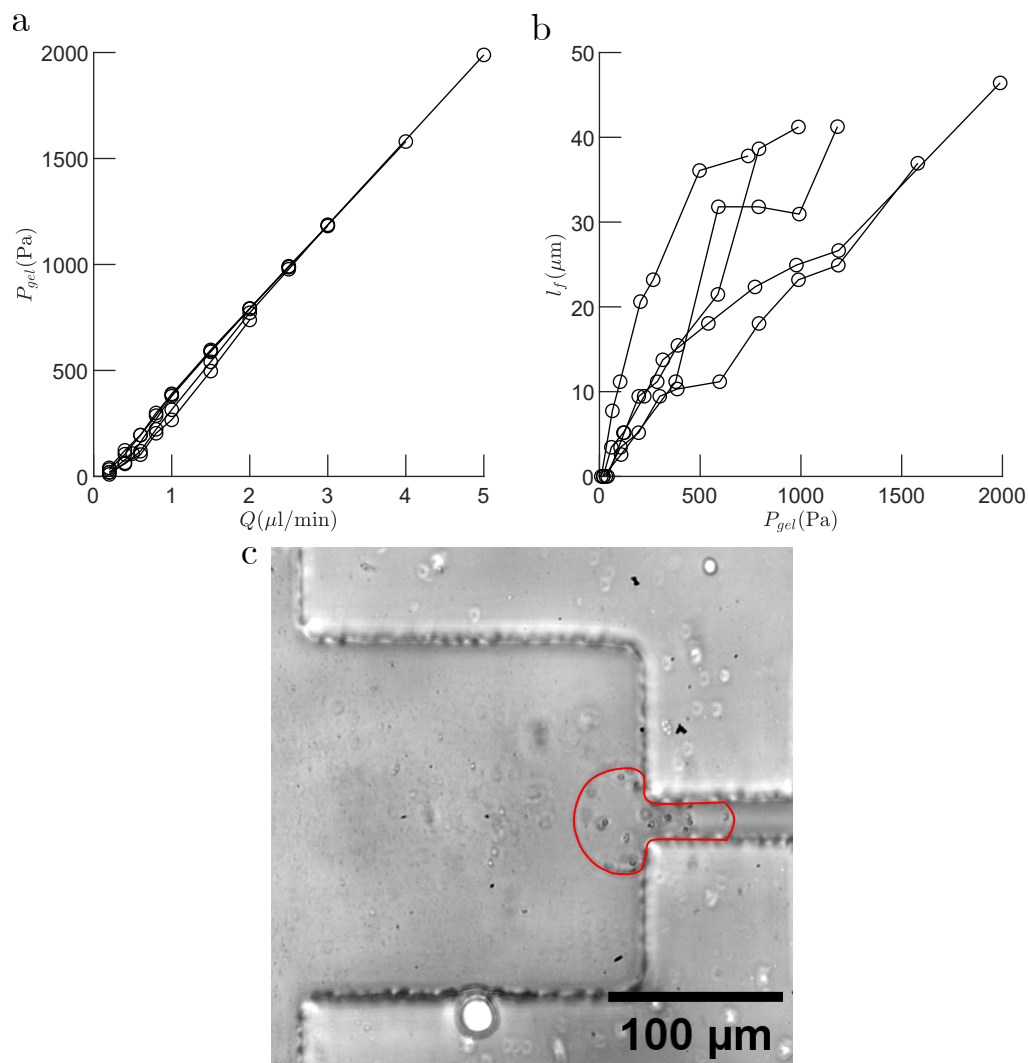


Figure 3.10: (a) A comparison of pressure and supplied flow rate for data corresponding to microgels from batch Gel C, corresponding to a diameter of $d = 84.2 \pm 1.1 \mu\text{m}$, and an effective elasticity of $E^* = 48.6 \pm 24.9 \text{ Pa}$. (b) A comparison of the penetration, l_f of microgels from batch Gel C with the pressure applied to the gel, P_{gel} . (c) A micrograph of a small, soft gel from batch Gel C which was stuck in the trap slit due to friction. The outline of the microgel has been highlighted in red for ease of viewing.

smaller constriction would better allow the microgel to push back against the entry to the constriction. Regardless, because these microgels would not return to their rest position upon arresting the flow and thus setting $P_{\text{gel}} = 0$, the relationship between deformation and pressure becomes challenging to evaluate. If for example a small variation in P_{gel} were to cause the microgel to further penetrate the constriction, the measured value of l_f may be artificially inflated. It is for this reason that I decided to separate these samples from the general data to analyze.

3.3.4 Simulated Trapped Microgel Deformation

The displacement and deformation of the simulated microgel behaves similarly to that of the experimental microgels. When fitted to a power law, the displacement of the microgel with increased pressure behaves like that of the stiff experimental microgels, where $l \sim P_{\text{gel}}^{0.24}$, see Fig. 3.11a and Fig. 3.9b. This is particularly important for validating the simulation, as it indicates that the approximation for pressure distribution used in this simulation accurately reflects the experimental data. Furthermore, insights gained from this simulation may be useful not only for viewing the deformation of the microgel in three dimensions, but also for building a model to describe the deformation of trapped microgels.

The simulated elongation of the microgel also behaves like that of the experimental microgels, see Fig. 3.11b and Fig. 3.9c, although the penetration of the microgel is nearly identical to the overall displacement for small values of l . This may be simply because the range of l measured in this simulation is smaller than that of the experiments. It may also reflect the limitation in how these simulations were performed. Because the fluid and structural simulations were uncoupled, the distribution of pressure in the solid simulations does not evolve exactly with the pressure distribution predicted by the fluid simulations. These differences are however minor, as the overall slope for the simulated data is $l_f/l = 1.13$ compared with 1.23 for the experimental.

The contact between the microgel and constriction entry, b_c , in Fig. 3.11c increases sharply before becoming nearly constant in a way that is reminiscent of the stiff microgels in Fig. 3.9d. The absolute values of the simulated b_c are however smaller than those experimental values by approximately $5 \mu\text{m}$. This may have more to do with the limitations of the experiments than the simulation itself. As the experimental b_c was measured by identifying on micrographs of trapped gels where contact occurred, it is possible that parts of the microchannel obscured the precise location of contact between the microgel and channel. Additionally, as with comparing l_f and l , the possibility that the distribution of pressure is not a perfect fit may also influence these results.

The height of the microchannel seems to play only a small role in determining the displacement and deformation of the microgel. In Fig. 3.11a-c, there is never more than a 5% difference in values for l , l_f or b_c at a given pressure. This is despite the fact that simulations predict that the microgel does come into contact with the floor and ceiling of the microchannel. Fig. 3.11d shows the displacement of the microgel as pressure is increased. As expected from the experimental data, the microgel slumps outward as it progressively deforms. This expanding perpendicular to the

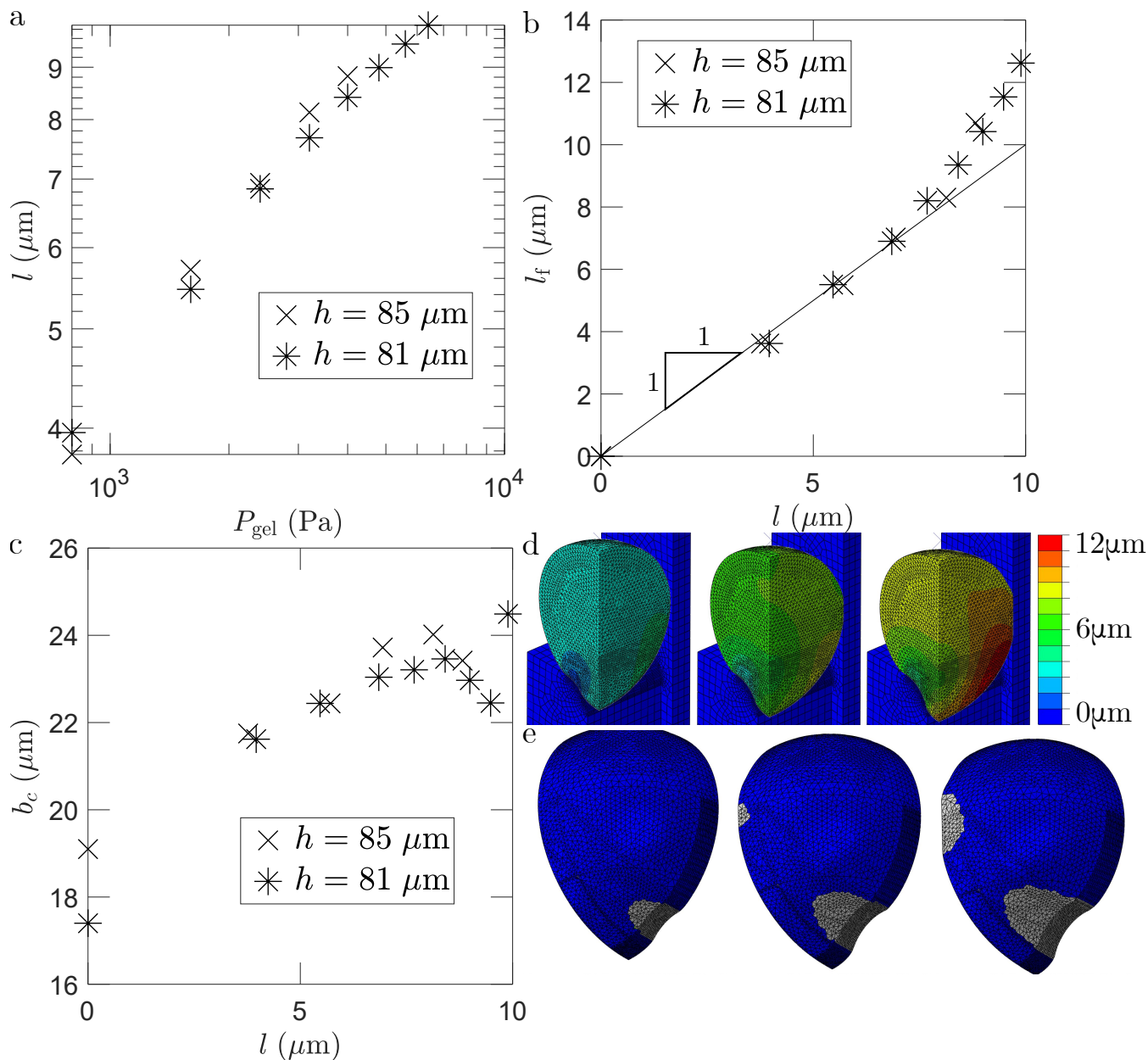


Figure 3.11: Data for the simulated microgel quarter section as it is pulled into the microfluidic constriction. This simulated microgel has a diameter of $d = 80 \mu\text{m}$, and elasticity of $E^* = 11.4 \text{ kPa}$, while the trap measures $w = 15 \mu\text{m}$ and $r_c = 15 \mu\text{m}$, with a height of either $h = 81 \mu\text{m}$ or $h = 85 \mu\text{m}$. See Fig. 3.6 for details. (a) The displacement l of the microgel compared with the maximum negative applied pressure P_{gel} . (b) The penetration of the microgel into the constriction, l_f , compared with the displacement of the microgel, l . A reference line is provided. (c) The contact between the simulated microgel and microchannel, b_c , compared with the displacement of the microgel, l . (d) A comparison of the overall deformation of the microgel, corresponding to $h = 85 \mu\text{m}$, and from left to right $P_{\text{gel}} = 800 \text{ Pa}$, $P_{\text{gel}} = 2400 \text{ Pa}$ and $P_{\text{gel}} = 4000 \text{ Pa}$. The scale bar indicates total nodal displacement relative to $P_{\text{gel}} = 0$. (e) An opposite view of the microgel highlighting contact between the microgel and the microchannel in white. Deformation states correspond from left to right to $P_{\text{gel}} = 800 \text{ Pa}$, $P_{\text{gel}} = 2400 \text{ Pa}$ and $P_{\text{gel}} = 4000 \text{ Pa}$.

displacement l occurs both in the direction of the constriction width, b_c , but also towards the floor and ceiling of the microchannel (shown as the blue wall on the right hand side of Fig. 3.11d). The contact between the microchannel and microgel is highlighted in Fig. 3.11e, which shows that although initially the microgel may only contact the corner of the microfluidic trap, it will be forced outward to contact the floor/ceiling of the trap as well under greater displacement into the channel. The influence of d/h therefore can be neglected when constructing a model for the deformation of the microgel, at least when considering the parameters l , l_f and b_c .

3.4 Contact Theory and Microgel Deformation

There is a clear correlation between increasing pressure and increased displacement and deformation of a microgel as it enters a constriction trap. This relationship is not a simple linear correlation however, and must account not only for the pressure and displacement, but also the geometry of the microchannel and microgel, as well as microgel elasticity. To understand what the interplay between these factors, it is necessary to first consider the forces acting upon the microgel.

The deformation of microgels entering into a constriction can be thought of as coming from the interaction of the forces acting on the microgel from the flow, and the reaction forces as this flow pushes the microgel into its constriction. Shear is unexpected to play a major role, as comparing shear to pressure in the microchannel reveals that $\frac{P_{\text{gel}}d}{\mu(Q_{\text{thru}}/wh)} > 10^3$. This leaves contact between the microgel and microchannel, and the pressure drop across the microgel as the main forces at play.

Hertzian contact mechanics, first developed by Heinrich Hertz in 1881, outlines the deformation of two bodies in contact [14, 59, 138, 94]. Assuming the two bodies in contact are linearly elastic and undergoing small deformations, without any adhesion between the surfaces, the area of contact can be related to the force normally applied at the point of contact. It is this body of theory which I use to explain the deformation of a trapped microgel.

To model the contact between the microgel and the trap, it is necessary to simplify the contact, based on where contact is actually occurring. As the corners of the trap are rounded and are where contact first occurs, we focus on this area, approximating the corners as two cylinders, while the microgel remains approximately spherical (see Fig. 3.12a).

To begin, we consider the contact mechanics of a sphere and cylinder as described in Barber [14], as two ellipsoids in contact. In this case, one ellipsoid, the sphere, has equal radii of $d/2$, while the cylinder is an infinitely long ellipsoid with radii of ∞ and r_c . For such a case, the area of contact between the sphere and the cylinder can be approximated as an ellipse of major radius a and minor radius b . We can relate the contact penetration l_c , as shown in Fig. 3.12b, to the major radius of contact, a , as shown in Fig. 3.12c, by

$$l_c = \frac{\mathcal{Z}^2 a^2 (\mathcal{K}(\mathcal{Z}) - \mathcal{E}(\mathcal{Z}))}{d\mathcal{K}(\mathcal{Z})}, \quad (3.11)$$

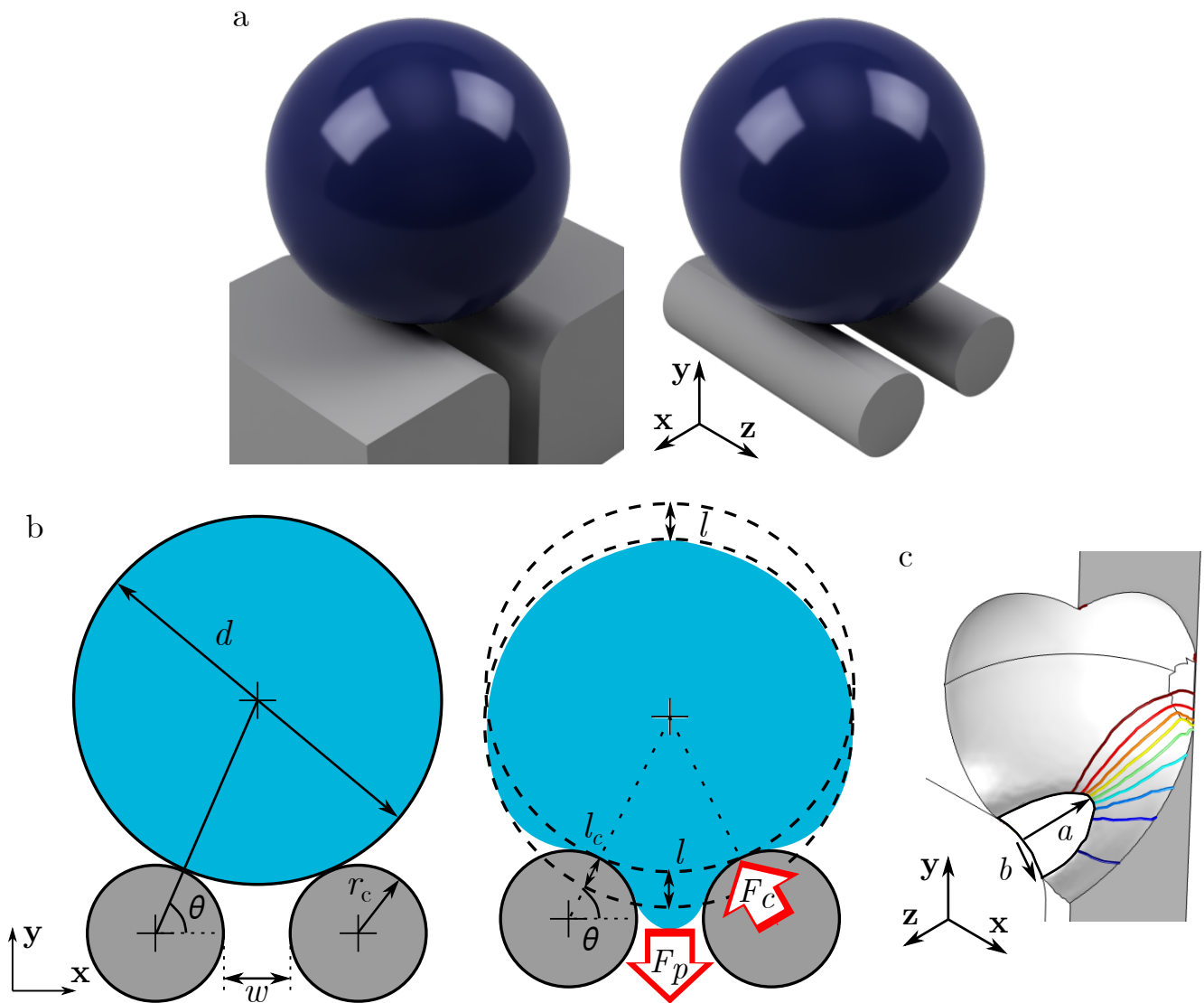


Figure 3.12: (a) A comparison of the trap geometry (left) with the “sphere balanced between two cylinders” approximation made in this analysis (right). (b) A two dimensional projection of the microgel sitting on the trap corners, in both an undeformed (left) and deformed (right) state. The trap corners here are represented as two cylinders. The deformed microgel shows a comparison of the penetration length, l_c with microgel displacement, l , as well as the pressure and contact forces, F_p and F_c respectively. Note that the label for the leftmost F_c was omitted to facilitate reading. (c) Isometric view of the contact between the microgel and the trap corners, highlighting the major and minor radii of contact, a and b respectively. The gray material represents the fluid phase between the microgel and trap, shown as a quarter section for ease of viewing.

where \mathcal{Z} the eccentricity of contact [14]. $\mathcal{K}(\mathcal{Z})$ and $\mathcal{E}(\mathcal{Z})$ are elliptic integrals of the complete first and second kind respectively:

$$\mathcal{K}(\mathcal{Z}) = \int_0^{\pi/2} \frac{d\phi}{\sqrt{1 - \mathcal{Z}^2 \sin^2 \phi}} \quad (3.12)$$

and

$$\mathcal{E}(\mathcal{Z}) = \int_0^{\pi/2} \sqrt{1 - \mathcal{Z}^2 \cos^2 \phi} d\phi. \quad (3.13)$$

The eccentricity of contact is defined as

$$\mathcal{Z} = \sqrt{1 - \left(\frac{b}{a}\right)^2}, \quad (3.14)$$

and can be approximated for high aspect ratio contact using the formula

$$\frac{2r_c}{2r_c + d} \approx (1 - \mathcal{Z}^2) \left(\ln \frac{\sqrt{1 - \mathcal{Z}^2}}{4} - 1 \right). \quad (3.15)$$

Accounting for the non-circular contact formed between the two bodies, the major radius of contact is related to the applied force F_c by

$$a = \left(\frac{3dF_c(\mathcal{K}(\mathcal{Z}) - \mathcal{E}(\mathcal{Z}))}{4\pi\mathcal{Z}^2 E^*} \right)^{\frac{1}{3}}, \quad (3.16)$$

where E^* represents the combined elastic modulus of both bodies [14]. In the present case the microgel is much softer than the channel walls and therefore the elastic modulus of both bodies is approximately that of the microgel $E^* = \frac{E}{1-\nu^2}$, where E is the elastic modulus of the gel and ν its Poisson's ratio. The radii of contact, a and b can be related to one another by 3.14.

Returning to the microgel in question, while we have described the deformation of a sphere in contact with a cylinder, neither the contact radii, a and b , nor the contact penetration, l_c are easily measured from the real microgel. These can however be related to the translation of the microgel into its slit, l , as shown in Fig. 3.12b. These two properties are related by the position of the microgel such that:

$$l_c = l \sin \theta, \quad (3.17)$$

where θ is the angle created between the centre of the microgel and the trap walls. Simple trigonometry shows that the angle is related to the microgel position by

$$\tan \theta = \frac{\sqrt{(r_c + d/2)^2 - (r_c + w/2)^2} - l}{w/2 + r_c}. \quad (3.18)$$

We model the forces acting upon the microgel to result from the pressure field while ignoring frictional forces. This force F_p is considered to act in the direction of the slit, as it is open in that direction, while the contact force F_c is perpendicular to the trap corner. This can be seen illustrated roughly in the free body diagram of Fig. 3.12b.

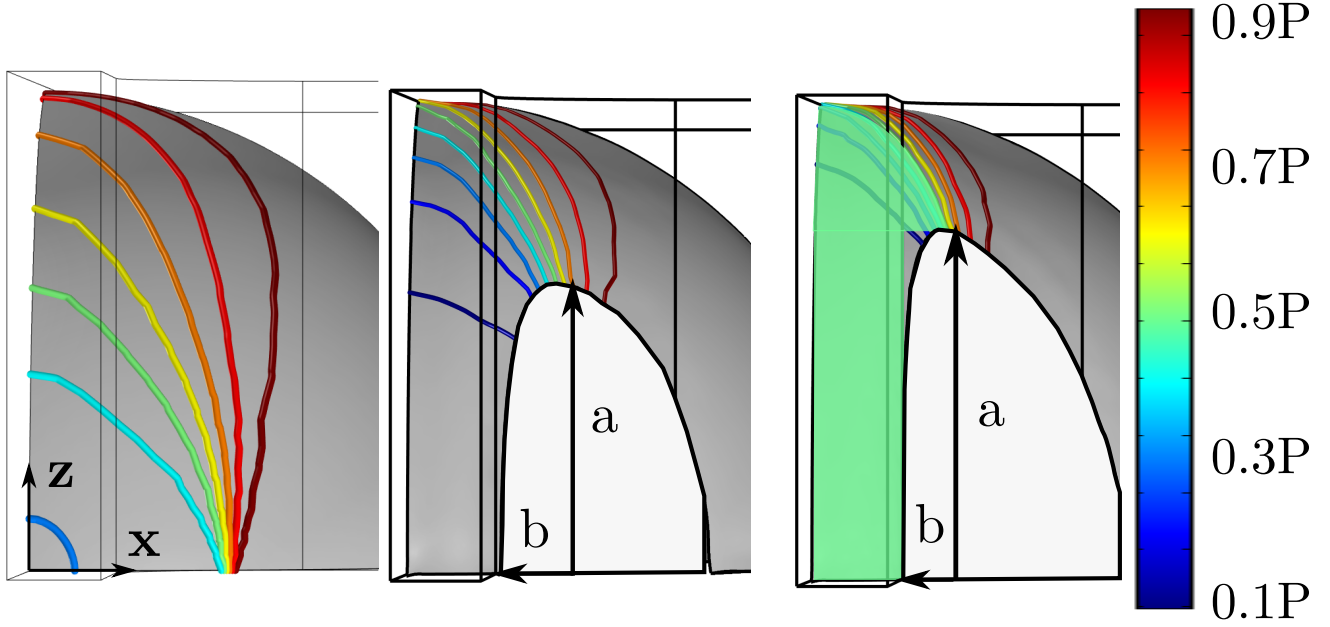


Figure 3.13: Three projections of pressure isobars onto the bottom of the microgel. Perspective is given from the bottom of the slit looking towards the microgel. Microgels shown from left to right correspond to 0 deformation, deformation under $P_{\text{gel}}/E = 0.12$ and $P_{\text{gel}}/E = 0.2$, respectively. The approximated region over which the pressure is applied is highlighted in green in the rightmost panel. The color bar shows the fraction of the inlet pressure, P , corresponding to each isobar.

Mechanical equilibrium implies that

$$F_c = \frac{F_p}{2 \sin \theta}. \quad (3.19)$$

The force acting on the microgel is calculated by multiplying the pressure across the gel (P_{gel}) by the area over which the pressure is applied. This area is approximated as the sum of the area of a rectangle of size aw plus the area of rounded triangle, as shown by the green shaded area in the right panel of Fig. 3.13. This leads to the approximation below:

$$F_p \approx 2P_{\text{gel}} \left[aw + \frac{2}{3} \left(\frac{d}{2} - a \right) (w + 2r_c(1 - \cos \theta)) \right]. \quad (3.20)$$

A relationship between the microgel deformation and the pressure applied across it can then be obtained by combining Eqs. 3.20 and 3.16. This results in a relationship between a and P_{gel} that includes the geometric parameters as well as the gel elastic modulus:

$$a = \left\{ \frac{3P_{\text{gel}}d}{4\pi E^* \sin \theta} \left[aw + \frac{2}{3} \left(\frac{d}{2} - a \right) (w + 2r_c(1 - \cos \theta)) \right] \mathcal{F}_2(\mathcal{Z}) \right\}^{1/3}. \quad (3.21)$$

Finally, by combining Eqs. 3.17 and 3.11 the major radius of contact is related to the translation of the trapped microgel, approximated here by the motion of its back side, l as

$$l = \frac{2a^2}{d \sin \theta} \mathcal{F}_1(\mathcal{Z}), \quad (3.22)$$

where the eccentricity terms in Eqs.3.22 and 3.22 can be summarized as

$$\mathcal{F}_1(\mathcal{Z}) = \mathcal{Z}^2 \left(1 - \frac{\mathcal{E}(\mathcal{Z})}{\mathcal{K}(\mathcal{Z})} \right), \quad (3.23)$$

$$\mathcal{F}_2(\mathcal{Z}) = \frac{\mathcal{K}(\mathcal{Z}) - \mathcal{E}(\mathcal{Z})}{\mathcal{Z}^2}. \quad (3.24)$$

3.5 Hertzian Contact Between a Microgel and Trap Corners

3.5.1 Modeling Microgel Displacement into Trap

The expected theoretical value of the re-scaled gel displacement l_{theory}/d was calculated from Eqs. 3.21 and 3.22 and compared to the experimentally and numerically computed values of l/d , as shown in Fig. 3.14. The theory collapses the data onto a master curve, particularly for small deformations, where $l/d < 0.1$, and remains a considerable collapse compared with that seen in Fig. 3.9b up until $l/d < 0.2$. Beyond this, l_{theory}/d tends to over-predict the data. In the case of the medium stiffness microgels, $E^* = 1.5 \pm 0.4$ kPa, the data seems to remain well predicted much further beyond the other microgel samples. Where $l/d < 0.2$, the regression between l/d and l_{theory}/d gives a slope of 0.97 and a coefficient of determination of $R^2 = 0.76$. This is a strong fit considering not only the wide range of P_{gel} and l in the experimental data, but also the non negligible uncertainty within test conditions. Additionally, while there does seem to be some variation in fit between different microgel samples, there is not apparent affect of w on the fit of l/d .

The limit of $l/d < 0.1$ corresponds with $l/w \approx 0.5$, accepting some variation depending upon d and w . The first limitation of the model presented in Eq. 3.22 is that of small deformations. In general, Hertzian contact mechanics are only valid for small deformations [14]. Furthermore, this model behaves as if there is only one point of contact: between the microgel and the corner of the slit, however the microgel is in fact in contact with two corners. The stress distribution within a simulated microgel is shown in Fig. 3.15. When the deformation of the microgel is smaller, the concentration of stress is localized on one side of the plane of symmetry. As deformation is increased however, this region of high stress moves towards and intersects with the plane of symmetry. At this point, the stress deformation localized at the trap corners are interacting with each other, which is not accounted for in the model described above.

The differences in l_{theory}/d between different microgel samples shown in Fig. 3.14 are more challenging to explain. In this case, both the stiff and soft microgels deviate from the prediction given by Eq. 3.22 at approximately the same point, while the medium microgel more closely follows the prediction nearly until $l/d = 0.3$. In this case it is unlikely be an over or underestimated effect of elasticity, as it would be expected that this effect would be more or

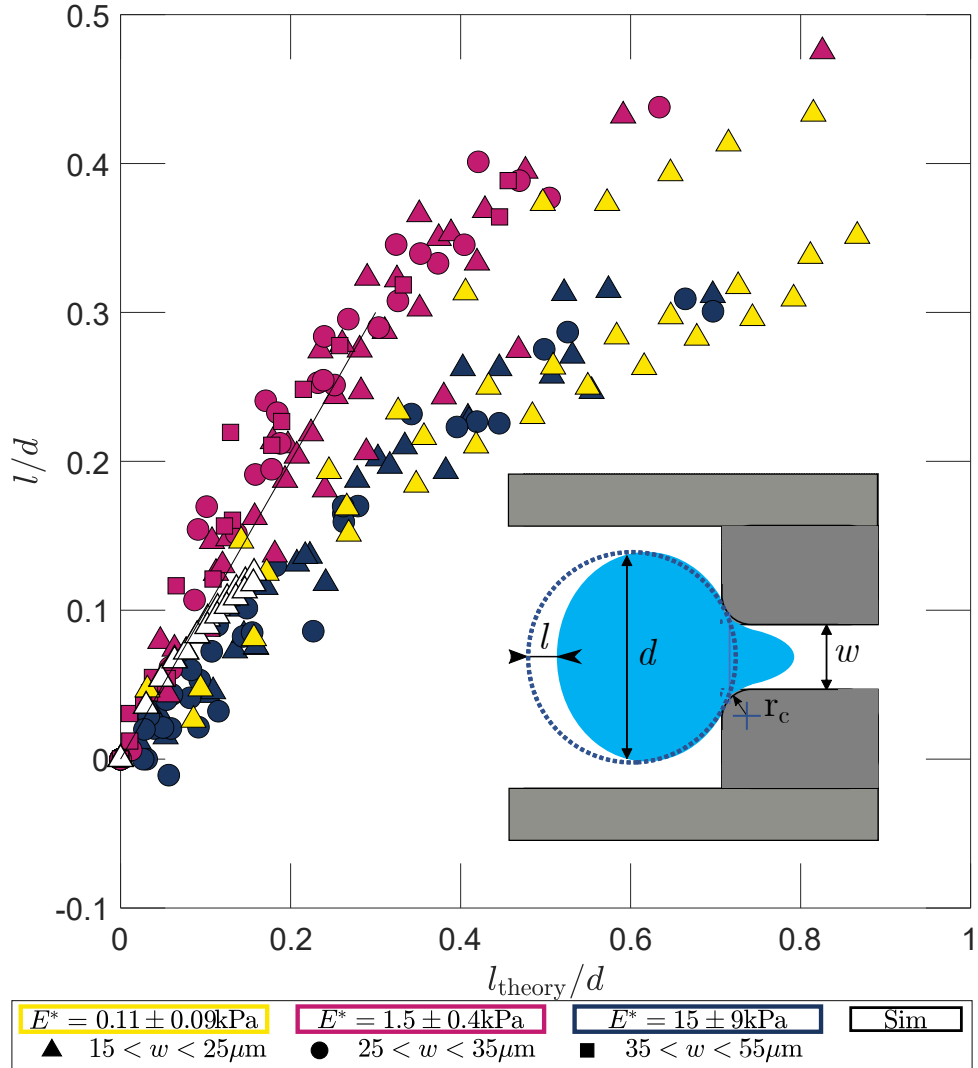


Figure 3.14: A comparison of the displacement of the microgel predicted by Eq. 3.22 with that measured experimentally (color) and by simulation (white). The inset is simply included to remind readers the physical significance of l and d and where $l_{\text{theory}} = \mathcal{F}(w, r_c, d, P_{\text{gel}}, E^*)$. A reference line of $y = x$ is provided to compare goodness of fit of the model. Data shown is limited to $l/d < 0.3$ to better focus on the range of interest to this model.

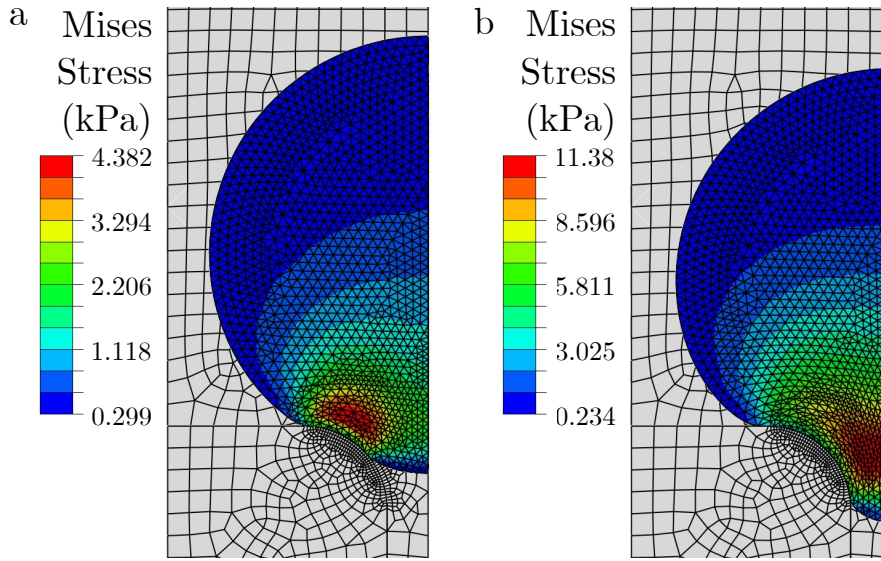


Figure 3.15: A comparison of stress distribution within a simulated microgel. Microgels shown are undergoing (a) $P_{\text{gel}} = 800 \text{ Pa}$ and $l/d = 0.045$ and (b) $P_{\text{gel}} = 6400 \text{ Pa}$ and $l/d = 0.16$. Symmetry is imposed on the right side of the semicircle shown. Elemental Mises stresses are shown, with color bar provided.

less pronounced for the stiff or soft microgels as well. The size of the microgels also offers little explanation, as the soft and medium microgels both share approximately the same diameter, $d \approx 135 \mu\text{m}$, and were contained within the same microchannels.

The first possibility for this discrepancy due to microgel sample is that there is some aspect of the microgels unaccounted for here that would change their deformation under load. The three microgels were all made at different times, with the soft microgel being four months younger than the medium microgels, which were themselves two months younger than the stiff microgels. It is possible the microgel properties beyond elasticity had changed in the intervening time, such as their poro-elasticity or Poisson ratio. This is ultimately unlikely, as the microgels were tested for elasticity on the same day, and tested in this trap on the same week. In particular, it is expected that the effective microgel stiffness will increase with water loss, which is expected to occur under compressive strains such as those experienced here [110]. This water loss was not however systematically measured here as it would require a three dimensional perspective on the experimental microgels, and therefore this must be left as conjecture.

A second possibility is that the relative height of the microchannel, d/h had an effect on the deformation of the microgels at large values. The medium stiffness microgels had a confinement of $d/h = 0.99$ compared with $d/h = 0.92$ in the case of the soft microgels. While this is not supported by the existing simulations, which seem to indicate the microchannel height has a minimal effect on microgel displacement, these simulations only extended to values of $l/d = 0.16$. It may be that microchannel height has an effect at larger values of l/d , which may involve some interplay of the distribution of pressure and the internal distribution of stresses on the microgel.

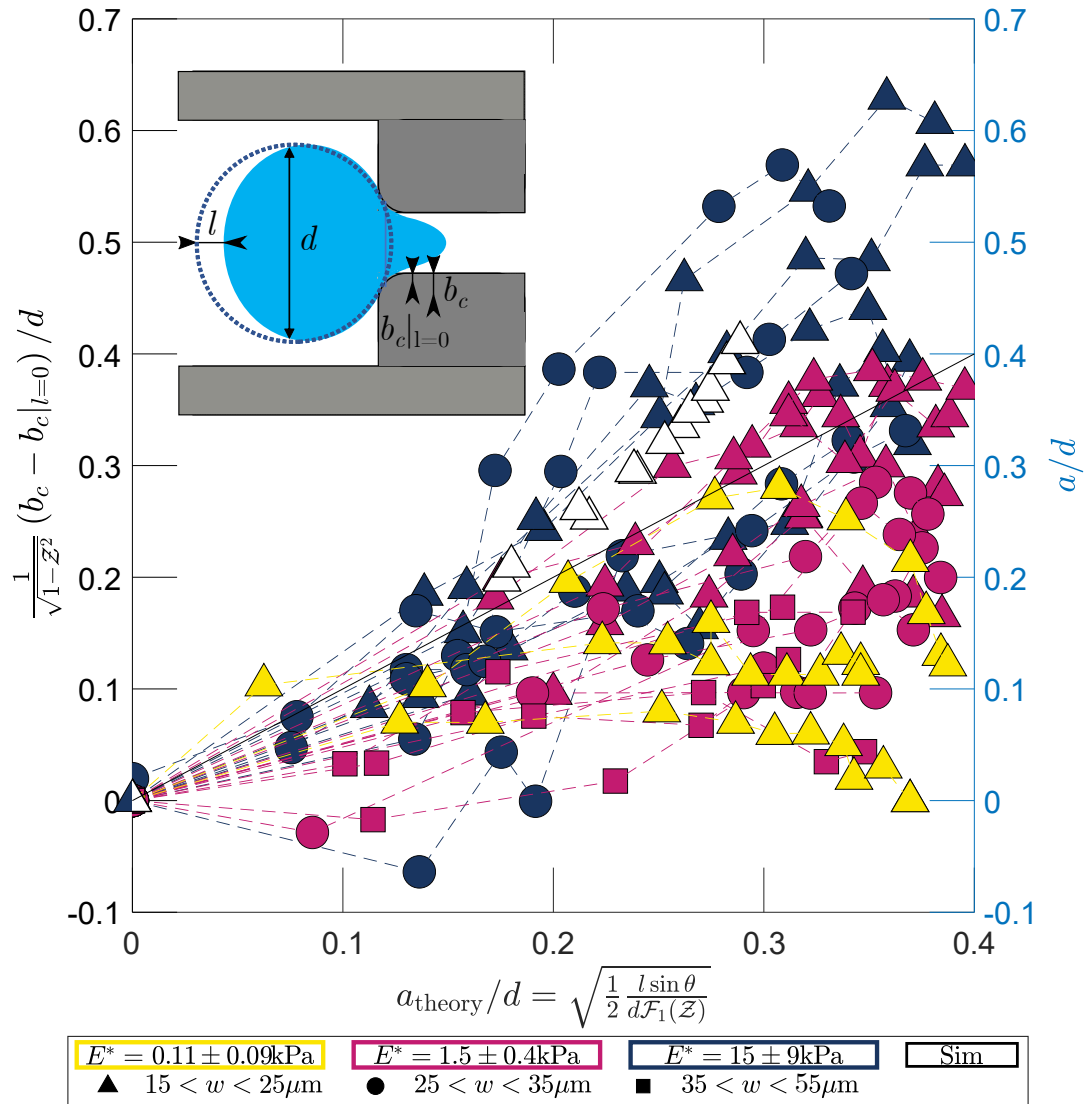


Figure 3.16: A comparison of the deformation of the microgel with that predicted by Hertzian contact theory. The left axis corresponds to experimental data, while the right corresponds to simulation data. The value of $b_{c|l=0}$ corresponds to the value of b_c for a single set of experiments with the same microgel for which displacement is 0, as indicated by the inset. The simulated a is measured directly. A reference line $y = x$ is provided for reference.

3.5.2 Microgel Deformation from Microgel Displacement

Rearranging Eq.3.22, the major radius of contact can be written as

$$a = \sqrt{\frac{1}{2} \frac{ld \sin \theta}{\mathcal{F}_1(\mathcal{Z})}}. \quad (3.25)$$

This contact is perpendicular to the field of view of the microscope. The minor radius of contact, b , however is in the field of view, and is related to a by Eq. 3.14. The actual minor radius of contact however was also challenging to accurately measure. Instead, the linear contact between the microgel and microchannel, b_c (see Fig. 3.9a), is used here as a proxy for this radius, as one should grow approximately in lock step with the other. To further improve the comparison, it is useful to transform b_c relative to $l = 0$, to instead compare $b_c - b_c|_{l=0}$, such that both the measured and theoretical contact radius begin at 0.

By transforming l using Eq. 3.25, we see more clearly the relationship between l , d and b_c , see Fig. 3.16. a_{theory}/d seems to trend linearly with $\frac{b_c - b_c|_{l=0}}{d\sqrt{1-\mathcal{Z}^2}}$, especially for smaller deformations. There is however considerable spread between different experimental series, resulting in a relatively poor overall fit. This is likely due in part to the difficulty posed in measuring b_c using micrographs, as the precise point of contact between microgel and microchannel can be hard to identify due to variations from manufacturing in the microchannel surface. As mentioned above, there was a good deal of practical uncertainty due to micron-scale variations in the microchannel geometry. While these effects are minor relative to the total microgel displacement, they do have a more direct effect on both measuring b_c , and on its real evolution with as the microgel moves into the slit. This is especially important at small values of b_c , as it evolves and plateaus quickly. The limitations of the model in Eq. 3.25 are also apparent in Fig. 3.16. While the predicted correlation of b_c with \sqrt{ld} holds for the majority of contact, at larger values of l/d , contact in some cases decreases with increasing displacement. This of course is a geometric inevitability, as in order to fully enter the trap slit, the microgel will eventually have no contact with the entry to the slit. The relationship between b_c/d and l/d in this range is varies depending on the microgel elasticity. A decrease in contact occurs for the soft microgels at the high end of l/d , however the trend $a^2 \sim ld$ still holds for most experiments in the medium and stiff microgels. In all cases, the boarder prediction of Eq. 3.25 that $a^2 \sim ld$ holds for all gels up until where $a_{\text{theory}}/d = 0.25$, marking a reasonable limitation

The simulated microgel had its major radius of contact measured directly, and can be seen compared with the prediction a_{theory}/d alongside the experimental data in Fig. 3.2. The correlation in this case between a_{theory}/d and a/d is linear and falls well within the range of values measured experimentally. The prediction underestimates a/d , linear fit by a factor of 1.55. This reflects a limitation in the theory used to predict a . The cause of this systemic error is unclear, especially given the strong fit of the theoretical prediction of l/d with the simulated data. While $a^2 \sim ld$ does seem to hold, the actual contact may be increased due to there being more than a single point of contact between the microgel and channel, unlike the proposed model.

To summarize, contact mechanics does predict the microgel deformation in terms of the contact area between the microgel and microchannel (inferred from b_c and a). This is an extension of the same model used to predict $l(P_{\text{gel}})$. There is however considerably more noise in the experimental measure of b_c compared with l . Furthermore, at large deformations, $l/d > 0.25$, this model begins to break down, reflecting the microgel transitioning from being in contact with the entry to the constriction, to being in the constriction itself. Finally, the simulation of microgel contact seems to indicate a systematic error in the model which requires further investigation to identify if this is due to element stress interactions between points of contact.

3.6 Discussion

3.6.1 Extending Trapped Microgels to Penetrating Microgels

The penetration of microparticles into circular constrictions is well studied. Theret *et al.* used a similar geometry in order to develop micropipette aspiration, measuring the elasticity of small objects by sucking them into a pipette [157]. Similar studies for tapered pipettes [176, 173, 111] and even rectangular constrictions [57, 104, 117] have been performed. In all cases, experiments neglect fluid flow around the trapped particle, and often assume axisymmetry. In doing so the models presented were able to accommodate not only the static deformation of particle, but also how that particle will deform as it further penetrates into a constriction. The geometry studied here is fundamentally different, involving flow past and around the trapped microgel, as well as a very different geometry of contact.

The particles in these experiments were only ever observed in an equilibrium state, however particles entering constrictions are dynamic. The question thus arises, can the deformation modeled here also be applied to microgels as they dynamically penetrate into the microfluidic constriction. To do this, we compare the fluid inertia to the elasticity of the microgel, using the Cauchy number $Cy = \frac{\rho U^2}{E^*} = \left(\frac{Q}{w_{\text{ch}}h}\right)^2 \frac{\rho}{E^*}$. The range of experiments performed here, the largest Cauchy number is $Cy = \left(\frac{(100 \mu\text{l}/\text{min})}{(200 \mu\text{m})(140 \mu\text{m})}\right)^2 \frac{(1 \text{ kg}/\text{l})}{(1.5 \text{ kPa})} = 0.049$, indicating that the microgel elasticity remains dominant over any deforming fluid effects. As the microgel density is almost that of water, the same conclusions made from the Cauchy number for the fluid-structure interaction at the microgel boundary can also be applied to the microgel itself. The deformation of the microgel will be dominated by the elastic effects of the contact between microgel and microchannel, with negligible effects from the inertia of the microgel impacting the trap. In other words, the entry of microgels into constrictions, similar to that described in this work, is an uncoupled fluid-structure interaction, and well described by a steady state analysis. The forces dominating the deformation of the microgel are therefore indeed the pressure, and elastic effects of the gel.

These experiments only consider the microgel as it begins to enter the trap, maintaining contact with trap surface perpendicular to the direction of flow. Neglecting friction, the position of the microgel as this model has outlined is a balance of the pressure pushing the microgel into the slit, and the surface of the channel pushing the microgel away.

As the microgel penetrates the slit, this surface contact, changes, first growing, but then after shrinking, which we observe when measuring b_c . In effect this separates the penetration of the microgel into the slit into two modes. The first, shown in these experiments the reaction forces from contact are equal to that from pressure. In the second however, the microgel is always being deformed by the pressure, and is unable to balance the contact reaction and pressure, as the contacting area begins to decrease, thereby quickly moving the particle into the slit. Both of these phases were observed experimentally, as the limit in flow rates tested was due to the microgels passing completely through the trap.

The experiments performed here look at the penetration of a microgel into a one dimensional constriction under static flow conditions, looking only at the steady state response of the microgel. Furthermore, the model presented is only applicable to microgels during the first portion of microgel penetration, where the deformation is relatively small and the stresses of different points of contact minimally interact. Despite these limitations, I argue here that the experiments and model presented lay the groundwork for a more general model of the entry of soft spheres into constrictions. As the Cauchy number in these experiments is low, the deformation of the microgel comes primarily from contact, neglecting impact. Furthermore, the passage of the microgel into the constriction beyond the validity of this model is rapid and unstable. As such, the deformation of the microgels becomes independent from flow, deforming on a geometric basis. There is therefore reason to believe that this model can be generalized to more dynamic scenarios, and warrants further investigation into the matter.

3.6.2 Elastic Modulus of Trapped Microgels

One of the most common applications of microfluidic constrictions historically has been to measure the elastic properties of the particles that flow into them [157, 104, 173, 57, 117, 121]. Given the good agreement between theory and measurement shown in Fig. 3.14, it is possible to measure the effective elasticity of particles as they pass into a simple 1 dimensional constriction as well. Rewriting Eq. 3.25 and 3.21, the elasticity by regression from

$$E^{*1/3} = \frac{1}{a} \left(\frac{3dP_{\text{gel}}(aw + (d/2 - a)(w + 2r_c(1 - \cos \theta)))}{8\pi \sin \theta} \mathcal{F}_2(\mathcal{Z}) \right)^{1/3}, \quad (3.26)$$

where a is calculated as described in Eq. 3.25. The results of elasticities analyzed by this method are compared with those found by microindentation in Tab. 3.3. In general there is a good agreement between the data measured using microindentation and the constriction method proposed here. With the exception of the soft microgel, all samples fall within the range of uncertainties of the other. The magnitude of the uncertainties is also similar between the two methods, although the degree sample to sample does change.

One dimensional constrictions are relatively simple to construct using conventional PDMS based microfluidics, requiring no alignment of lithographic masks, no specialized glass pipettes, and no specialized piezo controllers. They can also be placed in series with relative ease, as they were in these experiments. That being said, the

	Gel A/Stiff	Gel B/Medium	Gel D/Soft
Diameter, d (μm)	83.4 ± 2.9	139 ± 2.1	129 ± 1.8
Microindentation, E^* (Pa)	$(1.5 \pm 0.9) * 10^4$	$(1.5 \pm 0.4) * 10^3$	110 ± 87
1D Constriction, E^* (Pa)	$(1.8 \pm 0.4) * 10^4$	$(1.0 \pm 0.7) * 10^3$	447 ± 93

Table 3.3: A comparison of microgel elasticities as measured by microindentation and by the microfluidic slit-trap. Note that elasticities measured by the trap had data limited to within the range $l/d < 0.2$.

throughput of this method is still limited when compared with other "on a chip" methods of measuring microgel elasticity, such as with micropipette on a chip [104]. This may be surmountable however if instead of a bypass to provide pressure, a pressure controller is used. This would eliminate the need for using tracer particles to estimate the pressure provided by the syringe pump. Alternatively, while still using a syringe pump, the separatrix could be reconstructed using dyed flows, similar to how comparators measure resistance [166].

3.6.3 Limitations of the Microgel Trap

In this work, small and soft microgels were tested that were omitted from analysis because they became too readily stuck in the trap. The microgels tested here however are not so exceptionally soft that they are unique in the realm of microfluidics, as microgels have been used experimentally with elasticities in the range of $E^* \sim 10\text{Pa}$ [134, 183]. To measure their penetration into a one dimensional constriction such as the one used in the slit-trap, it is necessary to understand why the microgel was caught. There were two sets of microgels tested in these experiments with $E^* < 1\text{ kPa}$, with the physically larger of the two behaving similarly to the medium and stiff microgels, *i.e.* with respect to following Eq. 3.22. Because of this, I previously suggested that increasing the ratio w/d would reduce the relative friction between the microgel and microchannel. In practice, to measure the elasticity of an extremely soft microgel using a constriction trap, the constriction would have to be sufficiently small, such as $w/d > 0.15$, which was the case for the large but soft microgels tested.

On the opposite end of the spectrum, hard microgels may also be difficult to analyze using the method proposed here. The microchannels used here were made in PDMS, with an elastic modulus of $E \sim 1\text{MPa}$. In the analysis here, this is neglected, however for microgels with a similar elastic modulus, the deformation of the microchannel will need to be taken into account, adding significant complexity to the analysis, beyond simply adapting the effective elasticity of contact pair. Furthermore, the pressures necessary to deform a stiff microgel will increase linearly with the elasticity of the microgel, as predicted by Eq. 3.21. At sufficiently high pressures, the microchannel may not only deform, but be damaged. The simplest method to overcome this limitation is to increase the elastic modulus of the microchannel material and use a stronger bond between substrates (glass and PDMS in the case of this work). This is not necessarily a simple task, as it may require using a more complicated fabrication process, depending on the specific application. As a method of measuring microgel and particle elasticity, the microfluidic constriction trap is therefore best suited to microgels with elasticities below $E^* < 100\text{kPa}$.

Finally, the microgel trap has thus far only been tested on microgels at equilibrium, where $dl/d\tau = 0$, where τ represents time. I hypothesized that due to the low C_y in these scenarios, microgel impact would have a negligible effect compared with the contact forces at play. This however deserves further experimental investigation in order to validate it. By varying Q with respect to τ , the dynamic response of $dl/d\tau$ can also be measured, both as a response to step-wise changes in Q and more gradual changes in Q . As hydrogels are typically visco and poro-elastic, the microgel response to flow may also be further affected by the rate of loading [164, 134]. In order to reliably measure P_{gel} , the microchannel must be stiff enough to negligibly deform when Q is changed, something not considered in this study. In doing so, not only should it be possible to measure any time dependent effects on the microgels, but it should also be possible to measure the visco-elasticity of the microgels in measuring their dynamic response.

3.7 Conclusion

The entry of particles into microfluidic constrictions requires understanding how this penetration will deform the particle. The problem becomes more complex when the particle and constriction are non-conforming, allowing for leaks and a full three dimensional particle deformation. In this chapter I investigated the deformation of microgels penetrating a one dimensional constriction, by trapping microgels in a slit-trap and applying increasing pressure upon the microgel. The microgel deforms in three dimensions, and using simulations validated against experimental measurements, the displacement of the microgel is compared with how it deforms around the microchannel, increasing the area of contact. By making some simple geometric approximations to how pressure is applied to the microgel, deformation and displacement can be related to the applied pressure by adapting classical Hertzian contact mechanics.

The model proposed here is limited to the specific one dimensional constriction tested as well as limited to the early stages of entry into the constriction. The Hertzian model proposed here relies on the assumption that stresses are localized at the points of contact between the microgel and trap corners. This only holds true for relatively small deformations. Further beyond this region of validity, the microgel begins to enter into the constriction due to the contact forces being incapable of equating with the pressure pushing the microgel into the constriction. The model is also limited to a specific non-axisymmetric geometry. Despite this, there is good reason to believe that the modeling used here is more general, and could be adapted to a wide range of geometries, beyond the simple one dimensional constriction.

The simple microfluidic slit-trap, combined with the model developed to describe the deformation of particles, has a novel application in the realm of mechanical characterization. The data presented here has a similar precision to that of microindentation and other methods of measuring elasticity. While beyond the scope of this work, with some modifications, the slit-trap could be modified in order to rapidly test the elasticity of a large sample of microgels, and has the advantage of requiring very little specialized equipment not readily available to most microfluidic laboratories.

While this chapter has focused on the deformation of a trapped microgel, the entry of particles into constrictions is not simply a structural problem, but an interaction between the microgel mechanics and the fluid forces. This was touched on briefly here when considering the distribution of pressure across the face of the microgel. The other side of the same problem to consider is this: if the deformation of the microgel affects the pressure on the microgel, which in turn affects its deformation, how exactly does the deformation of a trapped microgel affect the flow past itself?

Chapter 4

Non-Linear Leaky Flow Around A Deforming Trapped Particle

4.1 Introduction

Solid deformations can have a major influence on fluid flow in the regime of strong fluid-structure coupling. A wide range of complex behaviors, including oscillations that lead to catastrophic failures or blockages, can be observed when the inertial effects of the fluid and solid couple together [135]. Recently an increased attention has been paid to the effect of a low Reynolds number flow on an elastic fiber [1], with particular focus on the transport [114] and deformation [56] of slender elastic fibers by the flow [55].

Two-way flow-structure coupling has been studied in the case of deformable tubes, in which elastic deformations of the tube walls led to strong modifications of the fluid flow. Wall elasticity effects were shown to stabilize the flow distribution into a bifurcation [17] and to suppress the emergence of viscous fingering in a Hele-Shaw cell [137]. More extreme cases emerged in the case of air-liquid flows within flexible tubes, where surface tension led to a complete airway closure [79]. These effects of wall elasticity of the fluid flow have been used to explain sap flow in green plants [91, 19], flow through cellular micropores [22] or to create soft valves for technological applications [97, 115, 30, 22], see Fig. 4.1a-c.

A different class of problems for which the two-way coupling can lead to extreme modifications of the flow consists of the case of a soft particle being pushed into an orifice. This problem is encountered in many microfluidic applications, such as during the flow and encapsulation of hydrogels [3, 99] or for the characterization of cells and other soft materials [117, 57, 139, 159, 184, 176]. It is also closely related to clogging or sieving particles [78, 54, 6, 156, 81, 10, 179]. In many of these cases a spherical particle is pushed into a rectangular slit, which allows for a leakage flow around the particle [117, 139, 96, 184]. But in spite of the interest for applications, the physics that

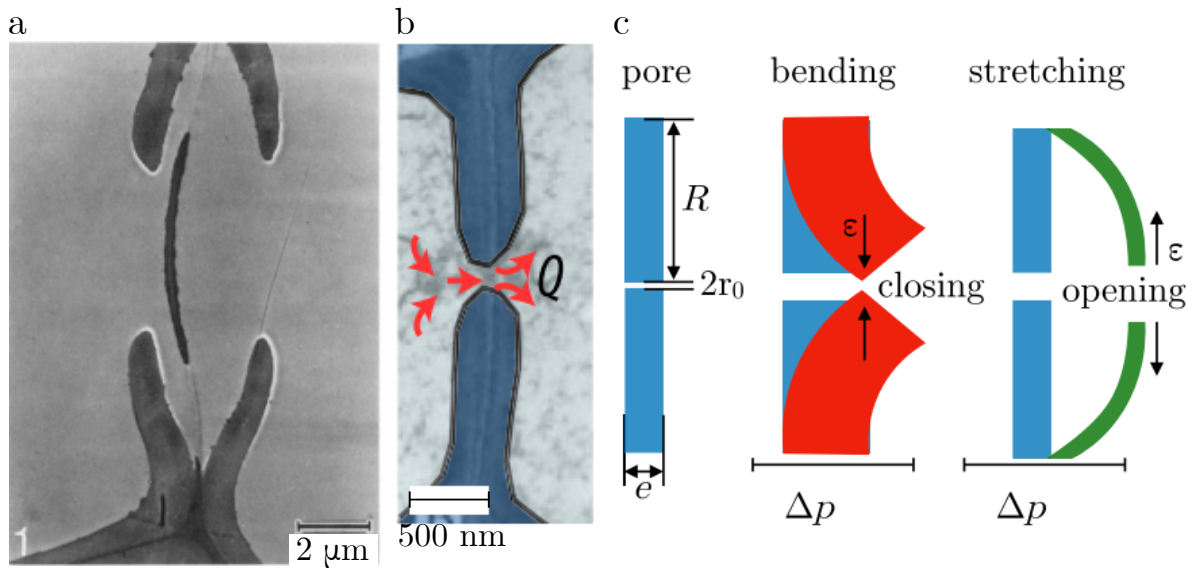


Figure 4.1: Soft valves effectively control flow through them by deforming depending upon the pressure applied, and are found in nature. (a) A cross sectional view of a xylem bordered pit membrane from *Pinus Sylvestris*. As pressure increases the membrane is forced to close, regulating water flow within the tree. Reproduced from Bauch *et al.* [19]. (b) A diaphragm septum in a cell wall which regulates flow through it. reproduced from Louf *et al.*, originally from Boekhout *et al.* [115, 22] (c) A model of the septum diagram shown in part (b), demonstrating two modes of regulating flow in response to changes in pressure difference. Reproduced from Louf *et al.* [115].

determines the equilibrium between leaky flow and particle deformation has not been explored.

In the previous chapter, I developed a model for the deformation of a microgel entering into a one dimensional constriction. Focusing specifically on the contact between the corners of the constriction and the spherical microgel, I developed a model relating the pressure to the displacement and deformation of the microgel based on Hertzian contact. What remains to be explained is how this deforming microgel interacts with the normally linear pressure-flow relationship through the microfluidic channel. In this chapter, I develop a model for this non-linear relationship, and compare it with the flow and deformation experiments undertaken in the previous chapter.

4.2 Methods

4.2.1 Experimental Overview

The data used in this chapter picks up where the previous chapter left off. To briefly summarize the experiments performed, microgels flowed into a microfluidic trap in the thrupass line. Once plugged, excess microgels flow through the bypass line as the thrupass line becomes partially plugged. The microfluidic channel is summarized in Fig. 4.2a. Switching to a carrier fluid containing tracer microbeads, the pressure on the microgel is applied using the bypass line, with the distribution of flow described by the resistance diagram in Fig. 4.2b. The fraction of flow passing by the thrupass, Q_{thru}/Q and bypass, Q_{byp}/Q is reconstructed from the streamlines created by the tracer

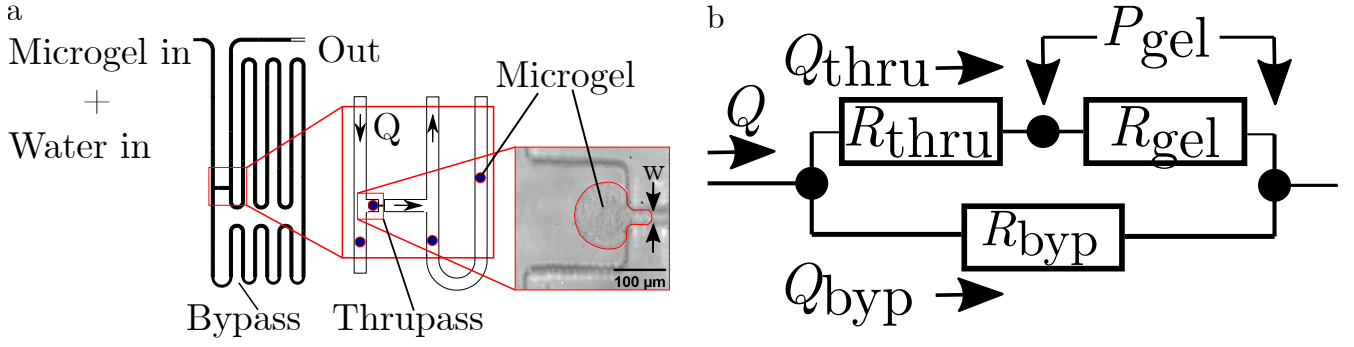


Figure 4.2: A review of the experiment explained in detail in the previous chapter. (a) A diagram of the microfluidic channel used in this experiment. Zooming in there is the thru pass line where the microgel is trapped, and zooming further there is a micrograph of a trapped microgel. (b) A resistance diagram corresponding to the microchannel, including highlighting the resistances due to the bypass, R_{byp} , thru pass, R_{thru} and microgel, R_{gel} .

microbeads. The resistance added by the microgel, R_{gel} is calculated relative to the thru pass resistance, R_{thru} and bypass resistance, R_{byp} as

$$R_{gel} = \frac{(Q - Q_{thru})R_{byp}}{Q_{thru}} - R_{thru}, \quad (4.1)$$

where Q represents the total fluid flow through the microchannel. The pressure passing the microgel can be deduced from Eq. 4.1 as

$$P_{gel} = (Q - Q_{thru})R_{byp} - R_{thru}Q_{thru}. \quad (4.2)$$

Recalling that the microchannel resistances, R_{byp} and R_{thru} are described by

$$R_{ch} = \frac{\alpha(w_{ch}/h)\mu z_{ch}}{w_{ch}^2 h^2}, \quad (4.3)$$

where μ is the fluid viscosity and z_{ch} , w_{ch} and h are the length, width and height of the rectangular microchannel respectively. The subscript ch refers to either the bypass, byp or thru pass, $thru$. The shape factor is described as

$$\alpha\left(\frac{w_{ch}}{h}\right) = \frac{\pi^3\left(\frac{w_{ch}}{h}\right)^2}{8} \left(\sum_{n=1,3,5,\dots} \frac{\left(\frac{w_{ch}}{h}\right)}{\pi n^4} - \frac{2}{\pi^2 n^5} \tanh \frac{n\pi\left(\frac{w_{ch}}{h}\right)}{2} \right)^{-1} \quad (4.4)$$

[127].

The microgels tested in this chapter are the same as in the previous chapter, omitting the soft and small microgels which were omitted there as well. The batches of microgels tested are comprised of a soft, $E^* = 110 \pm 87$ Pa and large microgel, $d = 129 \pm 1.8 \mu\text{m}$, a medium, $E^* = 1.5 \pm 0.4$ kPa and large microgel, $d = 139 \pm 2.1 \mu\text{m}$ and a stiff, $E^* = 15 \pm 0.9$ Pa and small microgel $d = 83.4 \pm 2.9 \mu\text{m}$. The microgels in question were made of a similar photoactivated polyethylene glycol (PEG) mixture, varying the PEG-Diacrylate content and molecular weight, as explained in Ch. 2.

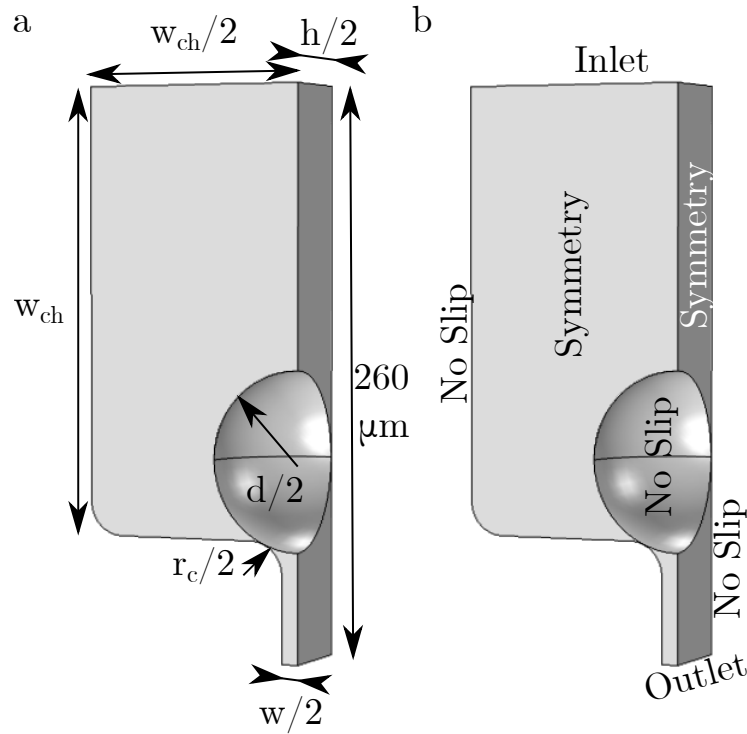


Figure 4.3: (a) A diagram of the simulated microchannel with an undeformed, spherical microgel cutout. The microchannel is cut into quarter sections, and dimensions for the channel width, w_{ch} , height, h , constriction/slit width w and channel corner, r_c are included, as well as the microgel diameter, d . To capture flow downstream from the microgel, a $z = 60 \mu\text{m}$ length of the constriction is also included. (b) The same diagram of the simulated microchannel as in (a), annotated with the boundary conditions on each surface. Inlet and outlet pressures are provided as uniform P_{in} and P_{out} respectively.

4.2.2 Simulation Overview

In order to better visualize and predict flow around the trapped microgels, an uncoupled series of fluid simulations were performed using the geometry of the deformed microgels described in the previous chapter. The fluid simulation was performed in the COMSOL multiphysics simulation environment (COMSOL, Grenoble, France) using standard laminar flow. The fluid used in the simulation was water at $T = 20C$.

The geometry was made to represent the fluid domain in the solid simulations previously undertaken. Because of symmetry, the channel was cut into a quarter section, which allowed for more efficient simulation. First, a fluid domain corresponded to an empty microchannel was made, corresponding to dimensions $w = 15 \mu\text{m}$, $r_c = 15 \mu\text{m}$ and either $h = 81 \mu\text{m}$ or $h = 85 \mu\text{m}$, see Fig. 4.3a for full channel dimensions. Exported computer aided design models of deformed microgels from the previous solid simulations were imported and aligned with the microchannel. Microgel deformations corresponded to pressures ranging from $P_{gel} = 0$ to $P_{gel} = 6.4 \text{ kPa}$. The microgels were then subtracted from the fluid domain. In order to avoid thin element membranes, the microgels were moved to overlap with the trap corner by up to $0.5 \mu\text{m}$. The mesh was set to the COMSOL physics controlled normal sized mesh. When increasing the mesh density to extra fine, no significant change in output was measured.

As flow is laminar, the pressure-flow relationship is expected to be linear, i.e. $P = QR$. Therefore, the resistance

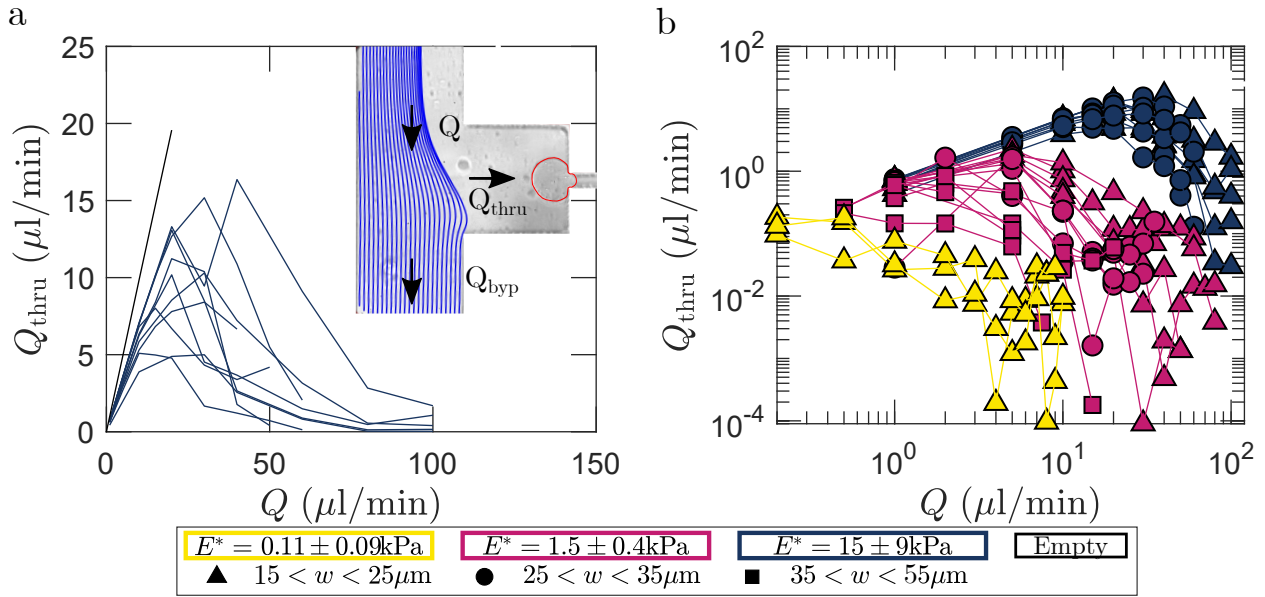


Figure 4.4: (a) A comparison of the flow through the thrupass, Q_{thru} with the total inlet flow rate Q for microgels where $E^* = 15 \pm 9$ kPa and diameter $d = 83.4 \pm 2.9$ μm . This is compared with the flow relationship for an empty microchannel, $h = 85$ μm and $w = 31$ μm . The inset shows a micrograph of a trapped microgel with flow rate directions labeled. Streamlines reconstructed from videos of the tracer beads in flow are overlaid to the micrograph in order to show how Q_{thru} and Q_{byp} are determined. (b) A comparison of flow through the thrupass with inlet flow rate for all different microgels tested. This is placed on a log-log plot in order to compare the different scales for each of the microgels.

from these simulations can be assumed to come directly from the microgel geometry, as the fluid properties remain constant in these experiments. To measure the resistance, a uniform inlet pressure of $P_{\text{in}} = 1$ kPa and an outlet pressure of $P_{\text{out}} = 0$ were set as boundary conditions. The microgel, as well as microchannel surfaces were set to no slip boundary condition, and the cut planes of symmetry were set to the symmetry boundary condition. A diagram of the fluid domain is displayed in Fig. 4.3b. Resistance was measured from the simulations by measuring the total flow at the outlet boundary, such that

$$R_{\text{sim}} = (P_{\text{in}} - P_{\text{out}})/Q_{\text{sim}}. \quad (4.5)$$

The minimal cross sectional area between the microgels and the microchannel was estimated by locating the node at which the magnitude of velocity was maximized, and creating a cut plane in the direction of the velocity vector. The Area of this cut plane corresponds approximately to that of the minimal cross sectional area, due to conservation of volume.

4.3 Results

4.3.1 Proportion of Flow Trough a Microgel Trap

In the absence of a microgel, increasing the flow rate Q at the inlet led to an increase of the flow rate Q_{thru} , with the ratio between Q_{thru} and Q being given by the ratio of the hydrodynamic resistances between the thrupass and bypass channels. When a microgel was trapped by the narrow slit, increasing the flow rate Q at the inlet led to a non-monotonic behavior of the flow rate Q_{thru} through the thrupass channel. At first, increasing Q led to an increase in Q_{thru} , until a maximum value of Q_{thru} was reached; increasing Q beyond a critical value then led to a decrease in the flow rate Q_{thru} , see Fig. 4.4a. The initial rate of increase of Q_{thru} with Q follows closely to that of the empty microchannel as well. At high enough values of Q , the microgel plugged the thrupass channel entirely and all the flow was redirected to the bypass channel. This non-monotonic relationship between Q_{thru} and Q reveals a strong non-linear hydrodynamic resistance added by the microgel. This relationship holds for both the soft, $E^* = 110 \pm 87$ Pa, and medium, $E^* = 1.5 \pm 0.9$ kPa, microgels, see Fig. 4.4b.

4.3.2 Added Resistance of a Trapped Microgel

The portion of flow past the microgel is dictated by the changes in the hydrodynamic resistance added by the deformed trapped particle. The value of R_{gel} increased dramatically with flow rate, spanning nearly 6 orders of magnitude when the flow rates covered 2 orders of magnitude (see Fig. 4.5a). The rate of this increase depended on the gel elasticity: stiffer gels ($E^* \approx 10^4$ Pa) led to a slower increase in resistance than softer gels ($E^* \approx 10^2$ Pa). Additionally, there is a weaker tendency for resistance to increase more quickly for smaller constriction widths, noticeable most of all when comparing the smallest to largest widths in the case of the medium stiffness microgel, where the differences in widths is more pronounced.

The increase in resistance was associated with a displacement of the microgel as it deformed and penetrated into the slit, see Fig. 4.5b. There is a considerable collapse of the data when comparing R_{gel} with l , with each of the different microgel samples showing a similar trends of increasing resistance. Additionally, the differences in R_{gel} with respect to w seen in Fig. 4.5a are no longer noticeable.

The Reynolds number in the vicinity of the microgel, $Re = 2 \frac{Q_{\text{thru}} \rho}{\mu(h+w)}$ achieved a maximum value of $Re = 2.6$, while the mean value was $Re = 0.3$. This puts the flow squarely in the laminar regime, and approaching the Stokes flow regime. For this regime of flow, hydrodynamic resistance is governed by Poiseuille flow. Specifically, the resistance is dictated by the geometry through which flow passes and the viscosity of the fluid, and is independent of any inertial effects from fluid velocity. This is supported by the data, which shows considerable collapse when comparing microgel displacement with resistance, however the question of how exactly the microgel deformation is causing this resistance remains unanswered. To understand how resistance is influenced by microgel deformation,

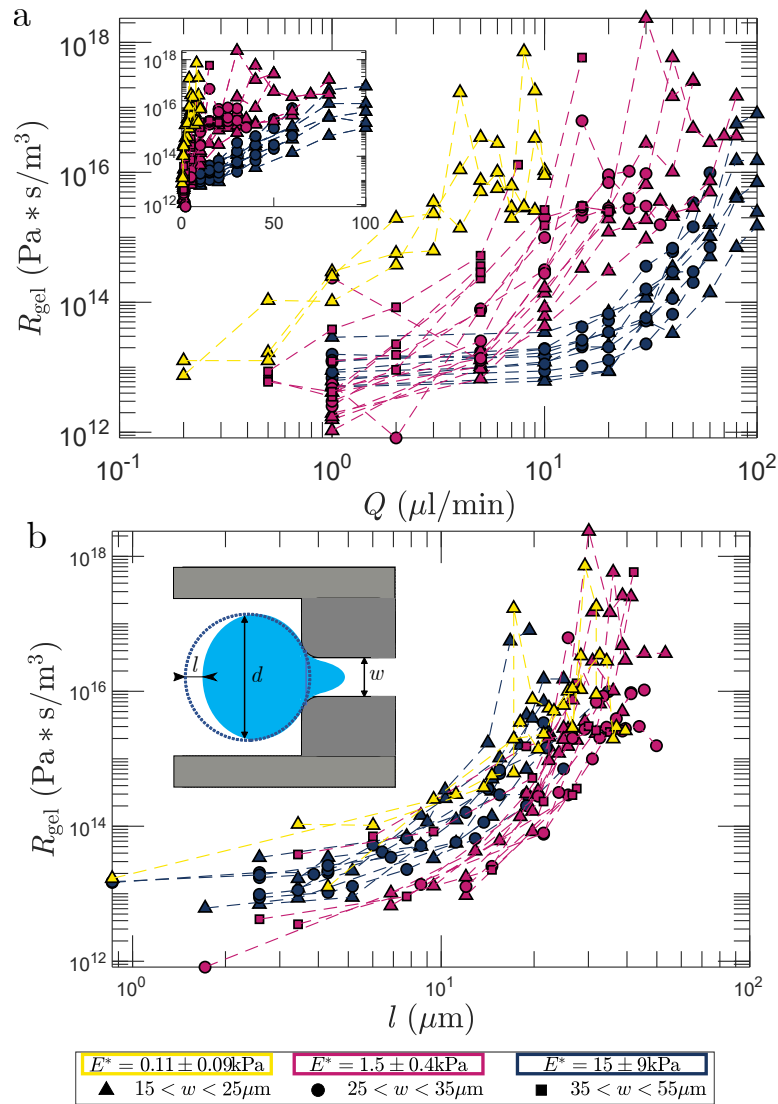


Figure 4.5: (a) The added hydrodynamic resistance of a trapped microgel compared with the flow rate at the channel inlet. An inset is provided showing the same data on a log-linear scale to aid the reader. (b) The added hydrodynamic resistance of a trapped microgel compared with the displacement of the microgel into the microchannel. The inset shows a diagram of a deformed microgel with displacement labeled.

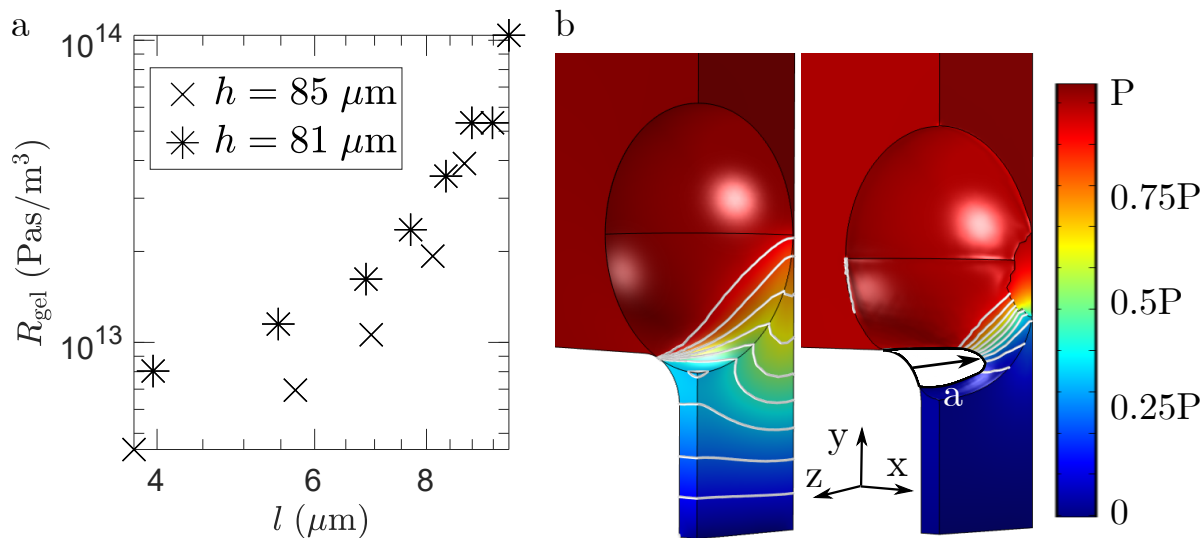


Figure 4.6: (a) The simulated hydrodynamic resistance of deformed and trapped microgels, compared with their displacement. (b) Simulation of the flow around an undeformed microgel (left), and a one deformed under a simulated pressure of $P_{\text{gel}} = 4 \text{ kPa}$ (right). Color indicates the pressure normalized by the inlet pressure P . Isobars are shown in white. Note how the deformed microgel focuses the pressure drop into a narrow area. x and y directions represent the imaging plane.

it is necessary to identify where this resistance is occurring. To put it in other words, it is necessary to quantitatively and qualitatively observe the change in pressure around a trapped microgel.

4.3.3 Simulating Poiseuille Flow Around a Deformed Microgel

Quantitatively, the simulated resistance increased in much the same way as seen with the experimental microgels. Fig. 4.6a shows the hydrodynamic resistance increased slowly at first with displacement, but the rate increasing considerably with increased deformation. This is in agreement with the experimental data, which showed about an order of magnitude change of R_{gel} in the first decade of l before increasing upwards of 4 in the next. Fig. 4.6a also shows the influence of microchannel height on resistance. In each simulation, the microgel was set to the same undeformed diameter, $d = 80 \text{ } \mu\text{m}$, however the height changed, leaving a clearance of $h - d = 1 \text{ } \mu\text{m}$ in one case and $h - d = 5 \text{ } \mu\text{m}$ in the other. In their undeformed state, this resulted in $R_{\text{gel}}|_{h=81} / R_{\text{gel}}|_{h=85} = 1.64$. The magnitude decreased with increasing deformation, however the difference remains. This may help to explain the differences within microgel samples for the different resistances. As the uncertainty of d for each of the microgel samples is close to the range presented in this simulation, it would help to explain some of the variation, although not all, as within samples there is often an order of magnitude difference in the measured value of R_{gel} , see Fig. 4.5b.

In the absence of deformation, the pressure drop in the channel occurred both around the spherical gel particle and in the slit, as shown by the isobars in the fluid simulation in Fig. 4.6b, left panel. When the gel deformed however, the pressure drop was focused over a short distance upstream of the slit, corresponding to the region where the flow was focused through a narrow gap, see Fig. 4.6b, right panel. This cross-sectional area is denoted as Λ . This

concentration of the pressure drop indicates that the resistance to flow was due the the bulb like protrusion of the gel between the channel corner and back wall, as opposed to due to the finger like protrusion into the slit of the trap.

4.4 Poiseuille Flow Around Deformed Microgels

The physical reason behind the focusing of the pressure drop can be understood by measuring the dependence of R_{gel} on Λ . The Hagen-Poiseuille equation is a specific solution to the Navier-Stokes equations for pressure driven laminar flow, called Poiseuille flow. In this case, the pressure driven flow rate is described by

$$Q = \frac{dP}{dz} \frac{\Lambda(z)^2}{\alpha\mu}, \quad (4.6)$$

Where in this case $\Lambda(z)$ is the cross sectional area of the flow, z is the direction of flow and α is the shape factor. Rewriting this in terms of hydrodynamic resistance, the resistance is defined as

$$R = \frac{\alpha z \mu}{\Lambda^2}. \quad (4.7)$$

Flow around the trapped microgel is not so simple as a strait channel, as both the cross sectional area and flow direction change considerably, see Fig. 4.7a. To add another layer of complexity, the region in which most pressure drop occurs becomes shorter along the streamlines as well, further complicating matters.

The area through which the fluid must pass is bounded by a 3D geometrical shape that is defined by the curved bead shape and the channel walls. Here I approximate this shape by a triangle with two vertices located at the contact points between the microgel and the device, while the third vertex is located at the intersection between the slit and the top wall of the channel. This triangle, of surface area Λ , is drawn on Fig. 4.7b. Considering the area of a triangle to be equal to $\frac{1}{2} \times \text{base} \times \text{height}$, the area of this triangle can be estimated from the position of the microgel. From the diagram shown in Fig. 4.7b, the base of the triangle can be seen to measure $\frac{h}{2} - a$, where h is the height of the microchannel. Meanwhile, the height of the triangle can be determined from the Pythagorean identity as $\sqrt{(w/2 + r_c(1 - \cos \theta))^2 + (d \sin \theta_0/2 - l - a/2)^2}$ where $\theta_0 = \theta(l = 0)$. Therefore, the section area can be estimated as

$$\Lambda \approx \frac{1}{2} \left(\frac{h}{2} - a \right) \sqrt{\left(\frac{d \sin \theta_0}{2} - l - \frac{a}{2} \right)^2 + \left(\frac{w}{2} + r_c(1 - \cos \theta) \right)^2}, \quad (4.8)$$

Note however that the flow passes through four of such openings, so that the total area that the fluid can pass through is 4Λ .

Equation 4.8 can be slightly simplified by recalling first that the microchannel height is selected to closely match the size of the microgels, $d/h = 1 \pm 0.1$. As a result we can consider $d \approx h$. Moreover, the range of d/w values

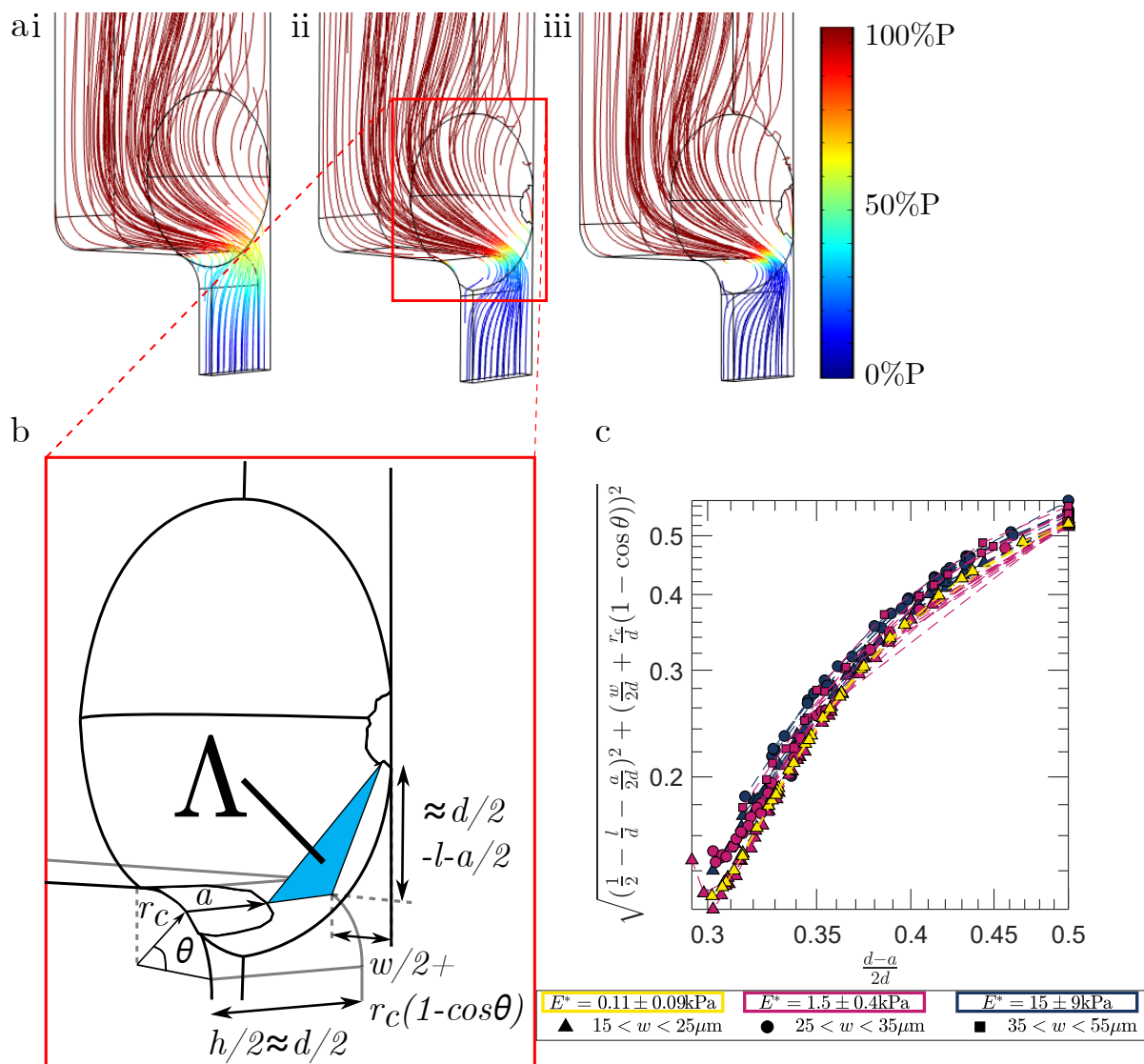


Figure 4.7: Streamlines of flow around trapped microgels. Microgels from left to right, are deformed under pressures of (i) $P_{\text{sim}}/E = 0$, (ii) $P_{\text{sim}}/E = 0.12$ and (iii) $P_{\text{sim}}/E = 0.2$. Streamline colors represent the value of the pressure along the streamline. (b) A magnified diagram showing the dimensional makeup of Λ . (c) A comparison of the base and height of the triangle which makes up Λ , each normalized by the microgel diameter.

that are considered in this study yield a value of $\sin \theta_0 > 0.9$, and therefore $\sin \theta_0 \approx 1$ and $\cos \theta_0 \approx 0$. These two approximations allow us to write

$$\Lambda \approx \left(\frac{d}{4} - \frac{a}{2} \right) \sqrt{\left(\frac{d}{2} - l - \frac{a}{2} \right)^2 + \left(\frac{w}{2} + r_c(1 - \cos \theta) \right)^2}. \quad (4.9)$$

Because a is in a direction perpendicular to the imaging plane, it is inferred by considering the contact mechanics problem of a spherical elastic bead, of diameter d and elastic modulus E^* , being pressed with a pressure P_{gel} on top of two cylinders of equal radius r_c and spaced by w [14]. The displacement of the gel l_{theory} due to this forcing was found to relate to the major axis a of the ellipsoidal contact between the microgel and the trap, modulated by a combination of the geometrical parameters of the problem (see Ch. 3 for full derivation):

$$l_{\text{theory}} = \frac{2a^2}{d \sin \theta} \mathcal{F}_1\left(\frac{r_c}{d}\right), \quad (4.10)$$

where $\mathcal{F}_1\left(\frac{r_c}{d}\right)$ is a function that describes the shape of contact (see Ch. 3, Eq. 3.23) and θ is the angle created between the microgel, the corner and the slit (see Fig. 4.7b). The area Λ of the spacing between gel bead and sidewalls is similarly estimated from Eq. 4.9, by measuring the geometric parameters d, w, r_c and l . Using Eq. 4.10, a is estimated at each imposed flow rate as well.

The area described by Λ is only an approximation of the actual shape, as it neglects the curvature of the microgel. Qualitatively however, the curvature does not change dramatically in this section. Furthermore, the triangle described in Eq. 4.9 is relatively constant in shape. Comparing its base to height, see Fig. 4.7c, there is an approximately linear slope, $R^2 = 0.97$, resulting in only minor increases in α . The maximum change calculated for these values assuming a triangular orifice is $\alpha_{\text{max}}/\alpha_{\text{min}} = 1.29$ [127]. As such, in this analysis changes in α are neglected. Contrary to the trend of slight increasing α with decreasing Λ is the decreasing z where pressure change occurs. While the volume in which pressure loss occurs does decrease according to Fig. 4.7a, this shrinkage can be assumed to be related directly to the area of Λ , such that

$$\frac{R_{\text{gel}}}{R_0} \sim \left(\frac{\Lambda_0}{\Lambda} \right)^{C_0}, \quad (4.11)$$

where the R_0 and Λ_0 refers to the undeformed case, *i.e.* at the lowest flow rate tested. Assuming a gradual decrease in cross sectional area for Poiseuille flow, $C_0 \approx 2$, as described by Eq. 4.7.

Noting these assumptions for Poiseuille flow, R_{gel}/R_0 is plotted as a function of $(\Lambda_0/\Lambda)^2$ in Fig. 4.8. The plot shows an excellent collapse for all experimental and numerical results and indicates that R_{gel} scales as Λ^{-2} . The collapse of the measurements of R_{gel} on a single master curve shows that the resistance to flow is indeed due to the deformation of the soft solid upstream of the slit which in turn determines the size of the gap that the flow must go through. Moreover, the rapid increase of R_{gel} makes it the dominant source of pressure drop compared with a

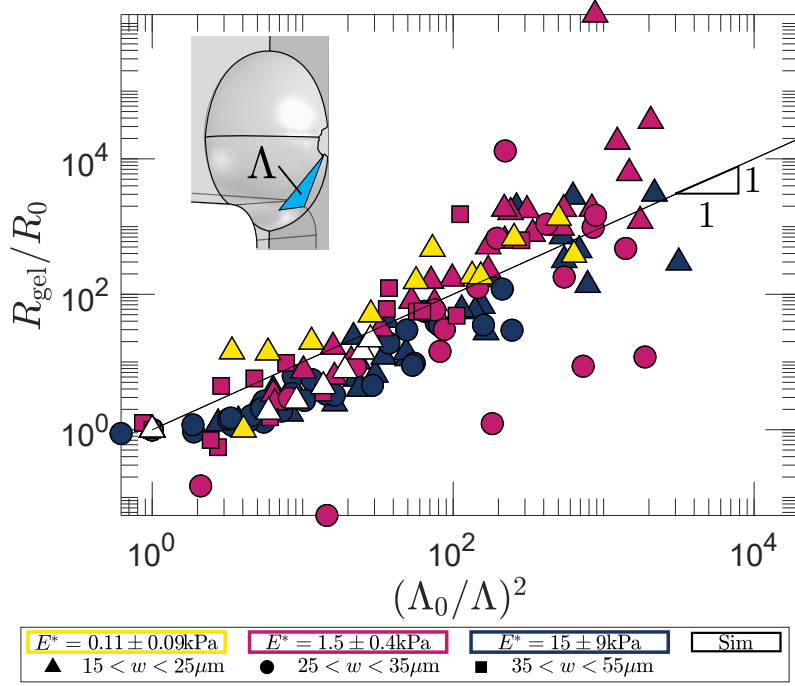


Figure 4.8: The measured gel hydrodynamic resistance R_{gel} as a function of the area Λ of the triangle through which the flow must pass (see inset). R_{gel} and Λ are respectively normalized by the resistance to flow R_0 and the area Λ_0 in the absence of gel deformation. A unity line is provided for reference.

the other sections in the rest of the microchannel.

4.5 Valve Behaviour of Deformed Microgels

This increased resistance also helps to explain the deformation behavior seen in Ch. 3. The added resistance due to flow focusing couples back to modify the shape of the microgel. This determines the values of l and a , which are related together by Eq. 4.10. Recalling from Ch. 3 that a depends on the ratio $\mathcal{P} = P_{\text{gel}}/E^*$ and a combination of the geometric parameters, which yields an implicit relationship between mechanical and geometric effects:

$$a = \left\{ \frac{3\mathcal{P}d}{4\pi \sin \theta} \left[aw + \frac{2}{3} \left(\frac{d}{2} - a \right) (w + 2r_c(1 - \cos \theta)) \right] \mathcal{F}_2(\mathcal{Z}) \right\}^{1/3}. \quad (4.12)$$

where $\mathcal{F}_2(\frac{r_c}{d})$ is another function of the shape of contact with the corner (see Ch. 3, Eq. 3.24).

Thus far, the individual links between pressure, deformation and resistance of the trapped microgel have been described. It is now possible to quantitatively understand the relationship between the pressure P_{gel} on the trapped soft bead and the flow Q_{thru} it lets pass through. The flow past the trapped microgel is proportional to the changes in pressure across the microgel and the resistance posed by the microgel

$$Q_{\text{thru}} = P_{\text{gel}}/R_{\text{gel}}. \quad (4.13)$$

However, the resistance posed by the microgel is not a constant, but instead increases as the microgel penetrates further into the trap. The data show that $\frac{R_{\text{gel}}}{R_0} = \left(\frac{\Lambda_0}{\Lambda}\right)^2$. Therefore, it is possible to combine Eqs .4.13 with 4.11 and 4.9, showing how the flow is a function of the gel shape:

$$Q_{\text{thru}} = \frac{P_{\text{gel}}}{R_0 \Lambda_0^2} \times \left(\frac{d}{4} - \frac{a}{2}\right)^2 \left[\left(\frac{d}{2} - l - \frac{a}{2}\right)^2 + \left(\frac{w}{2} + r_c(1 - \cos \theta)\right)^2 \right]. \quad (4.14)$$

4.5.1 Simplifying the Valve Behaviour

Eq. 4.14 can be re-written by using the formulas for a and l from Eqs. 4.10 and 4.12 to obtain

$$Q = C_1 \mathcal{P} \left(1 - C_2 \mathcal{P}^{1/3}\right)^2 \left(\left(1 - C_3 \mathcal{P}^{2/3}\right)^2 + C_4^2 \right), \quad (4.15)$$

where flow has been nondimensionalized as $Q = \frac{Q_{\text{thru}} R_0}{E^*}$ and the geometric constants, $C_1 - C_4$ are functions of a , d , r_c and w :

$$C_1 = \frac{d^2}{(d/2)^2 + (w/2 + r_c(1 - \cos \theta_0))^2} \quad (4.16)$$

$$C_2 = \left(\frac{3 \left(aw + \frac{2}{3} \left(\frac{d}{2} - a\right)(w + 2r_c(1 - \cos \theta))\right) \mathcal{F}_2(r_c, d)}{4\pi d^2 \sin \theta} \right)^{1/3} \quad (4.17)$$

$$C_3 = C_2^2 \frac{2\mathcal{F}_1(r_c, d)}{\sin \theta} + \frac{C_2}{2\mathcal{P}^{1/3}} \quad (4.18)$$

$$C_4 = \frac{w}{d} + \frac{2r_c}{d} (1 - \cos \theta). \quad (4.19)$$

The factors $C_1 - C_4$ are not entirely constant, as a and θ are subject to change with increasing pressure. For practical purposes, the contact angle can be simplified by it as the angle of contact at the midpoint, $\theta = \pi/4$, and recalling that $\cos \theta_0 \approx 0$. The position of contact between the microgel and channel wall is approximated $l+a/2 \approx 2.4l$ from the simulations. Finally, recall that the approximation of force due to pressure described in Eq. 3.20 as:

$$F_P \approx P_{\text{gel}} d \left(\frac{w}{2} + r_c(1 - \sqrt{1/2}) \right). \quad (4.20)$$

Using these simplifications, the formulas for $C_1 - C_4$ simplify to:

$$C_1 \approx \frac{d^2}{d^2 + (w + 2r_c)^2} \quad (4.21)$$

$$C_2 \approx \left(\frac{3 \left(w/2 + r_c(1 - \sqrt{1/2}) \right) \mathcal{F}_2(r_c, d)}{2\sqrt{2}\pi d} \right)^{1/3} \quad (4.22)$$

$$C_3 \approx 3.4 C_2^2 \mathcal{F}_1(r_c, d) \quad (4.23)$$

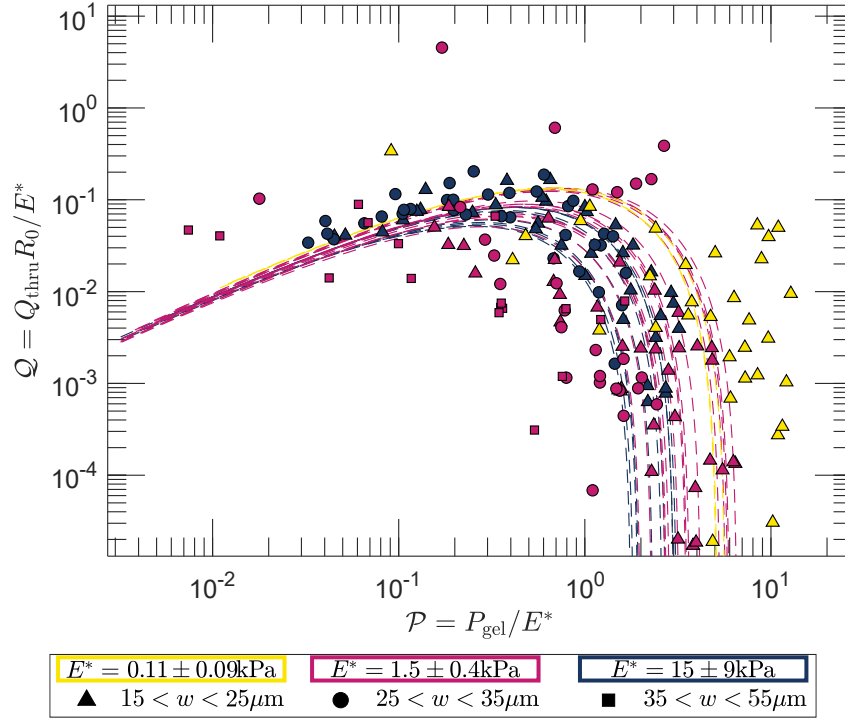


Figure 4.9: Comparison of flow rate through the obstructed thrupass channel, shown in points, with the predicted flow rate, shown as dashed lines. Normalized flow rates, Q , are given as a function of the normalized pressure \mathcal{P} for the full range of pressures tested experimentally. The data here is limited to $l/d > 0.3$ for ease of reading.

$$C_4 \approx \frac{w}{d} + \frac{2r_c}{d} \left(1 - \sqrt{1/2}\right). \quad (4.24)$$

From Eq. 4.15 it is possible to predict the evolution of Q_{thru} as the driving pressure is increased. Fig. 4.9 shows the data collapsing onto the range of theoretical curves. It is notable how well the data collapses, with an interquartile range of Q_{theory}/Q of 0.7 to 10.5. For small values of \mathcal{P} the pressure does not lead to significant deformation of the microgel, such that further increasing \mathcal{P} leads to a nearly linear increase in Q . When the pressure is increased beyond $\mathcal{P} \approx 1$ ($P_{\text{gel}} \approx E^*$) the microgel deforms, which increases the value of R_{gel} and leads to a decrease in the flow rate through the slit.

4.5.2 Maximum Flow Rate Through a Microgel Valve

Eq. 4.15 shows that the dimensionless flow rate Q depends only on the dimensionless pressure \mathcal{P} and on the geometry of the slit, through the parameters $C_1 - C_4$. For a given geometry it follows that Q traces a unique curve, of parameter \mathcal{P} , whose maximum value Q_{max} thus only depends on the geometry of the slit. Therefore the maximum dimensional flow rate $Q_{\text{max}} = Q_{\text{max}} E^* / R_0$ scales linearly with the Young modulus of the gel E^* : a soft gel deforms right away and plugs the channel at low pressures, while a stiff gel allows higher flow to go through. This linear increase is confirmed by comparing the largest measured flow rate with the prediction of Q_{max} , as shown in Fig. 4.10a.

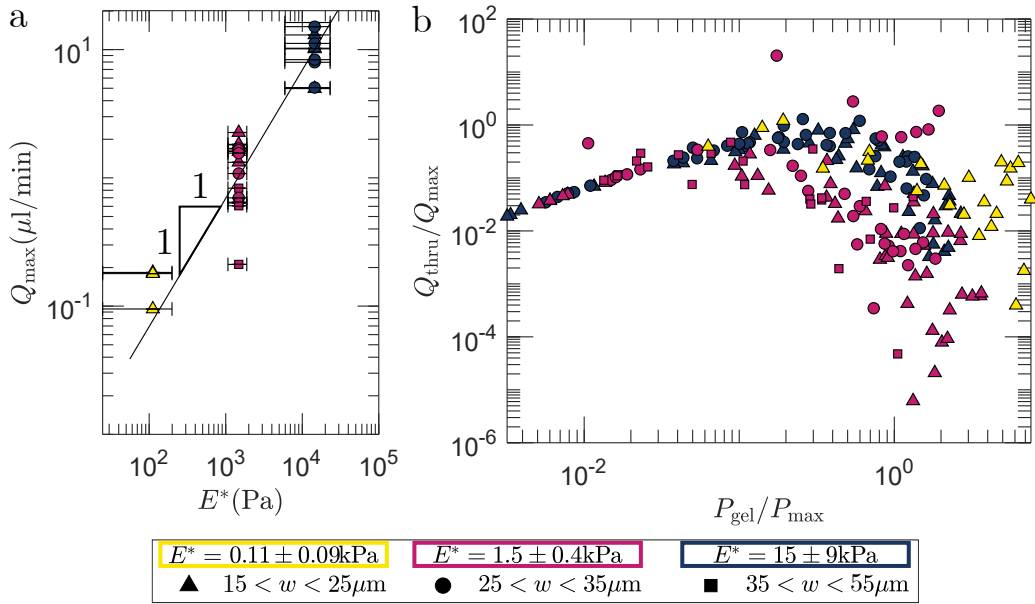


Figure 4.10: (a) Maximum experimental flow rate Q_{\max} past the microgel as a function of the Young's modulus E^* of the trapped bead. Points: Experimental data. Error bars represent 1 standard deviation. Line shown represents the linear best fit. (b) A comparison of flow rate through the obstructed thrupass channel, normalized to the predicted maximum flowrate, Q_{\max} and the pressure normalized to the pressure predicted to achieve the maximum flow rate, P_{\max} .

Rescaling the predicted flow rates and pressure by the predicted Q_{\max} and maximum pressure $P_{\max} = P_{\text{gel}}(Q_{\max})$, it is possible to evaluate the predictive power of the overall model. This comparison is shown in Fig. 4.10b. In general, the model accurately predicts the maximum flow rate, achieved by the valves, with the medium stiffness microgels over-predicting the maximum flow rate. More consistently is the over-prediction of when maximum flow will be achieved. These may be explained by discrepancies in the predictions of l and a , which were discussed in the previous chapter.

One implication of Eq. 4.15 is that of a cut off pressure, at which point $Q_{\text{thru}} = 0$, where $P_{\text{gel}} > P_{\max}$. This is supported from the data as shown in Fig. 4.8, where the flow rate begins rapidly decreasing. This was also observed qualitatively during experiments, as above the pressures tested, the microgels would typically fully pass into the constriction of the trap. This occurred rapidly with increases in flow rate. Quantitatively, the precise value of P_{plug} is beyond the scope of this study, as measuring Q_{thru} while the microgel is moving poses technical challenges, and additionally the pressure was often increased in steps. Furthermore, the geometry of Λ changes beyond the assumptions made here. Despite this, as the onset of plugging is rapid, the model presented here does suggest at what pressure plugging transitions to an unstable and purely transient phase.

The predictions made by Eq. 4.15 also indicate a complicated interplay of microchannel geometry. Fig. 4.11a-b shows the predicted effects of varying the microchannel geometry for a given microgel. In general, increasing w has the effect of decreasing Q_{\max} while reaching that point at a lower P_{gel} , while the opposite is seen by increasing r_c . While it may seem intuitive that a smaller constriction would more quickly limit flow, this seems to indicate the

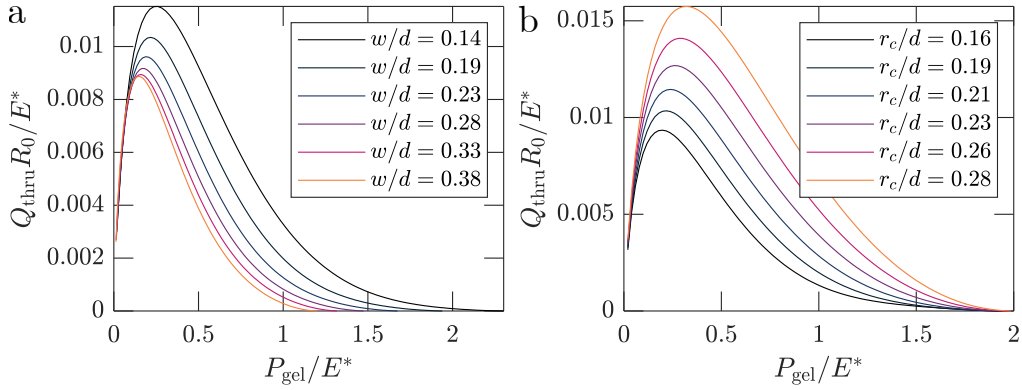


Figure 4.11: The theoretical flow rate predicted by Eq. 4.15 for a microgel with a diameter of $d = 80$, undeformed resistance of $R_0 = 1$ and elasticity of $E^* = 1$. (a) Predicted flow rates for a microfluidic trap with a corner radius of $r_c = 15$ for a range of different w . (b) Predicted flow rates for a microfluidic trap with a width of $w = 15$ for a range of different r_c .

opposite. As the microgel can more readily penetrate into the constriction with a larger w , the maximum flowrate is more limited, and at a lower pressure. Meanwhile, a sharper corner at the trap slit will force the microgel to deform more in the direction of the channel height, plugging more quickly. This analysis however should be taken with a grain of salt, as the analysis presented in this chapter neglects to predict R_0 , which is certainly dependant upon the microchannel and microgel geometry. Meanwhile, the trends in P_{\max} are less evident than those in Q_{\max} , and is overshadowed by noise in the data, see Fig. 4.9.

4.6 Discussion

4.6.1 Practical Application Trapped Microgels

The results presented here can impact several applications, beyond their scientific interest. They provide a physical basis to understand the encapsulation of soft beads in droplets, which has emerged as an important microfluidic technology [187]. In a different operation regime, the strong nonlinear relationship between pressure and flow rate can lead to the design of microfluidic nonlinear flow elements, such as check-valves or flow limiters. These devices play an important role in ensuring the robustness of fluid circuits and protecting against surges. Along with cutting off flow at high pressures, these valves can maintain flow near the maximum flow rate despite pressure variation. The analysis above shows that the maximum allowable flow rate scales linearly with E^* , thus providing a simple design rule.

4.6.2 Valve Model Limitations

While the model of the trapped microgel as a valve is in relatively good agreement with the data for the majority of the data, it relies on the contact modeling performed in Ch. 3. One specific limitation to the model was the range

of l/d which could be predicted. This is mitigated by the fact that resistance increases dramatically where l/d is large, however the fit of data is poorest at larger values of P_{gel} , corresponding to large l/d . More numerical models of $\Lambda(P_{\text{gel}})$ would allow for significant improvement on this front, extending the range of P_{gel}/E^* which are described beyond the model described in Ch. 3.

While $Q_{\text{max}} \sim E^*$ holds for these experiments, the influence of geometry is only accounted for as a scaling law, $R_{\text{gel}}/R_0 \sim (\Lambda/\Lambda_0)^{-2}$. As mentioned above, the R_0 is not calculated and is instead measured experimentally. While this can easily be overcome using simulations, these same simulations show that small changes in the fit of the microgel and microchannel can affect R_{gel} . Strict control over d and h must therefore be utilized so as to minimize $h - d$ if these microfluidic valves are to be used in practice. Similarly, the effective elasticity of the microgels in these tests had wide uncertainties, and this would need to be overcome in order to precisely predict Q_{max} .

The model presented here is also static, however particles entering into constrictions are a dynamic process. The range of experiments performed here, the largest Cauchy number is $Cy = \rho U^2 / E = \left(\frac{(100 \mu\text{l}/\text{min})}{(200 \mu\text{m})(140 \mu\text{m})} \right)^2 \frac{(1 \text{ kg/l})}{(1.5 \text{ kPa})} = 0.049$, indicating that elasticity dominates over inertial effects for these trapped microgels. It follows that the flow around the microgel will also be minimally affected by inertia of a microgel as it deforms. Microgels are however poro-elastic, meaning that their elastic effects will depend on the rate of loading [164, 134]. For the use of trapped microgels as a valve, this dynamic response will be particularly important. As a flow regulating valve, the trapped microgel will be used to maintain a nearly constant flow rate despite fluctuations in pressure. To design around this fact, understanding the dynamic response of microgels under changing pressures is necessary to properly design to maintain the desired flow rate. Further experiments are however required to investigate this phenomenon, in particular with particles that have had their full elastic profile described rather than only the steady state elastic response.

4.7 Conclusion

Not only does entering into a microfluidic constriction deform the the particle, but the particle pushes back on the flow, causing a spike in hydrodynamic resistance. By coupling the deformation of the trapped microgel particle with its resistance, a valve model of flow is constructed. Noting that pressure drop is dominated by the minimal cross section of flow, I modeled resistance as proportional to the inverse of this area squared. Combining this model with the deformation model described in the previous chapter, I was able to model the valve behaviour of the flow past a trapped gel. This novel model is in relative agreement with the data, reflecting a rise to a maximum possible flow rate before plugging flow completely. Both the maximum flow rate and plugging pressure are predicted accurately by the model, in particular noting that the maximum flow rate is linearly proportional to particle elasticity.

Despite this, several challenges are posed when comparing the predicted to measured flow past trapped microgels. First and foremost are the propagation of uncertainties from the deformation modeling. As discussed in Ch.

3, the deformation modeling is only valid for small microgel deformations. Despite this the valve model presented here retains its general accuracy. Further investigation into the deformation of microparticles through their entire transition into a constriction will certainly improve the model presented here. Additionally, investigating the dynamic behavior of trapped microgels will pave the way for practical use as a valve. From a practical standpoint, improved precision in manufacturing of microgels and micro-channels will pave the way for adapting this work into practical microfluidic valves.

This chapter addressed specifically the fluid-structure interactions at play as a microparticle enters into a one dimensional constriction. After the pressure reaches its plugging limit, the contact forces become imbalanced and the microgel rapidly enters into the constriction. While this certainly has an effect on the flow past the particle, this period is short, and the particle quickly accelerates. Once in the constriction, the question of how a particle moves through the constriction remains, and poses a different set of fluid and structural questions to those posed for the entry into a constriction.

Chapter 5

Lubrication and Fluid Flow Around a Microgel Traveling Through a Square Channel

5.1 Introduction

Particles in both natural and laboratory microfluidic settings are often forced through narrow confinements, forcing the particle to deform and flow to adapt to pass around this obstruction. Red blood cells for example are regularly constrained while passing through the circulatory system, deforming dramatically to pass through capillaries less than half their diameter [87]. In doing so, they resist flow, creating a lubricating layer between the cell and capillary [60]. The passage of cells and capsules through microfluidic long constrictions has in particular been extensively studied, allowing for testing cells for disease [150, 144, 72], measuring cellular material properties [177, 72, 117], and cell sorting [177, 28, 29].

As a result of their confinement, particles press outward on the confining channel walls proportionately to their elastic modulus and degree of confinement, as described by Hertzian contact mechanics [14, 8, 184]. This is mechanically distinct from droplets or capsules, which are fluid filled and therefore have internal flow controlling their behavior [84, 18, 171, 25]. This elastic behaviour is not only dependant on the elasticity of the particle, but also the shape of confinement. Comparing two common microfluidic channel shapes, a circular microchannel will distribute stress evenly around its central axis compared with a square channel, which will concentrate stress where the microchannel is in contact with the particle, and result in gutters in the corners between the microgel and microchannel [14, 8, 184].

The presence of a particle within confined channels will also interact with the flow pushing the particle forward.

As demonstrated in chapters 3-4, the deformation of a microgel changes the flow path around the microgel, which in turn affects the pressure applied to the microgel, further affecting deformation in a two way coupled system. While a particle will maintain a constant shape when passing through a strait confined channel at steady state, the particles shape will still affect flow around it. Previous studies of the passage of microparticles through microfluidic channels have noted that the pressure necessary move a confined microparticle through a circular capillary increases as the particle becomes larger with respect to the capillary diameter [111, 109, 110]. Similar findings have been shown for the passage of microgels through square microchannels [96, 28, 184], however the mechanistic understanding of the phenomena is still incomplete.

Thus far this thesis has studied the fluid structure interaction of confined microgels as they enter into a one dimensional constriction. Once the microgel has entered into the constriction however, a new set of forces are applied on the particle. Moving through a region of constant confinement, the particle resists motion, and effectively adds a resistance to flow as it moves through the channel. In this chapter I move the focus away from one dimensional constrictions to instead investigate the passage of microgels through square microchannels.

Using a mixture of laminar flow and fluid structure interaction, this chapter intends to develop a model to describe the particle velocity and resistance to flow. I analyze the effect of fluid viscosity, microgel size and microgel elasticity to create as holistic a model of microgel passage as possible. To do so, I first measure the velocity and pressure drop across microgel particles within a microfluidic comparator. Due to the confinement of the microgel, the microgel nearly comes into contact with the microchannel on four sides, with only a thin layer of fluid between the microgel and microchannel, and gutters in the corners. I then split my analysis into two parts; one where fluid passes around the microgel without deforming the microgel, and a second where because of the thin fluid layer between the microgel and microchannel, the microgel is deformed from the pressures induced there. Finally I bring these two parts back together in order to suggest a hypothesis as to how the lubrication thickness changes with respect to particle confinement.

5.2 Methods

As the microgels pass through a microfluidic constricting channel, they increase the hydrodynamic resistance to flow through said channel. While in motion, the microgel interrupts the flow through the channel, forcing energy to be spent both on moving the microgel and flowing around the microgel. Effectively, for the same pressure at the inlet and outlet of the microchannel, a decrease in flow rate through the channel will be experienced when a microgel is passing through it. Due both to the brief passage of microgels through the microchannel, as well as the small overall scale, a specialized microfluidic channel is necessary to measure changes in resistance with both sufficient range and precision for the resistances added by the microgels.

5.2.1 Microfluidic Comparator: Measuring Resistance of Moving Microgels

A simple method of measuring pressure drop due to transport of bodies in a microfluidic channel is a microfluidic comparator, such as that shown in Fig. 5.1a. In effect, the resistance of a body, such as a microgel, flowing through a regular channel is compared with an identical channel without the moving body. Where the two channels meet, it is possible to compare the flow rates of each channel and calculate the resistance, noting their identical pressures, such that

$$\Delta P = Q_1 R_1 = Q_2 R_2 \quad (5.1)$$

where ΔP represents the pressure drop across the channel, Q represents the flow rate and R the channel resistance for the two (1 and 2) channels. The flow rate of the two channels is measured relatively by measuring the deflection of the streams, such as with embedded tracer particles, or by coloring the unperturbed inlet.

Several versions of comparator channels have been used in literature, including those with and without a split in the microchannel after the comparator region, and can be controlled by inlet pressure or inlet flow rate, depending upon the specific geometry [165, 166, 5, 88, 28]. In the case of this study, I opted to use a flow controlled comparator. This was done in order to avoid the need to control for any upstream effects introduced by injecting microgels into the system. Instead, the flow rate of the reference fluid and the one containing microgels are balanced and controlled, with deflection measured as microgel particles enter the second separation, see Fig. 5.1a-c. This kind of comparator also has the added benefit of not requiring device calibration to determine the inlet flow rates. Furthermore it allows for the independent control of the flow of microgels, and the carrier fluid which combine at the inlet, while precisely maintaining the balance of pressure downstream.

A resistance diagram of the comparator channels can be seen in Fig. 5.1b(iii). While the inlet resistances are included, it is only the post comparator channel resistance, R_0 and the added gel resistance, R_{gel} that are of interest to this work. As the pressure at the ink-gel mixture interface has a constant pressure, we can determine the resistance of the two channels as

$$P_c = R_0(Q + \Delta Q) = (R_0 + R_{\text{gel}})(Q - \Delta Q) \quad (5.2)$$

where P_c is the pressure difference between the comparator section, and the outlet, Q is the prescribed inlet flow rate for the ink and gel mixture channel, and ΔQ is the flow deflected away from the microgel. The channel resistance is calculated assuming a constant rectangular section and a constant viscosity, such that

$$R_0 = \alpha \frac{\mu z_{\text{ch}}}{w^2 h^2} \quad (5.3)$$

where μ is the fluid viscosity, z_{ch} the channel length, and w and h are the channel width and height respectively.

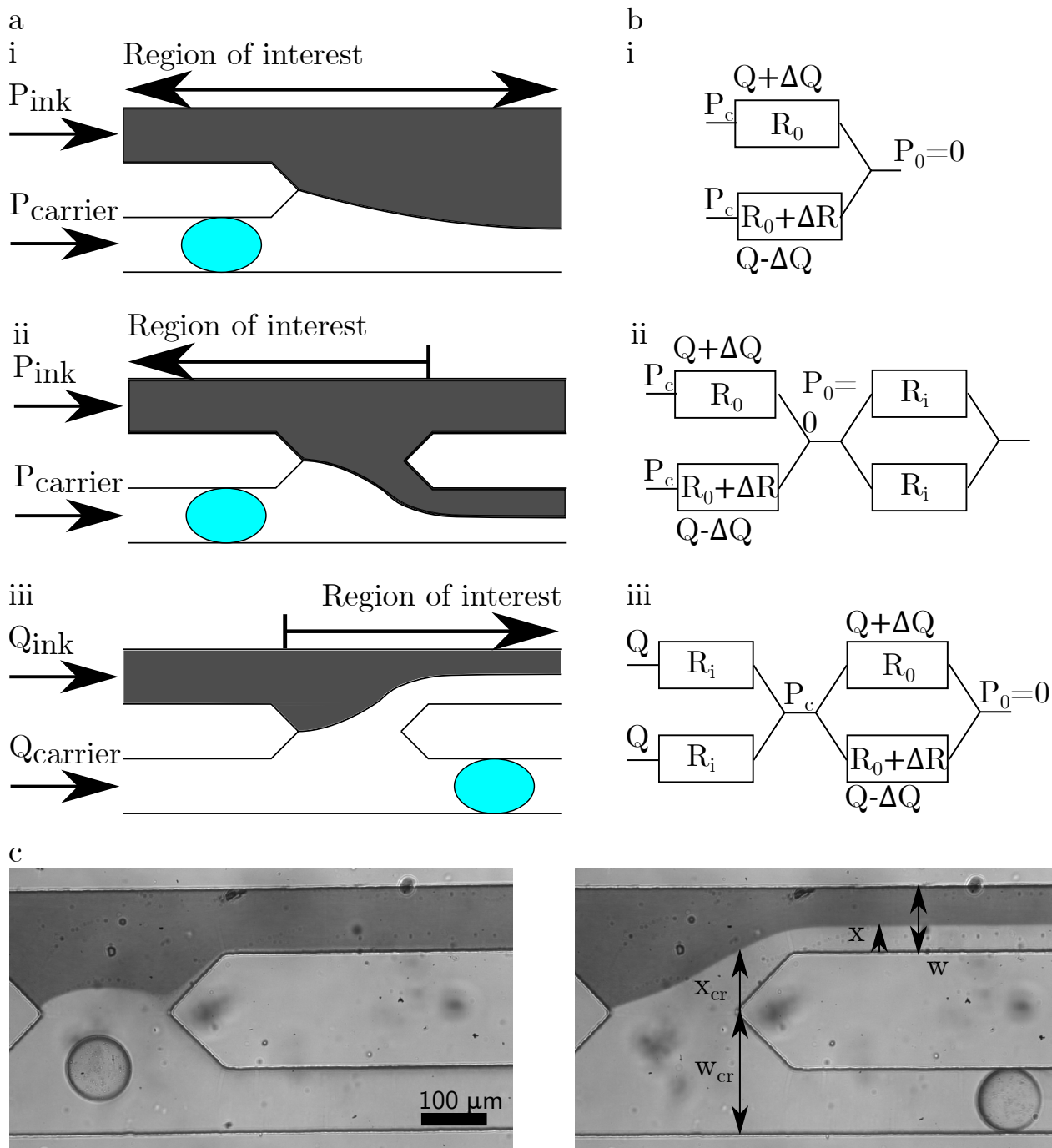


Figure 5.1: (a) Diagrams of various comparators as viewed from above. These comparators are controlled either by inlet pressure (i and ii) or by inlet flow rates (iii). Pressure controlled comparators measure the added resistance starting from the inlet, while flow driven comparators measure the resistance starting from after the comparator. The interface between the two flow streams can be read either as the streams merge towards the outlet (i) or relative to a split in the streams (ii and iii). The perturbing object (e.g. droplet or particle) is shown in blue in the test channel. The region of interest corresponds with the test channel and the comparator itself. (b) Resistance diagrams for various types of microfluidic comparators, corresponding to those in (a). (c) A micrograph of a flow driven comparator as a microgel enters into the comparator region (left), and as it passes through the comparator channel (right).

The shape factor for a rectangular channel is described in Mortensen *et al.* as a function of the aspect ratio of the channel [127, 68], w/h , such that

$$\alpha\left(\frac{w}{h}\right) = \frac{\pi^3(w/h)^2}{8} \left(\sum_{n=1,3,5,\dots}^{\infty} \left(\frac{(w/h)}{n^4\pi} - \frac{2}{\pi^2 n^5} \tanh\left(\frac{n\pi(w/h)}{2}\right) \right) \right)^{-1}. \quad (5.4)$$

In the case of a square channel, where $w = h$, this shape factor has a value of $\alpha(1) = 28.5$.

5.2.2 Measuring Flow in a Comparator

The resistance imposed by a moving particle is accompanied by a deflection in flow away from the particle in order to satisfy Eq. 5.2. As the two flows are coloured, it is possible to see the deflection, X and X_{cr} at the comparator, see Fig. 5.1c. As the flow passing through a microfluidic comparator is in the laminar regime, and typically the Stokes regime ($Re < 1$), there is minimal convective mixing present. Furthermore, for the fluid residence time in the comparator, the flow is moving faster than the rate of diffusion. This is validated simply by using the comparator without microgels present and seeing a clear interface which extends the length of the comparator to its furthest edge. With that in mind, in this experiment it was decided to use ink as the method of discerning the interface between the two inlets, as it is easily visible, while producing no fouling, nor having any measured effect on the bulk fluid viscosity.

The proportion of flow deflected at the comparator can easily be estimated by the steady state Stokes and continuity equations,

$$\mu \nabla^2 \vec{u} - \nabla P = 0 \quad (5.5)$$

$$\nabla \cdot \vec{u} = 0 \quad (5.6)$$

where \vec{u} is the fluid velocity in three dimensions. The exact solution to 5.5 for a rectangular cross section results in an infinite series expansion, however Vanapalli *et al.* suggest the use of a simplified formula described by Ismagilov *et al.* [165, 88], such that the fluid velocity in the channel is described by

$$u(x, y) = \left(1 - \left(\frac{2y}{h} \right)^2 \right) \left(1 - \left(\frac{2x}{w} \right)^m \right) \quad (5.7)$$

which describes flow velocity as independent in the \vec{x} (width) and \vec{y} (height) directions, while m is a function of the channel aspect ratio: $m = \sqrt{2}(h/w) + 0.89(w/h)$.

In the case of a deflected comparator interface, such as that shown in Fig. 5.1c, the proportion of flow can be

derived from the definition of flow rate, such that

$$\frac{\Delta Q}{Q} = \frac{\int_{-w/2}^{-w/2+x} \int_{-h/2}^{h/2} u(x,y) dy dx}{\int_{-w/2}^{w/2} \int_{-h/2}^{h/2} u(x,y) dy dx} \quad (5.8)$$

where x is the length from the inner channel wall to the ink interface, see Fig. 5.1c.

While the proportion of flow is most intuitively measured by measuring slightly downstream of the comparator, where the interface stabilizes and is described accurately by 5.7, the distances involved are often relatively small, resulting in poor accuracy when calculating $\Delta Q/Q$. To improve on this, we opted to measure the displacement of the interface from the tip of the comparator, as shown in Fig. 5.2b and described in Vanapalli *et al.* [166] when measuring the added resistance of droplets.

5.2.3 Experimental Materials and Protocol

The microfluidic comparator was first modeled using a vector graphics software (Inkscape, Inkscape Project), as shown in Fig. 5.2a. A photomask was then laser printed on an acrylic sheet (Micro Lithography Services LTD). Using the printed mask, a mold was made in SU-8 photoresist on a silicon wafer, using standard soft lithography techniques [125, 122]. Microchannel heights were verified by measuring the mold height using a scanning profilometer, measuring height at the centre and edges of the channel. A 10:1 (w/w) mix of Polydimethylsiloxane and crosslinker (PDMS, SYLGARD 184, Sigma Aldrich, Darmstadt Germany) was then poured over the mold, degassed, and baked for between 2 and 24 hours at 70°C. The PDMS microchannel was cut, had appropriate holes punched, and bonded to a glass microscope slide by plasma cleaning for 30s. Early troubleshooting indicated that microgels would be less likely to stick to the walls of the microchannel when the channel was made to be hydrophobic. To make the channel hydrophobic, before use, the channel was flooded with an electronics coating (NOVEC 1700, 3M Company, St Paul MN), and evaporated by heating the channel to 110°C for 30 min. This process was repeated for a total of 3 coatings.

The comparator in question was designed to work well with some of the microgels which had been made for work in previous chapters of this thesis. With that in mind, a main width of $w = 100 \mu\text{m}$ was selected such that the diameters of the microgels used here would range from slightly smaller, to significantly larger than the channel width. The outlet channels were separated by a total of $200 \mu\text{m}$ to aid in visually identifying the ink flow deflection. The channel height was set to $h = 95 \mu\text{m}$. Finally, the test channels have a length of $L = 2\text{mm}$, to allow for sufficient transit time and to easily identify the flow deflection. These dimensions are shown on Fig. 5.2b. Additionally, the channel has three inlets and a single outlet. The colored fluid enters in a single line, while a carrier and gel line combine upstream. This was done to allow tuning the frequency of microgels entering the comparator for easy analysis.

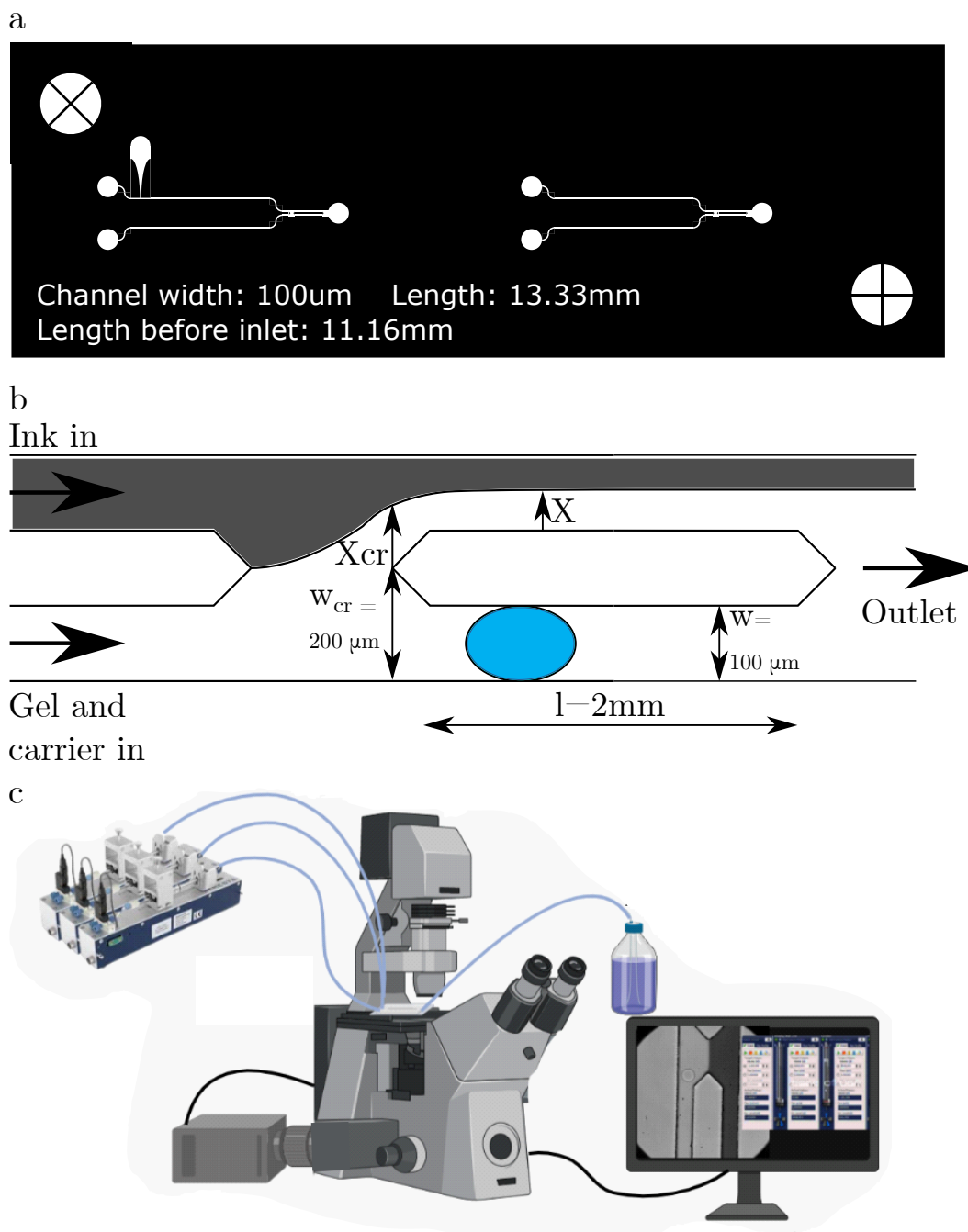


Figure 5.2: (a) The microfluidic mask used in this design, containing two different comparator channels. The principle difference between the two channels is the inclusion of a third inlet used to balance suspended gels and carrier fluid. The two inlet channel was used for measuring viscosity. The mask is shown at 2x scale. (b) An annotated diagram of the microfluidic comparator. Interface deflection measurements are indicated by X_{cr} at the comparator and X further down the channel. (c) A diagram showing the experimental setup. This includes syringe pumps, the microfluidic channel, microscope, camera, data acquisition and waste.

PEGDA % aq (v/v)	Diameter, d (μm)	Effective Elasticity, E^* (kPa)
9	85.3 ± 2.5	17.8 ± 5.1
9	104.9 ± 2.2	5.20 ± 1.20
9	124.6 ± 4.8	6.17 ± 3.33
12	97.3 ± 2.6	10.9 ± 1.7
12	108.1 ± 3.0	19.0 ± 12.8
18	109.5 ± 4.4	154 ± 125

Table 5.1: Summary of PEGDA microgels tested. All microgels were made of an aqueous solution containing 5 % (v/v) photoinitiator (2-hydroxy-2-methyl-1-phenyl-propan-1-one, Sigma Aldrich, Darmstadt Germany), contained a total of 65 % (v/v) PEG (mw 200) and PEGDA (mw 700), and 1 % SDS. Gels were photopolymerized in a flow focusing channel as described in Ch. 2. Elasticity measurements were made using the elasticity trap described in Ch. 3 ($n \geq 3$).

The layout of the experiment is illustrated in Fig. 5.2c. The microchannel was connected via 1mm OD tubing to syringes connected to a syringe pump (NEMESIS, CETONI GmbH, Korbussen Germany) which would be used to set the desired flow rates. The inlet flow rates for the ink line was set so that it would always be equal to that of the combined flows of the microgel and carrier lines. The comparator was viewed over a microscope using a high speed camera (FASTCAM SA4, Photron Europe Ltd, Buckinghamshire, GB) in order to accurately measure the speed of microgels passing by.

Poly-Ethylene glycerol (PEG) microgels were chosen for use in these experiments. A full description of their production can be found in a previous chapter, see Ch. 2. In order to control the elastic moduli of the microgels, the proportion of Poly-Ethylene glycerol Diacrylate (PEGDA) within the pre-gel mixture was varied from 6 to 18 %. The combined concentration of PEG, mw 200, and PEGDA, mw 700, was kept at a constant 65 % (v/v). The elastic moduli of the microgels was tested using a microfluidic trap, as described in a previous chapter, see Ch. 3. Diameters were measured in the microchannel where they were confined on only two sides. For $d/w < 1.4$, where $\nu < 0.4$, the diameter change perpendicular to the direction of confinement is less than 5 % as predicted by modified Tatara contact analysis [113]. A full description of the microgels tested here can be found in Table 5.1. Microgels were stored at room temperature in a solution containing 10 % sodium dodecyl sulfite (SDS, Sigma Aldrich, Darmstadt Germany) after washing and up until testing, where the solution was diluted to 1 % SDS, and was mixed with either water or aqueous glycerol.

The carrier and ink fluids were composed both of a solution containing 1 % SDS mixed in either water or a 1:1.1 water-glycerol mixture. The inclusion of SDS was done to further avoid any sticking of the microgels to the microchannel wall. The ink line was coloured by adding in 0.3 % black china ink, which was mixed and filtered through a $0.2 \mu m$ filter. This proportion was selected as it provided an visually obvious interface to measure against, while negligibly affecting the other fluid properties.

The viscosity of the SDS mixture, as well as the glycerol were measured using the microfluidic comparator, and were compared against pure water at 20C, with a viscosity of $\mu = 1mPas$. The flow rate of the compared fluid was modified against that of water until the interface between the two was precisely equal, such that $x_{cr} = 0$, see

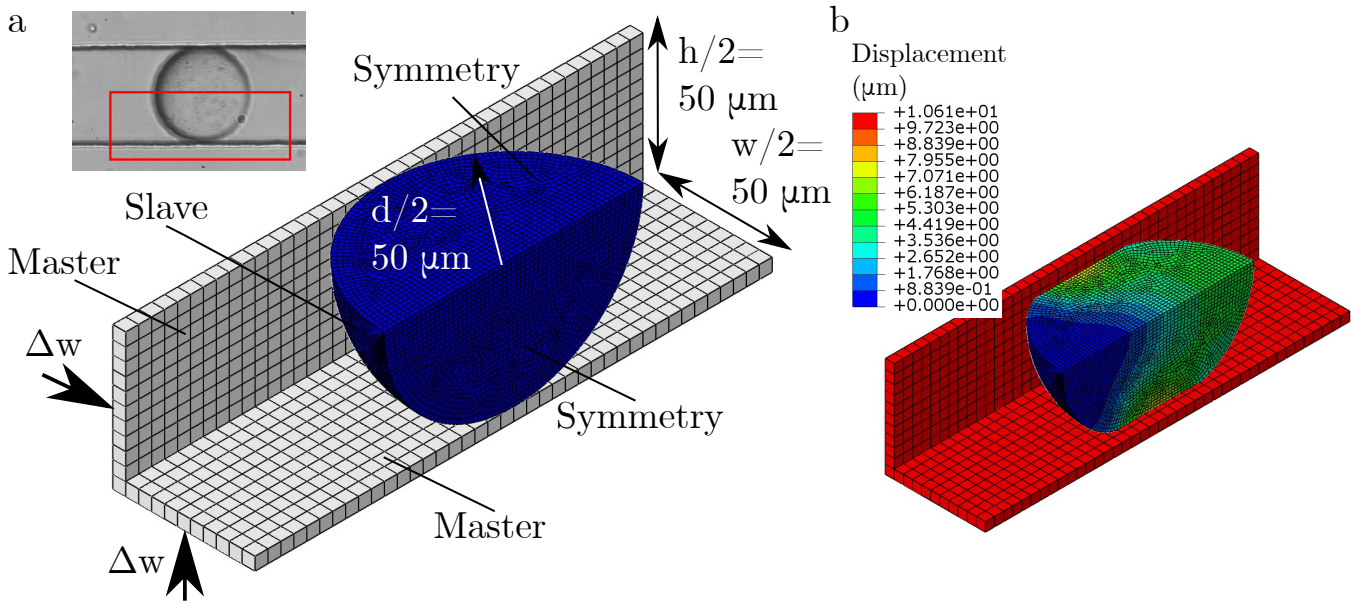


Figure 5.3: (a) A diagram showing the contact simulation between the microgel (blue) and microchannel (grey). Channel and microgel dimensions are listed, as well as the cut planes of symmetry. The master and slave designations refer to the contact declarations done for the static explicit simulation. Contact was undertaken by advancing the microchannel a distance of Δw towards the microgel. An inset highlighting the cut plane on an experimental micrograph of a moving microgel is provided for reference. (b) A deformed microgel in contact with the advancing microchannel wall. Colouring represents total displacement in order to better illustrate the deformation. The displacement of the microchannel walls corresponds with $\Delta w = 7.5 \mu\text{m}$.

Fig. 5.2b. This meant that the two comparator channels contained only their respective fluids (drastically simplifying the analysis done here). Using 5.3, and noting that the geometry of the two channels are identical, 5.2 can be rewritten in terms of only the respective viscosities such that

$$Q_i \mu_i = Q_{ref} \mu_{ref} \quad (5.9)$$

where the subscripts i and ref refer to the fluid being measured, and the reference fluid, water respectively. The viscosities of the fluids were estimated as $\mu_{SDS} = 0.001 \text{Pas}$ and $\mu_{glycerol} = 0.016 \text{Pas}$.

5.2.4 Solid and Fluid Simulation Design

A combination of fluid and solid simulations were used to help understand the mechanics of microgel transport through a square constriction channel. These simulations were undertaken separately, first estimating the solid deformation due to confinement within the microchannel, and then exporting the deformed microgel geometry to a fluid simulation to measure fluid flow around a microgel. As the microgel is travelling in an approximately square microchannel, the simulation was cut along the \vec{x} and \vec{y} axes of symmetry, see Fig. 5.3a, which both aids qualitative analysis, and also reduces computation time.

Solid simulations were performed in the ABAQUS CAE environment (Dassault Systems, Vélizy-Villacoublay,

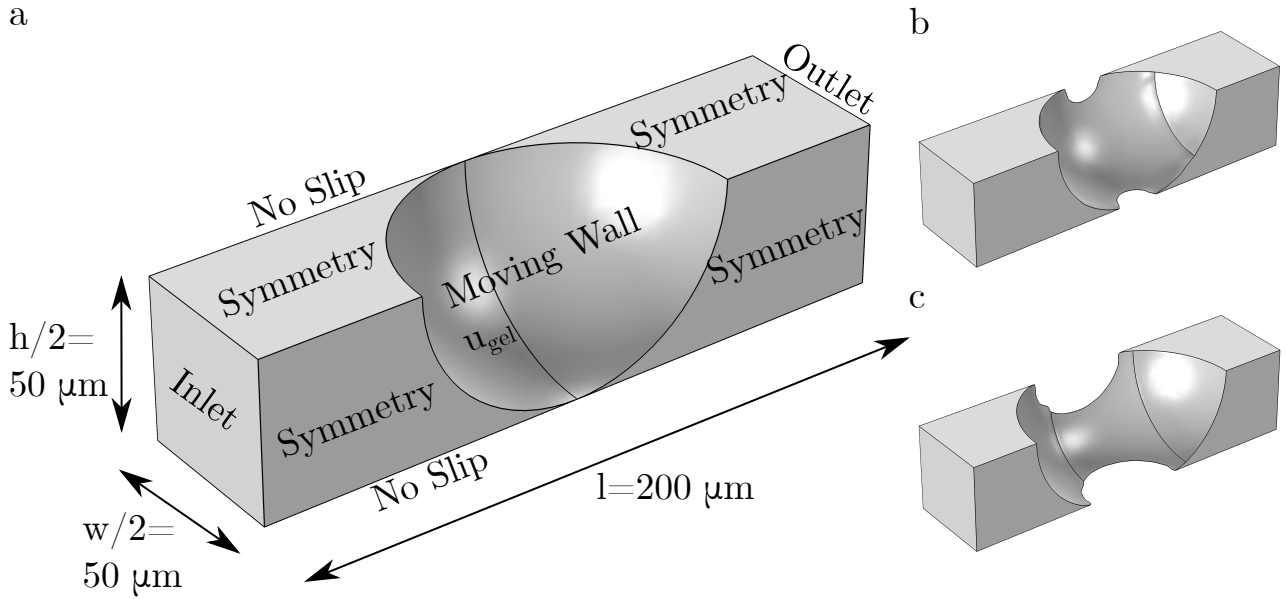


Figure 5.4: (a) A diagram outlining the model parameters for the simulated flow around the confined microgel. The domain was cut along the lines of symmetry. This microgel in particular is undeformed, i.e. $d = 100 \mu\text{m}$. The microgel surface was set to move at a constant velocity, u_{gel} , the outlet was set to a constant pressure $P = 0$ and inlet pressure was declared to correspond with pressure drop across the microgel, $P = P_{\text{gel}}$. (b) A simulated fluid domain corresponding with $d = 104 \mu\text{m}$. (c) A simulated fluid domain corresponding with $d = 115 \mu\text{m}$.

France). To measure the effect of confinement between the walls of the channel and the microgel, a microgel of constant diameter was progressively constrained by moving the channel walls towards the microgel, see Fig. 5.3a-b. The channel is set to be rigid, as in the experiments its elasticity is significantly greater than the microgels in question, with a typical Young's modulus of $E \sim 1 - 10 \text{ MPa}$ [89, 95]. As the microchannel walls were considered rigid, they were declared the master contact surface, while the microgel was declared the slave, with symmetry imposed on its cut sides. The contact simulations were done using a dynamic explicit solver.

The initial size of the microgel was set to be $h = w = 100 \mu\text{m}$, which would then decrease by Δw over the course of the simulation, see Fig. 5.3a. Meanwhile, the microgel diameter was kept at a constant $d_0 = 100 \mu\text{m}$. The simulated microgel had an elasticity of $E = 10 \text{ kPa}$ and Poisson ratio of $\nu = 0.35$, selected to be representative of a typical PEG microgel [27]. The results were then rescaled such that $w = 100 \mu\text{m}$, and d varied with confinement in order to be reflective of the experiments, i.e. $d = \frac{w}{w - \Delta w} d_0$. Other parameters, such as contacting area and force were scaled accordingly.

The Computer Aided Design (CAD) models of the deformed microgels were exported and rescaled from the solid simulation to a fluid simulation in the COMSOL multiphysics environment, (COMSOL, Grenoble, France). The fluid simulations were performed assuming laminar flow, with water as the fluid. A negative of the solid simulation was made by exporting the deformed microgel model to the fluid simulation, and subtracting it from the volume of an unoccupied microchannel. In order to overcome the numerical challenges of simulating precisely overlapping surfaces, the microgel was simulated as having been moved towards the microchannel by $0 - 0.5 \mu\text{m}$ to create a

significant overlap, see Fig. 5.4a-c. While flow through the thin layer between the microgel and the microchannel is significant to this study, this region of flow was studied separately from the rest of the fluid domain.

The fluid simulation performed here was used mainly to understand the flow through the gutters around the microgel while the microgel was moving. To do so, an inlet pressure of $P = 0.1$ kPa or $P = 0$ and outlet pressure of $P = 0$ were set for all simulations. Meanwhile, the surface of the microgel was set to be a moving wall with a velocity of $u_{\text{gel}} = 0.1$ m/s, or $u_{\text{gel}} = 0$. No slip boundary conditions were applied to all microchannel surfaces with symmetry applied appropriately on the cut planes, as shown in Fig. 5.4a.

Meshing was performed mostly ad-hoc in this work, as results could be easily validated by comparison with experimental data. In the case of the solid simulation, the mesh was seeded with a density of $1.75 \mu\text{m}$ using a standard hex-dominant mesh. In the fluid simulations, the built in COMSOL physics based mesh at normal and fine were both tested, finding no change in results.

5.3 Experimental Results

5.3.1 Microgel Velocity, Fluid Velocity and Microgel Confinement

The transport of microgels is in response to the fluid flowing around it. A series of micrographs of a sample microgel passing through the comparator and test channel are shown in Fig. 5.5a-b. As the microgel enters into the comparator, it becomes confined only by the microchannel height. While the microgel is in the comparator section, it briefly decreases the flow of the carrier, creating a "wave" of the ink, shown at $\tau = -0.035$ s. The microgel moves through the comparator relatively slowly until it reaches the entry of the test channel, where it accelerates and is pulled through the channel. Once the microgel is in the test channel, it accelerates to a steady state velocity almost instantaneously, see Fig. 5.5b. As it is the transit through the test channel constriction which is of interest here, the gel velocity is thus defined as $u_{\text{gel}} = (dz_{\text{gel}}/d\tau) |_{z_{\text{gel}} > 0}$, where $\tau = 0$ and $z_{\text{gel}} = 0$ occur when the microgel first enters the test channel. During this steady state, the interface between the ink and carrier fluids also reaches a steady state until the microgel exists the test channel downstream.

The velocity of the microgels is heavily dependant upon the fluid velocity within the test channel, see Fig. 5.5c. The microgel velocity increases approximately linearly with the mean fluid velocity, $u_{\text{fluid}} = (Q - \Delta Q)/wh$, with a mean slope of $du_{\text{gel}}/du_{\text{fluid}} = 0.95$. Fig. 5.5 also shows this trend to be independent of either fluid viscosity or microgel elasticity. The microgel velocity increases with respect to the microgel diameter. In fact, if the data is isolated to that of unconfined microgels, $d < w = 95 \mu\text{m}$, the microgel velocity is in fact greater than the mean fluid velocity. It is worth noting that fluid velocity is not evenly distributed within the channel, with a maximum fluid velocity greater than the mean. It follows that the confinement of the microgel has an effect on the velocity of the microgel, which raises the question of how the additional confinement influences the microgel velocity.

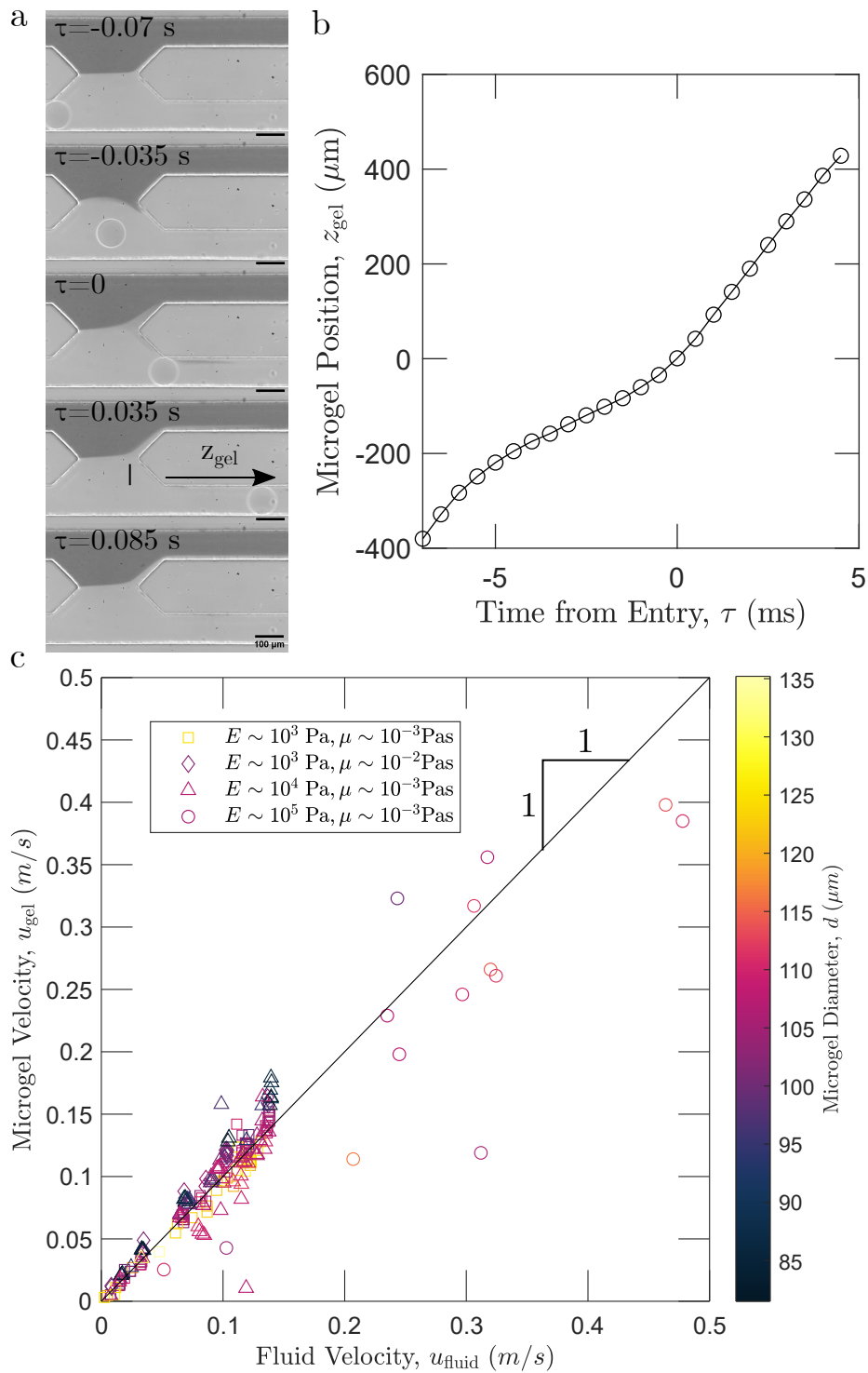


Figure 5.5: (a) Sample micrographs showing the progression of a microgel entering into the comparator region and progressing into the test channel. The microgel in question corresponds with a diameter of $d = 102 \mu\text{m}$ and an elasticity of $E^* = 5.2 \pm 1.2 \text{kPa}$. (b) The position of the microgel shown in (a) over time, relative to when the microgel enters the test channel. (c) A comparison of the velocities of microgels with the mean fluid velocity, $u_{\text{fluid}} = (Q - \Delta Q)/wh$, and microgel diameter.

5.3.2 Resistance of a Microgel in a Square Channel

The resistance of the microgel changes considerably depending upon the microgel size, increasing by several orders of magnitude, see Fig. 5.6a. At first glance, the relationship between microgel resistance and diameter may seem uncorrelated, however if the different fluid viscosities are accounted for, a more consistent trend of increasing resistance with increased diameter appears. The flow in the microchannel is laminar for all experiments, as the Reynolds number ranges from $Re = \frac{u_{\text{fluid}} \rho w}{\mu} \in (0.04, 45)$, while turbulence occurs at $Re > 2300$. For laminar flow, the resistance increases proportionately with the viscosity of the fluid, $R \propto \mu$. The resistance shown in Fig. 5.6 increases by approximately an order of magnitude, while $\mu_{\text{glycerol}}/\mu_{\text{SDS}} = 16$. The increase in resistance with increasing microgel diameter is intuitive, both because larger microgels will obstruct more flow around them, and also because more of the microgel will be in contact with the sides of the microchannel.

Unlike with viscosity, Fig. 5.6a shows the elasticity of the microgel to have a minimal impact on the resistance. This is despite the microgels elasticity spanning $E^* = 5.2$ kPa to $E^* = 154$ kPa, indicating that if the elasticity of the microgel has any effect, it is minor. Finally Fig. 5.6a shows the fluid flow rate has only a minor influence on the resistance. In general, increasing flow rates has the effect of decreasing the overall resistance.

As the flow is laminar, the added pressure drop due to the microgel can be assumed to be occurring locally to the microgel, such that

$$P_{\text{gel}} = R_{\text{gel}}(Q - \Delta Q). \quad (5.10)$$

Using this, the data in Fig. 5.6a can be transformed in terms of the pressure across the microgel, as shown in Fig. 5.6b. Again pressure increases both with microgel diameter and with carrier viscosity, with the data clustering more closely together. Still, there is considerable spread within the data. Unlike with when comparing Resistance to flow rate, the microgel velocity seems to have no clear effect on the pressure.

Normalizing the pressure by the microgel elasticity, the trends described in Fig. 5.6b become more obvious, see Fig. 5.7. Looking only at the data for the low viscosity carrier fluid, which spans a wider range of confinement, a correlation of $P_{\text{gel}}/E^* \sim (d/w)^{8.4}$ can be fitted with a coefficient of variation of $R^2 = 0.72$. It is worth noting that this fit is only to illustrate the magnitude of scaling. Meanwhile, the effect of viscosity remains constant, increasing pressure approximately ten fold.

The confinement alone however does not fully explain the drop in pressure measured. Similar to the data measured in Ch. 3 and 4, there is a wide variation in resistance. In this case however the variation in E^* of the microgels does not seem to be a likely cause, as it was shown to have a negligible influence despite fully spanning nearly 2 orders of magnitude. Regardless, by normalizing P_{gel}/E^* , any effects of elasticity are expected to be accounted for. In the case of this study, minor variations in microgel diameter are also accounted for. Finally, there is little reason to believe that the channel itself has a major impact on the data, as the process to manufacture channels should result in nearly identical surface roughness. What does change between tests however is the

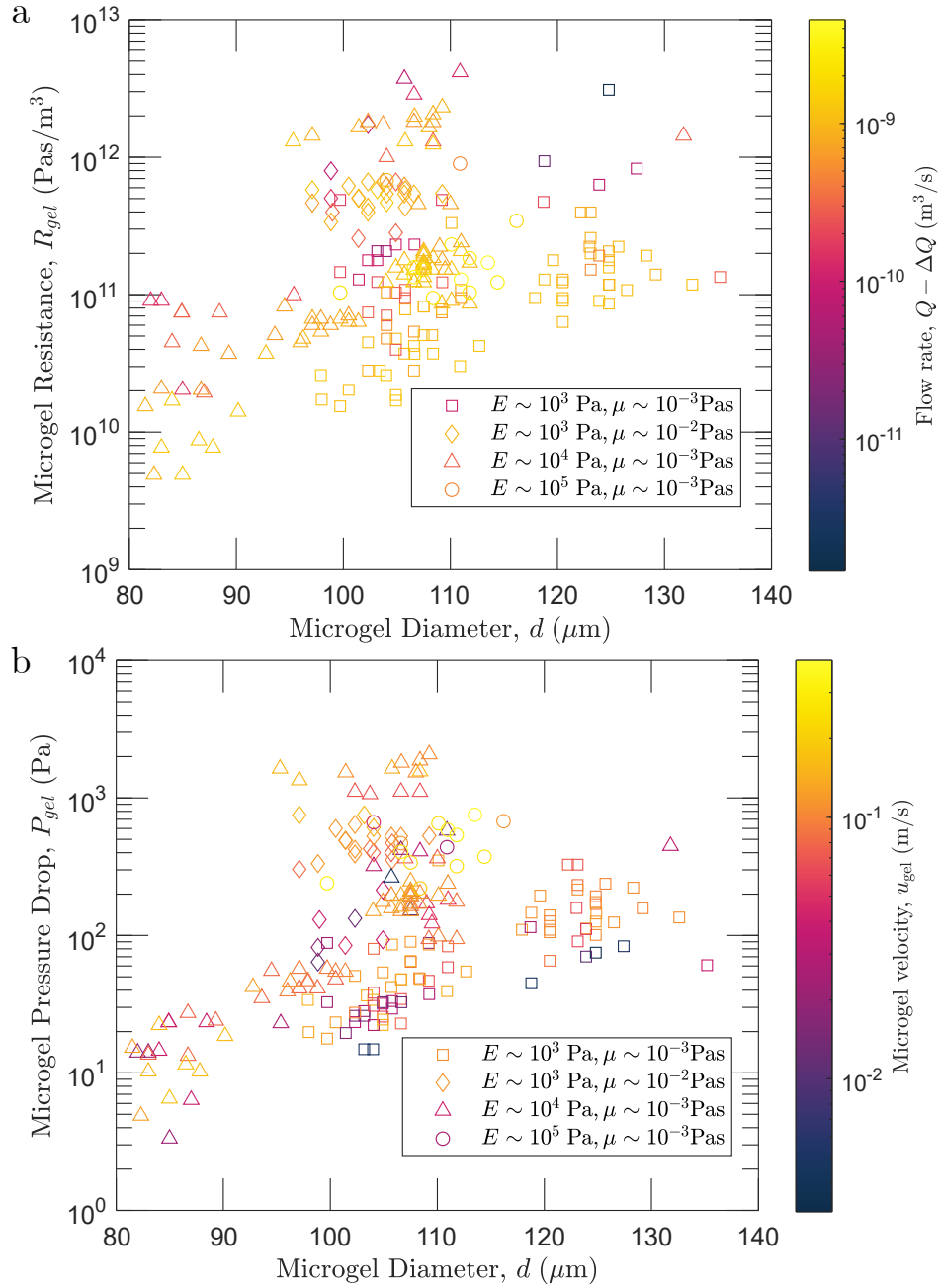


Figure 5.6: (a) A comparison of the added resistance to flow in the test channel R_{gel} with the diameter of the microgels d and the flow passing through the test channel, $Q - \Delta Q$. (b) A comparison of the pressure drop which occurs across the moving microgel, P_{gel} with its diameter, d and the microgel velocity u_{gel} . Symbols classify experiments by microgel elasticity, E^* and the fluid viscosity μ .

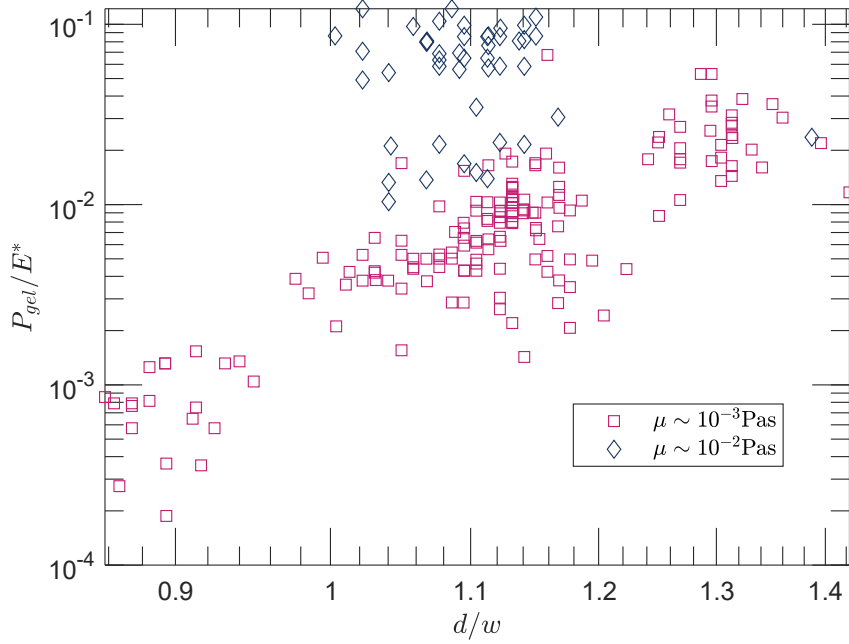


Figure 5.7: A comparison of normalized pressure drop across the microgel P_{gel}/E^* with degree of confinement, d/w . Data has been separated into that using a water solution and that using a glycerol solution.

velocity of the fluid phase and microgel, which also spans a wide range.

5.3.3 Linking Microgel Velocity and Pressure

Accounting for both confinement and pressure, Fig. 5.8 shows the how the microgel velocity changes relative to the carrier fluid velocity. Here, the trend of decreasing $u_{\text{gel}}/u_{\text{fluid}}$ with increasing confinement is made clear in light of the effect of pressure. Fig. 5.8 shows the relative velocity increase with increase in relative pressure drop. This trend also overlaps heavily with changes in viscosity, reflecting the increase in pressure with respect to viscosity shown in Fig. 5.7.

5.4 Simulated Dry Confinement of a Microgel in a Square Channel

Before analyzing the flow around a confined microgel, it is necessary to understand the deformation of the confined microgel independent of the flow. Where $P_{\text{gel}}/E^* \ll 1$, deformations of the microgel are expected to be predominantly due to the contact forces between the microgel and the microchannel wall, excepting where local pressure increases to where $P_{\text{gel}} \sim E^*$. While the deformations of a sphere contacting a flat wall are explained by Hertzian contact mechanics [14, 59, 138], the constriction of a sphere on four sides is mathematically complicated to model. Instead I opt to use numerical methods to modify the existing Hertzian contact equations.

The deformation of a microgel by constriction within a square channel was simulated by approaching a corner against a quarter section of a microgel and then rescaling such that the channel width, w , remains constant and the

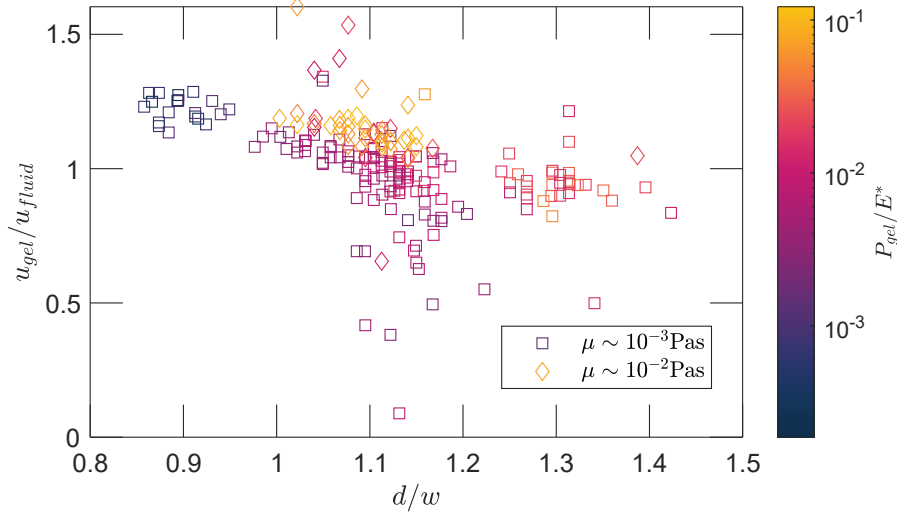


Figure 5.8: A comparison of the change in relative velocity, u_{gel}/u with changes in microgel confinement d/w , as well as the relative pressure P_{gel}/E^* .

microgel diameter, d , changes. The evolution of the deformation of a constrained microgel is plotted in Fig. 5.9a. As the microchannel moves towards the microgel, the microgel elongates in the perpendicular to the channel walls. Meanwhile, the contact area and contact pressure increases with increasing confinement.

5.4.1 Microgel Deformation

For single sided contact, where a sphere moves a distance of $l = (d - w)/2$ (corresponding to the confinement of the microgel tested here) towards a flat plane, the radius of contact is expected to scale by

$$a_{\text{Hertz}} = \frac{1}{2} \sqrt{d(d - w)} \quad (5.11)$$

such that the contact area is

$$\Lambda_{\text{ct,Hertz}} = \pi a_{\text{Hertz}}^2 \quad (5.12)$$

The contact area is compared with the equivalent microgel diameter in Fig. 5.9b, showing an quadratic relationship between Λ_{ct} and d ($R^2 > 0.99$ in all cases). To correct for the effects of confinement on four sides, a prefactor has been added such that $\Lambda_{\text{ct}} = C_{\text{ct}} \Lambda_{\text{ct,Hertz}}$. Letting C_{ct} be a power law of $(\frac{d}{w})$, the confinement correction factor is determined from the simulation for $\nu = 0.35$ as

$$C_{\text{ct}} = 1.2 \left(\frac{d}{w} \right)^{1.6}, \quad (5.13)$$

with a coefficient of determination of $R^2 = 0.99$. This fit is shown alongside the data in Fig. 5.9b.

As the simulated Poisson ratio of the microgel increases, so does the contact area. The contact area remains

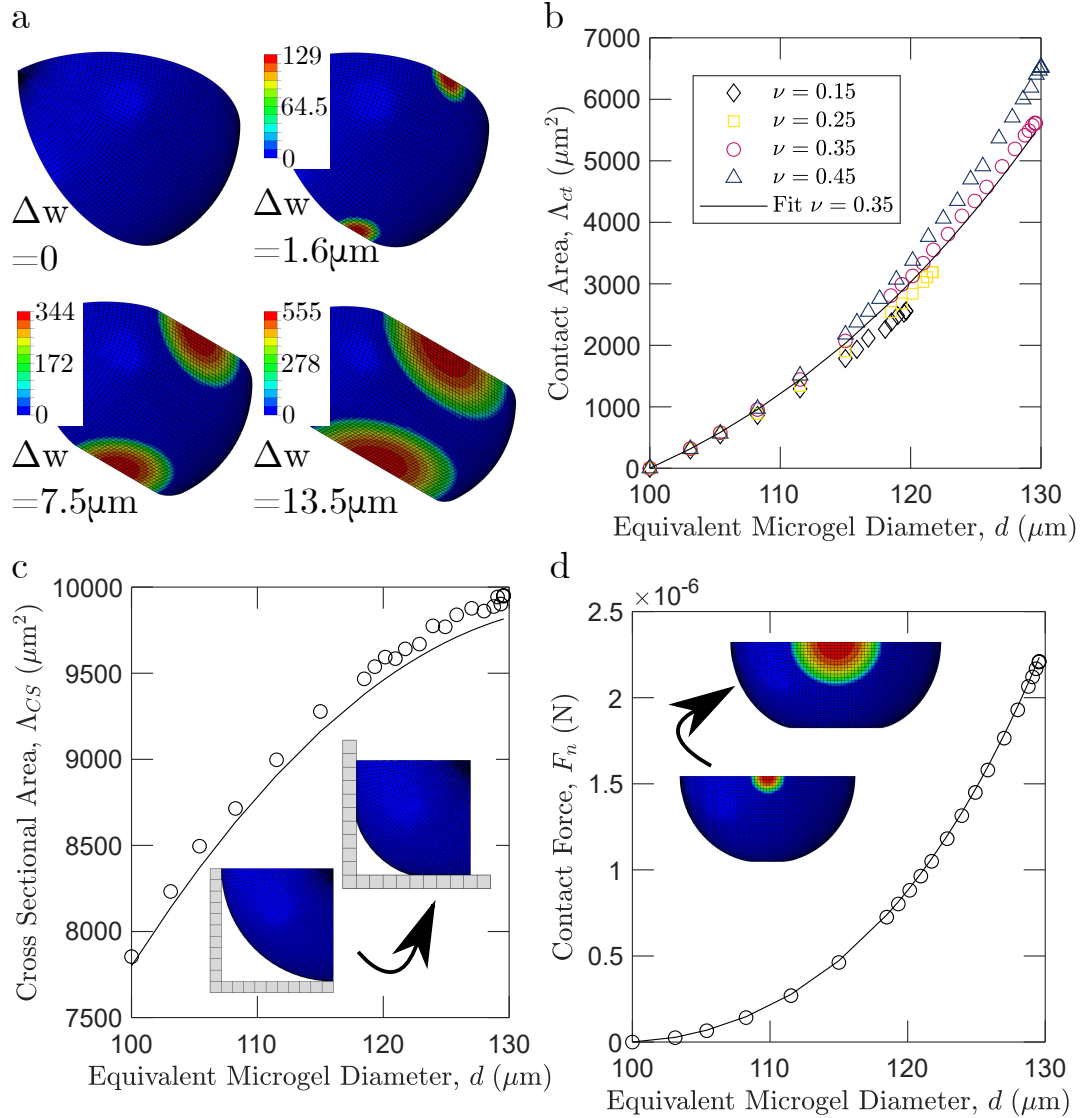


Figure 5.9: (a) The simulated contact pressure distribution across a quarter section of a microgel as the microchannel walls are moved towards the microgel by a distance of Δw . Color bars represent contact pressure, in Pa. (b) Simulated contact area as a function of the rescaled microgel diameter. The microgel diameter was rescaled such that $w = 100 \mu\text{m}$, and contact area was rescaled accordingly. A range of Poisson ratio, ν was also tested to validate the use of $\nu = 0.35$ for the model microgel. The best fit for $\nu = 0.35$ is plotted alongside the data. (c) Simulated cross sectional area as a function of rescaled microgel diameter. The microgel diameter was rescaled such that $w = 100 \mu\text{m}$, and cross sectional area was rescaled accordingly. The solid line represents the best fit described in the text. The inset shows visually the cross sectional view of the microgel. (d) Contact pressure as a function of rescaled microgel diameter. The solid line represents the best fit described in the text. The inset shows the growing area and contact pressure as confinement increases. The microgel diameter was rescaled such that $w = 100 \mu\text{m}$. Force was rescaled assuming $E^* = 1 \text{ kPa}$.

the same order however, with $\frac{\Lambda_{ct}|\nu=0.45}{\Lambda_{ct}|\nu=0.15} = 1.22$ at $d = 115 \mu\text{m}$. Because literature estimates for the Poisson ratio of PEG based gels is $\nu \approx 0.35$ [27], the numerically calculated deformation at this Poisson ratio is used for the remainder of the analysis. If the PEG gel samples made in this work do deviate from $\nu = 0.35$, it will likely not be by enough to invalidate the overall analysis, leading only to slight systematic error in the estimation of deformation and contact force.

The cross sectional area of the simulated microgel is seen in the inset of Fig. 5.9c. Unlike the contact area, the cross sectional area is not as easily predicted by simple single surface contact mechanics. It can however easily be deduced to be bounded by $\frac{\pi}{4}d^2 \leq \Lambda_{cs} \leq w^2$, as when unconfined it will simply be the cross section of an undeformed microgel, and on the other end is bounded by the confining microchannel. The simulated cross sectional area was fit to the microgel confinement such that,

$$\Lambda_{cs} = w^2 \left(-1.55 \left(\frac{d}{w} \right)^2 + 4.24 \left(\frac{d}{w} \right) - 1.91 \right), \quad (5.14)$$

with a coefficient of determination of $R^2 > 0.99$. One prediction from this fit is that beyond $d/w = 1.33$, the microchannel is expected to be entirely clogged, i.e. $\Lambda_{cs} = w^2$. Beyond this confinement, the cross sectional area must be assumed to be $\Lambda_{cs} = w^2$. This effectively limits the range where modeling flow around the microgel separately from the lubricating layer, as at $d/w > 1.33$ the gutters through which flow can pass outside of the lubricating contact region are negligible.

5.4.2 Contact Force on a Confined Microgel

As the microgel becomes more confined and the contact area grows, so does the contact pressure, and therefore so does the force acting on the microgel from the microchannel. Returning to the contact of a sphere and a flat surface, Hertzian contact mechanics predicts that the force grows with the displacement, $(d - w)/2$ as

$$F_{n,\text{Hertz}} = \frac{1}{3} E^* d^{1/2} (d - w)^{3/2}. \quad (5.15)$$

To account for the confinement however, a correction factor based on the confinement is added such that $F_n = C_n F_{n,\text{Hertz}}$. This correction factor is empirically fit as a power law of the confinement such that

$$C_n = 1.2 \left(\frac{d}{w} \right)^4 \quad (5.16)$$

with a fit of $R^2 > 0.99$. The choice of power law was made purely to simplify analysis.

To summarize, in order to the motion of and fluid flow around a confined microgel, it is necessary to understand the deformation of the microgel independent of fluid forces, due to the confinement itself. Specifically, this simulation

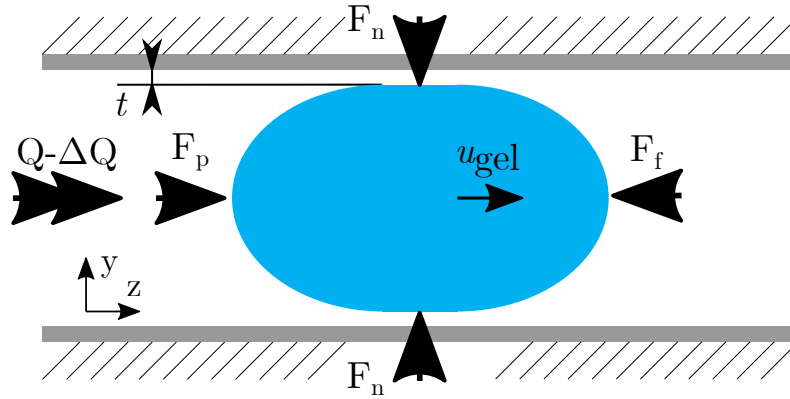


Figure 5.10: The forces on a microgel during steady state transit through a test channel. At steady state, the frictional F_f and pressure driven F_p forces are balanced. The compressive forces due to confinement and fluid pressure, F_n are balanced with themselves. The direction of fluid flow and microgel motion are indicated. The lubrication layer is approximated by the height t . Due to the approximately square geometry of the microchannel, the force balance is the same from the top and side of the microgel.

was used to measure the contact area between the microgel and microchannel, Λ_{ct} , the cross sectional area of the microgel in the direction of the microchannel, Λ_{cs} , and the contact force of the microgel pressing on the microchannel, F_n . In the case of Λ_{ct} and F_n , the simulation results were compared with those predicted by Hertzian contact mechanics, and an empirical prefactor was included. These prefactors were fit to a power law to simplify analysis later in this study.

5.5 Forces Balance of a Confined Microgel

A free body diagram of the microgel in the test channel, see Fig. 5.10, identifies three main forces acting upon the microgel: force due to pressure, F_p , a frictional force counter the direction of pressure, F_f , and the normal contact forces between the microgel and its container, F_n . As the microgel is moving at a steady state (see Fig. 5.5b), it can be assumed that these forces are in equilibrium, i.e. $F_f = F_p$. In both perpendicular directions to the motion of the microgel, the normal force is equated with itself.

5.5.1 Pressure Force

In the case of force moving the microgel, it is reasonable to assume that pressure is the only factor at play for a number of reasons. First, the microgel is moving at roughly the same speed as the the mean fluid velocity. Given that $d/w > 0.8$, the mean velocity of the streamlines which intersect with the microgel must also be nearly that of the overall mean flow rate. Secondly, the flow in the microchannel is laminar, $Re < 45$. While this is outside the regime of Stokes flow, it is still distinctly laminar, and as such turbulent effects are not expected to have any influence on the experiment. Finally, as the microgel is small and moving horizontally, there are no gravitational effects on the

microgels motion. With all of this in mind, the force due to pressure can be approximated by

$$F_p = \Lambda_{cs} P_{gel}, \quad (5.17)$$

where Λ_{cs} is the cross sectional area of the microgel in the microchannel. The specific size of this area will depend upon the microgel geometry within the confinement.

5.5.2 Normal Force

The normal force acting upon the microgel comes from two sources. The first is the constriction of the microgel by the channel. As the microgel is considerably softer than the microchannel (For PDMS $E^* \sim 1 - 10$ MPa [89, 95]), deformation due to contact is expected to be almost entirely localized in the microgel. For small two sided sandwiching contact, the normal force is expected to scale as $F_{n,Hertz} \propto E^* d^{1/2} (d-w)^{3/2}$ per conventional Hertzian contact mechanics [14]. In case of these experiments however, there is contact on four sides of the microgel, which will change the the distribution and magnitude of force. This is corrected using the simulation of dry contact performed above, combining Eqs. 5.18 and 5.16 such that

$$F_n = C_n F_{n,Hertz} = 0.3 \left(\frac{d}{w} \right)^4 E^* d^{1/2} (d-w)^{3/2}. \quad (5.18)$$

The second component of the normal force acting on the microgel comes from the fluid phase. Both the pressure drop across the microgel, and the ambient pressure will deform the microgel within the microchannel. The magnitude of this component of the normal force is expected to be much smaller than the normal force due to dry contact. The first reason for this is because in almost all experiments $\frac{P_{gel}}{2E^*} \ll 0.1$, resulting in only minor deformation of the microgel. Secondly, evidence of deformation on the scale of contact deformation would be visible on the micrographs, showing a gap between the microgel and microchannel, which is not visible for the confined microgels tested.

The pressure is not distributed evenly around the microgel. In addition to the pressure drop occurring across the body of the microgel, the motion of the microgel will also affect the pressure, especially where the microgel surface is close to the channel wall. Simplifying flow to the Stokes Regime (although the same holds true for intermediary laminar regimes as well), the local pressure gradient is solved using Eq. 5.5 such that $dP/dz \sim d^2u/dx^2$. Assuming now slip flow however, where the microgle and channel approach, the velocity difference remains constant $\Delta u = u_{gel}$, while the space between the microgel and microchannel Δx approaches 0. This in turn means that the pressure in this region approaches infinite on front side of the microgel and decreases equally at the rear, which is obviously non-physical. To remedy this, a lubricating fluid of thickness t occurs, as shown in Fig. 5.10. This lubricating layer balances the pressure within the fluid with the deformation of the microgel away from the wall. Meanwhile, because

this thickness is small, at least too small to measure using this experiments micrographs ($t \leq 2 \mu\text{m}$), the normal force applied to the microgel is expected to only increase slightly from that of dry contact.

5.5.3 Friction Force

This lubricating layer is also the primary source of friction. Noting that shear stress is defined as $\sigma = \mu \partial u / \partial x$, the greatest shear stress acting on the microgel will be localized at the lubricating region. As the microgel is moving at a $u_{\text{gel}} \approx u_{\text{fluid}}$, on most of the surface of the microgel σ will be small. The exception is in the vicinity of where the microgel nearly contacts the microchannel. In this region, because the fluid thickness is small, the lubrication approximation can be applied. In this case, $\partial u / \partial x \approx u_{\text{gel}} / t$. With this in mind, the frictional force can be approximated by

$$F_f \approx 4 \int_{\Lambda_{\text{ct}}} \sigma d\Lambda = 4 \int_{\Lambda_{\text{ct}}} \frac{\mu u_{\text{gel}}}{t} d\Lambda, \quad (5.19)$$

where Λ_{ct} is the area of contact between the microgel and microchannel, noting that there is contact on four sides of the microgel.

5.5.4 Analysis of Gutter and Lubrication Domains

Having identified the forces at play on the microgel, we can relate the pressure to the microgel velocity by $F_f = F_p$ such that

$$P_{\text{gel}} \Lambda_{\text{cs}} = \frac{4\mu u_{\text{gel}} \Lambda_{\text{ct}}}{\bar{t}}, \quad (5.20)$$

noting that \bar{t} is a surface averaged lubricating thickness such that $\bar{t}^{-1} = \int_{\Lambda_{\text{ct}}} \frac{1}{t} d\Lambda$ this is intended to account for any variation in the thickness, be it from roughness or changes in pressure. This relates the microgel velocity to the pressure drop across the microgel, however the fluid-structure interaction giving rise to the lubricating thickness remains unexplained. Additionally, while this does link P_{gel} to u_{gel} , the resistance of the microgel is not fully explained, as $R_{\text{gel}} = P_{\text{gel}} / (Q - \Delta Q)$. Therefore, an additional model between the flow rate, or equivalently u_{fluid} needs to be established with P_{gel} and u_{gel} .

One strategy for modeling this scenario is to separate the problem into two domains. First, P_{gel} is related to u_{gel} by investigating the frictional effects in the lubricating regions of the microgel, bounded by Λ_{ct} . Noting that the volume bounded by $\Lambda_{\text{ct}} \times \bar{t}$ is expected to be small, and that fluid velocity in the lubrication regime will have a mean velocity of $\frac{1}{2} u_{\text{gel}}$, the flow in this region can be assumed to only minimally effect the overall flow around the microgel, except by changing u_{gel} and P_{gel} . Therefore, for the fluid domain outside of the lubricating regime, the overall flow can be reconstructed in reverse, by combining the effects of u_{gel} and P_{gel} to arrive at a mean fluid velocity, u_{fluid} .

5.6 Flow Through Microgel Gutters

An additional use of the deformed microgels found by simulation is having a complete three dimensional CAD model of the confined microgel body. Exporting the CAD models to fluid simulation, it is possible to evaluate the flow around the deformed microgels. Flow streamlines around a sample microgel can be seen in Fig. 5.11a. The microgel in question is moving at a velocity of $u_{\text{gel}} = 0.1 \mu\text{m/s}$, with a pressure drop of $P_{\text{gel}} = 100 \text{ Pa}$, which is within the range of experimental velocities and pressures. This is essentially looking at the problem in reverse, by establishing the fluid flow rate as a function of the microgel pressure drop and velocity, instead of the flow rate causing the pressure and microgel velocity.

The pressure and velocity of the microgel both influence the flow velocity. In order to analyse this link, it is necessary to separate the problem into its pressure driven part, and its velocity driven part. Then, having analyzed the relationship between P_{gel} and u_{fluid} , and u_{gel} and u_{fluid} independently, the two can be recombined using superposition. This is reminiscent of analysis of Couette-Poiseuille flow, although strictly speaking the velocity induced flow from the microgel is not Couette flow, as flow is not simply induced from shear between the microgel and fluid. The superposition is illustrated in Fig. 5.11a.

The assumption of superposition was validated by measuring the simulated flux at the channel outlet for flow induced by both P_{gel} and u_{gel} and comparing it with Poiseuille flow, and Couette-like flow. The results of that analysis are that $Q_{\text{sim}}(P_{\text{gel}} = 100 \text{ Pa}, u_{\text{gel}} = 10 \text{ mm/s}) = 3.2 * 10^{-11} \text{ m}^3/\text{s}$, while the Poiseuille flow case resulted in $Q_{\text{sim}}(P_{\text{gel}} = 100 \text{ Pa}, u_{\text{gel}} = 0) = 1.1 * 10^{-11} \text{ m}^3/\text{s}$, and the Couette-like flow resulted in $Q_{\text{sim}}(P_{\text{gel}} = 0, u_{\text{gel}} = 10 \text{ mm/s}) = 2.1 * 10^{-11} \text{ m}^3/\text{s}$. When comparing the scenarios, the superposition is validated as $Q_{\text{sim}}(P_{\text{gel}} = 100 \text{ Pa}, u_{\text{gel}} = 10 \text{ mm/s}) \approx Q_{\text{sim}}(P_{\text{gel}} = 0, u_{\text{gel}} = 10 \text{ mm/s}) + Q_{\text{sim}}(P_{\text{gel}} = 100 \text{ Pa}, u_{\text{gel}} = 0) = 2.1 * 10^{-11} \text{ m}^3/\text{s}$.

The relative influences of P_{gel} and u_{gel} on $u_{\text{fluid}} = Q_{\text{sim}}/w^2$ can be seen in Fig. 5.11b with respect to degree of confinement. Because u_{fluid} is expected to scale differently for pressure driven and velocity driven flow, it is normalized differently for the two cases. In the case of velocity driven flow, the reference velocity is simply the microgel velocity, $u_0 = u_{\text{gel}}$. In the case of pressure driven flow, the flow rate is expected to follow the Poiseuille equation, scaling linearly with the pressure drop imposed, therefore the reference velocity is set at $u_0 = \frac{P_{\text{gel}}}{R_0 w^2}$. The reference resistance is simply the resistance of an empty microchannel, $R_0 = 28 \frac{\mu\text{zch}}{w^4}$.

While the influence of P_{gel} on u_{fluid} decreases with increasing d/w , the influence of u_{gel} increases, see Fig. 5.11b. In both cases, the trends also taper off as d/w approaches 1.3, at which point u_{gel} is almost entirely responsible for u_{fluid} . Recalling that for $d/w = 1.33$, the microchannel is expected to be completely obstructed, this bounding case is to be expected. Beyond this point, there is no space for flow to pass around the microgel, excepting flow through the pores of the microgel which are neglected here, meaning that $R_{\text{gel}} \rightarrow \infty$. Meanwhile, a simple mass balance shows that $u_{\text{fluid}} = u_{\text{gel}}$, which is what is shown as $d/w \rightarrow 1.3$.

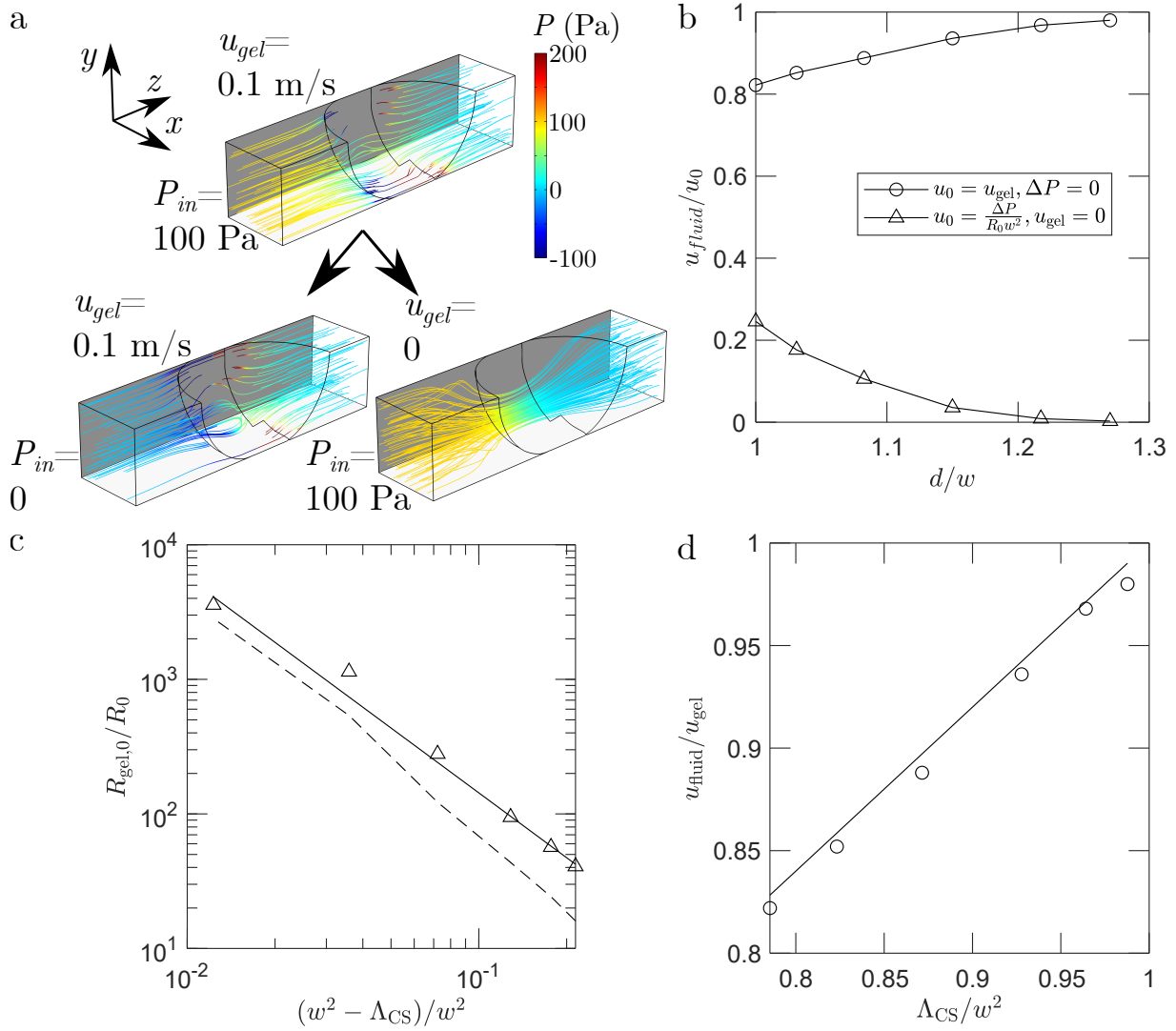


Figure 5.11: (a) A sample superposition of Poiseuille flow and Piston-Couette flow around a deformed microgel. The microgel in question corresponds with $d/w = 1.08$, $\nu = 0.35$. (b) The relative mean fluid velocity as a function of microgel confinement for Poiseuille and piston-Couette flow. The reference velocity, u_0 is the microgel velocity for piston/Couette flow and the mean velocity in an empty microchannel for Poiseuille flow. (c) The simulated relative resistance, $R_{gel,0}/R_0$, compared with the minimal relative fluid cross sectional area, $1 - \Lambda_{cs}/w^2$. The reference resistance is that of an empty microchannel, $R_0 = 28 \frac{\mu z_{ch}}{w^4}$. The dashed line represents the scaling law predicted by integrating the resistance over an approximation of the microgel body. The solid line represents the best fit described in the text. (d) The mean fluid velocity relative to the microgel velocity, u_{fluid}/u_{gel} with the occlusion of the the microchannel by the microgel, Λ_{CS}/w^2 . The solid line represents the best fit described in the text.

5.6.1 Pressure Driven Flow

In the case of pressure driven flow across the microgel, we suppose that resistance from the microgel obstruction is geometric. For Poiseuille flow through a tube-like geometry, where the cross section changes gradually, the resistance can be described by

$$R \approx \int_{z_{ch}} \frac{\mu\alpha(z)dz}{\Lambda_{cso}(z)^2} \quad (5.21)$$

where the shape factor α in this case is unique to the shape of the outlet [26]. The solution to Eq. 5.21 in the gutter R_{cso} and end caps of the deformed microgel, R_{dome} can be found in Appendix A. The sections of the microgel occur in series.

The minimal cross sectional area through which flow can pass in these experiments is given by $w^2 - \Lambda_{cs}$, and the resistance to flow around a deformed microgel is plotted alongside it in Fig. 5.11c. The simulated resistance was calculated by measuring the outlet flow, and comparing it with pressure, such that $R_{gel0} = (P_{in} - 0)/Q_{sim}$. Fitting to a power law, the simulated resistance scales with respect to this empty cross sectional area as

$$\frac{R_{gel,0}}{R_0} = 3.6 \left(1 - \frac{\Lambda_{cs}}{w^2}\right)^{-1.6}, \quad (5.22)$$

with a coefficient of determination of $R^2 = 0.98$, see fig. 5.11. This can be compared with the theoretical results described in Eq. A.7, where the minimal theoretical cross sectional area is given by $1 - \Lambda_{cs}/w^2 = (1 - \pi/4)(1 - a/w)^2$. Fig. 5.11c shows the predicted $R_{gel,0}$ to be underestimated compared with the simulation results, particularly at small Λ_{cs} , *i.e.* minimal constrictions. In general both the simulation and best fit are in agreement with the resistance predicted by Eq.A.7. Where discrepancies do exist, it is likely due more to the approximations used to calculate the theoretical friction, *i.e.* simplifying the microgel geometry.

5.6.2 Boundary Velocity Driven Flow

Neglecting the effects of Poiseuille flow, the effect of microgel velocity on fluid velocity can be studied in isolation. In effect, the microgel is a combination of pushing flow forward, what I call here piston flow, and Couette flow which occurs in the space between the microgel and the microchannel walls. The piston flow is simply the displaced fluid from the microgel volume, *i.e.*

$$Q_{piston} = u_{gel}\Lambda_{cs}. \quad (5.23)$$

As mentioned above, this implies that in the extreme case where $\Lambda_{cs} = w^2$, a simple mass balance necessitates that $u_{fluid} = u_{gel}$. Conversely, if the particle were negligibly small, the impact of its cross section on flow would also be negligible, and the particle would behave like a streamline tracer.

Meanwhile, Couette flow occurs in the gutters around the microgel, where shear from the microgel surface pulls

fluid along. In the case of Couette flow, the flow can be found by solving the Stokes equation over the domain of the gutter around the microgel at its minimal cross section. While the exact solution to this is beyond the scope of this work, it is possible to estimate the scaling of this Couette flow. Using the same assumption as in the analysis of Poiseuille flow, that the corner takes the shape of $\Lambda_{\text{cso}}(d = w) = w^2 - \Lambda_{\text{cs}}$. Couette flow through a scaled geometry will scale with respect to the moving surface velocity, such that $u(x, y) \propto u_{\text{gel}}$. Furthermore, the total flow rate through this section can be expected to scale linearly with the $\Lambda_{\text{cso}}(d = w)$, such that

$$Q_{\text{piston}} = C_{\text{piston}} u_{\text{gel}} (w^2 - \Lambda_{\text{cs}}), \quad (5.24)$$

where C_{piston} is constant relating to the solution of Couette flow through Λ_{cso} . This solution is achieved where the curved boundary of Λ_{cso} (corresponding to the microgel) is in motion, and the flat surfaces (corresponding to the microchannel) are static.

Combining the Couette and Piston flow from Eqs. 5.23 and 5.24, we have a description of the Couette/Piston flow such that

$$\frac{u_{\text{fluid}}}{u_{\text{gel}}} = C_{\text{piston}} + (1 - C_{\text{piston}}) \frac{\Lambda_{\text{cs}}}{w^2}. \quad (5.25)$$

The mean fluid velocity is compared with the simulated microgel cross sectional area in Fig. 5.11d. Here a linear relationship between the obstructive area and flow velocity is established, such that

$$\frac{u_{\text{fluid}}}{u_{\text{gel}}} = 0.8 \frac{\Lambda_{\text{cs}}}{w^2} + 0.2, \quad (5.26)$$

with a coefficient of determination of $R^2 > 0/99$. This is in good agreement with the theory described in Eq. 5.25, which predicts a linear relationship between u_{fluid} and Λ_{cs} . It also effectively numerically solves for $C_{\text{Couette}} = 0.2$.

5.6.3 Superposition of Flow

In both the Poiseuille flow case, and the piston/Couette flow, the flow rates are found to be functions of Λ_{cs} . By imposing laminar flow superposition, it is possible to estimate the combined effect of these two flow regimes on the flow around the moving microgel. By combining Eqs. 5.22 and 5.26, noting that $Q = P/R$ and $u_{\text{fluid}} = Q/w^2$, the mean flow past the microgel is estimated by

$$u_{\text{fluid}} = u_{\text{Poiseuille}} + u_{\text{piston}} = u_{\text{gel}} \left(0.2 + 0.8 \frac{\Lambda_{\text{cs}}}{w^2} \right) + \frac{P_{\text{gel}}}{3.6 w^2 R_0 \left(1 - \frac{\Lambda_{\text{cs}}}{w^2} \right)^{-1.6}} \quad (5.27)$$

The predicted and experimental u_{fluid} are plotted against one another in Fig. 5.12. The model and data are in good agreement with $R^2 = 0.91$, which is notable given the several orders of magnitude the data spans. The trend

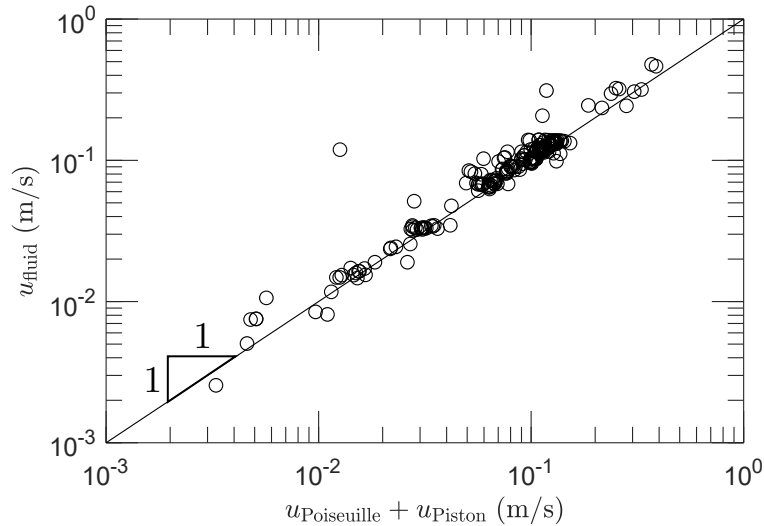


Figure 5.12: A comparison of the fluid flow predicted by superposition of the Poiseuille flow past a static microgel and the piston/Couette flow from a moving microgel, with the experimental fluid flow rate. A unity line is provided for reference.

shown in Fig. 5.12 holds for data beyond $d/w = 1.33$ as well. Recalling again Fig. 5.8, beyond this point the range of $u_{\text{gel}}/u_{\text{fluid}}$ approach unity, with the general decreasing trend with respect to d/w tapering off.

There is a slight under prediction of the data shown in Fig. 5.12. The model constructed to predict fluid flow here only considers flow through the gutters, and neglects any flow through the lubrication domain. This unaccounted for flow may represent fluid passing through the lubricating domain rather than the microgel gutters. The good agreement between data and the model however does validate the assumption that flow through the lubricating region is small compared with the total flow.

Using a combination of modeling and fluid simulations, in this part of the chapter, I have been able to link the pressure and velocity of the a moving microgel with the fluid flow around it. This was done by employing superposition of the Poiseuille flow around a static microgel, with the Couette-piston flow induced by the microgel motion. This model has been compared with experimental data and found a good fit. The question remains however, what relates the pressure drop across the microgel with the microgel velocity? Put in other words: what is the effect of lubricating friction on the motion of the microgel?

5.7 Flow in the Lubricating Layer

In order to describe the pressure drop across the microgel, P_{gel} , with the velocity of the microgel, u_{gel} , it is necessary to return to the lubrication region of flow. This region is approximated by the area of dry contact between the microgel and the microchannel, Λ_{ct} , with a local thickness of t . Using the force balance illustrated previously in Fig. 5.10, and noting that the microgel is moving at a steady state, it can be assumed that the pressure and friction forces are in equilibrium: $F_f = F_p$. Using this equilibrium, and recalling the calculations of F_p and F_f from Eq. 5.19 and 5.17

respectively, the link between P_{gel} , u_{gel} and t is made explicit by Eq. 5.20. It follows therefore that in order to fully describe the motion and pressure of a microgel, it is necessary to understand the friction force of the microgel, and how that changes with respect to u_{gel} .

5.7.1 Friction and Lubrication

The experimental friction on acting on the microgel can be seen plotted against the confinement force and a viscous velocity parameter, μu_{gel} in Fig. 5.13a. It is worth pointing out that because $F_n(d < w) = 0$, data for unconfined microgels is omitted here. The friction force increases both with respect to F_n and also with respect to μu_{gel} . With respect to F_n , the increase in friction is reminiscent of dry linear friction, however when controlling for μu_{gel} , the scaling is nonlinear. Accounting for μu_{gel} , and approximate fit of friction gives $F_f \sim F_n^{\approx 1/2}$. The factor μu_{gel} is compared as it is proportional to the shear stress between the microgel and microchannel. It follows that the frictional force increases with the shear factor, as in simple Reynolds lubrication, $F_f \sim \mu \Delta u = \mu u_{\text{gel}}$. Of the other hypothesized components of F_f from Eq. 5.19, influence of Λ_{ct} is not shown here. Both Λ_{ct} and F_n are functions of d/w , see Eqs. 5.11 and 5.15, indicating the effects of Λ_{ct} will be made redundant by the inclusion of F_n .

The component of friction not accounted for in Fig. 5.13a is the thickness of the lubricating layer, \bar{t} . This is compared naively with the size and velocity of the moving microgel in Fig. 5.13b. Below confinement, $d < w$, the lubricating thickness can be inferred to scale with the minimal distance between the microgel and microchannel, *i.e.* $\bar{t} = \frac{1}{2}(w - d)$. When confined, the thickness of this lubricating layer is generally considerably smaller than the microchannel, $\bar{t} < 4 \mu\text{m}$, with most data being one to two order smaller. Some values exceed the limit $\bar{t} = 2 \mu\text{m}$ for visibility under the microscope, however this is simply a mean value, meaning the actual detachment from the wall may appear as merely a decrease in Λ_{cs} , and even at $\bar{t} = 4 \mu\text{m}$ visible detachment between microgel and microchannel will be difficult to identify from the present micrographs. Additionally, the magnitude of the measured lubricating thicknesses are in agreement with similar experiments performed by Khan *et al.* [96], which shows the estimated lubrication thickness for a channel of width $w \approx 10 \mu\text{m}$ to be $0.1 \mu\text{m} < \bar{t} < 1 \mu\text{m}$ for microgels compressed at $1 < d/w < 1.1$.

Fig. 5.13b shows that with the exception of unconfined microgels, there is no obvious correlation between \bar{t} and d . This is contrary to experiments performed in Khan *et al.* [96], which showed an exponential decrease in lubricating thickness with respect to d/w . This may reflect the experimental setup taken, as in those experiments, P_{gel} was kept constant, varying u_{gel} , while here both variables change along with confinement. In Fig. 5.13, the lubrication thickness does have a weak trend of increasing with increasing microgel velocity, which is here independent of confinement.

The friction due to the microgel, F_f is shown to be dependant upon both the normal contacting force F_n and the viscous velocity, μu_{gel} . Meanwhile, using the same methodology, there seems to be only a weak correlation between

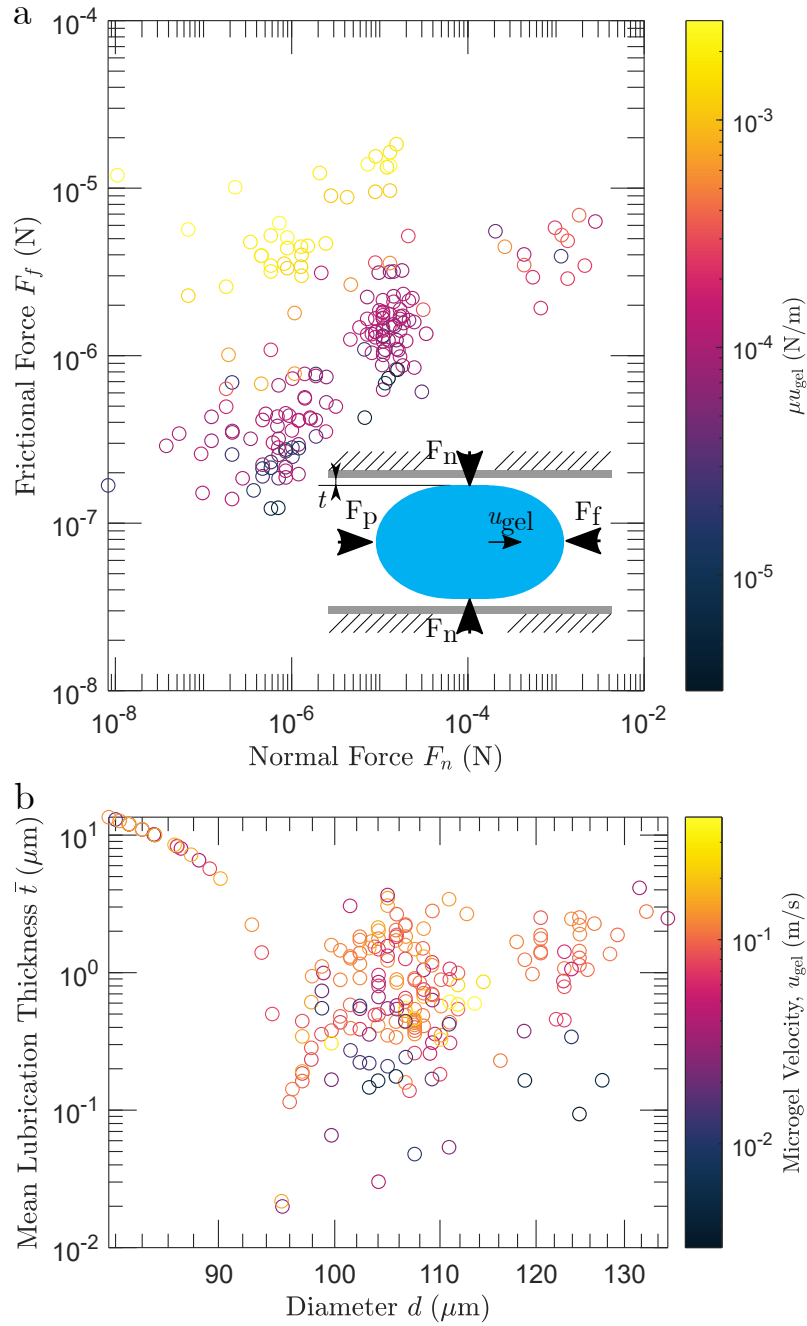


Figure 5.13: (a) A comparison of the steady state frictional force, $F_f = F_p$ acting on the microgel with the compressive force, F_n and the viscous velocity, μu_{gel} . A free body diagram of the microgel is provided as an inset. (b) The mean lubricating thickness, \bar{t} as a function of microgel diameter, d and velocity u_{gel} .

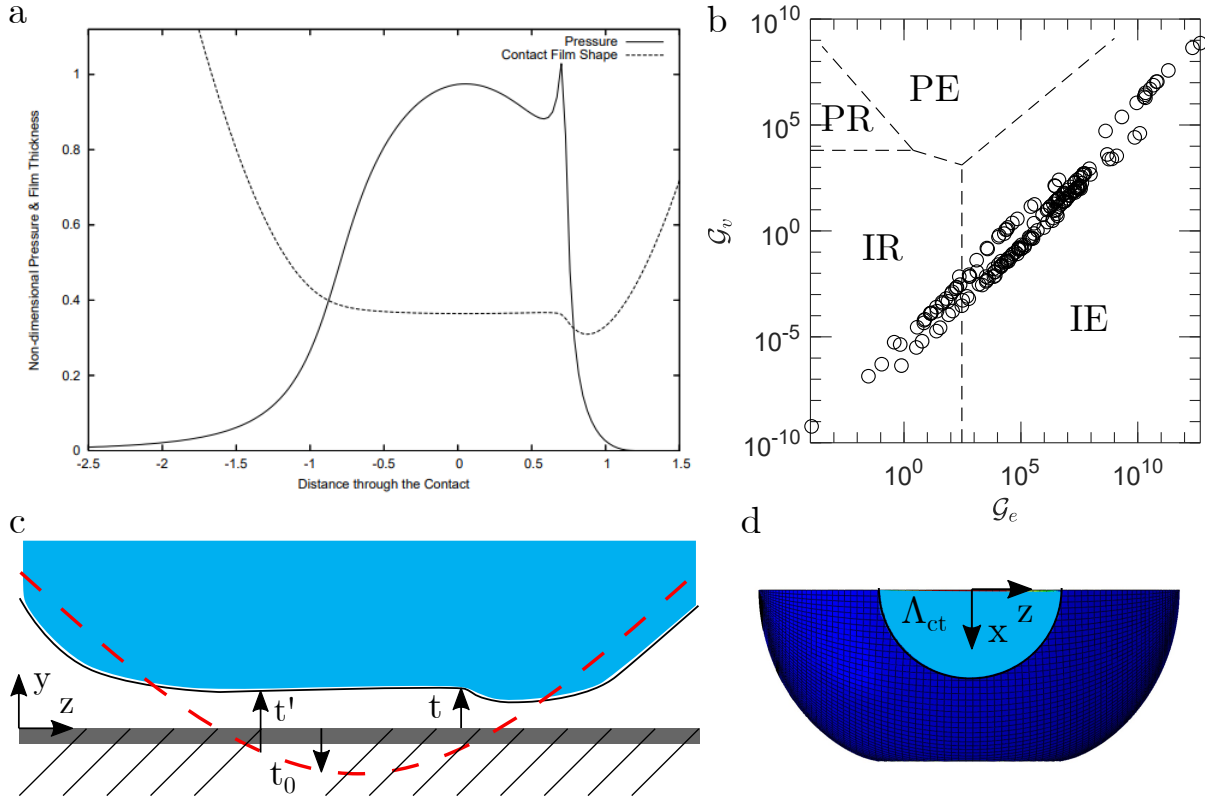


Figure 5.14: (a) A typical solution for pressure and film thickness for an elastohydrodynamic lubricating contact. Adapted from Zargari *et al.* [181] (b) A diagram of elastohydrodynamic lubrication regimes depending on the parameters $\mathcal{G}_e = \mathcal{W}^{8/3}/U^2$ and $\mathcal{G}_v = \mathcal{G}\mathcal{W}^3/U^2$. The regions are divided into the piezo viscous rigid (PR), piezo viscous Elastic (PE), isoviscous rigid (IR) and isoviscous elastic (IE) regions. Adapted from Esfahanian *et al.* [58] (c) A diagram of the microgel (blue) separation from the wall (grey, hatched) due to the lubricating layer of height t . The local deformation t_0 is illustrated as well, relative to the undeformed microgel outline in red. The profile of t is a rough estimation of a typical EHL. (d) A diagram of a half section of the microgel with the lubrication region, Λ_{ct} highlighted. This region corresponds with the area of the microgel in contact with the microchannel in the absence of any lubricating fluid.

the mean lubrication thickness, \bar{t} and microgel velocity. In order to explain these correlations, it is necessary to dive deeper, and examine the fluid structure interactions associated with the lubrication of a deformable material.

5.7.2 Conventional Soft Lubrication Modeling

Because the lubricating layer between the microgel and microchannel is thin, the lubricating film can be considered entirely in the Stokes regime, as $Re = \frac{u_{gel} t \rho}{\mu} < 1$. Additionally, the fluids used in this experiment are expected to behave in a Newtonian manner and remain incompressible. Finally, the microgel is moving at a steady state. With that in mind, Eq. 5.5 can be simplified to the steady state Reynolds lubrication equation:

$$\frac{\partial}{\partial x} \left(t^3 \frac{\partial P}{\partial x} \right) + \frac{\partial}{\partial z} \left(t^3 \frac{\partial P}{\partial z} \right) = 6(u_{gel} + u_{wall}) \frac{\partial t}{\partial z} \quad (5.28)$$

where u_{gel} is in the direction of \vec{z} , and in the case of this experiment $u_{\text{wall}} = 0$. The directions \vec{x} and \vec{y} are interchangeable, i.e. there is symmetry between the four lubricating films. The full derivation of the Reynolds lubrication equation was done by Reynolds in 1886 can be found elsewhere [155, 77, 142].

One of the implications of Eq. 5.28 is a the variation in pressure throughout the lubricating film depending on t . Furthermore, a simple force balance establishes that the pressure within the lubricating layer must be sufficient to push the bead from the microchannel. In the case of a constricted microgel, the fluid pressure must therefore be sufficient to deform the microgel further than contact mechanics. Assuming Hertzian contact between the microgel and the microchannel, the lubricating layer must also satisfy

$$t'(x, z) = \frac{2\pi}{E^*} \iint \frac{P}{\sqrt{(x-x')^2 + (z-z')^2}} dx' dz' \quad (5.29)$$

where x' and z' span the domain of Λ_{ct} [14, 138, 76]. The actual lubrication thickness must account for the local deformation of the microgel due to confinement, $t_0(x, z)$, see Fig. 5.14c. This distance corresponds to the approach and curvature of the microgel, where at the centre of contact $t_0(0, 0) = \frac{1}{2}(d - w)$, see Fig. 5.14d for coordinates. Combining this with Eq. 5.29, the lubricating thickness becomes

$$t(x, z) = t'(x, z) - t_0(x, z). \quad (5.30)$$

Finally, as a necessary boundary condition, the total normal force between the microgel and microchannel must be equal to the integral of pressure over the entire lubricating domain, such that

$$F_n = \int_{\Lambda_{\text{ct}}} P d\Lambda, \quad (5.31)$$

noting that this force will necessarily be greater than the unlubricated contact force, although due to the small size of t , the magnitude of the value will only be slightly increased, as $F_n \propto (d/2 - w/2 + t)^{3/2}$.

The system of equations described in Eqs. 5.28-5.31 represent a two dimensional partial differential system, and cannot be readily solved by hand, instead requiring numerical methods. One of the earliest numerical attempts to solve the elasto-hydrodynamic lubrication (EHL) equations (Eqs. 5.28-5.31) in two dimensions was performed by Hamrock and Dowson in 1976 [76]. In agreement with experimental data, they found that a profile where the lubricating thickness slowly decreased before suddenly decreasing right before the edge of the domain bounded by Λ_{ct} . A typical EHL solution for t and P along a contact centre-line is shown in Fig. 5.14 [181].

Hamrock and Dowson described the t at several points over the lubrication domain [76, 77], notably the central and minimal contact thickness, as well as the friction coefficient

$$\mathcal{F} = F_f/F_n. \quad (5.32)$$

The friction coefficient and the non-dimensional lubrication thickness ,

$$\mathcal{H} = \frac{2t}{d}, \quad (5.33)$$

was shown to be a function of the normalized contact force and velocity and viscosity, defined as

$$\mathcal{W} = \frac{4F_n}{d^2 E^*} \quad (5.34)$$

$$\mathcal{U} = \frac{2\mu u_{\text{gel}}}{dE^*} \quad (5.35)$$

$$\mathcal{G} = \beta E^* \quad (5.36)$$

respectively, where β is the pressure-viscosity term, relating how viscosity increases under pressure. The relationship between these parameters can be simplified by considering the lubrication regime, which describes what parameters will be significant in describing the lubricating film.

The specific lubrication regime can be further inferred from

$$\mathcal{G}_e = \frac{\mathcal{W}^{8/3}}{\mathcal{U}^2} \quad (5.37)$$

and

$$\mathcal{G}_v = \frac{\mathcal{G}\mathcal{W}^3}{\mathcal{U}^2}, \quad (5.38)$$

Using literature estimates for β for water a glycerol ($\beta = 0.75 \text{ GPa}^{-1}$ and $\beta = 2 \text{ GPa}^{-1}$ respectively [161]), the lubrication domain is determined by plotting \mathcal{G}_e and \mathcal{G}_v over a phase diagram, such as in Fig. 5.14b [76, 58, 123]. While the data covers several orders of magnitude of \mathcal{G}_e and \mathcal{G}_v , all values are in the isoviscous regime, with most falling within the isoviscous elastic regime. The isoviscous regime refers to the where fluid viscosity is unchanged by the pressure of the lubricating domain, as opposed to piezoviscous, where changes in μ become relevant to the lubrication. In effect, this allows the analysis going forward to neglect the effects of \mathcal{G} .

Several numerical and experimental studies have been performed to model the lubrication in the isoviscous elastic regime, sometimes called soft EHL, with a brief summary listed in Tab. 5.2. Because the lubrication is in the isoviscous elastic domain, EHL theory dictates that the friction and lubrication should be able to be described as functions of \mathcal{W} and \mathcal{U} . In recent years, particular interest in soft EHL has increase, slightly modifying the older elastic isoviscous EHL models to account for particularly soft materials, such as hydrogels [123, 145]. Many of these use a similar methodology to Hamrock and Dowson [76], describing the various points of interest on the lubricating domain, or the total friction from lubrication. In general however, there is a tendency to increase lubricating thickness with increasing velocity, as well as decreasing thickness with increasing contact force. In general these empirical

Source	Conditions	Correlation
Hamrock and Dowson [76]	Elastic isoviscous contact, solved numerically and fitted experimentally.	$\frac{t}{d} _{\text{exit}} \propto \left(\frac{\mu u}{dE^*}\right)^{0.65} \left(\frac{F_n}{d^2 E^*}\right)^{-0.21}$
Nijenbanning <i>et al.</i> [131]	A multi-level solution of point contact for viscous elastic contact.	$\frac{t}{d} _{\text{centre}} \propto \left(\frac{\mu u}{dE^*}\right)^{0.6} \left(\frac{F_n}{d^2 E^*}\right)^{-0.13}$
Marx <i>et al.</i> [123]	Soft isoviscous sliding contact of polyurethane and polymethy-methacrylate on a hard interferometry surface.	$\frac{t}{d} _{\text{exit}} \propto \left(\frac{\mu u}{dE^*}\right)^{0.55} \left(\frac{F_n}{d^2 E^*}\right)^{-0.07}$
Hooke [82]	Numerical model of soft EHL, noting side and rear exit regimes.	$\frac{t}{d} _{\text{exit}} \propto \left(\frac{\mu u}{dE^*}\right)^{0.6} \left(\frac{F_n}{d^2 E^*}\right)^{-0.13}$
Sadowski and Stupkiewicz [145]	Friction of hard on soft, soft on soft or soft on hard sliding sphere.	$\frac{F_f}{F_n} \propto \left(\frac{\mu u d}{F_n}\right)^{0.55}$
De Vicente <i>et al.</i> [44]	Friction of a soft rolling sphere on a moving plate.	$\frac{F_f}{F_n} \propto SRR \left(\frac{\mu u}{dE^*}\right)^{0.71} \left(\frac{F_n}{d^2 E^*}\right)^{-0.76}$
Cartas-Ayala [28]	Cells passing through a square microchannel	$\frac{F_f}{\mu u d} \propto \left(\frac{F_n}{\mu u d}\right)^{0.35}$
Khan <i>et al.</i> [96]	Passage of microgels and cells through a square channel.	$\frac{\Delta P d}{\mu u} \propto \left(\frac{d}{w}\right)_i^C$

Table 5.2: A summary of some models of soft EHL between a spherical particle and flat surface. Models predict both friction and lubrication layer thickness.

equations take the form of

$$\mathcal{H} = C_H \mathcal{U}^{C_U} \mathcal{W}^{C_W}. \quad (5.39)$$

and

$$\mathcal{F} = C_F \mathcal{U}^{C_U^F} \mathcal{W}^{C_W^F}. \quad (5.40)$$

In the absence of numerical solutions of friction, the fitting of parameters for \mathcal{F} and \mathcal{H} can still illustrate the governing physics in the lubrication between the microgel and microchannel.

5.7.3 Lubrication, Velocity and Contact Force

Considering that the microgels are moving in the elastic isoviscous EHL regime, the lubricating thickness and thus friction are expected to be functions of \mathcal{W} and \mathcal{U} . The normalized lubrication thickness \mathcal{H} is plotted against \mathcal{W} and \mathcal{U} in Fig. 5.15a. The trends in lubricating thickness here become much clearer, compared with Fig. 5.13b, showing \mathcal{H} increasing both with \mathcal{U} and \mathcal{W} .

The friction coefficient, \mathcal{F} , is plotted against the velocity and compression coefficients in Fig. 5.15b. The trends shown in Fig. 5.13a hold here also, showing that \mathcal{F} increase with \mathcal{U} , while decreasing with \mathcal{W} . The relationship also suggests that the effects of compression and velocity can be treated independently, such that $\mathcal{F} = f(\mathcal{U})g(\mathcal{W})$, as the changes in \mathcal{F} with respect to \mathcal{U} and \mathcal{W} hold independently. This greatly simplifies empirical analysis, allowing for a linear fit of data to be performed.

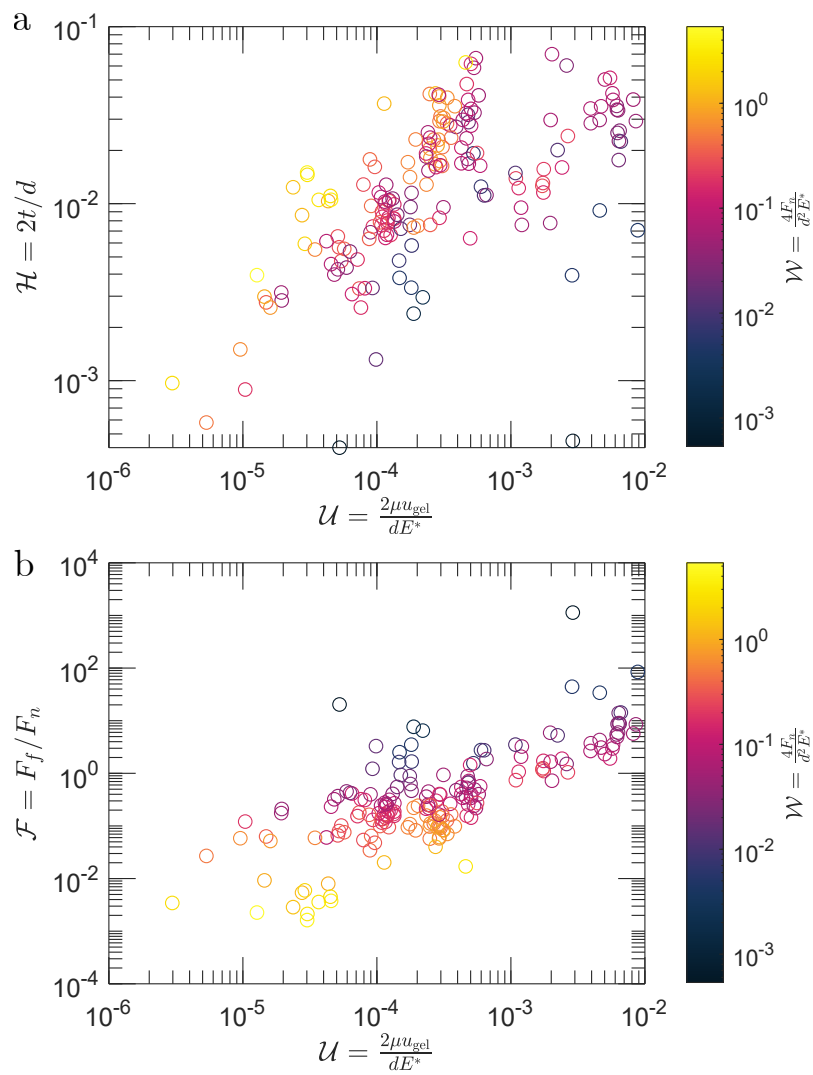


Figure 5.15: (a) Friction coefficient presented as a function of the nondimensionalized velocity and compression. (b) Lubricating thickness coefficient presented as a function of the nondimensionalized velocity and compression.

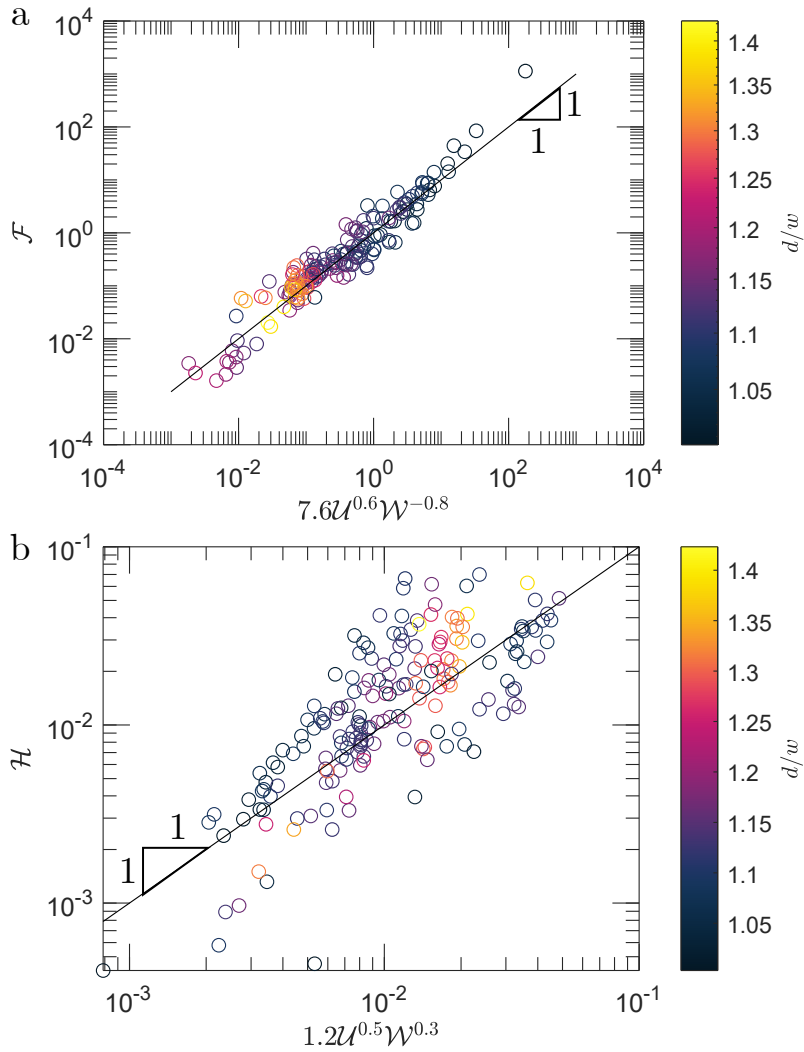


Figure 5.16: (a) A best fit of the friction coefficient with the normalized velocity and constriction. This is also compared with the microgel confinement. Data has a coefficient of determination. A reference line is provided to aid comparing the fit of the data. (b) A best fit of the lubrication layer thickness with the normalized velocity and constriction. This is also compared with the normalized mean pressure. Data has a coefficient of determination. A reference line is provided to aid comparing the fit of the data.

5.7.4 Empirical Models of Friction and Lubrication

Applying the same empirical methods to model friction as found in literature, a best fit model for friction was found where

$$\mathcal{F} = 7.6U^{0.6}W^{-0.8}, \quad (5.41)$$

with a coefficient of determination of $R^2 = 0.92$. This prediction can be seen compared with the experimental values in Fig. 5.16a. The empirical fit is in very good agreement with the experimental data, and is unaffected by the degree of confinement.

Unlike most other models of EHL lubrication, Cartas-Ayala measured the frictional coefficient of cellular bodies traveling in a microchannel, meaning the moving body was confined on all sides [28]. In this study, the data was

fit to a prediction which can be rewritten as $\mathcal{F} \propto \left(\frac{\mathcal{U}}{\mathcal{W}}\right)^{0.65}$. This is in good agreement with the fit proposed here. Limiting the fit to the form $\mathcal{F} \propto \left(\frac{\mathcal{U}}{\mathcal{W}}\right)^{C_U \mathcal{W}}$, Eq. 5.41 can be rewritten as $\mathcal{F} \propto \left(\frac{\mathcal{U}}{\mathcal{W}}\right)^{0.7}$, which is within the bounds of uncertainty of the model predicted by Cartas-Ayala. While validating the experimental fit performed here, it also further highlights the effect that confinement in a square microchannel has on the soft EHL.

Performing the same empirical fitting on the lubrication thickness, the mean lubrication thickness scales as

$$\mathcal{F} = 1.2\mathcal{U}^{0.5}\mathcal{W}^{0.3} \quad (5.42)$$

with a coefficient of determination of $R^2 = 0.58$. This is illustrated in Fig. 5.16b. The quality of this fit is not as strong as that of friction, with an data often deviating from the prediction by a factor of ten. Additionally the degree of confinement has a no clear impact on the fit.

Comparing Eq. 5.42 with literature, Marx *et al.* developed a model of lubrication thickness specifically with soft EHL in mind. The prediction has lubrication thickness scaling as $\mathcal{H} = 2.7\mathcal{U}^{0.55}\mathcal{W}^{-0.07}$. In both cases $C_U = 0.53 \pm 0.05$, however there is a much greater difference in C_W . The value of C_W being positive in Eq. 5.42 is especially challenging to interpret. Effectively, the greater the contact force between the microgel and microchannel, the greater the lubrication thickness, as $\mathcal{W} \propto F_n$. Recalling Eq. 5.15, this also indicates that the lubricating thickness increases in size with increasing confinement. The most significant difference between the experiments in Marx, and most of the EHL models presented in Tab. 5.2, is the confinement of the microgel.

While confinement is unaccounted for in Eq. 5.42, the data in Fig. 5.16b show no correlation between d/w and \mathcal{H} . This effectively rules out any significant effects of the eccentricity of Λ_{ct} , as well as other purely geometric factors, as the dry deformation of the microgel is entirely a function of d/w in these experiments. Several studies have also identified surface roughness as a factor in the effective lubrication thickness [93, 145, 67, 116], however this is also unlikely to be the case here. In these experiments, the same microfluidic mold was used to create the PDMS comparators, meaning that there should be no systematic influence of surface roughness. The pressure distribution around the microgel however is different and unaccounted for by the confinement, \mathcal{U} and \mathcal{W} .

5.8 Lubrication Film and Pressure

5.8.1 Film Thickness and Pressure

While pressure is generally small enough to not noticeably deform the microgel, at scale of the lubrication film, these small changes in dimension may be more significant. In general, $P_{gel}/E^* \sim 10^{-4} - 10^{-1}$, putting the pressure nearly on the scale of the elasticity of the microgel. Furthermore, the pressure is not constant in the fluid around the

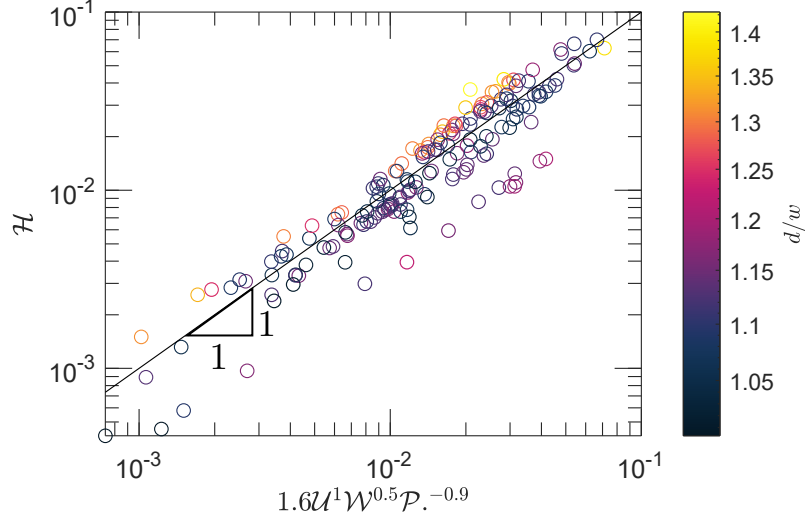


Figure 5.17: The lubrication layer thickness compared with the predicted thickness, including a contact force term, a velocity term and a mean pressure term.

microgel, instead decreasing gradually by P_{gel} . To account for this,

$$\mathcal{P} = \frac{P_{\text{gel}}}{2E^*} \quad (5.43)$$

which reflects the mean pressure at the borders of the lubrication domain.

The new empirical fit of the lubrication thickness is developed using the same methodology as for Eq. 5.42 such that

$$\mathcal{H} = 1.6UW^{0.5}\mathcal{P}^{-0.9} \quad (5.44)$$

with a coefficient of determination of $R^2 = 0.91$. This correlation is compared with the data in Fig. 5.17. This is a considerable improvement over the prediction made in Eq. 5.42 by accounting for the hydrodynamic effects of confinement on the lubrication. The figure does indicate that there is some further effect of confinement upon the lubrication thickness, however this effect is minor.

5.8.2 Mass Balance in the Lubricating Layer

The correlation in Eq. 5.44 still predicts that the lubricating thickness increases with the confining force on the gel, which is counter-intuitive. This is further complicated by the negative correlation with respect to pressure drop across the microgel. Looking at the lubrication layer in isolation, there is no easy way to explain this phenomena. Increasing W means there is more force to overcome to push the microgel away from the channel wall. Meanwhile, decreasing \mathcal{P} means at the start of the lubricating layer will have less pressure to push the microgel away from the wall. Furthermore, the trend of \mathcal{H} increasing with W is not seen in any elastohydrodynamic lubrication models for single contact lubrication, see Tab. 5.2.

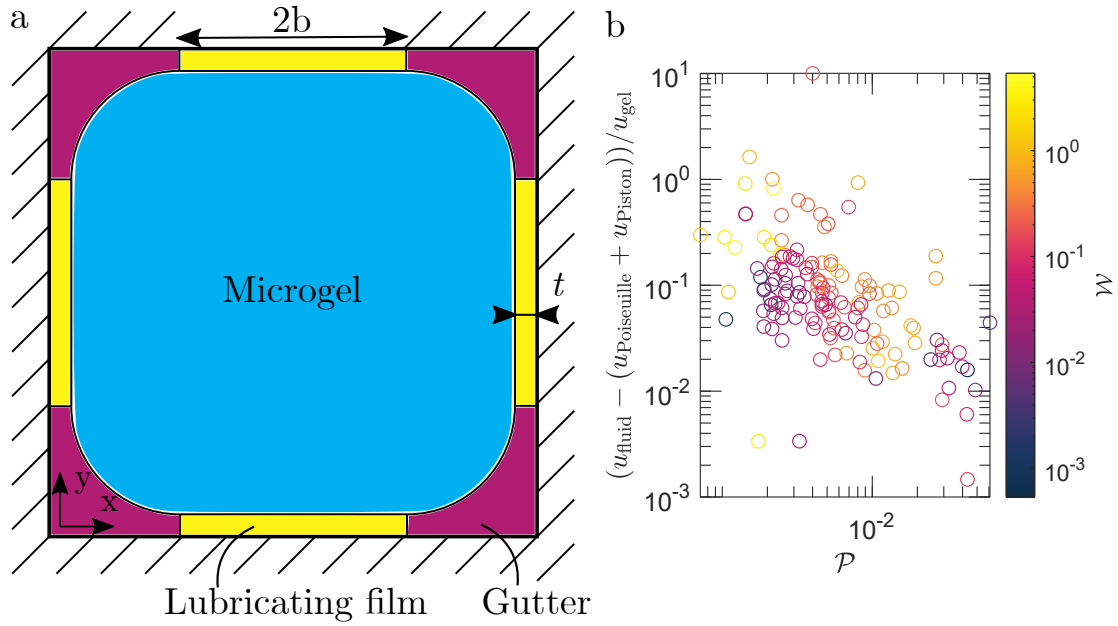


Figure 5.18: (a) A diagram of a confined microgel, highlighting the lubrication domain (yellow) and the gutters (violet) around the microgel. The in question microgel is cut perpendicular to the channel at its midpoint. (b) A comparison of the flow through the lubricating film, represented by $(u_{\text{fluid}} - u_{\text{Piston}} - u_{\text{Poiseuille}})/u_{\text{gel}}$, compared with the nondimensional contact force, \mathcal{W} and pressure, \mathcal{P} .

What differentiates the lubrication of a confined microgel from flooded soft EHL lubrication is the confinement on all sides, along with the fluid flow around the microgel. This means that there will be an uneven distribution of pressure around the border of the lubrication domain, due to flow in the gutters. In numerical solutions of EHL where a sphere is in contact with a flat plane, flow will exit the lubrication layer both in the direction of the moving ball, but also out the sides of the lubricating layer [76, 58, 123]. With flow passing through the gutters around the microgel however, the fluid which can exit the lubrication layer into the gutters is limited, forcing more flow through the rear of the microgel.

It follows that understanding the lubricating thickness between the microgel and microchannel means accounting for the flow through the gutters around the microgel. Recall that the model of flow through the gutters in Eq. 5.27 slightly underestimates the experimentally measured flow. In this case, the total flow through the microchannel was assumed to be the result of superposition of Poiseuille flow through the gutters and a combination of Couette flow through the gutters and displaced volume of the microgel. Now accounting for the flow through the lubricating layer, Q_{lube} , mass conservation dictates that flow through the microchannel should be described by

$$u_{\text{fluid}}w^2 = (u_{\text{Poiseuille}} + u_{\text{Piston}})w^2 + Q_{\text{lube}}. \quad (5.45)$$

This separation of flow domains is illustrated in Fig. 5.18a, with four gutters and four lubrication regions.

Flow in the lubricating domain can be modeled similarly to flow within the gutters around the microgel, by Couette-Poiseuille flow, as predicted for Reynolds Lubrication, see Eq. 5.28. This lubrication domain is bounded

approximately by the dry contacting area of the microgel, Λ_{ct} . This domain occupies an ellipse of radii a and b , with a parallel to flow. For the purposes of this analysis, the domain of Λ_{ct} is approximated as circular, *i.e.* $a \approx b$. At its widest, the lubricating domain perpendicular to flow measures $2a \times \bar{t}$, approximating the height of the lubricating domain to be approximately the mean lubricating thickness, $t \approx \bar{t}$. The Couette flow through this region can therefore be approximated by

$$Q_{\text{lube,C}} = \frac{u_{\text{gel}}}{2} (2a\bar{t}). \quad (5.46)$$

To further simplify analysis of flow through the lubricating regime, we approximate the pressure drop through the lubrication domain by P_{gel} . The Poiseuille flow through a long, thin and wide section is expected to scale such that

$$Q_{\text{lube,P}} \sim P_{\text{gel}} \bar{t}^3. \quad (5.47)$$

In these experiments however, \bar{t} is small, meaning that when adding $Q_{\text{lube,C}}$ with $Q_{\text{lube,P}}$, the contribution of the Poiseuille flow will be minor. Therefore, we neglect the contribution of the Poiseuille flow through the lubricating layer, such that

$$Q_{\text{lube}} = 4 \left(\frac{u_{\text{gel}}}{2} \bar{t} (2a) \right). \quad (5.48)$$

Combining Eqs. 5.48 and 5.45, the lubricating thickness can be estimated to scale such that

$$\frac{\bar{t}}{w} \sim \frac{u_{\text{lube}}}{u_{\text{gel}}} = \frac{u_{\text{fluid}} - u_{\text{Piston}} - u_{\text{Poiseuille}}}{u_{\text{gel}}}. \quad (5.49)$$

The right hand side of Eq. 5.49, corresponding to the lubricating flow velocity and called $\frac{u_{\text{lube}}}{u_{\text{gel}}}$ for simplicity, is compared with $\mathcal{P} = \frac{P_{\text{gel}}}{2E^*}$ and $\mathcal{W} = \frac{F_n}{d^2 E^*}$ in Fig. 5.18. There is a decrease in flow through the lubricating layer as \mathcal{P} increases. There is however only a very weakly positive correlation between the lubricating flow velocity and \mathcal{W} .

The relationship between $u_{\text{lube}}/u_{\text{gel}}$ and \mathcal{P} shown in Fig. 5.18 indicates that the lubricating thickness will also decrease with increasing \mathcal{P} . This trend is expected given the correlation shown in Fig. 5.17 and Eq. 5.44. In effect, as the pressure is increased more flow passes through the gutters in lieu of through the lubricating layer. The rate of decrease however is slower than described in Eq. 5.44, with $u_{\text{lube}}/u_{\text{gel}} \sim \mathcal{P}^{0.5}$. The relationship between \mathcal{W} and $u_{\text{lube}}/u_{\text{gel}}$ however is too weak to say anything with respect Eq. 5.44.

It is challenging to explain these discrepancies between models, however it is worth keeping in mind the whole geometry of the lubricating layer. The scaling suggested in Eq. 5.49 assumes a constant width, however the actual area of the lubricating film is elliptical. Furthermore, this lubricating film is not actually a flat height, \bar{t} , but instead varies throughout the entire domain. This makes the scaling proposed in Eq. 5.49 only a rough approximation.

Despite the approximate nature of Eq. 5.49, it does suggest an explanation for the mechanism behind the correlation described in Eq. 5.44. As pressure increases so does the Poiseuille flow through the microgel gutters.

Meanwhile, as the lubrication layer is thin, the increase in flow due to the pressure change is minimal. In effect, the larger pressure drop across the microgel the larger the proportion of the total flow through the microchannel passes through the gutters of the microgel. This in turn decreases the flux through the lubricating layer, which scales with the lubricating layer thickness.

An additional explanation which is not explored here is that as the pressure drop across the microgel increases, the pressure boundary around the lubricating layer changes. This changes the flow path through the lubrication film in turn, pulling fluid directly through the lubrication layer, and preventing flow out into the microgel gutters. This is further limited by the microgel gutter cross sectional area. As this area decreases, there is even less space for fluid to flow out of the lubricating layer and into the gutters. In effect, as confinement increases, the flow from the lubricating layer and into the surrounding gutters becomes limited. This hypothesis however cannot be confirmed with the current data, as flow between the lubricating layer and gutters is not considered. Instead, numerical methods are necessary in order to determine the path of flow through the lubricating layer, by solving Eqs. 5.28-5.31 and thereby the overall lubricating layer thickness.

5.9 Future Work

5.9.1 Solving the Lubrication Equations and Generalizing Confined EHL

For unconfined EHL, the far field boundary for pressure can be assumed uniform. The analysis here highlights that this difference greatly affects the lubrication between microgel and microchannel, as confinement imposes a pressure boundary, which changes the flow within the lubrication layer. It is worth highlighting that the factors listed in Eq. 5.49 are coupled. Recalling Fig. 5.7 the normalized pressure, \mathcal{P} can be shown to increase with d/w . Furthermore, P_{gel} and u_{gel} are related to u_{fluid} and thus $Q - \Delta Q$. This highlights the limitations of the uncoupled approach to analyzing the flow around a confined moving microgel by splitting it into the fluid domain and the EHL domain.

Numerically solving the EHL equations allows for further validation of the analysis presented here, and will allow for testing the specific effects of pressure distribution on the lubrication domain. The specific mechanism hypothesized here to be responsible for the decreasing lubrication thickness with increased microgel confinement however will require accounting for the surrounding fluid domain and the coupling involved. The development of such a numerical solution to the fluid-structure interaction of the EHL of a confined microgel is beyond the scope of this work.

This study also did not account for either the surface roughness of microgel-microchannel contact, nor any poroelastic behavior of the microgel. While in a scenario such as the one tested here flow will preferentially flow around the microgel rather than through it, as the gutters around the microgel disappear flow may be forced through

the microgel pores, further affecting the lubrication film thickness. Surface roughness also almost certainly affects the resistance of microgels passing through a constriction, though how this compares with the current models simple point contact roughness [93, 145, 67, 116]. Similarly other surface effects such as hydrophobicity of the microgel and microchannel may also play a role in the lubrication regime. Additionally, this analysis only considered approximately square microchannels. As the aspect ratio of the microchannel increases however, both the flow around and through the lubrication domain will be affected, leaving a further avenue for investigation.

5.9.2 Multiphasic Resistance

The experiment performed in this chapter investigated the resistance of microgels surrounded by either a water and SDS solution, or a glycerol, water and SDS solution, *i.e.* the experiments performed here were biphasic. One unexplored question however is how particles are lubricated in a multiphase flow. Emulsions have been studied with respect to EHL in macroscopic experiments [154, 170, 186], however to the authors' knowledge this has not been studied in microfluidic systems. This is relevant because as this chapter has demonstrated, the lubrication thickness is greatly affected by microfluidic confinement. The study of multiphasic lubrication in a microfluidic environment is further differentiated from macroscopic lubrication as the size of the particle being lubricated is typically on the scale of the droplets contained within the lubrication. At this length scale for a microgel to be lubricated by two phases, the microgel would have to be encapsulated within a droplet, moving through an immiscible carrier phase.

One possible future direction for the research laid out in this chapter is to extend the analysis to include a second fluid phase. Within the realm of microfluidics, droplets are often used as carriers of particles, isolating their contents from one another. Droplet based genetic sequencing for example involves isolating single cells with large hydrogel droplets, and transporting them to where the cells can be analyzed [187, 99, 98]. A thorough understanding of this lubrication could allow for better optimization and design of these and similar systems.

One challenge in studying microfluidic multiphasic lubrication will be the encapsulation of microgels. The mode of injecting microgels into the microchannel will have to be considered such that the microgel can be injected while contained within a droplet. One possibility is to inject droplets of a fluid containing a dilute suspension of microgels. Accounting for the added resistance of empty droplets [166, 18, 171], the resistance of lubricated microgels can be considered in isolation. This problem would also introduce several new variables to the problem of microgel lubrication, including the viscosity of the carrier fluid, and the surface tension between the two fluid phases, as well as the volume of the encapsulating droplet.

5.10 Conclusion

In this chapter I experimentally measured the resistance and velocity of microgels moving through a square microchannel, showing the resistance to increase with confinement, while the relative microgel velocity decreases with confinement. Using solid simulations combined with Hertzian contact theory, two fluid domains were identified around the microgel: the first, where the microgel nearly contacts the microchannel, was governed by thin film lubrication, while the rest of the fluid domain behaved as a three dimensional laminar flow. Using superposition, the flow around the microgel was modeled as a combination of Poiseuille and Couette flow, thereby linking the fluid velocity with the microgel velocity and pressure drop across the microgel. Meanwhile, in the lubrication domain, the friction due to lubrication was modeled by adopting empirical elastohydrodynamic lubrication modeling. While the friction factor grows faster with respect to velocity than typical one sided lubrication, it is in good agreement with previous studies of confined lubrication.

Comparing the mean lubrication thickness to the compression and velocity of the microgel, the lubrication thickness grows with respect to the microgel velocity as well as with confinement. While this may seem surprising, I hypothesize that this may be due to the flow through the gutters around the microgel. As the microgel becomes more confined, flow through the gutters becomes more restricted, pushing fluid back into the lubricating domain. This is further supported by accounting for the pressure drop affecting the lubrication thickness. Further analysis is however necessary to establish the exact mechanism causing lubrication thickness to increase with confinement, notably numerically solving the elastohydrodynamic lubrication equations for a confined microgel

The work done in this chapter lays the groundwork for further understanding the motion of soft bodies in microfluidic constrictions. Neither the porosity, nor the surface conditions were considered in this analysis, however both are expected to have a major impact on the transport of microgels. As rectangular microchannels are commonly used in microfluidics for tasks such as transporting cells or even microgels, understanding the resistance these particles impose is an important design consideration. Noting the coupled relationship between flow rate, microgel velocity and pressure drop, this work also opens up a new avenue of analysis for multi-phase flows involving microgels, where both the microgel velocity and the pressure around the microgel will have an impact on the fluid interfaces as well.

Chapter 6

Conclusion and Prospects

In this thesis, I have investigated the entry of microgels into microfluidic constrictions, and how they progress through these constrictions. The analysis presented separates the physics into two separate domains, before recombining to create a wholistic model of the fluid structure interaction of microfluidic particle transport.

At the beginning of my thesis, the focus was on the ordered encapsulation of particles into droplets [3, 4, 37]. This process acts as an important component microfluidic droplet genetic analysis [99, 99, 187]. The triggering of droplet encapsulation allows for droplets to form around particles at precise rates, such that each drop has a single particle. The prevailing explanation for this phenomena is that as the particles and their droplet phase enter into a microchannel constriction, they resist flow and cause a droplet to pinch off behind them. Early experiments which I undertook seemed to support this theory, showing that unordered droplets would trigger encapsulation only if the particle entered into a constriction. Otherwise, the droplet would form around the microgel undisturbed. It became clear over the course of these experiments that it was necessary to better understand the resistance posed by a microgel as it entered into the constriction so as to understand it's upstream effects. It also became clear that these questions about particle passage into and through a microfluidic constriction were themselves quite profound questions which this thesis has only begun to explore.

6.1 Making and Testing Microgels

The passage of particles through constrictions is a broad topic within microfluidics, ranging from red blood cells in circulatory capillaries, to spherical hydrogels carrying genetic test material. In order to study the passage of elastic bodies in general, I chose a set of hydrogel spheres of to act as model particles, due to their ease of production and range of elastic properties. Polyethylene glycol droplets were emulsified in a microfluidic "flow focuser" emulsifier and then photo-polymerized into solid hydrogels within the microchannel. One of the most important early steps in this thesis was to characterize these microgels for elastic modulus and size. In general, while monodisperse

microgel droplets were easy to manufacture, there was still a wide variation in mechanical properties, likely due to the limitations of polymerizing microgel emulsions within a microfluidic channel. Still, due to the sensitivity to chemical makeup, the microgels tested in this thesis had elastic moduli spanning $E \sim 100$ Pa to $E \sim 100$ kPa.

6.2 Microgel Deformation in a Constriction Trap

While passage through axisymmetric constrictions have been explored at length, the passage of particles into rectangular constrictions is considerably more challenging to model. To investigate the penetration of particles into a rectangular slit, I used a trap-bypass channel, where increasing pressure progressively pushed the microgel into a narrow section of microchannel. With the aid of fluid and solid contact simulations, I developed a model based on Hertzian contact mechanics that describes both the displacement of the microgel into the microfluidic channel, as well as its deformation outwards during this process. Importantly, this model couples the deformation with the flow around the trapped microgel: as the pressure increases, the microgel is forced to deform, thereby changing the distribution of pressure.

The deformation model is in general agreement with experimental data when the microgel deformation is relatively small however, at larger deformation its assumptions become violated. Furthermore, while the displacement is in agreement with the data provided, the change in contact radius with the channel walls had considerable between experiments. It is possible this is due to a limitation in the model provided, however the degree of uncertainty instead points to challenges in measurement. Small variations in position of the microgel were challenging to measure using the micrographs procured, but had a noticeable impact on this measurement. The practical test of the model was to compare the elastic modulus with that measured by microindentation. In this case, the model was capable of predicting the elasticity to within the degree of uncertainty of both measurement systems.

The experiment done here lays the groundwork for a novel microfluidic method of measuring particle elasticity, which uses only a single layer microfluidic mold, and requires neither glass pipettes or precision force cantilevers. Future work in this field will include some modifications of the microchannel before the model can be initialized for a wider range of particles. This is due to the sensitivity towards smaller and softer particles, and channel robustness for stiffer particles.

These experiments also only considered steady state trapped gels. While this is important to understanding how particles enter into non-conforming constrictions such as the one dimensional constriction used here, the model used here has not been tested for a dynamic microgel. Investigation into the time dependent response of microgels to changes in pressure is needed to fully understand the penetration of microgels into a microfluidic constriction. These experiments have the added benefit of extending the practical applications of the slit trap to measure the visco-elastic properties of the particles trapped within them. This is particularly useful, as hydrogels typically exhibit visco-elasticity which was not tested for in these experiments.

6.3 Valve Behavior of Trapped Microgels

The experiments measuring microgel deformation into a constriction had a coupled relationship with the flow around the microgel. As the microgel penetrated into the constriction, it partially plugged the constriction, forcing flow to pass through an shrinking area. In the experiments measuring trapped microgel deformation, I also observed that this leaky flow past the microgel does not progress linearly with the applied pressure. Instead, at low pressures, flow past the microgel increased with pressure until the microgel sufficiently plugged the constriction. At that point, flow past the microgel decreased until the channel was fully plugged. Because the flow past the microgel was laminar, I modeled the resistance to flow around the microgel as a Poiseuille flow, dependant upon the geometry of the deformed microgel. Extending this model further, I then integrated the model of microgel deformation that was previously developed, creating a new valve model of a plugging microgel.

The valve model showed a complicated relationship with the microchannel geometry, which depended upon both microgel diameter, microchannel corner radius, and the constriction width. The model also showed that the maximum flow rate was linearly proportional to the elastic modulus of the microgel. While the model does under-predict the pressure at which the maximum flow rate will occur, the experimental maximum flow rate itself is in good agreement with the model.

The trapped microgel phenomenon presented here has the potential to be implemented practically as a microfluidic valve. By trapping microgels in slit traps, it is possible to create a simple regulating valve that limits and regulates flow over a wide range of pressure. This could, for example, be used in microfluidic systems where dampening the flow rate is necessary, maintaining the downstream flow rate will remain close to the maximum flow rate. Such a valve, however, would need to be sensitive to the rate of change of pressure upstream, which was not considered in these experiments. This further supports the need to dynamically characterize the behavior of trapped microgels. Even if quasi-static considerations are possible in the fluid domain around the microgels, the visco-elasticity of the microgels may affect the dynamic response of the microgel trap valve. The steady state modeling developed in this thesis provides a good basis for a holistic model of leaky flow around a trapped microgel.

6.4 Lubrication of a Microgel in a Square Channel

The second set of experiments in my thesis studied the motion of microgels through square constrictions. In this case, the entry into the microchannel was neglected, looking solely at the steady state passage through the channel. Using a microfluidic comparator, I measured the added resistance of microgels as they passed through the microchannel, as well as the velocity of the microgel. I found that the resistance of the microgel increased as the microgel became more confined, and that the velocity decreased with confinement relative to the fluid velocity.

Noting the coupling between fluid velocity, particle velocity and resistance, and thus pressure drop across the

microgel, I decided to model the passage of the microgel in two different domains. The first domain considered fluid flow around the microgel, excluding where the microgel was in contact with the microchannel. This domain considered the microgel to be rigid, deforming only as a result of the confinement of the microchannel. In this domain, the model of fluid flow was solved as a modified Couette-Poiseuille flow, *i.e.* using the superposition of pressure driven flow around the microgel, and flow from the microgel motion neglecting pressure.

In contrast, the second domain looked at where the microgel was almost in contact with the microchannel. In this domain, I considered the fluid-structure interaction of the microgel which deforms away from the microchannel wall to create a lubricating film. Using empirical lubrication analysis, I showed how friction increases between the microgel and microchannel as the microgel velocity increases, as well as with increased confinement.

Building on the analysis of lubricating friction, I also measured the mean thickness of the lubricating layer. Like the friction coefficient, the lubrication thickness increased with respect to microgel velocity. Curiously, the lubricating thickness also increased as the microgel became more confined. Conversely, when the pressure drop across the microgel increased, lubrication thickness was also found to decrease. I hypothesize that this is due to the pressure distribution within the microchannel. As the microgel becomes more confined, resistance to flow passing around the microgel increases, at which point more fluid is forced into the lubricating layer, thereby increasing the thickness. This effect is mitigated however if the pressure drop across the microgel is small, thereby pushing less fluid into the lubricating layer.

While some simple scaling arguments can be used to help explain the hypothesis of the behavior of the lubricating layer, the lubrication equation coupled with Hertzian solid mechanics leads to a complicated set of differential equations. Due to their complexity, these equations must be solved numerically, which was beyond the scope of this thesis. To fully understand why the lubricating layer grows with respect to increased microgel confinement, solutions to these equations will likely be necessary, as direct measurement of the lubrication layer is challenging.

6.5 Concluding Remarks

These experiments lay the groundwork for understanding droplet triggering in multiphase flows. The experiments presented here can also be extended to better understand not only the transport of microgels, but also the effect this has on droplet flow. Understanding the dynamic entry of a microgel into a microfluidic constriction will help develop a more profound model of how the penetration affects flow upstream. This will in turn give evidence to the mechanism involved in droplet triggering. The inclusion of a droplet phase in the measurement of the lubrication of confined microgels would also help to better understand droplet formation, as the investigation into how specifically the droplet and carrier phase behave in steady state will improve the analysis.

Finally, microfluidic constrictions have demonstrated themselves as a both simple, cheap and adaptable method of testing particle and cellular properties. The experiments and models presented in this thesis have extended the

understanding of this simple technology one step further. Furthermore, the models proposed here provide a strong basis for work ranging from lab-on-a-chip cell sorting to improved rapid genetic testing technologies.

Appendix A

Theoretical Flow Around a Microgel

In the case of pressure driven flow across the microgel, we suppose that resistance from the microgel obstruction is geometric. For Poiseuille flow through a tube-like geometry, where the cross section changes gradually, the resistance can be described by

$$R \approx \int_{z_{ch}} \frac{\mu\alpha(z)dz}{\Lambda_{cso}(z)^2}, \quad (\text{A.1})$$

where the shape factor α in this case is unique to the shape of the outlet [26]. As resistance is dominated by regions of minimal cross sectional area, the majority of resistance can be assumed to be localized in the gutters around the microgel, highlighted in the inset of Fig. A.1a. In this area, the cross section perpendicular to flow can be approximated by a square corner bounded by a quarter circle, such that the area is described by $\Lambda_{cso}(z) = (1 - \pi/4)w_{cso}(z)^2$, where w_{cso} is the width of the corner. Noting that the volume highlighted in the figure inset is bounded by the region of Λ_{ct} , this contact area can be approximated by an ellipse with major and minor radii of a and b respectively. To simplify analysis here, let $a \approx b$, such that the contact area is a circle. Letting $z = 0$ correspond with the centre of the contact ellipse, the width of the cross sectional area can be described as $w_{cso} = w - \sqrt{a^2 - z^2}$ such that

$$\Lambda_{cso}(z) = \left(1 - \frac{\pi}{4}\right)w^2 \left(1 - \sqrt{\left(\frac{a}{w}\right)^2 - \left(\frac{z}{w}\right)^2}\right)^2. \quad (\text{A.2})$$

With this in mind, Eq. A.1 can be rewritten as

$$R_{gel,cso} \approx \frac{\mu\alpha}{4w^4} \int_{-a}^a \frac{dz}{\left(\left(1 - \frac{\pi}{4}\right) \left(1 - \sqrt{\left(\frac{a}{w}\right)^2 - \left(\frac{z}{w}\right)^2}\right)^2\right)^2}, \quad (\text{A.3})$$

noting that α will remain constant throughout the region as the shape bounded by Λ_{cso} remains constant. Approximating the area of Λ_{cso} as a right angle triangle, the shape factor can be solved as $\alpha \approx 101$, using the method described in Mortensen *et al.* [127]. A factor of 1/4 has also been included to account for the four gutters around the

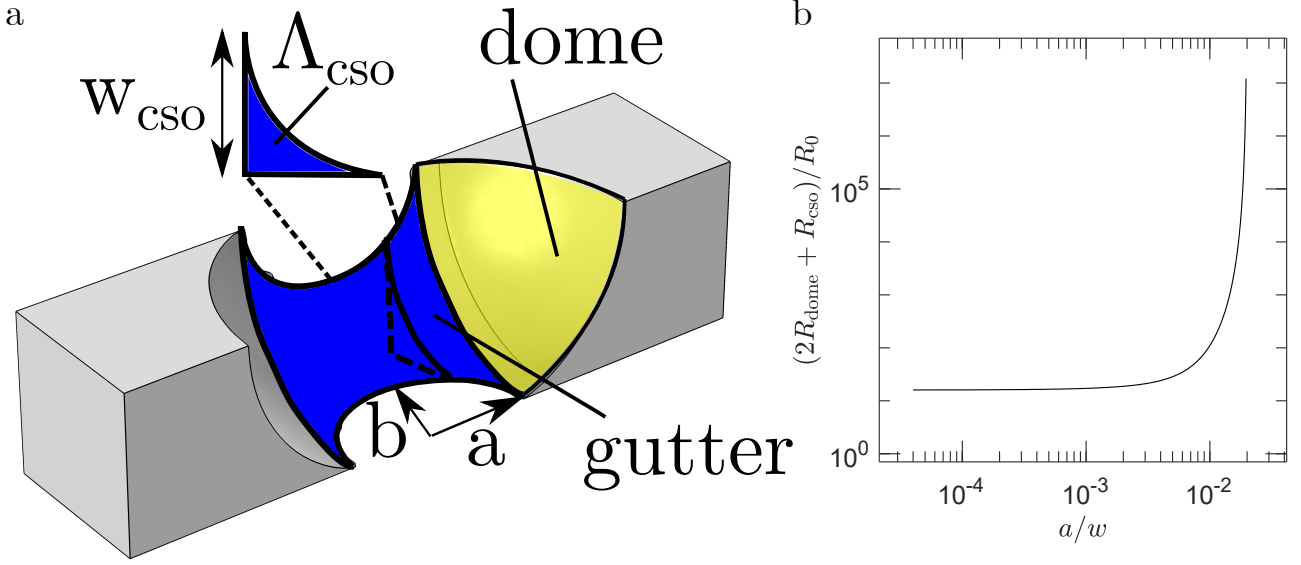


Figure A.1: (a) A diagram of the gutter around a microgel passing through a square confinement. The serial sections through which flow passes are labeled for the gutter and dome parts of the deformed microgel. (b) A comparison of the relative predicted microgel resistance $(2R_{\text{dome}} + R_{\text{CSO}})/R_0$ with the relative contact radius, a/d .

microgel, as per the parallel resistance rule. Finally, this can be normalized by the resistance of an empty channel, see Eq. 5.3 such that

$$\frac{R_{\text{gel,CSO}}}{R_0} \approx \frac{\alpha}{0.55z_{\text{ch}}} \int_0^a \frac{dz}{\left(1 - \frac{\pi}{4}\right)^2 \left(1 - \sqrt{\left(\frac{a}{w}\right)^2 - \left(\frac{z}{w}\right)^2}\right)^4}. \quad (\text{A.4})$$

Evaluating this integral using a numerical mathematics software suite (Wolfram Mathematica, Wolfram Research, Oxfordshire, UK), the relative resistance is described by

$$\frac{R_{\text{gel,CSO}}}{R_0} \approx \frac{39w}{z_{\text{ch}}} \left(\frac{a' \left(\sqrt{a'^2 - 1} (a'^4 - 10a'^2) - 6a' (4 + a'^2) \left(\tanh^{-1} \frac{1+ia'}{\sqrt{1-a'^2}} - \tanh^{-1} \sqrt{\frac{2}{1+a'}} - 1 \right) \right)}{6(a'^2 - 1)^{7/2}} \right), \quad (\text{A.5})$$

where $a' = a/w$.

The above however only accounts for the resistance due to the gutter around the microgel. There is also resistance due to the ends of the microgel. While at large deformations where Λ_{CSO} is small, the resistance will dominate, when $a \approx 0$, the resistance from the rest of the microgel is also relevant. Using the same methodology as above, but for a semisphere on either end of the microgel, the resistance of the dome section can be estimated as

$$\frac{R_{\text{gel,dome}}}{R_0} \approx \frac{\alpha}{28z_{\text{ch}}} \int_0^{w/2} \frac{dz}{4 \left(1 - \frac{\pi}{4} \left(1 - \left(\frac{z}{2w}\right)^2\right)\right)^2}. \quad (\text{A.6})$$

Noting that resistance is dominated for this annular section by where flow is most confined, we can estimate $\alpha \approx 101$, as was done previously for the gutter resistance. With that assumption in mind, Eq. A.6 solves as $R_{\text{gel,dome}}/R_0 =$

$16w/z_{\text{ch}}$.

The sections of the microgel occur in series. As such the total resistance of the confined microgel where $u_{\text{gel}} = 0$ can be written as

$$R_{\text{gel}0} = 2R_{\text{gel,dome}} + R_{\text{gel,cso}}. \quad (\text{A.7})$$

This can be seen plotted against the radius of contact, a in Fig. A.1b.

Bibliography

- [1] Fluid-structure interactions in low-Reynolds number flows. In C. Duprat and H. Stone, editors, *Soft Matter Series*, pages P001–P004. Royal Society of Chemistry, Cambridge, 2015. ISBN 978-1-84973-813-2. doi: 10.1039/9781782628491-FP001. URL <http://ebook.rsc.org/?DOI=10.1039/9781782628491-FP001>.
- [2] F. Abasalizadeh, S. V. Moghaddam, E. Alizadeh, E. akbari, E. Kashani, S. M. B. Fazljou, M. Torbati, and A. Akbarzadeh. Alginate-based hydrogels as drug delivery vehicles in cancer treatment and their applications in wound dressing and 3D bioprinting. *Journal of Biological Engineering*, 14(1):8, Dec. 2020. ISSN 1754-1611. doi: 10.1186/s13036-020-0227-7. URL <https://jbioleng.biomedcentral.com/articles/10.1186/s13036-020-0227-7>.
- [3] A. R. Abate, C.-H. Chen, J. J. Agresti, and D. A. Weitz. Beating Poisson encapsulation statistics using close-packed ordering. *Lab on a chip*, 9(18):2628–2631, 2009. ISSN 1473-0197. doi: 10.1039/b909386a. URL <https://www.ncbi.nlm.nih.gov/pubmed/19704976>.
- [4] A. R. Abate, A. Rotem, J. Thiele, and D. A. Weitz. Efficient encapsulation with plug-triggered drop formation. *Physical review. E, Statistical, nonlinear, and soft matter physics*, 84(3 Pt 1):031502, 2011. ISSN 1539-3755. doi: 10.1103/PhysRevE.84.031502. URL <https://www.ncbi.nlm.nih.gov/pubmed/22060374>.
- [5] M. Abkarian, M. Faivre, and H. A. Stone. High-speed microfluidic differential manometer for cellular-scale hydrodynamics. *Proceedings of the National Academy of Sciences*, 103(3):538–542, Jan. 2006. ISSN 0027-8424, 1091-6490. doi: 10.1073/pnas.0507171102. URL <https://pnas.org/doi/full/10.1073/pnas.0507171102>.
- [6] G. C. Agbangla, P. Bacchin, and E. Climent. Collective dynamics of flowing colloids during pore clogging. *Soft Matter*, 10(33):6303–6315, 2014. ISSN 1744-683X, 1744-6848. doi: 10.1039/C4SM00869C. URL <http://xlink.rsc.org/?DOI=C4SM00869C>.
- [7] M. Aghaamoo, Z. Zhang, X. Chen, and J. Xu. Deformability-based circulating tumor cell separation with conical-shaped microfilters: Concept, optimization, and design criteria. *Biomicrofluidics*, 9(3):034106, May 2015. ISSN 1932-1058. doi: 10.1063/1.4922081. URL <http://aip.scitation.org/doi/10.1063/1.4922081>.

- [8] S. M. Ahmmed, N. S. Suteria, V. Garbin, and S. A. Vanapalli. Hydrodynamic mobility of confined polymeric particles, vesicles, and cancer cells in a square microchannel. *Biomicrofluidics*, 12(1):014114, Jan. 2018. ISSN 1932-1058. doi: 10.1063/1.5018620. URL <http://aip.scitation.org/doi/10.1063/1.5018620>.
- [9] A. Aich, Y. Lamarre, D. P. Sacomani, S. Kashima, D. T. Covas, and L. G. de la Torre. Microfluidics in Sickle Cell Disease Research: State of the Art and a Perspective Beyond the Flow Problem. *Frontiers in Molecular Biosciences*, 7:558982, Mar. 2021. ISSN 2296-889X. doi: 10.3389/fmolb.2020.558982. URL <https://www.frontiersin.org/articles/10.3389/fmolb.2020.558982/full>.
- [10] S. Alborzi, B. G. Clark, and S. M. Hashmi. Soft particles facilitate flow of rigid particles in a 2D hopper. *Soft Matter*, 18(21):4127–4135, 2022. ISSN 1744-683X, 1744-6848. doi: 10.1039/D2SM00318J. URL <http://xlink.rsc.org/?DOI=D2SM00318J>.
- [11] A. S. Alketbi, Y. Shi, H. Li, A. Raza, and T. Zhang. Impact of PEGDA photopolymerization in microstereolithography on 3D printed hydrogel structure and swelling. *Soft Matter*, 17(30):7188–7195, 2021. ISSN 1744-683X, 1744-6848. doi: 10.1039/D1SM00483B. URL <http://xlink.rsc.org/?DOI=D1SM00483B>.
- [12] S. L. Anna. Droplets and Bubbles in Microfluidic Devices. *Annual Review of Fluid Mechanics*, 48(1):285–309, Jan. 2016. ISSN 0066-4189, 1545-4479. doi: 10.1146/annurev-fluid-122414-034425. URL <https://www.annualreviews.org/doi/10.1146/annurev-fluid-122414-034425>.
- [13] R. Augustine, A. H. Aqel, S. N. Kalva, K. Joshy, A. Nayeem, and A. Hasan. Bioengineered microfluidic blood-brain barrier models in oncology research. *Translational Oncology*, 14(7):101087, July 2021. ISSN 19365233. doi: 10.1016/j.tranon.2021.101087. URL <https://linkinghub.elsevier.com/retrieve/pii/S1936523321000796>.
- [14] J. Barber. *Contact Mechanics*, volume 250 of *Solid Mechanics and Its Applications*. Springer International Publishing, Cham, 2018. ISBN 978-3-319-70938-3 978-3-319-70939-0. doi: 10.1007/978-3-319-70939-0. URL <http://link.springer.com/10.1007/978-3-319-70939-0>.
- [15] J.-C. Baret. Surfactants in droplet-based microfluidics. *Lab Chip*, 12(3):422–433, 2012. ISSN 1473-0197, 1473-0189. doi: 10.1039/C1LC20582J. URL <http://xlink.rsc.org/?DOI=C1LC20582J>.
- [16] J.-C. Baret, F. Kleinschmidt, A. El Harrak, and A. D. Griffiths. Kinetic Aspects of Emulsion Stabilization by Surfactants: A Microfluidic Analysis. *Langmuir*, 25(11):6088–6093, 2009. ISSN 0743-7463. doi: 10.1021/la9000472. URL <https://doi.org/10.1021/la9000472>.
- [17] C. N. Baroud, S. Tsikata, and M. Heil. The propagation of low-viscosity fingers into fluid-filled branching networks. *Journal of Fluid Mechanics*, 546(-1):285, Dec. 2005. ISSN 0022-1120, 1469-7645. doi: 10.1017/S0022112005007287. URL http://www.journals.cambridge.org/abstract_S0022112005007287.

- [18] C. N. Baroud, F. Gallaire, and R. Dangla. Dynamics of microfluidic droplets. *Lab on a chip*, 1(16):232–245, 2010. ISSN 1473-0197. doi: 10.1039/c001191f. URL <https://www.ncbi.nlm.nih.gov/pubmed/20559601>.
- [19] J. Bauch, W. Liese, and R. Schultze. The morphological variability of the bordered pit membranes in gymnosperms. *Wood Science and Technology*, 6(3):165–184, 1972. ISSN 0043-7719, 1432-5225. doi: 10.1007/BF00351575. URL <http://link.springer.com/10.1007/BF00351575>.
- [20] K. D. Belfield and J. V. Crivello, editors. *Photoinitiated Polymerization*, volume 847 of *ACS Symposium Series*. American Chemical Society, Washington, DC, Mar. 2003. ISBN 978-0-8412-3813-8 978-0-8412-1951-9. doi: 10.1021/bk-2003-0847. URL <https://pubs.acs.org/doi/book/10.1021/bk-2003-0847>.
- [21] T. Billiet, M. Vandenhoute, J. Schelfhout, S. Van Vlierberghe, and P. Dubruel. A review of trends and limitations in hydrogel-rapid prototyping for tissue engineering. *Biomaterials*, 33(26):6020–6041, Sept. 2012. ISSN 01429612. doi: 10.1016/j.biomaterials.2012.04.050. URL <https://linkinghub.elsevier.com/retrieve/pii/S0142961212004899>.
- [22] T. Boekhout, Y. Yamada, A. Weijman, H. Roeymans, and W. Batenburg-Van Der Vegte. The Significance of Coenzyme Q, Carbohydrate Composition and Septal Ultrastructure for the Taxonomy of Ballistoconidia-Forming Yeasts and Fungi. *Systematic and Applied Microbiology*, 15(1):1–10, Feb. 1992. ISSN 07232020. doi: 10.1016/S0723-2020(11)80129-3. URL <https://linkinghub.elsevier.com/retrieve/pii/S0723202011801293>.
- [23] J. V. Boussinesq. Mémoire sur l'influence des frottements dans les mouvements réguliers des fluides. *Journal de Mathématiques Pures et Appliquées*, 13:377–424, 1868.
- [24] N. Bremond, A. R. Thiam, and J. Bibette. Decompressing Emulsion Droplets Favors Coalescence. *Physical Review Letters*, 100(2):024501, Jan. 2008. ISSN 0031-9007, 1079-7114. doi: 10.1103/PhysRevLett.100.024501. URL <https://link.aps.org/doi/10.1103/PhysRevLett.100.024501>.
- [25] F. P. Bretherton. The motion of long bubbles in tubes. *Journal of Fluid Mechanics*, 10(02):166, Mar. 1961. ISSN 0022-1120, 1469-7645. doi: 10.1017/S0022112061000160. URL http://www.journals.cambridge.org/abstract_S0022112061000160.
- [26] H. Bruus. *Theoretical microfluidics*. Number 18 in Oxford master series in physics. Oxford University Press, Oxford ; New York, 2008. ISBN 978-0-19-923508-7 978-0-19-923509-4. OCLC: ocn156817008.
- [27] J. Cappello, V. d'Herbemont, A. Lindner, and O. du Roure. Microfluidic In-Situ Measurement of Poisson's Ratio of Hydrogels. *Micromachines (Basel)*, 11(3):318, 2020. ISSN 2072-666X. doi: 10.3390/mi11030318. URL <https://www.ncbi.nlm.nih.gov/pubmed/32204340>.

- [28] M. A. Cartas Ayala. *Hydrodynamic resistance and sorting of deformable particles in microfluidic circuits*. PhD Thesis, Massachusetts Institute of Technology, 2013. URL <http://hdl.handle.net/1721.1/79312>.
- [29] M. A. Cartas-Ayala and R. Karnik. Time limitations and geometrical parameters in the design of microfluidic comparators. *Microfluidics and Nanofluidics*, 17(2):359–373, Aug. 2014. ISSN 1613-4982, 1613-4990. doi: 10.1007/s10404-013-1302-x. URL <http://link.springer.com/10.1007/s10404-013-1302-x>.
- [30] E. Chappel. A Review of Passive Constant Flow Regulators for Microfluidic Applications. *Applied Sciences*, 10(24):8858, Dec. 2020. ISSN 2076-3417. doi: 10.3390/app10248858. URL <https://www.mdpi.com/2076-3417/10/24/8858>.
- [31] K. Chawla, editor. *Biomaterials for Tissue Engineering: Methods and Protocols*, volume 1758 of *Methods in Molecular Biology*. Springer New York, New York, NY, 2018. ISBN 978-1-4939-7739-0 978-1-4939-7741-3. doi: 10.1007/978-1-4939-7741-3. URL <http://link.springer.com/10.1007/978-1-4939-7741-3>.
- [32] S. Chawla, S. Midha, A. Sharma, and S. Ghosh. Silk-Based Bioinks for 3D Bioprinting. *Advanced Healthcare Materials*, 7(8):e1701204–n/a, 2018. ISSN 2192-2640. doi: 10.1002/adhm.201701204. URL <https://onlinelibrary.wiley.com/doi/abs/10.1002/adhm.201701204>.
- [33] J. R. Choi, K. W. Yong, J. Y. Choi, and A. C. Cowie. Recent advances in photo-crosslinkable hydrogels for biomedical applications. *BioTechniques*, 66(1):40–53, 2019. ISSN 0736-6205. doi: 10.2144/btn-2018-0083. URL <http://dx.doi.org/10.2144/btn-2018-0083>.
- [34] Y. H. Choi, S. S. Lee, D. Lee, H. S. Jeong, and S. Kim. Composite Microgels Created by Complexation between Polyvinyl Alcohol and Graphene Oxide in Compressed Double-Emulsion Drops. *Small*, 16(9):e1903812–n/a, 2020. ISSN 1613-6810. doi: 10.1002/smll.201903812. URL <https://onlinelibrary.wiley.com/doi/abs/10.1002/smll.201903812>.
- [35] B. G. Chung, K.-H. Lee, A. Khademhosseini, and S.-H. Lee. Microfluidic fabrication of microengineered hydrogels and their application in tissue engineering. *Lab on a chip*, 12(1):45–59, 2012. ISSN 1473-0197. doi: 10.1039/C1LC20859D. URL <https://www.ncbi.nlm.nih.gov/pubmed/22105780>.
- [36] H. J. Chung and T. G. Park. Surface engineered and drug releasing pre-fabricated scaffolds for tissue engineering. *Advanced Drug Delivery Reviews*, 59(4):249–262, 2007. ISSN 0169-409X. doi: 10.1016/j.addr.2007.03.015. URL <http://dx.doi.org/10.1016/j.addr.2007.03.015>.
- [37] I. C. Clark and A. R. Abate. Microfluidic bead encapsulation above 20 kHz with triggered drop formation. *Lab on a chip*, 18(23):3598–3605, 2018. ISSN 1473-0197. doi: 10.1039/C8LC00514A. URL <https://www.ncbi.nlm.nih.gov/pubmed/30362490>.

- [38] T. Cubaud and T. G. Mason. Capillary threads and viscous droplets in square microchannels. *Physics of Fluids*, 20(5):053302–11, 2008. ISSN 1070-6631. doi: 10.1063/1.2911716. URL <http://dx.doi.org/10.1063/1.2911716>.
- [39] M. D. Scott, K. Matthews, and H. Ma. Assessing the Vascular Deformability of Erythrocytes and Leukocytes: From Micropipettes to Microfluidics. In I. Ahmed Hamed Khalil, editor, *Current and Future Aspects of Nanomedicine*. IntechOpen, May 2020. ISBN 978-1-78985-869-3 978-1-78985-870-9. doi: 10.5772/intechopen.90131. URL <https://www.intechopen.com/books/current-and-future-aspects-of-nanomedicine/assessing-the-vascular-deformability-of-erythrocytes-and-leukocytes-from-micropipettes-to-microfluidics>
- [40] A. C. Daly, L. Riley, T. Segura, and J. A. Burdick. Hydrogel microparticles for biomedical applications. *Nature Reviews Materials*, 5(1):20–43, Jan. 2020. ISSN 2058-8437. doi: 10.1038/s41578-019-0148-6. URL <http://www.nature.com/articles/s41578-019-0148-6>.
- [41] R. Dangla, E. Fradet, Y. Lopez, and C. N. Baroud. The physical mechanisms of step emulsification. *Journal of Physics D: Applied Physics*, 46(11):114003, 2013. ISSN 0022-3727. doi: 10.1088/0022-3727/46/11/114003. URL <https://hal-polytechnique.archives-ouvertes.fr/hal-00996486>.
- [42] R. Dangla, S. C. Kayi, and C. N. Baroud. Droplet microfluidics driven by gradients of confinement. *PNAS*, 110(3):853–858, 2013. doi: 10.1073/pnas.1209186110.
- [43] P. M. Davidson, G. R. Fedorchak, S. Mondésert-Deveraux, E. S. Bell, P. Isermann, D. Aubry, R. Allena, and J. Lammerding. High-throughput microfluidic micropipette aspiration device to probe time-scale dependent nuclear mechanics in intact cells. *Lab on a Chip*, 19(21):3652–3663, 2019. ISSN 1473-0197, 1473-0189. doi: 10.1039/C9LC00444K. URL <http://xlink.rsc.org/?DOI=C9LC00444K>.
- [44] J. de Vicente, J. Stokes, and H. Spikes. The Frictional Properties of Newtonian Fluids in Rolling–Sliding soft-EHL Contact. *Tribology Letters*, 20(3-4):273–286, Dec. 2005. ISSN 1023-8883, 1573-2711. doi: 10.1007/s11249-005-9067-3. URL <http://link.springer.com/10.1007/s11249-005-9067-3>.
- [45] D. Debroy, J. Oakey, and D. Li. Interfacially-mediated oxygen inhibition for precise and continuous poly(ethylene glycol) diacrylate (PEGDA) particle fabrication. *Journal of Colloid And Interface Science*, 510 (Journal Article):334–344, 2018. ISSN 0021-9797. doi: 10.1016/j.jcis.2017.09.081. URL <http://dx.doi.org/10.1016/j.jcis.2017.09.081>.
- [46] C. Decker and A. D. Jenkins. Kinetic Approach of O₂ Inhibition in Ultraviolet- and Laser-Induced Polymerizations. *Macromolecules*, 18(6):1241–1244, 1985. doi: <https://doi.org/10.1021/ma00148a034>.

- [47] F. Della Sala, M. Biondi, D. Guarnieri, A. Borzacchiello, L. Ambrosio, and L. Mayol. Mechanical behavior of bioactive poly(ethylene glycol) diacrylate matrices for biomedical application. *Journal of the Mechanical Behavior of Biomedical Materials*, 110:103885, Oct. 2020. ISSN 17516161. doi: 10.1016/j.jmbbm.2020.103885. URL <https://linkinghub.elsevier.com/retrieve/pii/S1751616120304392>.
- [48] C. L. Delley and A. R. Abate. Microfluidic particle zipper enables controlled loading of droplets with distinct particle types. *LAB on a chip*, 20(14):2465–2472, 2020. ISSN 1473-0197. doi: 10.1039/D0LC00339E.
- [49] D. Dendukuri and P. S. Doyle. The Synthesis and Assembly of Polymeric Microparticles Using Microfluidics. *Advanced Materials*, 21(41):4071–4086, Nov. 2009. ISSN 09359648, 15214095. doi: 10.1002/adma.200803386. URL <https://onlinelibrary.wiley.com/doi/10.1002/adma.200803386>.
- [50] D. Dendukuri, K. Tsoi, T. A. Hatton, and P. S. Doyle. Controlled Synthesis of Nonspherical Microparticles Using Microfluidics. *Langmuir*, 21(6):2113–2116, 2005. ISSN 0743-7463. doi: 10.1021/la047368k. URL <http://dx.doi.org/10.1021/la047368k>.
- [51] D. Dendukuri, T. A. Hatton, P. S. Doyle, J. Collins, and D. C. Pregibon. Continuous-flow lithography for high-throughput microparticle synthesis. *Nature Materials*, 5(5):365–369, 2006. ISSN 1476-1122. doi: 10.1038/nmat1617. URL <http://dx.doi.org/10.1038/nmat1617>.
- [52] D. Dendukuri, S. S. Gu, D. C. Pregibon, T. A. Hatton, and P. S. Doyle. Stop-flow lithography in a microfluidic device. *Lab on a chip*, 7(7):818, 2007. ISSN 1473-0197. doi: 10.1039/b703457a. URL <https://www.ncbi.nlm.nih.gov/pubmed/17593999>.
- [53] D. Dendukuri, P. Panda, R. Haghgooeie, J. M. Kim, T. A. Hatton, and P. S. Doyle. Modeling of Oxygen-Inhibited Free Radical Photopolymerization in a PDMS Microfluidic Device. *Macromolecules*, 41(22):8547–8556, 2008. ISSN 0024-9297. doi: 10.1021/ma801219w. URL <http://dx.doi.org/10.1021/ma801219w>.
- [54] E. Dressaire and A. Sauret. Clogging of microfluidic systems. *Soft Matter*, 13(1):37–48, 2017. ISSN 1744-683X, 1744-6848. doi: 10.1039/C6SM01879C. URL <http://xlink.rsc.org/?DOI=C6SM01879C>.
- [55] O. du Roure, A. Lindner, E. N. Nazockdast, and M. J. Shelley. Dynamics of Flexible Fibers in Viscous Flows and Fluids. *Annual Review of Fluid Mechanics*, 51(1):539–572, Jan. 2019. ISSN 0066-4189, 1545-4479. doi: 10.1146/annurev-fluid-122316-045153. URL <https://www.annualreviews.org/doi/10.1146/annurev-fluid-122316-045153>.
- [56] C. Duprat, H. Berthet, J. S. Wexler, O. du Roure, and A. Lindner. Microfluidic in situ mechanical testing of photopolymerized gels. *Lab on a Chip*, 15(1):244–252, 2015. ISSN 1473-0197, 1473-0189. doi: 10.1039/C4LC01034E. URL <http://xlink.rsc.org/?DOI=C4LC01034E>.

- [57] M. Elias, A. Dutoya, A. Laborde, A. Lecestre, C. Montis, L. Caselli, D. Berti, B. Lonetti, C. Roux, and P. Joseph. Microfluidic characterization of biomimetic membrane mechanics with an on-chip micropipette. *Micro and Nano Engineering*, 8:100064, Aug. 2020. ISSN 25900072. doi: 10.1016/j.mne.2020.100064. URL <https://linkinghub.elsevier.com/retrieve/pii/S2590007220300198>.
- [58] M. Esfahanian and B. J. Hamrock. Fluid-Film Lubrication Regimes Revisited. *Tribology Transactions*, 34(4): 628–632, Jan. 1991. ISSN 1040-2004, 1547-397X. doi: 10.1080/10402009108982081. URL <http://www.tandfonline.com/doi/abs/10.1080/10402009108982081>.
- [59] A. C. Fischer-Cripps. *Introduction to contact mechanics*. Mechanical engineering series. Springer, New York, 2nd ed edition, 2007. ISBN 978-0-387-68187-0 978-0-387-68188-7.
- [60] J. M. Fitz-Gerald. Mechanics of red-cell motion through very narrow capillaries. *Proceedings of the Royal Society of London. Series B. Biological Sciences*, 174(1035):193–227, Nov. 1969. ISSN 0080-4649, 2053-9193. doi: 10.1098/rspb.1969.0088. URL <https://royalsocietypublishing.org/doi/10.1098/rspb.1969.0088>.
- [61] S. Gabler, J. Stampfl, T. Koch, S. Seidler, G. Schuller, H. Redl, V. Juras, S. Trattnig, and R. Weidisch. Determination of the viscoelastic properties of hydrogels based on polyethylene glycol diacrylate (PEG-DA) and human articular cartilage. *International Journal of Materials Engineering Innovation*, 1(1):3, 2009. ISSN 1757-2754, 1757-2762. doi: 10.1504/IJMATEI.2009.024024. URL <http://www.inderscience.com/link.php?id=24024>.
- [62] P. Garstecki, H. A. Stone, and G. M. Whitesides. Mechanism for Flow-Rate Controlled Breakup in Confined Geometries: A Route to Monodisperse Emulsions. *PHYSICAL REVIEW LETTERS*, page 4, 2005.
- [63] B. Geraud, L. Bocquet, and C. Barentin. Confined flows of a polymer microgel. *The European Physical Journal E*, 36(3):30, Mar. 2013. ISSN 1292-8941, 1292-895X. doi: 10.1140/epje/i2013-13030-3. URL <http://link.springer.com/10.1140/epje/i2013-13030-3>.
- [64] B. González-Bermúdez, G. V. Guinea, and G. R. Plaza. Advances in Micropipette Aspiration: Applications in Cell Biomechanics, Models, and Extended Studies. *Biophysical Journal*, 116(4):587–594, 2019. ISSN 0006-3495. doi: 10.1016/j.bpj.2019.01.004. URL <http://www.sciencedirect.com/science/article/pii/S0006349519300207>.
- [65] D. R. Gossett, W. M. Weaver, A. J. Mach, S. C. Hur, H. T. K. Tse, W. Lee, H. Amini, and D. Di Carlo. Label-free cell separation and sorting in microfluidic systems. *Analytical and Bioanalytical Chemistry*, 397(8):3249–3267, Aug. 2010. ISSN 1618-2642, 1618-2650. doi: 10.1007/s00216-010-3721-9. URL <http://link.springer.com/10.1007/s00216-010-3721-9>.

- [66] C. B. Goy, R. E. Chaile, and R. Madrid, E. Microfluidics and hydrogel: A powerful combination. *Reactive and Functional Polymers*, 145(104314), 2019. ISSN 1381-5148. doi: 10.1016/j.reactfunctpolym.2019.104314. URL <http://www.sciencedirect.com/science/journal/13815148>.
- [67] J. Guegan, A. Kadiric, and H. Spikes. A Study of the Lubrication of EHL Point Contact in the Presence of Longitudinal Roughness. *Tribology Letters*, 59(1):22, July 2015. ISSN 1023-8883, 1573-2711. doi: 10.1007/s11249-015-0549-7. URL <http://link.springer.com/10.1007/s11249-015-0549-7>.
- [68] C. Gueronprez, S. Michelin, and C. N. Baroud. Flow distribution in parallel microfluidic networks and its effect on concentration gradient. *Biomicrofluidics*, 9(5):054119, Sept. 2015. ISSN 1932-1058. doi: 10.1063/1.4932305. URL <http://aip.scitation.org/doi/10.1063/1.4932305>.
- [69] M. M. Guest, T. Bond, R. G. Cooper, and J. R. Derrick. Red Blood Cells: Changes in Shape in Capillaries. *Science*, 142(3795):1319–1321, 1963. doi: 10.1126/science.142.3597.1319.
- [70] L. Guillou, A. Babataheri, P.-H. Puech, A. I. Barakat, and J. Husson. Dynamic monitoring of cell mechanical properties using profile microindentation. *Scientific Reports*, 6(1):21529, Aug. 2016. ISSN 2045-2322. doi: 10.1038/srep21529. URL <http://www.nature.com/articles/srep21529>.
- [71] M. Guo and H. M. Wyss. Micromechanics of soft particles. *Macromolecular materials and engineering*, 296(3-4):223–229, 2011. ISSN 1438-7492. doi: 10.1002/mame.201000359. URL <https://www.narcis.nl/publication/RecordID/oai:pure.tue.nl:publications%2Ffc2efe423-7175-4196-85d6-2a912f38a0c0>.
- [72] Q. Guo, S. Park, and H. Ma. Microfluidic micropipette aspiration for measuring the deformability of single cells. *Lab on a Chip*, 12(15):2687, 2012. ISSN 1473-0197, 1473-0189. doi: 10.1039/c2lc40205j. URL <http://xlink.rsc.org/?DOI=c2lc40205j>.
- [73] Q. Guo, S. P. Duffy, K. Matthews, A. T. Santoso, M. D. Scott, and H. Ma. Microfluidic analysis of red blood cell deformability. *Journal of Biomechanics*, 47(8):1767–1776, June 2014. ISSN 00219290. doi: 10.1016/j.jbiomech.2014.03.038. URL <https://linkinghub.elsevier.com/retrieve/pii/S0021929014002085>.
- [74] N. V. Gupta and H. G. Shivakumar. Investigation of Swelling Behavior and Mechanical Properties of a pH-Sensitive Superporous Hydrogel Composite. page 13, 2012.
- [75] Z. A. A. Hamid and K. W. Lim. Evaluation of UV-crosslinked Poly(ethylene glycol) Diacrylate/Poly(dimethylsiloxane) Dimethacrylate Hydrogel: Properties for Tissue Engineering Application. *Procedia Chemistry*, 19(Journal Article):410–418, 2016. ISSN 1876-6196. doi: 10.1016/j.proche.2016.03.032. URL <http://dx.doi.org/10.1016/j.proche.2016.03.032>.

- [76] B. J. Hamrock and D. Dowson. ISOTHERMAL ELASTOHYDRODYNAMIC LUBRICATION OF POINT CONTACTS II - ELLIPTICITY PARAMETER RESULTS. 98(3):375–381, 1976. doi: <https://doi.org/10.1115/1.3452861>.
- [77] B. J. Hamrock, S. R. Schmid, and B. O. Jacobson. *Fundamentals of fluid film lubrication*. Number 169 in Mechanical engineering. Marcel Dekker, New York, 2nd ed edition, 2004. ISBN 978-0-8247-5371-9.
- [78] K. Harth, J. Wang, T. Börzsönyi, and R. Stannarius. Intermittent flow and transient congestions of soft spheres passing narrow orifices. *Soft Matter*, 16(34):8013–8023, 2020. ISSN 1744-683X, 1744-6848. doi: 10.1039/D0SM00938E. URL <http://xlink.rsc.org/?DOI=D0SM00938E>.
- [79] A. L. Hazel and M. Heil. Surface-tension-induced buckling of liquid-lined elastic tubes: a model for pulmonary airway closure. *Proceedings of the Royal Society A: Mathematical, Physical and Engineering Sciences*, 461(2058):1847–1868, June 2005. ISSN 1364-5021, 1471-2946. doi: 10.1098/rspa.2005.1453. URL <https://royalsocietypublishing.org/doi/10.1098/rspa.2005.1453>.
- [80] R. M. Hochmuth. Micropipette aspiration of living cells. *Journal of Biomechanics*, 33(1):15–22, Jan. 2000. ISSN 00219290. doi: 10.1016/S0021-9290(99)00175-X. URL <https://linkinghub.elsevier.com/retrieve/pii/S002192909900175X>.
- [81] X. Hong, K. W. Desmond, D. Chen, and E. R. Weeks. Clogging and avalanches in quasi-two-dimensional emulsion hopper flow. *Physical Review E*, 105(1):014603, Jan. 2022. ISSN 2470-0045, 2470-0053. doi: 10.1103/PhysRevE.105.014603. URL <https://link.aps.org/doi/10.1103/PhysRevE.105.014603>.
- [82] C. J. Hooke. Calculation of Clearances in Soft Point Contacts. *Journal of Tribology*, 110(1):167–173, Jan. 1988. ISSN 0742-4787, 1528-8897. doi: 10.1115/1.3261558. URL <https://asmedigitalcollection.asme.org/tribology/article/110/1/167/436672/Calculation-of-Clearances-in-Soft-Point-Contacts>.
- [83] C. Hu, J. Kearn, P. Urwin, C. Lilley, V. O’ Connor, L. Holden-Dye, and H. Morgan. StyletChip: a microfluidic device for recording host invasion behaviour and feeding of plant parasitic nematodes. *Lab Chip*, 14(14):2447–2455, 2014. ISSN 1473-0197, 1473-0189. doi: 10.1039/C4LC00292J. URL <http://xlink.rsc.org/?DOI=C4LC00292J>.
- [84] X.-Q. Hu, A.-V. Salsac, and D. Barthès-Biesel. Flow of a spherical capsule in a pore with circular or square cross-section. *Journal of Fluid Mechanics*, 705:176–194, Aug. 2012. ISSN 0022-1120, 1469-7645. doi: 10.1017/jfm.2011.462. URL https://www.cambridge.org/core/product/identifier/S0022112011004629/type/journal_article.
- [85] S. Huang, A. Undisz, M. Diez-Silva, H. Bow, M. Dao, and J. Han. Dynamic deformability of Plasmodium falciparum-infected erythrocytes exposed to artesunate in vitro. *Integr. Biol.*, 5(2):414–422, 2013. ISSN 1757-

9694, 1757-9708. doi: 10.1039/C2IB20161E. URL <https://academic.oup.com/ib/article/5/2/414-422/5204178>.

- [86] D. K. Hwang, J. Oakey, M. Toner, J. A. Arthur, K. S. Anseth, S. Lee, A. Zeiger, K. J. Van Vliet, and P. S. Doyle. Stop-Flow Lithography for the Production of Shape-Evolving Degradable Microgel Particles. *Journal of the American Chemical Society*, 131(12):4499–4504, Apr. 2009. ISSN 0002-7863, 1520-5126. doi: 10.1021/ja809256d. URL <https://pubs.acs.org/doi/10.1021/ja809256d>.
- [87] P. A. Iuzzo, editor. *Handbook of Cardiac Anatomy, Physiology, and Devices*. Springer International Publishing, Cham, 2015. ISBN 978-3-319-19463-9 978-3-319-19464-6. doi: 10.1007/978-3-319-19464-6. URL <http://link.springer.com/10.1007/978-3-319-19464-6>.
- [88] R. F. Ismagilov, A. D. Stroock, P. J. A. Kenis, G. Whitesides, and H. A. Stone. Experimental and theoretical scaling laws for transverse diffusive broadening in two-phase laminar flows in microchannels. *Applied Physics Letters*, 76(17):2376–2378, Apr. 2000. ISSN 0003-6951, 1077-3118. doi: 10.1063/1.126351. URL <http://aip.scitation.org/doi/10.1063/1.126351>.
- [89] K. Izdihar, H. R. Abdul Razak, N. Supion, M. K. A. Karim, N. H. Osman, and M. Norkhairunnisa. Structural, Mechanical, and Dielectric Properties of Polydimethylsiloxane and Silicone Elastomer for the Fabrication of Clinical-Grade Kidney Phantom. *Applied Sciences*, 11(3):1172, Jan. 2021. ISSN 2076-3417. doi: 10.3390/app11031172. URL <https://www.mdpi.com/2076-3417/11/3/1172>.
- [90] R. K. Jain. Determinants of Tumor Blood Flow: A Review. *Cancer Research*, 48:2641–2658, 1988.
- [91] K. H. Jensen, K. Berg-Sørensen, H. Bruus, N. M. Holbrook, J. Liesche, A. Schulz, M. A. Zwieniecki, and T. Bohr. Sap flow and sugar transport in plants. *Reviews of Modern Physics*, 88(3):035007, Sept. 2016. ISSN 0034-6861, 1539-0756. doi: 10.1103/RevModPhys.88.035007. URL <https://link.aps.org/doi/10.1103/RevModPhys.88.035007>.
- [92] H. Jeong, S.-C. Jun, J.-Y. Cheon, and M. Park. A review on clogging mechanisms and managements in aquifer storage and recovery (ASR) applications. *Geosciences journal (Seoul, Korea)*, 22(4):667–679, 2018. ISSN 1226-4806. doi: 10.1007/s12303-017-0073-x. URL <https://www.kci.go.kr/kciportal/ci/sereArticleSearch/ciSereArtiView.kci?sereArticleSearchBean.artiId=ART002372609>.
- [93] P. Jesda and W. Khanittha. Rough Soft-EHL with Non-Newtonian Lubricant. *Applied Mechanics and Materials*, 736:57–63, Mar. 2015. ISSN 1662-7482. doi: 10.4028/www.scientific.net/AMM.736.57. URL <https://www.scientific.net/AMM.736.57>.

- [94] K. L. Johnson. One Hundred Years of Hertz Contact. *Proceedings of the Institution of Mechanical Engineers*, 196(1):363–378, June 1982. ISSN 0020-3483, 2058-1203. doi: 10.1243/PIME_PROC_1982_196_039_02. URL http://journals.sagepub.com/doi/10.1243/PIME_PROC_1982_196_039_02.
- [95] I. D. Johnston, D. K. McCluskey, C. K. L. Tan, and M. C. Tracey. Mechanical characterization of bulk Sylgard 184 for microfluidics and microengineering. *Journal of Micromechanics and Microengineering*, 24(3):035017, Mar. 2014. ISSN 0960-1317, 1361-6439. doi: 10.1088/0960-1317/24/3/035017. URL <https://iopscience.iop.org/article/10.1088/0960-1317/24/3/035017>.
- [96] Z. S. Khan, N. Kamyabi, F. Hussain, and S. A. Vanapalli. Passage times and friction due to flow of confined cancer cells, drops, and deformable particles in a microfluidic channel. *Convergent Science Physical Oncology*, 3(2):024001, Mar. 2017. ISSN 2057-1739. doi: 10.1088/2057-1739/aa5f60. URL <https://iopscience.iop.org/article/10.1088/2057-1739/aa5f60>.
- [97] D. Kim and D. J. Beebe. A bi-polymer micro one-way valve. *Sensors & Actuators: A. Physical*, 136(1):426–433, 2007. ISSN 0924-4247. doi: 10.1016/j.sna.2006.11.004. URL <https://www.sciencedirect.com/science/article/pii/S0924424706006960>.
- [98] A. M. Klein and E. Macosko. InDrops and Drop-seq technologies for single-cell sequencing. *Lab on a chip*, 17(15):254–2541, 2017. ISSN 1473-0197. doi: 10.1039/c7lc90070h. URL <https://www.ncbi.nlm.nih.gov/pubmed/28721415>.
- [99] A. M. Klein, L. Mazutis, I. Akartuna, N. Tallapragada, A. Veres, V. Li, L. Peshkin, D. A. Weitz, and M. W. Kirschner. Droplet Barcoding for Single-Cell Transcriptomics Applied to Embryonic Stem Cells. *Cell*, 161(5):1187–1201, 2015. ISSN 0092-8674. doi: 10.1016/j.cell.2015.04.044. URL <http://dx.doi.org/10.1016/j.cell.2015.04.044>.
- [100] T. Kong, L. Wang, H. M. Wyss, and H. C. Shum. Capillary micromechanics for core-shell particles. *Soft Matter*, 10(18):3271, 2014. ISSN 1744-683X, 1744-6848. doi: 10.1039/c3sm53066c. URL <http://xlink.rsc.org/?DOI=c3sm53066c>.
- [101] K. Krutkramelis, B. Xia, and J. Oakey. Monodisperse polyethylene glycol diacrylate hydrogel microsphere formation by oxygen-controlled photopolymerization in a microfluidic device. *Lab on a chip*, 16(8):1457–1465, 2016. ISSN 1473-0197. doi: 10.1039/c6lc00254d. URL <https://www.ncbi.nlm.nih.gov/pubmed/26987384>.
- [102] J. R. Lange, J. Steinwachs, T. Kolb, L. A. Lautscham, I. Harder, G. Whyte, and B. Fabry. Microconstriction Arrays for High-Throughput Quantitative Measurements of Cell Mechanical Properties. *Biophysical journal*, 109(1):26–34, 2015. ISSN 0006-3495. doi: 10.1016/j.bpj.2015.05.029. URL <https://search.datacite.org/works/10.1016/j.bpj.2015.05.029>.

- [103] A. Lashkaripour, C. Rodriguez, N. Mehdipour, R. Mardian, D. McIntyre, L. Ortiz, J. Campbell, and D. Densmore. Machine learning enables design automation of microfluidic flow-focusing droplet generation. *Nature Communications*, 12(1):1–14, 2021. ISSN 2041-1723. doi: 10.1038/s41467-020-20284-z. URL <https://www.nature.com/articles/s41467-020-20284-z>.
- [104] L. M. Lee and A. P. Liu. The Application of Micropipette Aspiration in Molecular Mechanics of Single Cells. *Journal of nanotechnology in engineering and medicine*, 5(4):0408011–0408016, 2014. ISSN 1949-2944. doi: 10.1115/1.4029936. URL <http://dx.doi.org/10.1115/1.4029936>.
- [105] L. M. Lee and A. P. Liu. A microfluidic pipette array for mechanophenotyping of cancer cells and mechanical gating of mechanosensitive channels. *Lab on a chip*, 15(1):264–273, 2015. ISSN 1473-0197. doi: 10.1039/C4LC01218F. URL <https://www.ncbi.nlm.nih.gov/pubmed/25361042>.
- [106] S. Lee, X. Tong, and F. Yang. Effects of the poly(ethylene glycol) hydrogel crosslinking mechanism on protein release. *Biomaterials Science*, 4(3):405–411, 2016. ISSN 2047-4830, 2047-4849. doi: 10.1039/C5BM00256G. URL <http://xlink.rsc.org/?DOI=C5BM00256G>.
- [107] W. Lee, L. M. Walker, and S. L. Anna. Role of geometry and fluid properties in droplet and thread formation processes in planar flow focusing. *Physics of Fluids*, 21(3):032103, Mar. 2009. ISSN 1070-6631, 1089-7666. doi: 10.1063/1.3081407. URL <http://aip.scitation.org/doi/10.1063/1.3081407>.
- [108] W. Lee, N. Kalashnikov, S. Mok, R. Halaoui, E. Kuzmin, A. J. Putnam, S. Takayama, M. Park, L. McCaffrey, R. Zhao, R. L. Leask, and C. Moraes. Dispersible hydrogel force sensors reveal patterns of solid mechanical stress in multicellular spheroid cultures. *Nature Communications*, 10(1):144, Dec. 2019. ISSN 2041-1723. doi: 10.1038/s41467-018-07967-4. URL <http://www.nature.com/articles/s41467-018-07967-4>.
- [109] S. Li, H. Yu, T.-D. Li, Z. Chen, W. Deng, A. Anbari, and J. Fan. Understanding transport of an elastic, spherical particle through a confining channel. *Applied Physics Letters*, 116(10):103705, Mar. 2020. ISSN 0003-6951, 1077-3118. doi: 10.1063/1.5139887. URL <http://aip.scitation.org/doi/10.1063/1.5139887>.
- [110] Y. Li, E. Kumacheva, and A. Ramachandran. The motion of a microgel in an axisymmetric constriction with a tapered entrance. *Soft Matter*, 9(43):10391, 2013. ISSN 1744-683X, 1744-6848. doi: 10.1039/c3sm51594j. URL <http://xlink.rsc.org/?DOI=c3sm51594j>.
- [111] Y. Li, O. S. Saryyer, A. Ramachandran, S. Panyukov, M. Rubinstein, and E. Kumacheva. Universal behavior of hydrogels confined to narrow capillaries. *Scientific Reports*, 5(1):17017, Dec. 2015. ISSN 2045-2322. doi: 10.1038/srep17017. URL <http://www.nature.com/articles/srep17017>.
- [112] Y.-J. Li, Y.-N. Yang, H.-J. Zhang, C.-D. Xue, D.-P. Zeng, T. Cao, and K.-R. Qin. A Microfluidic Micropipette Aspiration Device to Study Single-Cell Mechanics Inspired by the Principle of Wheatstone Bridge. *Micromachines*,

10(2):131, Feb. 2019. ISSN 2072-666X. doi: 10.3390/mi10020131. URL <http://www.mdpi.com/2072-666X/10/2/131>.

- [113] K. K. Liu, D. R. Williams, and B. J. Briscoe. The large deformation of a single micro-elastomeric sphere. *Journal of Physics D: Applied Physics*, 31(3):294–303, Feb. 1998. ISSN 0022-3727, 1361-6463. doi: 10.1088/0022-3727/31/3/008. URL <https://iopscience.iop.org/article/10.1088/0022-3727/31/3/008>.
- [114] Y. Liu, B. Chakrabarti, D. Saintillan, A. Lindner, and O. du Roure. Morphological transitions of elastic filaments in shear flow. *Proceedings of the National Academy of Sciences*, 115(38):9438–9443, Sept. 2018. ISSN 0027-8424, 1091-6490. doi: 10.1073/pnas.1805399115. URL <https://pnas.org/doi/full/10.1073/pnas.1805399115>.
- [115] J.-F. Louf, J. Knoblauch, and K. H. Jensen. Bending and Stretching of Soft Pores Enable Passive Control of Fluid Flows. *Physical review letters*, 125(9):098101, 2020. ISSN 0031-9007. doi: 10.1103/PhysRevLett.125.098101. URL <https://search.proquest.com/docview/2442215477>.
- [116] A. A. Lubrecht and C. H. Venner. Elastohydrodynamic lubrication of rough surfaces. *Proceedings of the Institution of Mechanical Engineers, Part J: Journal of Engineering Tribology*, 213(5):397–404, May 1999. ISSN 1350-6501, 2041-305X. doi: 10.1243/1350650991542767. URL <http://journals.sagepub.com/doi/10.1243/1350650991542767>.
- [117] Y. Luo, D. Chen, Y. Zhao, C. Wei, X. Zhao, W. Yue, R. Long, J. Wang, and J. Chen. A constriction channel based microfluidic system enabling continuous characterization of cellular instantaneous Young's modulus. *Sensors and Actuators B: Chemical*, 202:1183–1189, Oct. 2014. ISSN 09254005. doi: 10.1016/j.snb.2014.05.028. URL <https://linkinghub.elsevier.com/retrieve/pii/S0925400514005474>.
- [118] E. Z. Macosko, A. Basu, R. Satija, J. Nemes, K. Shekhar, M. Goldman, I. Tirosh, A. R. Bialas, N. Kamitaki, E. M. Martersteck, J. J. Trombetta, D. A. Weitz, J. R. Sanes, A. K. Shalek, A. Regev, and S. A. McCarroll. Highly Parallel Genome-wide Expression Profiling of Individual Cells Using Nanoliter Droplets. *Cell*, 161(5):1202–1214, 2015. ISSN 0092-8674. doi: 10.1016/j.cell.2015.05.002. URL <http://dx.doi.org/10.1016/j.cell.2015.05.002>.
- [119] M. Mak and D. Erickson. A serial micropipette microfluidic device with applications to cancer cell repeated deformation studies. *Integrative Biology*, 5(11):1374–1384, Nov. 2013. ISSN 1757-9708. doi: 10.1039/c3ib40128f. URL <https://academic.oup.com/ib/article/5/11/1374/5204231>.
- [120] H. Manikantan and T. M. Squires. Surfactant dynamics: hidden variables controlling fluid flows. *Journal of Fluid Mechanics*, 892:P1, June 2020. ISSN 0022-1120, 1469-7645. doi: 10.1017/jfm.2020.170. URL https://www.cambridge.org/core/product/identifier/S0022112020001706/type/journal_article.

- [121] C. D. Markert, X. Guo, A. Skardal, Z. Wang, S. Bharadwaj, Y. Zhang, K. Bonin, and M. Guthold. Characterizing the micro-scale elastic modulus of hydrogels for use in regenerative medicine. *Journal of the Mechanical Behavior of Biomedical Materials*, 27:115–127, Nov. 2013. ISSN 17516161. doi: 10.1016/j.jmbbm.2013.07.008. URL <https://linkinghub.elsevier.com/retrieve/pii/S1751616113002397>.
- [122] R. Martinez-Duarte and M. J. Madou. SU-8 Photolithography and Its Applications in Microfluidics. In S. K. Mitra and S. Chakraborty, editors, *Microfluidics and Nanofluidics Handbook Fabrication, Implementation and Applications*, pages 229–244. CRC Press, 1 edition, 2017. ISBN 978-1-138-07238-1. doi: 10.1201/b11188-11. URL <https://www.taylorfrancis.com/books/9781439816738/chapters/10.1201/b11188-11>.
- [123] N. Marx, J. Guegan, and H. A. Spikes. Elastohydrodynamic film thickness of soft EHL contacts using optical interferometry. *Tribology International*, 99:267–277, July 2016. ISSN 0301679X. doi: 10.1016/j.triboint.2016.03.020. URL <https://linkinghub.elsevier.com/retrieve/pii/S0301679X16300287>.
- [124] V. Miralles, A. Huerre, F. Malloggi, and M.-C. Jullien. A Review of Heating and Temperature Control in Microfluidic Systems: Techniques and Applications. *Diagnostics*, 3(1):33–67, Jan. 2013. ISSN 2075-4418. doi: 10.3390/diagnostics3010033. URL <http://www.mdpi.com/2075-4418/3/1/33>.
- [125] S. K. Mitra and S. Chakraborty. *Microfluidics and Nanofluidics Handbook: Fabrication, Implementation, and Applications*. 1 edition, 2017. ISBN 978-1-138-07238-1.
- [126] E. M. Moore and J. L. West. Bioactive Poly(ethylene Glycol) Acrylate Hydrogels for Regenerative Engineering. *Regenerative Engineering and Translational Medicine*, 5(2):167–179, June 2019. ISSN 2364-4133, 2364-4141. doi: 10.1007/s40883-018-0074-y. URL <http://link.springer.com/10.1007/s40883-018-0074-y>.
- [127] N. A. Mortensen, F. Okkels, and H. Bruus. Reexamination of Hagen-Poiseuille flow: Shape dependence of the hydraulic resistance in microchannels. *Physical review. E, Statistical, nonlinear, and soft matter physics*, 71 (5 Pt 2):057301–Poiseuille flow: Shape dependence of the hydraulic resistance in microchannels', Physical Review E, vol. 71, no. 5, pp. 057301. <https://doi.org/10.1103/PhysRevE.71.057301>, 2005. ISSN 1539-3755. doi: 10.1103/PhysRevE.71.057301. URL <https://www.ncbi.nlm.nih.gov/pubmed/16089701>.
- [128] L. Mugerli, A. Lety-Stefanska, N. Landreau, R. F.-X. Tomasi, and C. N. Baroud. Quantifying the sol–gel process and detecting toxic gas in an array of anchored microfluidic droplets. *Lab on a Chip*, 20(2):236–243, 2020. ISSN 1473-0197, 1473-0189. doi: 10.1039/C9LC00750D. URL <http://xlink.rsc.org/?DOI=C9LC00750D>.
- [129] Z. Nie, S. Xu, M. Seo, P. C. Lewis, and E. Kumacheva. Polymer Particles with Various Shapes and Morphologies Produced in Continuous Microfluidic Reactors. *Journal of the American Chemical Society*,

127(22):8058–8063, June 2005. ISSN 0002-7863, 1520-5126. doi: 10.1021/ja042494w. URL <https://pubs.acs.org/doi/10.1021/ja042494w>.

- [130] Z. Nie, W. Li, M. Seo, S. Xu, and E. Kumacheva. Janus and Ternary Particles Generated by Microfluidic Synthesis: Design, Synthesis, and Self-Assembly. *Journal of the American Chemical Society*, 128(29):9408–9412, July 2006. ISSN 0002-7863, 1520-5126. doi: 10.1021/ja060882n. URL <https://pubs.acs.org/doi/10.1021/ja060882n>.
- [131] G. Nijenbanning, C. Venner, and H. Moes. Film thickness in elastohydrodynamically lubricated elliptic contacts. *Wear*, 176(2):217–229, Aug. 1994. ISSN 00431648. doi: 10.1016/0043-1648(94)90150-3. URL <https://linkinghub.elsevier.com/retrieve/pii/0043164894901503>.
- [132] T. Nisisako, S. Okushima, and T. Torii. Controlled formulation of monodisperse double emulsions in a multiple-phase microfluidic system. *Soft Matter*, 1(1):23–27, 2005. doi: 10.1039/B501972A. URL <https://pubs.rsc.org/en/content/articlelanding/2005/sm/b501972a>.
- [133] X. Niu, S. Gulati, J. B. Edel, and A. J. deMello. Pillar-induced droplet merging in microfluidic circuits. *Lab on a Chip*, 8(11):1837, 2008. ISSN 1473-0197, 1473-0189. doi: 10.1039/b813325e. URL <http://xlink.rsc.org/?DOI=b813325e>.
- [134] M. L. Oyen. Mechanical characterisation of hydrogel materials. *International Materials Reviews*, 59(1):44–59, Jan. 2014. ISSN 0950-6608, 1743-2804. doi: 10.1179/1743280413Y.0000000022. URL <http://www.tandfonline.com/doi/full/10.1179/1743280413Y.0000000022>.
- [135] M. P. Paidoussis, S. J. Price, and E. de Langre. *Fluid-Structure Interactions Cross-Flow-Induced Instabilities*. Cambridge University Press, 1 edition, 2010. ISBN 978-0-511-76079-2.
- [136] M. Piagnerelli, K. Z. Boudjeltia, M. Vanhaeverbeek, and J.-L. Vincent. Red blood cell rheology in sepsis. *Intensive Care Medicine*, 29(7):1052–1061, July 2003. ISSN 0342-4642, 1432-1238. doi: 10.1007/s00134-003-1783-2. URL <http://link.springer.com/10.1007/s00134-003-1783-2>.
- [137] D. Pihler-Puzović, R. Périllat, M. Russell, A. Juel, and M. Heil. Modelling the suppression of viscous fingering in elastic-walled Hele-Shaw cells. *Journal of Fluid Mechanics*, 731:162–183, Sept. 2013. ISSN 0022-1120, 1469-7645. doi: 10.1017/jfm.2013.375. URL https://www.cambridge.org/core/product/identifier/S0022112013003753/type/journal_article.
- [138] V. L. Popov, M. Heß, and E. Willert. *Handbook of Contact Mechanics: Exact Solutions of Axisymmetric Contact Problems*. Springer Berlin Heidelberg, Berlin, Heidelberg, 2019. ISBN 978-3-662-58708-9 978-3-662-58709-6. doi: 10.1007/978-3-662-58709-6. URL <http://link.springer.com/10.1007/978-3-662-58709-6>.

- [139] P. Preira, M.-P. Valignat, J. Bico, and O. Théodoly. Single cell rheometry with a microfluidic constriction: Quantitative control of friction and fluid leaks between cell and channel walls. *Biomicrofluidics*, 7(2):024111, Mar. 2013. ISSN 1932-1058. doi: 10.1063/1.4802272. URL <http://aip.scitation.org/doi/10.1063/1.4802272>.
- [140] D. Qin, Y. Xia, and G. M. Whitesides. Soft lithography for micro- and nanoscale patterning. *Nature Protocols*, 5(3):491–502, Mar. 2010. ISSN 1754-2189, 1750-2799. doi: 10.1038/nprot.2009.234. URL <http://www.nature.com/articles/nprot.2009.234>.
- [141] A. Ranga, S. Gobaa, Y. Okawa, K. Mosiewicz, A. Negro, and M. P. Lutolf. 3D niche microarrays for systems-level analyses of cell fate. *Nature Communications*, 5(1):4324, Sept. 2014. ISSN 2041-1723. doi: 10.1038/ncomms5324. URL <http://www.nature.com/articles/ncomms5324>.
- [142] O. Reynolds. On the Theory of Lubrication and Its Application to Mr. Beauchamp Tower’s Experiments, Including an Experimental Determination of the Viscosity of Olive Oil. *Philosophical Transactions of the Royal Society of London*, 177:157–234, 1886. doi: doi:10.1098/rstl.1886.0005.
- [143] G. Ronteix, S. Jain, C. Angely, M. Cazaux, R. khazen, P. Bousso, and C. N. Baroud. High resolution microfluidic assay and probabilistic modeling reveal cooperation between T cells in tumor killing. *Nature Communications*, 13:3111, 2022. doi: <https://doi.org/10.1038/s41467-022-30575-2>.
- [144] M. J. Rosenbluth, W. A. Lam, and D. A. Fletcher. Analyzing cell mechanics in hematologic diseases with microfluidic biophysical flow cytometry. *Lab on a Chip*, 8(7):1062, 2008. ISSN 1473-0197, 1473-0189. doi: 10.1039/b802931h. URL <http://xlink.rsc.org/?DOI=b802931h>.
- [145] P. Sadowski and S. Stupkiewicz. Friction in lubricated soft-on-hard, hard-on-soft and soft-on-soft sliding contacts. *Tribology International*, 129:246–256, Jan. 2019. ISSN 0301679X. doi: 10.1016/j.triboint.2018.08.025. URL <https://linkinghub.elsevier.com/retrieve/pii/S0301679X18304213>.
- [146] S. Sart, G. Ronteix, S. Jain, G. Amselem, and C. N. Baroud. Cell Culture in Microfluidic Droplets. *Chem. Rev.*, page 36, 2022.
- [147] R. Schlüßler, S. Möllmert, S. Abuhattum, G. Cojoc, P. Müller, K. Kim, C. Möckel, C. Zimmermann, J. Czarske, and J. Guck. Mechanical Mapping of Spinal Cord Growth and Repair in Living Zebrafish Larvae by Brillouin Imaging. *Biophysical Journal*, 115(5):911–923, Sept. 2018. ISSN 00063495. doi: 10.1016/j.bpj.2018.07.027. URL <https://linkinghub.elsevier.com/retrieve/pii/S0006349518309135>.
- [148] L. W. Schwartz, H. M. Princen, and A. D. Kiss. On the motion of bubbles in capillary tubes. *Journal of Fluid Mechanics*, 172(-1):259, Nov. 1986. ISSN 0022-1120, 1469-7645. doi: 10.1017/S0022112086001738. URL http://www.journals.cambridge.org/abstract_S0022112086001738.

- [149] B. Sebastian and P. S. Dittich. Microfluidics to Mimic Blood Flow in Health and Disease. *Annual Review of Fluid Mechanics*, 50(1):483–504, Jan. 2018. ISSN 0066-4189, 1545-4479. doi: 10.1146/annurev-fluid-010816-060246. URL <https://www.annualreviews.org/doi/10.1146/annurev-fluid-010816-060246>.
- [150] J. P. Shelby, J. White, K. Ganesan, P. K. Rathod, and D. T. Chiu. A microfluidic model for single-cell capillary obstruction by *Plasmodium falciparum* -infected erythrocytes. *Proceedings of the National Academy of Sciences*, 100(25):14618–14622, Dec. 2003. ISSN 0027-8424, 1091-6490. doi: 10.1073/pnas.2433968100. URL <https://pnas.org/doi/full/10.1073/pnas.2433968100>.
- [151] R. F. Shepherd, J. C. Conrad, S. K. Rhodes, D. R. Link, M. Marquez, D. A. Weitz, and J. A. Lewis. Microfluidic Assembly of Homogeneous and Janus Colloid-Filled Hydrogel Granules. *Langmuir*, 22(21):8618–8622, Oct. 2006. ISSN 0743-7463, 1520-5827. doi: 10.1021/la060759+. URL <https://pubs.acs.org/doi/10.1021/la060759%2B>.
- [152] R. F. Shepherd, P. Panda, Z. Bao, K. H. Sandhage, T. A. Hatton, J. A. Lewis, and P. S. Doyle. Stop-Flow Lithography of Colloidal, Glass, and Silicon Microcomponents. *Advanced Materials*, 20(24):4734–4739, Dec. 2008. ISSN 0935-9648, 1521-4095. doi: 10.1002/adma.200801090. URL <https://onlinelibrary.wiley.com/doi/10.1002/adma.200801090>.
- [153] B. V. Slaughter, S. S. Khurshid, O. Z. Fisher, A. Khademhosseini, and N. A. Peppas. Hydrogels in Regenerative Medicine. *Advanced Materials*, 21(32-33):3307–3329, Sept. 2009. ISSN 09359648, 15214095. doi: 10.1002/adma.200802106. URL <https://onlinelibrary.wiley.com/doi/10.1002/adma.200802106>.
- [154] A. Z. Szeri. On the flow of emulsions in tribological contacts. *Wear*, 200:12, 1996. doi: doi:10.1016/s0043-1648(96)07251-1.
- [155] A. Z. Szeri. *Fluid film lubrication*. Cambridge University Press, Cambridge ; New York, 2nd ed edition, 2011. ISBN 978-0-521-89823-2. OCLC: ocn656772007.
- [156] R. Tao, M. Wilson, and E. R. Weeks. Soft particle clogging in two-dimensional hoppers. *Physical Review E*, 104(4):044909, Oct. 2021. ISSN 2470-0045, 2470-0053. doi: 10.1103/PhysRevE.104.044909. URL <https://link.aps.org/doi/10.1103/PhysRevE.104.044909>.
- [157] D. P. Theret, M. J. Levesque, M. Sato, R. M. Nerem, and L. T. Wheeler. The Application of a Homogeneous Half-Space Model in the Analysis of Endothelial Cell Micropipette Measurements. *Journal of biomechanical engineering*, 110(3):190–199, 1988. ISSN 0148-0731. doi: 10.1115/1.3108430. URL <http://dx.doi.org/10.1115/1.3108430>.

- [158] W. Thielicke and E. J. Stamhuis. PIVlab- Towards User-Friendly, Affordable and Accurate Digital Particle Image Velocimetry in MATLAB. *Journal of Open Research Software*, 2, 2014. doi: doi:10.5334/jors.bl.
- [159] S. Tlili, F. Graner, and H. Delanoë-Ayari. A microfluidic platform to investigate the role of mechanical constraints on tissue reorganization. preprint, Biophysics, Mar. 2022. URL <http://biorxiv.org/lookup/doi/10.1101/2022.03.16.484527>.
- [160] M. Tokeshi. *Applications of Microfluidic Systems in Biology and Medicine*, volume 7 of *Bioanalysis Advanced Materials, Methods and Devices*. Springer Nature, 2019. ISBN 978-981-13-6228-6.
- [161] G. E. Totten. *Handbook of Hydraulic Fluid Technology*. CRC Press, 0 edition, Oct. 2011. ISBN 978-0-429-09284-8. doi: 10.1201/b11225. URL <https://www.taylorfrancis.com/books/9781420085273>.
- [162] N. Träber, K. Uhlmann, S. Girardo, G. Kesavan, K. Wagner, J. Friedrichs, R. Goswami, K. Bai, M. Brand, C. Werner, D. Balzani, and J. Guck. Polyacrylamide Bead Sensors for in vivo Quantification of Cell-Scale Stress in Zebrafish Development. *Scientific Reports*, 9(1):17031, Dec. 2019. ISSN 2045-2322. doi: 10.1038/s41598-019-53425-6. URL <http://www.nature.com/articles/s41598-019-53425-6>.
- [163] M. V. Turturro, D. M. V. Rendón, F. Teymour, and G. Papavasiliou. Kinetic Investigation of Poly(ethylene glycol) Hydrogel Formation via Perfusion-Based Frontal Photopolymerization: Influence of Free-Radical Polymerization Conditions on Frontal Velocity and Swelling Gradients: Kinetic Investigation of Poly(ethylene glycol) Hydrogel Formation via Perfusion-Based Frontal *Macromolecular Reaction Engineering*, 7(2):107–115, Feb. 2013. ISSN 1862832X. doi: 10.1002/mren.201200063. URL <https://onlinelibrary.wiley.com/doi/10.1002/mren.201200063>.
- [164] K. Upadhyay, G. Subhash, and D. Spearot. Hyperelastic constitutive modeling of hydrogels based on primary deformation modes and validation under 3D stress states. *International Journal of Engineering Science*, 154:103314, Sept. 2020. ISSN 00207225. doi: 10.1016/j.ijengsci.2020.103314. URL <https://linkinghub.elsevier.com/retrieve/pii/S0020722520301026>.
- [165] S. A. Vanapalli, D. van den Ende, M. H. G. Duits, and F. Mugele. Scaling of interface displacement in a microfluidic comparator. *Applied Physics Letters*, 90(11):114109, Mar. 2007. ISSN 0003-6951, 1077-3118. doi: 10.1063/1.2713800. URL <http://aip.scitation.org/doi/10.1063/1.2713800>.
- [166] S. A. Vanapalli, A. G. Banpurkar, D. van den Ende, M. H. G. Duits, and F. Mugele. Hydrodynamic resistance of single confined moving drops in rectangular microchannels. *Lab Chip*, 9(7):982–990, 2009. ISSN 1473-0197, 1473-0189. doi: 10.1039/B815002H. URL <http://xlink.rsc.org/?DOI=B815002H>.
- [167] D. Vera, M. García-Díaz, N. Torras, M. Álvarez, R. Villa, and E. Martínez. Engineering Tissue Barrier Models on Hydrogel Microfluidic Platforms. *ACS Applied Materials & Interfaces*, 13(12):13920–13933, Mar. 2021.

ISSN 1944-8244, 1944-8252. doi: 10.1021/acsami.0c21573. URL <https://pubs.acs.org/doi/10.1021/acsami.0c21573>.

- [168] G. T. Vladislavljević, N. Khalid, M. A. Neves, T. Kuroiwa, M. Nakajima, K. Uemura, S. Ichikawa, and I. Kobayashi. Industrial lab-on-a-chip: Design, applications and scale-up for drug discovery and delivery. *Advanced Drug Delivery Reviews*, 65(11-12):1626–1663, 2013. ISSN 0169-409X. doi: 10.1016/j.addr.2013.07.017. URL <http://dx.doi.org/10.1016/j.addr.2013.07.017>.
- [169] J. C. Weeks, W. M. Roberts, K. J. Robinson, M. Keaney, J. J. Vermeire, J. F. Urban, S. R. Lockery, and J. M. Hawdon. Microfluidic platform for electrophysiological recordings from host-stage hookworm and *Ascaris suum* larvae: A new tool for anthelmintic research. *International Journal for Parasitology: Drugs and Drug Resistance*, 6(3):314–328, Dec. 2016. ISSN 22113207. doi: 10.1016/j.ijpddr.2016.08.001. URL <https://linkinghub.elsevier.com/retrieve/pii/S2211320716300458>.
- [170] W. Wilson, Y. Sakaguchi, and S. Schmid. A dynamic concentration model for lubrication with oil-in-water emulsions. *Wear*, 161(1-2):207–212, Apr. 1993. ISSN 00431648. doi: 10.1016/0043-1648(93)90471-W. URL <https://linkinghub.elsevier.com/retrieve/pii/004316489390471W>.
- [171] H. Wong, C. J. Radke, and S. Morris. The motion of long bubbles in polygonal capillaries. Part 1. Thin films. *Journal of Fluid Mechanics*, 292:71–94, June 1995. ISSN 0022-1120, 1469-7645. doi: 10.1017/S0022112095001443. URL https://www.cambridge.org/core/product/identifier/S0022112095001443/type/journal_article.
- [172] P.-H. Wu, D. R.-B. Aroush, A. Asnacios, W.-C. Chen, M. E. Dokukin, B. L. Doss, P. Durand-Smet, A. Ekpenyong, J. Guck, N. V. Guz, P. A. Janmey, J. S. H. Lee, N. M. Moore, A. Ott, Y.-C. Poh, R. Ros, M. Sander, I. Sokolov, J. R. Staunton, N. Wang, G. Whyte, and D. Wirtz. A comparison of methods to assess cell mechanical properties. *Nature Methods*, 15(7):491–498, July 2018. ISSN 1548-7091, 1548-7105. doi: 10.1038/s41592-018-0015-1. URL <http://www.nature.com/articles/s41592-018-0015-1>.
- [173] H. M. Wyss, T. Franke, E. Mele, and D. A. Weitz. Capillary micromechanics: Measuring the elasticity of microscopic soft objects. *Soft matter*, 6(18):4550–4555, 2010. ISSN 1744-6848. doi: 10.1039/c003344h. URL <https://search.datacite.org/works/10.1039/c003344h>.
- [174] S. Xu, Z. Nie, M. Seo, P. Lewis, E. Kumacheva, H. A. Stone, P. Garstecki, D. B. Weibel, I. Gitlin, and G. M. Whitesides. Generation of Monodisperse Particles by Using Microfluidics: Control over Size, Shape, and Composition. *Angewandte Chemie*, 117(5):734–738, Jan. 2005. ISSN 0044-8249, 1521-3757. doi: 10.1002/ange.200462226. URL <https://onlinelibrary.wiley.com/doi/10.1002/ange.200462226>.

- [175] Y. Xu, G. Yu, R. Nie, and Z. Wu. Microfluidic systems toward blood hemostasis monitoring and thrombosis diagnosis: From design principles to micro/nano fabrication technologies. *VIEW*, 3(1):20200183, Jan. 2022. ISSN 2688-268X, 2688-268X. doi: 10.1002/VIW.20200183. URL <https://onlinelibrary.wiley.com/doi/10.1002/VIW.20200183>.
- [176] Y. Xu, H. Zhu, Y. Shen, A. P. M. Guttenplan, K. L. Saar, Y. Lu, D. Vigolo, L. S. Itzhaki, and T. P. J. Knowles. Micromechanics of soft materials using microfluidics. *MRS Bulletin*, 47(2):119–126, Feb. 2022. ISSN 0883-7694, 1938-1425. doi: 10.1557/s43577-022-00279-5. URL <https://link.springer.com/10.1557/s43577-022-00279-5>.
- [177] C. Xue, J. Wang, Y. Zhao, D. Chen, W. Yue, and J. Chen. Constriction Channel Based Single-Cell Mechanical Property Characterization. *Micromachines*, 6(11):1794–1804, Nov. 2015. ISSN 2072-666X. doi: 10.3390/mi6111457. URL <http://www.mdpi.com/2072-666X/6/11/1457>.
- [178] P. Xue, Y. Wu, N. V. Menon, and Y. Kang. Microfluidic synthesis of monodisperse PEGDA microbeads for sustained release of 5-fluorouracil. *Microfluidics and Nanofluidics*, 18(2):333–342, Feb. 2015. ISSN 1613-4982, 1613-4990. doi: 10.1007/s10404-014-1436-5. URL <http://link.springer.com/10.1007/s10404-014-1436-5>.
- [179] Y. Yoon, S. Kim, J. Lee, J. Choi, R.-K. Kim, S.-J. Lee, O. Sul, and S.-B. Lee. Clogging-free microfluidics for continuous size-based separation of microparticles. *Scientific Reports*, 6(1):26531, May 2016. ISSN 2045-2322. doi: 10.1038/srep26531. URL <http://www.nature.com/articles/srep26531>.
- [180] S. Yue, H. He, B. Li, and T. Hou. Hydrogel as a Biomaterial for Bone Tissue Engineering: A Review. *Nanomaterials*, 10(8):1511, July 2020. ISSN 2079-4991. doi: 10.3390/nano10081511. URL <https://www.mdpi.com/2079-4991/10/8/1511>.
- [181] E. A. Zargari, P. K. Jimack, and M. A. Walkley. An investigation of the film thickness calculation for elastohydrodynamic lubrication problems. page 7, 2007.
- [182] H. Zhang, L. Wang, L. Song, G. Niu, H. Cao, G. Wang, H. Yang, and S. Zhu. Controllable properties and microstructure of hydrogels based on crosslinked poly(ethylene glycol) diacrylates with different molecular weights. *Journal of Applied Polymer Science*, 121(1):531–540, July 2011. ISSN 00218995. doi: 10.1002/app.33653. URL <https://onlinelibrary.wiley.com/doi/10.1002/app.33653>.
- [183] X. Zhang, L. Li, and C. Luo. Gel integration for microfluidic applications. *Lab on a Chip*, 16(10):1757–1776, 2016. ISSN 1473-0197, 1473-0189. doi: 10.1039/C6LC00247A. URL <http://xlink.rsc.org/?DOI=C6LC00247A>.

- [184] Z. Zhang, J. Xu, and C. Drapaca. Particle squeezing in narrow confinements. *Microfluidics and Nanofluidics*, 22(10):120, Oct. 2018. ISSN 1613-4982, 1613-4990. doi: 10.1007/s10404-018-2129-2. URL <http://link.springer.com/10.1007/s10404-018-2129-2>.
- [185] S. Zheng, H. Lin, J.-Q. Liu, M. Balic, R. Datar, R. J. Cote, and Y.-C. Tai. Membrane microfilter device for selective capture, electrolysis and genomic analysis of human circulating tumor cells. *Journal of Chromatography A*, 1162(2):154–161, Aug. 2007. ISSN 00219673. doi: 10.1016/j.chroma.2007.05.064. URL <https://linkinghub.elsevier.com/retrieve/pii/S0021967307009478>.
- [186] D. Zhu, G. Biresaw, S. J. Clark, and T. J. Kasun. Elastohydrodynamic Lubrication With O/W Emulsions. *Journal of Tribology*, 116(2):310–319, Apr. 1994. ISSN 0742-4787, 1528-8897. doi: 10.1115/1.2927216. URL <https://asmedigitalcollection.asme.org/tribology/article/116/2/310/419391/Elastohydrodynamic-Lubrication-With-OW-Emulsions>.
- [187] R. Zilionis, J. Nainys, A. Veres, V. Savova, D. Zemmour, A. M. Klein, and L. Mazutis. Single-cell barcoding and sequencing using droplet microfluidics. *Nature protocols*, 12(1):44–73, 2016. ISSN 1750-2799. doi: 10.1038/nprot.2016.154. URL <https://search.datacite.org/works/10.1038/nprot.2016.154>.

Titre: Interaction Fluide-Structure des microgels dans les systemes microfluidiques simples

Mots clés: Microfluidiques, Mécanique des Fluides, Interaction Fluide-Structurelle, Mécaniques des Contacts, Hydrogels

Résumé: Quel est le rapport entre l'aspiration de perles de tapioca à travers une paille et les tests génétiques microfluidiques? Tous deux impliquent de faire passer des sphères molles à travers une constriction. Cette thèse étudie l'interaction fluide-structure de gels se comprimant à travers des constriction microfluidiques.

La première étude réalisée dans cette thèse examine comment une particule entre dans une constriction. Sous l'effet de l'écoulement, le microgel est poussé dans la constriction, se déforme, et finit par obstruer le canal. Ceci pose un problème fluide-structure géométriquement compliqué. Pour com-

prendre cette interaction, c'est d'abord nécessaire d'analyser la déformation du particule sous pression, et séparément d'analyser les flux autour d'une particule déformée. La résolution de ces deux aspects permet de fabriquer des valves microfluidiques, et donne accès à l'élasticité du gel.

La deuxième étude reprend après l'entrée d'un gel dans une constriction. Les billes de gel sont acheminées à travers un comparateur microfluidique afin de mesurer leur vitesse ainsi que la résistance hydrodynamique qu'elles ajoutent au canal. La friction des gels est due au couche lubrifiant, et dépend de la vitesse, de l'élasticité et de la taille du gel.

Title: Fluid Structure Interactions of Microgels in Simple Microfluidic Systems

Keywords: Microfluidics, Fluid Mechanics, Fluid-structure Interaction, Contact Mechanics, Hydrogels

Abstract: What does sucking a tapioca ball through a straw have to do with microfluidic genetic testing? Both involve pushing soft spheres through a constriction. This thesis investigates the fluid structure interaction of soft gels squeezing through microfluidic constrictions.

The first study done in this thesis looks at how a particle enters into a constriction. Fluid flow pushes the microgel into the constriction, deforming until it plugs the flow. This presents a geometrically complicated problem combining fluid and solid mechanics. To understand this problem, it is necessary to first separately

analyze the particle deformation under pressure, and the flow around a deformed particle. Solving these two aspects allows for making microfluidic flow limiting valves and also measuring gel elasticity.

The second study picks up after a gel has entered into a constricting channel. Gel beads are flowed through a microfluidic comparator in order to measure the added resistance of the gel, as well as their velocity. The friction of the gels is due to the lubricating fluid between it and the channel, which depends on the gel speed, elasticity and size.